

Dissertation
submitted to the
Combined Faculty of Natural Sciences and Mathematics
of the Ruprecht-Karls-Universität of Heidelberg, Germany
for the degree of
Doctor of Natural Sciences

Put forward by
Marta Reina Campos
born in Barcelona, Spain
Oral examination: 22.10.2020

Formation and evolution of globular clusters
in a cosmological context

Referees: Dr. J. M. Diederik Kruijssen
Prof. Dr. Friedrich. K. Röpke

Zusammenfassung

Sternhaufen können in einer Vielzahl galaktischer Umgebungen beobachtet werden: von ihren momentanen Entstehungsplätzen wie den Scheiben der Antennae-Galaxien, bis hin zu den alten Kugelsternhaufen welche sich hauptsächlich im Halo der Milchstraße befinden. Dies legt nahe, dass die Evolution dieser rätselhaften Objekte mit der ihrer sie beherbergenden Galaxie zusammen hängt. Diese Doktorarbeit beschäftigt sich mit der Entstehung und Evolution von Sternhaufen in einem kosmologischen Kontext. Um dies zu erforschen werden analytische Modelle entwickelt, welche die Rolle der galaktischen Umgebung bei der Entwicklung der Sternhaufendemographie beschreiben. Dann wird eine Reihe von kosmologischen, hydrodynamischen Simulationen des E-MOSAICS Projektes von Galaxien mit Milchstraßenmasse genutzt, um zu untersuchen wie Sternhaufen entstehen und wie sie sich über die kosmische Geschichte hinweg entwickeln. Diese Simulationen werden ebenfalls verwendet, um zu bestimmen wie viel Sternhaufen zu dem Aufbau von stellaren Halos beitragen. Zuletzt präsentieren wir die EMP-Pathfinder Simulationen, welche die nächste Generation der Simulationen zur Co-Entstehung und Evolution von Sternhaufen und der sie umgebenden Galaxien in einer kalten, dichten kosmischen Umgebung darstellen. Aus diesen Untersuchungen wird die Schlussfolgerung gezogen, dass Sternhaufen eng mit ihren kosmischen Umgebungen verbunden sind. Daraus ergeben sich aufregende neue Forschungsrichtungen welche abschließend kurz diskutiert werden.

Abstract

Stellar clusters are observed in a variety of galactic environments, from their current formation sites like the disks of the Antennae galaxies to the old globular cluster populations which in the Milky Way mostly reside in the halo. This suggests that the evolution of these puzzling objects may be linked to that of their host galaxy. This thesis explores the formation and evolution of stellar clusters in a cosmological context. For that, analytical models are developed to describe the role of the galactic environment in shaping their demographics. A suite of cosmological, hydrodynamical simulations of Milky Way-mass galaxies from the E-MOSAICS project are used to study when stellar clusters form and how they evolve over cosmic history. These simulations are also employed to estimate the contribution of stellar clusters to the build-up of stellar haloes. Finally, the EMP-*Pathfinder* simulations are presented, which represent the next generation of simulations of the co-formation and evolution of stellar clusters alongside their host galaxies in a cold, dense cosmic environment. The conclusion drawn from these studies is that stellar clusters are tightly linked to their host cosmic environments. This leads to exciting new future directions that are briefly discussed.

Contents

Preface	iii
1 Introduction and background	1
1.1 Historical perspective on globular clusters	1
1.2 Stellar clusters across cosmic environments	4
1.3 Modelling the formation and evolution of stellar clusters	11
I Formation and evolution of globular clusters	
2 A unified model for the maximum mass scales of molecular clouds, stellar clusters and high-redshift clumps	19
2.1 Introduction	20
2.2 Model	21
2.3 Exploration of parameter space	23
2.4 Comparison to observations of clouds and clusters	26
2.5 Conclusions	33
3 A systematic analysis of star cluster disruption by tidal shocks – I. Controlled N-body simulations and a new theoretical model	37
3.1 Introduction	38
3.2 N-body simulations	40
3.3 Evolution of the mass and the size of the cluster	41
3.4 Discussion	43
3.5 Conclusions	51
II Globular clusters in a cosmological context	
4 Formation histories of stars, clusters, and globular clusters in the E-MOSAICS simulations	57
4.1 Introduction	58
4.2 The E-MOSAICS project	59
4.3 Formation histories of stars, clusters and globular clusters	61
4.4 Median ages of stars, clusters and GCs	64
4.5 Formation histories of metallicity subsamples of stars, clusters and GCs	65

4.6	Comparison to previous works	69
4.7	Conclusions	69
5	Dynamical cluster disruption and its implications for multiple population models in the E-MOSAICS simulations	73
5.1	Introduction	74
5.2	Dependence of cluster mass-loss on the galactic environment	75
5.3	Observed fraction of enriched stars	75
5.4	Reconciling models and observations	77
5.5	Discussion	79
6	The mass fraction of halo stars contributed by the disruption of globular clusters in the E-MOSAICS simulations	81
6.1	Introduction	82
6.2	Summary of the E-MOSAICS simulations	83
6.3	Mass fraction of halo stars formed in GCs	83
6.4	Comparison to the Milky Way	85
6.5	Summary	87
III Stellar clusters in a cold and dense cosmic environment		
7	Modelling the co-formation and evolution of stellar clusters and their host galaxies in EMP-<i>Pathfinder</i>	91
7.1	Stellar clusters and their host galaxies in EMP- <i>Pathfinder</i>	92
7.2	Initial conditions	112
7.3	Preliminary results	115
7.4	Appendices	117
8	Conclusions	131
8.1	Summary	131
8.2	Discussion and reflection	137
8.3	Future directions	142
Acknowledgements		145
Bibliography		147

Preface

The research presented in this thesis has been conducted at the Astronomisches Rechen-Institut - Zentrum für Astronomie at University of Heidelberg between September 2016 and July 2020.

This thesis is aimed at fostering our understanding of stellar cluster formation and evolution in a cosmic environment, and it is divided in three parts. Firstly, analytical models describing the processes leading to the formation of stellar clusters, and their evolution in a cosmological context are explored in Part I (Chapters 2 and 3). Then, in Part II we use simulated stellar cluster populations from self-consistent, hydrodynamical simulations to place constraints on when, how and where stellar clusters form and evolve (Chapters 4 to 6). Lastly, Part III presents the next generation of cosmological simulations of the co-formation and evolution of stellar clusters alongside their host galaxies while capturing the hierarchical nature of the ISM (Chapter 7).

The articles described in Chapters 2 to 6 (Reina-Campos and Kruijssen, 2017; Reina-Campos et al., 2018, 2019; Webb et al., 2019a; Reina-Campos et al., 2020) have been published in peer-reviewed international journals and are the result of collaboration with other authors, as listed below. In four of these articles, corresponding to Chapters 2 and 4 to 6, my contribution is that of a principal author, and in the fifth article, Chapter 3, the principal authorship is distributed equally among coauthors. A detailed description of my contribution to each multi-authored paper is included at the beginning of each chapter. All of them have been shared with and agreed upon by all of my coauthors. The published versions of the articles are included with permission from the journals. The full reference of the publications included in this thesis are:

- Chapter 2: Marta Reina-Campos and J. M. Diederik Kruijssen (2017). “A unified model for the maximum mass scales of molecular clouds, stellar clusters and high-redshift clumps”. MNRAS 469.2, 1282–1298. arXiv: 1704.00732 [astro-ph.GA]
- Chapter 3: Jeremy J. Webb et al. (2019a). “A systematic analysis of star cluster disruption by tidal shocks - I. Controlled N-body simulations and a new theoretical model”. MNRAS 486.4, 5879–5894. arXiv: 1812.00014 [astro-ph.GA]
- Chapter 4: Marta Reina-Campos et al. (2019). “Formation histories of stars, clusters, and globular clusters in the E-MOSAICS simulations”. MNRAS 486.4, 5838–5852. arXiv: 1905.02217 [astro-ph.GA]

- Chapter 5: Marta Reina-Campos et al. (2018). “Dynamical cluster disruption and its implications for multiple population models in the E-MOSAICS simulations”. MNRAS 481.3, 2851–2857. arXiv: 1809.03499 [astro-ph.GA]
- Chapter 6: Marta Reina-Campos et al. (2020). “The mass fraction of halo stars contributed by the disruption of globular clusters in the E-MOSAICS simulations”. MNRAS 493.3, 3422–3428. arXiv: 1910.06973 [astro-ph.GA]

Lastly, Chapter 7 presents an excerpt from a manuscript in preparation (Reina-Campos et al. in prep.) in which my contribution is that of the principal author.

In addition, during the development of this thesis I have also contributed to several other articles as a secondary author, which are listed below in inverse chronological order:

- Benjamin W. Keller et al. (2020). “Where did the globular clusters of the Milky Way form? Insights from the E-MOSAICS simulations”. MNRAS 495.4, 4248–4267. arXiv: 2005.05342 [astro-ph.GA]
- Nate Bastian et al. (2020). “The globular cluster system mass-halo mass relation in the E-MOSAICS simulations”. *arXiv e-prints*, arXiv:2005.05991, arXiv:2005.05991. arXiv: 2005.05991 [astro-ph.GA]
- Sebastian Trujillo-Gomez et al. (2020). “The kinematics of globular cluster populations in the E-MOSAICS simulations and their implications for the assembly history of the Milky Way”. *arXiv e-prints*, arXiv:2005.02401, arXiv:2005.02401. arXiv: 2005.02401 [astro-ph.GA]
- J. M. Diederik Kruijssen et al. (2020). “Kraken reveals itself – the merger history of the Milky Way reconstructed with the E-MOSAICS simulations”. *arXiv e-prints*, arXiv:2003.01119, arXiv:2003.01119. arXiv: 2003.01119 [astro-ph.GA]
- Joel L. Pfeffer et al. (2020). “Predicting accreted satellite galaxy masses and accretion redshifts based on globular cluster orbits in the E-MOSAICS simulations”. *arXiv e-prints*, arXiv:2003.00076, arXiv:2003.00076. arXiv: 2003.00076 [astro-ph.GA]
- Meghan E. Hughes et al. (2020). “The $[\alpha/\text{Fe}]$ - $[\text{Fe}/\text{H}]$ relation in the E-MOSAICS simulations: its connection to the birth place of globular clusters and the fraction of globular cluster field stars in the bulge”. MNRAS 491.3, 4012–4022. arXiv: 1912.01660 [astro-ph.GA]
- Joel L. Pfeffer et al. (2019b). “Young star cluster populations in the E-MOSAICS simulations”. MNRAS, arXiv:1907.10118, arXiv:1907.10118. arXiv: 1907.10118 [astro-ph.GA]
- Sebastian Trujillo-Gomez et al. (2019). “A model for the minimum mass of bound stellar clusters and its dependence on the galactic environment”. MNRAS 488.3, 3972–3994. arXiv: 1907.04861 [astro-ph.GA]

- Joel L. Pfeffer et al. (2019a). “The evolution of the UV luminosity function of globular clusters in the E-MOSAICS simulations”. MNRAS 487.4, 4550–4564. arXiv: 1906.01755 [astro-ph.GA]
- J. M. Diederik Kruijssen et al. (2019b). “The formation and assembly history of the Milky Way revealed by its globular cluster population”. MNRAS 486.3, 3180–3202. arXiv: 1806.05680 [astro-ph.GA]
- Meghan E. Hughes et al. (2019). “Fossil stellar streams and their globular cluster populations in the E-MOSAICS simulations”. MNRAS 482.2, 2795–2806. arXiv: 1810.09889 [astro-ph.GA]
- Christopher Usher et al. (2018). “The origin of the ‘blue tilt’ of globular cluster populations in the E-MOSAICS simulations”. MNRAS 480.3, 3279–3301. arXiv: 1807.03084 [astro-ph.GA]
- M. Messa et al. (2018). “The young star cluster population of M51 with LEGUS - II. Testing environmental dependences”. MNRAS 477, 1683–1707. arXiv: 1803.08527

Chapter 1

Introduction and background

Stellar clusters can loosely be defined as gravitationally-bound systems of stars that are confined in small regions of space. These objects exhibit great variety in their physical properties: some are almost perfectly spherical, whereas others are more irregular; some contain large numbers of stars and some are scarcely populated; some are almost as old as the Universe, whereas others are currently forming. These characteristics have led to their division in two categories, namely the ‘*globular*’ and the ‘*open*’ or galactic star clusters, but exceptions exist for each physical property considered. Understanding their formation and evolution is a major challenge that can only be overcome by studying their demographics and the imprint that the cosmic environment has left on them.

This introduction is organized as follows. Section 1.1 is devoted to reviewing the historical advent of the aforementioned categories and their associated properties, as well as early works using the stellar cluster population of the Milky Way to study its structure. A description of several models to understand the formation of these objects can be found in Section 1.2. There, we discuss the suggestion that stellar clusters are a continuous distribution of systems that undergo the same physical processes, in which the old and massive globular clusters represent the extreme population of clusters that formed at high-redshift and survived to the present day. Under this hypothesis, we describe the current observational knowledge of stellar clusters across cosmic environments. Finally, the current understanding of the formation and evolution of stellar clusters is introduced in Section 1.3, with emphasis on state-of-the-art numerical simulations of the co-formation and evolution of stellar clusters alongside their host galaxies.

1.1 Historical perspective on globular clusters

With the advent of telescopes, gazing at the night sky became a continuous source of exciting discoveries. From the phases of Venus described by Galileo Galilei and the development of Kepler’s laws of planetary motion back in the 17th century to the recent detection of gravitational waves, observing the night sky has continuously revolutionised our cosmogony. In order for this to happen, systematic observations and analyses of the collected data has been crucial to derive a new understanding of the origin of the Universe.

Around the mid-18th century, astronomers started to scan the skies with the aim of cataloguing the position and brightness of sidereal objects. Over the following hundred years, several surveys and catalogues of nebulae and star clusters observed from both hemispheres were published (e.g. Messier, 1781; Herschel, 1786, 1789, 1800; Dunlop, 1828; Herschel, 1864; Dreyer, 1888). The improvement of telescopes allowed each new catalogue to revise the measurements from the previous ones, and to expand our knowledge by adding more objects. The number of catalogued nebulae and star clusters grew by a factor of seventy in about hundred years: the Messier catalogue (Messier, 1781) contains about a hundred of nebulae and star clusters, whereas the New General Catalogue (Dreyer, 1888) contains 7840 objects.

Of particular interest are the three catalogues performed during the late 18th century by Sir Dr. William Herschel assisted by his sister Caroline (Herschel, 1786, 1789, 1800). Their systematic study of the northern skies led to the discovery of 2500 sidereal objects. These nebulae and star clusters were divided into different categories depending on their brightness and spatial extent: from the brightest and richest nebulae and stellar clusters to the more scattered and extended accumulation of stars. The term ‘*globular cluster of stars*’ is first used in these catalogues to refer to the brightest and roundest stellar clusters. Their spherical shape is argued to be caused by the presence of a central power that exerts a radially inwards force over the stars, and the extent of the spatial compression is suggested to be related with the time during which the forces have been experienced.

These remarkable suggestions are some of the first steps towards understanding the formation of stellar clusters¹. Herschel was encouraged by the hope that the great variety in shapes of the nebulae and stellar clusters would foster further progress on understanding their formation (Herschel, 1789). Since the publications of these early catalogues, there has been a growing interest in the nature of these objects, and there is a large body of literature currently addressing this question (e.g. see recent reviews by Krumholz et al., 2019; Adamo et al., 2020).

Once data on the brightness and position of nebulae and star clusters became available in standardized catalogues (e.g. Herschel, 1864; Dreyer, 1888; Bailey, 1908; Melotte, 1915), astronomers started to wonder about the peculiarities of these objects. The simultaneous observation of gaseous nebulae and stellar clusters introduced the notion of change in the static cosmogony accepted at the time, and researchers wondered whether these objects represented different moments in the evolution from gas to radiating stars (Airy, 1836). The globular shape of star clusters also drew attention, and the first statistical descriptions of stars within clusters were built on analogies to gas thermodynamics (e.g. Plummer, 1911; Jeans, 1916).

To dilucidate the nature of nebulae and star clusters, determining their physical properties became of paramount importance. Detailed observations of star clusters led to the discovery of variable Cepheid stars in them (e.g. Pickering, 1889), which were then used alongside the period-luminosity relation discovered by Miss Henrietta Swan Leavitt to determine the distance to these sidereal objects (e.g. Shapley, 1917, 1918a,c,d). Knowing the

¹In the context of this thesis, the term ‘stellar cluster’ has the implicit assumption of gravitational boundedness, whereas unbound stellar systems will be referred to as ‘associations’.

distances to star clusters revolutionized the accepted Galactic cosmogony², as it provided the first three-dimensional description of the stellar systems surrounding the Sun. The spatial distribution of clusters also fostered a debate about the nature of the observed nebulae: some authors argued them to be components of our Galaxy, whereas others suggested that they are independent galactic systems as the Milky Way (e.g. Curtis, 1917; Shapley, 1919; Shapley and Shapley, 1919; Curtis, 1920). This debate only settled for the latter suggestion after the observation of Cepheid stars in the Andromeda Galaxy (then Nebula), which allowed the first distance determinations to these extragalactic systems (Hubble, 1929).

Since the initial classifications by Herschel, stellar clusters had only been divided in different categories based on their shape and brightness, i.e. globular clusters are almost perfectly spherical and contain large numbers of stars compared to the more extended and less populated clusters. The three-dimensional spatial distribution of star clusters added a further division in these categories as they were observed in mutually exclusive regions: the globular and brightest clusters lie preferentially in the outer regions of the Galaxy, whereas open or galactic clusters are predominantly observed alongside the plane of the Galaxy (e.g. Shapley, 1918a; Trumpler, 1929, 1930a). Additionally, the brightest stars in globular clusters are observed to be preferentially redder relative to the bluer stars in the more extended clusters (Shapley, 1918b). When compared to theoretical stellar evolutionary tracks using colour magnitude diagrams, the brighter redder stellar populations of globular clusters were found to be older than the brightest bluer open clusters (Johnson, 1954).

This dicotomy in their properties fostered the idea that these two types of clusters are independent objects. ‘*Globular*’ clusters (GCs) are observed to be spherical and of similar physical size, to contain a larger number of stars and hence to have larger masses, to have brighter redder stellar populations and to populate the outskirts of the Galaxy. On the contrary, ‘*open*’ clusters are more irregular and extended, contain fewer stars and hence less mass, have brighter bluer stellar populations and preferentially occupy the plane of the Galaxy (e.g. Shapley, 1930; Trumpler, 1931). However, even in those early days of stellar cluster science, there were already some objects that did not fit in this binary categorization of objects: NGC5053 resembled an ‘open’ cluster, but it was also argued that it should be in the ‘globular’ category given its galactic position and number of variable stars (Trumpler, 1931).

Moreover, further analysis of the GC population in the Milky Way found two spatially and kinematically-distinct subpopulations of clusters that also differ in their mean metallicities³ (e.g. Kinman, 1959a,b; Zinn, 1985), thus explaining the bimodal nature of the Galactic metallicity distribution (first discussed by Harris and Canterna, 1979). Metal-poor clusters ($[\text{Fe}/\text{H}] \leq -0.8$) are observed to be spherically distributed about the Galaxy, without a net rotational velocity and with a large velocity dispersion, whereas metal-rich GCs ($[\text{Fe}/\text{H}] > -0.8$) have a flattened distribution and rotate with the Galactic disk. These

²Following standard conventions, in this thesis the term ‘Galactic’ is used to refer to properties of the Milky Way, in contrast to properties of other galaxies that are referred to as ‘galactic’.

³The metallicity is defined in terms of the ratio of iron abundance to hydrogen, $[\text{Fe}/\text{H}]$. This quantity is expressed relative to the solar iron abundance as, $[\text{Fe}/\text{H}] = \log_{10}(N_{\text{Fe}}/N_{\text{H}})_{\star} - \log_{10}(N_{\text{Fe}}/N_{\text{H}})_{\odot}$, where N_{Fe} and N_{H} are the number of atoms of iron and hydrogen, respectively, per unit of volume.

properties have been used to relate these subpopulations to the halo⁴ and the disk stellar populations, respectively, and to suggest that they probably formed under somewhat different conditions (Zinn, 1985), thus inspiring studies that model each formation channel independently (e.g. Moore et al., 2006).

In addition to understanding the nature of star clusters, knowing the distances and physical properties of these objects allowed to explore the Galaxy in a way that had not been possible before. The distance to the center of the Galaxy and its structure has been explored in a number of occasions using the three-dimensional distribution of star clusters (e.g. Shapley, 1918a; Arp, 1965; Woltjer, 1975; Harris, 1976; Frenk and White, 1982). The centroid of the stellar cluster systems has been estimated to be $\sim 8\text{--}9$ kpc away from the Earth towards a galactic longitude of 325° , thus suggesting a similar distance to the Galactic Center.

There are plenty of other examples of the use of stellar clusters to infer the structure of the Galaxy, as their bright luminosities and the estimations of their distances allowed astronomers to use them as beacons in the darkness. The superposition of star clusters relative to background giant molecular clouds has been used to determine the distances to those clouds and estimate the size of the Galaxy (Barnard, 1920). Moreover, the positions of open star clusters were also used to suggest a spiral pattern for our Galaxy (Trumpler, 1930b; Johnson et al., 1961). Lastly, the Milky Way was found to experience galactic rotation towards negative galactic longitudes using the motion of star clusters (Hayford, 1932). Some decades later, new observations of these motions were used to rederive the rotation curve of our Galaxy and to suggest the existence of a massive dark halo (Frenk and White, 1980).

Additionally, a plethora of studies have used the properties of stellar clusters to disentangle the formation history of the Milky Way (see a recent review by Helmi, 2020). From the observation that outer halo GCs have a wider range of ages than inner halo GCs for a given metallicity, Searle and Zinn, (1978) suggested that these objects originated in accreted protogalactic fragments that continued to fall into the Milky Way after the formation of its central component. This scenario has been widely discussed in the literature, and it was confirmed with the discovery of the accretion of the Sagittarius dwarf galaxy (Ibata et al., 1994). Moreover, the accreted GCs from the Sagittarius dwarf have been associated with the shallower branch in the age-metallicity relation of Galactic GCs (e.g. Forbes and Bridges, 2010; Massari et al., 2019; Forbes, 2020), which have led to the suggestion that this parameter space holds a great potential for tracing the formation and assembly history of galaxies using stellar cluster populations (e.g. Forbes and Bridges, 2010; Kruijssen et al., 2019a,b; Massari et al., 2019).

1.2 Stellar clusters across cosmic environments

Since the first suggestions about the nature and origin of stellar clusters (Herschel, 1789), many authors have used the latest available data on the physical properties of stellar cluster

⁴The stellar halo of a galaxy refers to the spherical distribution of stars that extends further than the galactic disk, and it typically contains the oldest and most metal-poor stars (see review by Helmi, 2008).

populations to put forward models describing the origin of these sidereal stellar systems. The basic assumption in these models is that the demographics of star clusters encode information about the mechanisms driving their formation and evolution. Depending on the conditions of the Universe argued to lead to the formation of clusters, these models can be split into two families. The first family of models assumes that special conditions in the early Universe were needed to form the massive and old globular stellar clusters (e.g. Peebles and Dicke, 1968; Fall and Rees, 1985). On the contrary, the second family relates the process of cluster formation as the outcome of regular star formation across cosmic evolution, in which the observed stellar cluster systems are the result of their evolution in a cosmological context over a Hubble time (e.g. Ashman and Zepf, 1992; Elmegreen and Efremov, 1997; Kruijssen, 2015).

In the first family of models, the formation of massive clusters is suggested to generally happen either prior or during the collapse of the galaxy. Among these models, many different scenarios have been considered; from thermal instabilities in the primeval fireball paradigm (i.e. the Big Bang) collapsing to typical GCs masses (Peebles and Dicke, 1968; Peebles, 1984), to metal-poor GCs forming either in rare overdense peaks at high-redshift ($z > 10$, Diemand et al. 2005; Boley et al. 2009), in colliding supershells from Population III hypernova explosions (Recchi et al., 2017), in high-speed collisions of dark matter (DM) subhaloes (Madau et al., 2020), in high-density regions along cosmic filaments before or during the collapse of the galaxy (Boylan-Kolchin, 2017), or in DM mini haloes (Griffen et al., 2010; Trenti et al., 2015). Other formation triggers have been suggested to be thermal instabilities in hot gas-rich haloes (Fall and Rees, 1985), and shock compression or cloud-cloud collisions (e.g. Gunn, 1980; McCrea, 1982; Murray and Lin, 1992; Harris and Pudritz, 1994; Vietri and Pesce, 1995; Larson, 1996; Cen, 2001). Despite the diversity of mechanisms suggested, these models agree that metal-poor GCs formed much earlier than the bulk of star formation ($z \sim 2$, e.g. Madau and Dickinson, 2014), and generally struggle at reproducing all the observed properties of these populations of objects (Kruijssen, 2014).

The latter family of models suggests that stellar clusters are a natural result of normal star formation over cosmic time, in which high gas density or pressure environments typically lead to the formation of more massive clusters (e.g. McCrea, 1961; Schweizer, 1987; Ashman and Zepf, 1992; Elmegreen and Efremov, 1997; Kravtsov and Gnedin, 2005; Elmegreen, 2010; Shapiro et al., 2010; Kruijssen, 2015). One of the main arguments in favour of this hypothesis is that it accounts for all products of star formation over cosmic history. These models assume that star clusters are part of a continuum whose physical properties are influenced by their natal sites and their subsequent evolution across cosmic environments. In this scenario, GCs represent the extreme massive, old and relatively metal-poor end of the distribution.

This hypothesis predicts a population of young and massive stellar clusters (YMCs) forming in environments of high gas pressure with high star formation rates (SFRs). These objects were first observed as populations of ‘blueish knots’ or ‘super star clusters’ from ground-based telescopes on starburst galaxies (van den Bergh, 1971; Arp and Sandage, 1985) and galaxy mergers (Schweizer, 1982; Lutz, 1991). Since then, multiple YMC populations have been observed in the local Universe with the *Hubble Space Telescope* (e.g. Holtzman

et al., 1992; Whitmore and Schweizer, 1995; Holtzman et al., 1996; Whitmore et al., 1999; Zepf et al., 1999), and their physical properties have been measured in detail (for recent reviews, see Portegies Zwart et al., 2010; Krumholz et al., 2019; Adamo et al., 2020). These observations provide strong support to the hypothesis that cluster formation traces periods of high intensity of star formation.

The physical mechanism driving the enhanced gas pressures leading to stellar cluster formation is under debate. Fostered by the early observations of YMC formation in interacting galaxies, some authors suggest that these high-pressure environments are predominantly triggered by galaxy mergers (e.g. Schweizer, 1987; Ashman and Zepf, 1992). In a more general approach, other authors argue that these high pressures are the result of cosmic evolution (e.g. Kruijssen, 2015), because higher redshift environments or more massive galaxies tend to have higher pressures than lower redshift environments (e.g. Tacconi et al., 2013). As discussed in Section 1.3, Keller et al., (2020) uses a state-of-the-art simulation of the co-formation and evolution of stellar clusters alongside their host galaxies to evaluate the importance of each formation channel in the present-day globular cluster population. They find that only a small percentage of the surviving massive clusters form in major mergers, but these are critical for redistributing the cluster populations from the gaseous disks to the outskirts in which they can survive until $z = 0$ (e.g. Elmegreen and Hunter, 2010; Kruijssen et al., 2011; Kruijssen, 2015).

Over the past decade, there have been several reviews addressing the similarity of properties between stellar cluster populations across cosmic environments (e.g. Portegies Zwart et al., 2010; Kruijssen, 2014; Krumholz et al., 2019; Adamo et al., 2020). Since the physical mechanisms governing the formation and evolution of star clusters might determine the distribution of their properties, we proceed to briefly summarize their main properties here.

1.2.1 Bound mass fraction

Star formation occurs in a clustered and hierarchically-distributed fashion due to the interplay between turbulence and gravity within the birth molecular gas clouds (e.g. Lada and Lada, 2003; Elmegreen, 2011; Krumholz et al., 2019). In this hierarchical process, the gravitational stability of the stellar systems is observed to decrease with decreasing gas density: massive gravitationally bound systems form from the densest gas regions, whereas unbound systems such as associations or moving groups are observed to form in lower density gas (e.g. Gieles and Baumgardt, 2008; Bastian et al., 2009; Gouliermis et al., 2015; Grasha et al., 2015, 2017a,b). A key quantity to study cluster formation is the fraction of stars forming in bound young star clusters, which some authors associate to a ‘*cluster formation efficiency*’ (CFE or Γ , Larsen and Richtler, 2000; Bastian, 2008; Kruijssen, 2012).

This quantity is challenging to measure observationally. A main point of debate over the recent years in the literature has been on how to select stellar clusters in extragalactic surveys such that there is no contamination from young unbound systems. Generally, studies use a criterium based on the shape of the stellar clusters: if only spherical shapes are considered, i.e. relaxed systems, unrelaxed and asymmetric bound systems might be

discarded at young ages, i.e. 1–10 Myr, whereas a looser asymmetric criteria can include unbound systems even in longer age ranges. Including asymmetrically-shaped clusters in the catalogues leads to an increased number of young objects, which biases the estimation of the CFE. For that reason, the stricter criterium of selecting relaxed systems is generally used (see discussion by Krumholz et al., 2019; Adamo et al., 2020).

In these studies, the fraction of star formation in bound clusters is found to correlate with the SFR surface density of the galaxy, both when considering clusters in narrow and wide age ranges, i.e. 1–10 Myr or 10–100 Myr (Adamo et al., 2020, see references therein). This correlation was suggested by Goddard et al., (2010), and since then, many surveys and studies have extended it to higher and lower SFR surface densities. Based on the hierarchical nature of star formation, Kruijssen, (2012) derives an analytical model in which the CFE strongly correlates with the gas density or pressure, and therefore indirectly with the SFR surface density, such that the densest gas environments form more mass in bound clusters. The predictions of this model reproduce well current measurements of the CFE across cosmic environments in the local Universe, and this model is commonly used in the literature.

1.2.2 Mass functions

The mass functions of YMC populations are well described by a power-law distribution of slope $\alpha = -2$, and some authors suggest that the lack of clusters at the high-mass end might indicate an exponential suppression of objects at masses higher than an upper scale M_c . This distribution is typically described as a Schechter function, $dN/dm \propto m^\alpha \exp(-m/M_c)$ (Schechter, 1976). The power-law shape is likely produced by the fragmentation of the gas clouds due to the balance between turbulence and gravitational collapse (Elmegreen, 2011).

The upper mass scale M_c is observed to depend on the galactic environment (Larsen, 2009; Adamo et al., 2015; Johnson et al., 2017; Messa et al., 2018), with galaxies like the Antennae which are experiencing higher SFR episodes (and higher gas pressures) forming more massive clusters. This mass scale is argued to reflect the maximum mass of the natal clouds from which clusters form (e.g. Kruijssen, 2014), and the maximum cloud mass scale has been suggested to be the maximum mass that can collapse in a centrifugally-unstable region (i.e. the Toomre mass, Toomre, 1964).

However, this hypothesis predicts an increasing trend towards outer radii, and it does not reproduce the lack of radial trend of this upper mass scale observed in a handful of galaxies (Adamo et al., 2015; Messa et al., 2018). In Chapter 2, we derive an analytical model in which the collapse of the centrifugally-unstable region can be halted by the stellar feedback of the newborn stars in the region, thus reducing the maximum cloud mass scale in certain galactic environments and producing a flat radial profile (Reina-Campos and Kruijssen, 2017). This model has been expanded to the lower mass limit of the mass function to account for the smallest stellar systems that can remain bound (Trujillo-Gomez et al., 2019).

Contrary to YMCs, GCs exhibit a mass function that is well described by a lognormal distribution with a turnover mass of $\sim 2 \times 10^5 M_\odot$ that is observed to be constant among galaxies (Brodie and Strader, 2006; Jordán et al., 2007). The universality of their mass

distributions has fostered a nature vs. nurture debate in the literature: some authors consider that GCs form with this peaked mass function (e.g. Fall and Rees, 1985; Parmentier and Gilmore, 2007), whereas other authors suggest that the evolution of star clusters can transform the exponentially-truncated power-law describing the masses of young star cluster populations into the peaked function observed among the old, massive clusters (e.g. Elmegreen and Efremov, 1997; Baumgardt, 1998; Fall and Zhang, 2001; McLaughlin and Fall, 2008; Kruijssen, 2015). The transformation of the mass function is argued to be mostly driven by tidal shock disruption, which dominates in the dense natal sites of star clusters. The disruption timescale is proportional to the cluster density (e.g. Spitzer, 1958; Prieto and Gnedin, 2008; Kruijssen et al., 2011), and if the density is proportional to the cluster mass, it implies that low-mass clusters are preferentially destroyed by shocks whereas higher-mass clusters can survive. For a more detailed discussion on disruption, see Section 1.2.3.

1.2.3 Age distributions

In our Galaxy, GCs have been observed to be much older than the open cluster population, with ages comparable to the age of the Universe (a median of 12.26 Gyr; Forbes and Bridges, 2010; Dotter et al., 2011; VandenBerg et al., 2013; Kruijssen et al., 2019b). However, the median ages of the most massive GCs in the Milky Way and the Magellanic Clouds (with masses $M > 10^5 M_{\odot}$ and $M > 5 \times 10^4 M_{\odot}$, respectively), show a decreasing trend with galaxy mass, with the massive GC population in the Small Magellanic Cloud being only ~ 7 Gyr old (Glatt et al., 2009, 2010, 2011; Baumgardt et al., 2013; Niederhofer et al., 2017; Martocchia et al., 2018). This age trend reflects the slower build-up of lower mass galaxies (i.e. ‘galaxy downsizing’, Baldry et al., 2004; Noeske et al., 2007; Whitaker et al., 2012), and provides further support to the hypothesis that stellar clusters are relics of intense periods of star formation.

In addition to the massive cluster formation observed at the present day in many interacting galactic systems in the local Universe, recent observations of high-redshift ($z \sim 3-6$) lensed galaxies using the *Very Large Telescope* have led to direct observations of proto-GC candidates in their natal environments (Bouwens et al., 2017; Johnson et al., 2017; Vanzella et al., 2017, 2019, 2020). Some of these objects are particularly intriguing, since their physical properties are very close to those expected of nascent GC at high redshift in terms of mass, size and star formation activity (e.g. GC1 described by Vanzella et al., 2017). Future observations of these stellar systems with the *James Webb Space Telescope* (JWST) and the next generation of 30-m class ground-based telescopes will improve our current understanding of cluster formation in high-redshift environments, and the role of massive clusters in the early Universe.

When representing the age distribution of a stellar cluster population as $\log_{10}(dN/dt/[yr^{-1}])$ relative to the logarithm of the cluster age in years, it generally can be described by a power-law function. For a constant cluster formation rate, the slope becomes steeper due to cluster disruption. By looking at this distribution as a function of cluster mass, studies find that more massive clusters present shallower slopes than less massive ones, suggesting that the cluster survival time, i.e. time until the star cluster is completely unbound, is

mass-dependent (Silva-Villa et al., 2014; Adamo et al., 2017; Messa et al., 2018).

Theoretical studies have long suggested that different physical mechanisms can disrupt stellar clusters by injecting energy to the stars (e.g. Spitzer, 1940; King, 1957; Spitzer, 1958; Spitzer and Harm, 1958; Hénon, 1961; van den Bergh, 1962; Bouvier and Janin, 1970; Baumgardt and Makino, 2003; Lamers et al., 2005a,b; Gieles et al., 2006, 2007; Prieto and Gnedin, 2008). These mechanisms are generally divided in two types depending on the source of the energy injection. Stellar evolution and relaxation-driven mass loss are considered internal evolutionary processes, with the former acting predominantly during the first 10–100 Myr. The latter, which is also referred to as evaporation or two-body interactions, dominates on longer timescales in gas-poor environments and its associated timescale grows with the mass of the cluster (e.g. Spitzer, 1940; Spitzer and Harm, 1958; Hénon, 1961; Spitzer and Hart, 1971; Spitzer, 1987; Giersz and Heggie, 1994; Lamers et al., 2005b; Gieles and Baumgardt, 2008).

The main external disruption mechanism is tidal shocks due to interactions with the surrounding gas substructure in the galaxy. This mechanism dominates in the dense and gas-rich environments in which massive clusters form (Lamers et al., 2005a; Gieles et al., 2006; Elmegreen, 2010; Elmegreen and Hunter, 2010; Kruijssen et al., 2012; Miholics et al., 2017), and it has thus been suggested that only the migration of stellar clusters from their natal sites to the galactic outskirts allows for cluster survival (Elmegreen, 2010; Kruijssen et al., 2011; Kruijssen, 2015; Pfeffer et al., 2018). Analytic derivations of the energy injected by tidal shocks find that the disruption timescale associated to tidal shocks scales with the strength of the shock and with the density of the cluster (Spitzer, 1958; Gnedin and Ostriker, 1999; Gnedin, 2003; Gieles et al., 2006; Binney and Tremaine, 2008; Prieto and Gnedin, 2008; Kruijssen et al., 2011), with loose clusters disrupting faster than compact objects. In the case of very compact clusters, the energy injected from tidal shocks first adiabatically expands the cluster before unbinding stars (Weinberg, 1994a,b,c; Gnedin, 2003).

These analytical derivations assume that the interactions are impulsive, i.e. that the duration of the shock is much shorter than the crossing time of the stellar system, in addition to other assumptions regarding the distribution function of the stars in clusters or the amount of mass lost given an increase in energy. With the aim of doing a systematic analysis of the influence of tidal shocks on stellar clusters, we present in Chapter 3 a suite of N -body simulations of individual clusters undergoing simplified tidal histories. By looking at the mass and size evolution of these simulated star clusters, we derive an empirical description for the shock disruption timescale that has shallower scalings with the cluster density and tidal field strength than the classical analytical description. For a given cluster density, this new formalism predicts a stronger disruptive effect for tidal shocks (Webb et al., 2019a).

1.2.4 Size and density distributions

Back in 1918, it was already noted that the diameter-parallax relation observed in star clusters, with smaller clusters being further away, implied a similar physical dimension of those clusters (Shapley, 1918a). Measuring the size of a cluster is more challenging than

measuring its age or mass because the cluster needs to be at least marginally resolved. Despite this limitation, nowadays there are measurements of the size of star clusters in a variety of nearby galaxies (see the compilation in Krumholz et al., 2019).

Given that the cluster density is crucial in driving their evolution, it is relevant to study any possible dependence between the sizes and the masses of clusters. By comparing stellar cluster populations in a handful of nearby galaxies, Krumholz et al., (2019) find a weak scaling between the mass and the radius of star clusters, both in terms of its slope and large scatter, over five orders of magnitude in mass. The authors also find that the size distribution seems to be bound at both the upper and lower scales, and most interestingly, that there is no distinction between the mass-size distributions of GCs and of young clusters in the disk of galaxies. This confirms the suggestion that star clusters have similar physical sizes (Shapley, 1918a), and it implies that the dependence of different cluster evolution mechanisms on the cluster density can be understood in terms of their mass. Hence, low-mass clusters disrupt faster due to two-body interactions and tidal shocks than massive clusters, thus potentially transforming the initial power-law mass function into a lognormal distribution (e.g. Elmegreen and Efremov, 1997).

1.2.5 Multiple stellar populations

The chemical composition of stars within clusters holds promising information about the composition of the natal cloud from which they formed, as well as about the processes of star and cluster formation. From their simple colour magnitude diagrams, stellar clusters have long been considered to represent single stellar populations that formed in a single burst of star formation (e.g. Johnson, 1954; Crampin and Hoyle, 1961). Open clusters are observed to be homogeneous in all of the chemical abundances that have been measured, but the majority of GCs seem to present light element abundance variations (e.g. Li, C, N, O, F, Na, Mg, and/or Al; Piotto et al., 2007; Carretta et al., 2010). These chemical inhomogeneities break the assumption of a single stellar population in the old, massive clusters, and are commonly referred to as ‘*multiple stellar populations*’.

Interestingly, not all of the observed GCs in the Milky Way and the Magellanic Clouds present these chemical inhomogeneities; R106 is a classical GC in terms of its age and mass, and it exhibits homogeneous chemical abundances (Villanova et al., 2013). A lack of N-enrichment has been found in massive clusters younger than 2 Gyr in the Magellanic Clouds (Martocchia et al., 2018). Additionally, older clusters exhibit a correlation between the amount of the N-enrichment and cluster age. Martocchia et al. suggest that age might be a relevant factor in the onset of multiple stellar populations in young clusters, because the strength of the enrichment might not be detectable at ages younger than ~ 2 Gyr.

Current models describing this phenomenon typically require multiple episodes of star formation in which part of the first generation of stars pollutes the pristine gas from which a second generation of stars forms. The combination of the small amounts of enriched material ejected by the typical polluters (e.g. de Mink et al., 2009) and the similar ratios of chemical subpopulations in clusters (e.g. Milone et al., 2017) imply that these models require stellar clusters to have been > 10 times more massive at birth, and to have lost the majority of the unpolluted stars by the present day. This is known as the ‘mass-budget’

problem in the literature, and there is currently no agreement regarding the polluter or the type of pollution required to reproduce all of the observed trends (for a recent review, see Bastian and Lardo, 2018).

These observational properties suggest that the formation and evolution of stellar clusters is strongly dependent on the cosmic environment: from the conditions leading to massive cluster formation in dense gas clouds being reflected in their mass distribution and abundance relative to field stars, to their survivability being set by the cosmic environments in which clusters reside over their lifetimes. For this reason, in order to model the formation and disruption of stellar clusters one needs to also account for the assembly and evolution of their host galaxies over cosmic time. Over the past decade, there have been great advances in the numerical modelling of stellar clusters. The next section presents a summary of these efforts.

1.3 Modelling the formation and evolution of stellar clusters

The environmental dependences imprinted in the distributions of the properties of stellar clusters imply that modelling the formation and evolution of these objects over cosmic history also requires a self-consistent description for the formation and evolution of their host galaxies. Such a holistic perspective calls for the description of the baryonic physics relevant for the formation of galaxies in a cosmological setting.

Over the past ten years, the numerical description of the co-formation and evolution of stellar clusters alongside their host galaxies has taken a major leap forward (see Forbes et al., 2018, for a recent review), with some studies being able to resolve the cold gas flows leading to massive cluster formation (Li et al., 2017; Kim et al., 2018; Li et al., 2018; Lahén et al., 2019; Ma et al., 2020a). These simulations consider different galactic environments for resolving the formation of massive clusters, from Milky Way-sized progenitors at $z > 2$ (Li et al., 2017, 2018) to a dwarf-dwarf merging system (Lahén et al., 2019), or dwarf galaxies at $z \sim 5$ (Kim et al., 2018; Ma et al., 2020a).

These studies represent the current state-of-the-art simulations of resolved clusters in a galactic context because of their detailed description of star cluster formation from the densest gas structures. In addition, these simulations allow to study the influence of the young clusters in their natal environment (e.g. Ma et al., 2020b). In order to resolve the birth sites of star clusters and their dynamical evolution in a cosmological context, spatial resolutions of the order of parsecs or even higher are needed. The extremely high spatial resolution required imposes strong constraints on the number of simulations that can be run and on the lowest redshift that can be reached, and so these simulations lack the statistical power for describing entire stellar cluster populations to the present day.

To circumvent this limitation, another avenue of exploration has consisted in adding a description of the formation of GCs⁵ while post-processing dark matter-only simulations to include baryons (Beasley et al., 2002; Muratov and Gnedin, 2010; Griffen et al., 2013;

⁵From here onwards, we refer to massive stellar clusters as such or as ‘globular clusters’ interchangeably.

Choksi et al., 2018; El-Badry et al., 2019; Choksi and Gnedin, 2019). These simulations hold immense statistical power, as the computational requirements for running many different merger trees are much smaller, and the cosmic evolution of a wide halo mass range can easily be studied (e.g. Choksi et al., 2018). However, these studies generally consider a simple description of the formation of stellar clusters and only partial evolution due to evaporation, with some studies not including any disruption at all (e.g. Beasley et al., 2002; El-Badry et al., 2019). An additional drawback of these semi-analytical models of galaxy formation is the lack of a spatially and temporally-resolved description of the galactic environment, which requires making additional assumptions about the influence of the cosmic environment on the stellar cluster populations.

A third approach to study the co-formation and evolution of stellar clusters alongside their host galaxies has been to identify GC candidates in hydrodynamical, cosmological simulations of galaxy formation to study their properties (e.g. Renaud et al., 2017; Halbesma et al., 2020). These studies typically use an empirical description of GCs to select a subset of the stellar particles as such. Their results should be taken with caution because they can be biased depending on the selection criteria used. For instance, in Renaud et al., (2017), an age cut implies a bias towards old ages of the GCs candidates relative to the overall stellar component of the galaxy.

A step forward is to consider that the observed GC populations represent the relics of intense star formation episodes at high redshift. In this scenario, a sub-grid model can be motivated based on the physics that is observed to be relevant for the formation and evolution of stellar clusters in the local Universe at present (MOSAICS; Kruijssen et al., 2011; Pfeffer et al., 2018) and later combined with hydrodynamical, cosmological simulations of galaxy formation (the E-MOSAICS project; Pfeffer et al., 2018; Kruijssen et al., 2019a). The E-MOSAICS project combines the MOdelling Star cluster population Assembly In Cosmological Simulations (MOSAICS; Kruijssen et al., 2011; Pfeffer et al., 2018) sub-grid description of stellar cluster formation and evolution and the EAGLE (Schaye et al. 2015, Crain et al. 2015) galaxy formation model.

This sub-grid approach holds a strong statistical power, as multiple cosmological simulations can be evolved to the present day with barely any overhead time from the cluster description, such that a variety of cosmic environments can be explored across the entire galaxy mass range. In addition, this method allows to evaluate whether this self-consistent description of the co-formation and evolution of stellar clusters alongside their host galaxies is sufficient to reproduce the observed stellar cluster populations, and to what extent stellar clusters can be used to trace the process of galaxy formation and assembly at $z = 0$.

Using this approach, the E-MOSAICS project has evolved to $z = 0$ the stellar cluster populations of 25 cosmological zoom-in simulations of present-day Milky Way-mass galaxies (Pfeffer et al., 2018; Kruijssen et al., 2019a), as well as those of all galaxies present in a cosmological volume of $(34.4 \text{ cMpc})^3$ (Crain et al. in prep.), at a baryonic mass resolution of $2.26 \times 10^5 M_\odot$. This periodic volume contains a total of 1706 galaxies with masses $M_{200} \geq 10^8 M_\odot$, including 80 Milky-Way mass galaxies (with masses $7 \times 10^{11} < M_{200}/M_\odot < 3 \times 10^{12}$), and even a low-mass galaxy cluster ($M_{200} \simeq 5 \times 10^{13} M_\odot$), as well as their simulated stellar cluster populations.

This self-consistent and environmentally-driven approach to cluster formation and evolution has been found to reproduce many observational properties of star cluster populations, such as their mass and age distributions (Pfeffer et al., 2018; Kruijssen et al., 2019a; Pfeffer et al., 2019b), the lack of massive metal-rich GCs (Usher et al., 2018), their age-metallicity relations (Kruijssen et al., 2019a), their kinematics (Trujillo-Gomez et al., 2020), or the total GC-halo mass relation (Bastian et al., 2020). For this thesis, we have used the suite of 25 cosmological zoom-in Milky Way-mass galaxies from the E-MOSAICS project to study how stellar clusters form and evolve in a cosmological context.

The formation histories of stars, clusters and GCs published in Reina-Campos et al., (2019) are studied in Chapter 4, where we find that the E-MOSAICS simulations reproduce the observational evidence that metal-poor GCs are older than the metal-rich subpopulations (e.g. Forbes and Bridges, 2010; Dotter et al., 2011; VandenBerg et al., 2013). In Chapter 5, we evaluate the dynamical disruption of stellar clusters in the E-MOSAICS simulations in the context of the mass-budget problem needed by models that attempt to explain the multiple stellar populations phenomenon. In the simulated stellar cluster populations, the most massive clusters ($M > 10^5 M_{\odot}$) are found to be only a factor 2–4 times more massive at birth, which is in conflict with the suggested models, and solutions are suggested to alleviate the discrepancy.

In addition to enabling the study of the formation and evolution of stellar clusters in a cosmological context, these simulations allow to unveil the potential role of massive stellar clusters as tracers of galaxy formation and assembly. Given that the properties of stellar cluster populations encode information about their natal sites and subsequent evolution (see discussion in Krumholz et al., 2019; Adamo et al., 2020), they can be used to reverse-engineer the conditions of their host galaxies over cosmic time. This idea has long been suggested and explored with observational data (e.g. see Shapley, 1918b, for an early example), but only now can it be fully explored with a complete description of the relation between the stellar clusters and their host environments.

In a recent example, the age-metallicity relation of the GCs in the Milky Way was used to reconstruct its assembly history (Forbes and Bridges, 2010; Kruijssen et al., 2019b; Massari et al., 2019; Kruijssen et al., 2020). Kruijssen et al., (2019b) find that our Galaxy experienced fifteen different accretion events, but only five of those satellite galaxies were massive enough to contribute their own population of stellar clusters: the ‘Sagittarius’ dwarf (Ibata et al., 1994), ‘Sequoia’ (Myeong et al., 2019), the progenitor of the ‘Helmi streams’ (Helmi et al., 1999), ‘*Gaia*-Enceladus’ or ‘Sausage’ (Belokurov et al., 2018; Helmi et al., 2018; Myeong et al., 2018), and ‘Kraken’. This last accretion event is predicted to have been the major accretion event the Milky Way has ever undergone (Kruijssen et al., 2020), and has since its prediction been found using *Gaia* DR2 kinematic data and SDSS/APOGEE⁶ chemical information (Massari et al., 2019; Horta et al., 2020a,b).

To further understand the contribution of satellites to the build-up of the stellar halo, an estimation of the amount of mass contributed by stellar clusters and GCs to the build-up of the galactic haloes in the 25 cosmological simulations of Milky Way-mass galaxies of the E-MOSAICS project is presented in Chapter 6 (Reina-Campos et al., 2020). We find that

⁶The APO Galactic Evolution Experiment (APOGEE) from the Sloan Digital Sky Survey (SDSS).

only a small percentage of the simulated haloes correspond to disrupted mass from stellar clusters, implying that galactic stellar haloes are mostly assembled from the accretion of dwarf satellites (as suggested by e.g. Deason et al., 2015; Belokurov et al., 2018; Helmi et al., 2018; Conroy et al., 2019).

Despite the remarkable success achieved by the E-MOSAICS simulations at linking the observed GCs with their birth environments, the lack of a description of the cold phase of the interstellar medium (ISM) in the EAGLE galaxy formation model represents a limitation for their simulated stellar clusters. This cold and dense gas phase is expected to dominate the graininess of the tidal field in galaxies, and its absence from the EAGLE model results in the stellar clusters being disrupted too slowly (see discussion in appendix D by Kruijssen et al., 2019a). This specially affects those stellar clusters that spend more time evolving in the gas-rich environments of their host galaxy, i.e. the young and metal-rich clusters. Thus, this restricts the predictive power of these simulations in the high-metallicity, as well as in the low-mass ($M < 10^5 M_{\odot}$) end of stellar cluster populations. In addition, massive stellar clusters are observed to be forming in the peaks of high-density and cold gas (e.g. Holtzman et al., 1992), so the inclusion of a multiphase description of the ISM in hydrodynamical, cosmological simulations is of paramount importance to accurately model the formation and evolution of stellar clusters.

In order to overcome these problems, we present in Chapter 7 the methods used in the suite of hydrodynamical, cosmological EMP-*Pathfinder* simulations (Reina-Campos et al. in prep.), as well as some preliminary results of the demographics of their stellar cluster populations. These cosmological zoom-in simulations describe the co-formation and evolution of stellar clusters alongside their host galaxies while capturing the hierarchical nature of the ISM. They include an improved MOSAICS sub-grid model for the formation and evolution of stellar clusters, and a description for the cold gas phase of the ISM via the six-element non-equilibrium chemistry network of the GRACKLE cooling library (Smith et al., 2017). These simulations also include a state-of-the-art description of stellar feedback that conserves energy and momentum, and which includes the ejecta in terms of mass, metals, yields, energy and momentum from AGB winds, SNe and SNIa. Additionally, these simulations evolve the individual isotopes of 30 elements between Li to Zn, making them an ideal framework with which to do galactic archaeology. This self-consistent description of the cold and dense gas and its interaction with local stellar feedback allows the modelling of the formation and evolution of stellar clusters in galaxies with a cold and clumpy medium, thus accurately describing where the entire distribution of clusters forms and how they evolve across cosmic history.

This thesis is a compilation of articles published by its author and a number of collaborators in international peer-reviewed journals (Chapters 2 to 6), as well as a manuscript in preparation that will be submitted shortly to an international journal (Chapter 7). The references to the articles can be found in the Preface and are also given before each of the publications, together with a description of the contributions of the author to each multi-authored paper.

Part I

Formation and evolution of globular clusters

Chapter 2

A unified model for the maximum mass scales of molecular clouds, stellar clusters and high-redshift clumps

Authors:

Marta Reina-Campos and J. M. Diederik Kruijssen

Published in *MNRAS* 469 (2017) 1282.

Reproduced with permission from the journal

Marta Reina-Campos is the principal author of this article. The original idea was suggested by Dr. Kruijssen, and Marta Reina-Campos developed it and derived the analytical model. Marta Reina-Campos performed the calculations, produced all the figures and wrote the manuscript. Both authors actively collaborated with corrections and suggestions to the manuscript, and Marta Reina-Campos performed the last improvements during the review process.



A unified model for the maximum mass scales of molecular clouds, stellar clusters and high-redshift clumps

Marta Reina-Campos[★] and J. M. Diederik Kruijssen[★]

Astronomisches Rechen-Institut, Zentrum für Astronomie der Universität Heidelberg, Mönchhofstraße 12-14, D-69120 Heidelberg, Germany

Accepted 2017 March 27. Received 2017 March 27; in original form 2016 December 21

ABSTRACT

We present a simple, self-consistent model to predict the maximum masses of giant molecular clouds (GMCs), stellar clusters and high-redshift clumps as a function of the galactic environment. Recent works have proposed that these maximum masses are set by shearing motions and centrifugal forces, but we show that this idea is inconsistent with the low masses observed across an important range of local-Universe environments, such as low-surface density galaxies and galaxy outskirts. Instead, we propose that feedback from young stars can disrupt clouds before the global collapse of the shear-limited area is completed. We develop a shear–feedback hybrid model that depends on three observable quantities: the gas surface density, the epicyclic frequency and the Toomre parameter. The model is tested in four galactic environments: the Milky Way, the Local Group galaxy M31, the spiral galaxy M83 and the high-redshift galaxy zC406690. We demonstrate that our model simultaneously reproduces the observed maximum masses of GMCs, clumps and clusters in each of these environments. We find that clouds and clusters in M31 and in the Milky Way are feedback-limited beyond radii of 8.4 and 4 kpc, respectively, whereas the masses in M83 and zC406690 are shear-limited at all radii. In zC406690, the maximum cluster masses decrease further due to their inspiral by dynamical friction. These results illustrate that the maximum masses change from being shear-limited to being feedback-limited as galaxies become less gas rich and evolve towards low shear. This explains why high-redshift clumps are more massive than GMCs in the local Universe.

Key words: stars: formation – ISM: clouds – globular clusters: general – galaxies: evolution – galaxies: formation – galaxies: star clusters: general.

1 INTRODUCTION

A large body of recent work has demonstrated that star formation in galaxies is correlated with the molecular gas (e.g. Bigiel et al. 2008; Leroy et al. 2008; Schruba et al. 2011; Leroy et al. 2013; Tacconi et al. 2013). Solomon et al. (1987) observed that the bulk of molecular gas in the Milky Way resides in the most massive giant molecular clouds (GMCs). Following from the correlation between the star formation rate (SFR) and the molecular gas, the most massive GMCs also contain most of the star formation activity in the galaxy (e.g. Murray 2011). Such star formation ‘hubs’ are observed to produce dense stellar clusters in the Universe (e.g. Longmore et al. 2014). It is unknown how these massive structures form, or what sets their extreme mass scale.

The most massive, high-redshift ($z \sim 1-3$) star-forming galaxies exhibit a more clumpy structure than their local-Universe

counterparts. The giant clumps have typical observed masses of $\sim 10^8-10^9 M_{\odot}$, but they can account for $\sim 10-20$ per cent of the SFR of their host galaxy (e.g. Genzel et al. 2011, Oklopčić et al. 2017, Soto et al. 2017). Oklopčić et al. (2017) use the FIRE simulations to study the giant clumps that dominate the morphology of massive high-redshift galaxies. They find that the high-redshift molecular clumps have similar star formation efficiencies and follow the same mass-size relations as local-Universe molecular clouds, so they suggest that the giant clumps might be analogous to GMCs in the local Universe.

While the formation physics of the most massive clusters are still poorly understood, be it young massive clusters (YMCs) or globular clusters, they represent an ideal opportunity to probe the most extreme forms of star formation. A popular hypothesis that is currently being tested is that globular clusters may be the high-redshift equivalent to the YMCs forming in the local Universe that have survived for a Hubble time (e.g. Kravtsov & Gnedin 2005, Elmegreen 2010, Shapiro, Genzel & Förster Schreiber 2010, Kruijssen 2015). If this hypothesis holds, then an understanding of the physics setting the maximum cluster mass scales would enable

[★]E-mail: reina.campos@uni-heidelberg.de (MR-C); kruijssen@uni-heidelberg.de (JMDK)

the use of globular clusters as tracers of the star-forming conditions in high-redshift environments.

The characteristic mass scale of the GMC mass function has been observed to depend on the hierarchical structure of the interstellar medium (ISM) and it is known to vary with the galactic environment (Hughes et al. 2013, Colombo et al. 2014, Freeman et al. 2017). Likewise, the young cluster mass function follows an exponentially truncated power law with index -2 (i.e. a Schechter 1976 function, e.g. Gieles et al. 2006, Larsen 2009, Bastian et al. 2012, Konstantopoulos et al. 2013), with values for the characteristic truncation mass M_c in the range $0.1\text{--}50 \times 10^5 M_\odot$. Moreover, the recovered truncation mass has been found to change as a function of galactocentric radius within the same galaxy by Adamo et al. (2015). As for GMCs, the observed variation suggests a dependence on the galactic environment. If stellar clusters form in the overdensities of the GMCs, one could expect a certain correspondence between the mass function of both objects, but cloud fragmentation and hierarchical cluster growth make this mapping non-trivial (e.g. Longmore et al. 2014). A possible way to overcome this problem is to only consider the maximum GMC and cluster mass scales because these must correspond to the optimal case of minimal fragmentation and maximal hierarchical growth.

Kruijssen (2014) suggested that the maximum GMC mass and the maximum stellar cluster mass might have a common origin and it may correspond to the maximum mass that could collapse against centrifugal forces, i.e. the Toomre mass. Toomre (1964) considers whether shear due to the rotation of the disc and the internal kinetic energy of the gas are sufficient to stop the collapse due to a gravitational instability. Toomre (1964) proposes that such shearing motions and centrifugal forces are the mechanisms setting the maximum region for collapse and derives the maximum size of the collapsing region, called Toomre length. For a given gas surface density, this length-scale directly provides the Toomre mass. This definition of a shear-limited mass scale has recent been put forward to explain the maximum mass of masses of GMCs, stellar clusters and high-redshift clumps, implying that shear is the only limiting factor mechanism (e.g. Dekel, Sari & Ceverino 2009; Kruijssen 2014; Adamo et al. 2015; Freeman et al. 2017). However, this idea assumes that the collapse of the shear-limited area can proceed fast enough to condense into a single object. In this paper, we show that, across an important part of parameter space, feedback from young stars disrupts the cloud before the global collapse of the shear-limited area is completed.

The idea that stellar feedback can end up destroying the molecular cloud in which stars form has been put forward several decades ago (e.g. Oort & Spitzer 1955; Larson 1981). In this work, we add the idea of cloud destruction by feedback to the classical Toomre approach and derive a self-consistent, simple model to simultaneously predict the maximum masses of molecular clouds and stellar clusters, from local galaxies out to the clumpy, star-forming systems observed at high redshift. We show that the feedback time (i.e. the time it takes for the stellar feedback to destroy the cloud) can be smaller than the free-fall time of the shear-limited region. In such a situation, the collapsed mass is smaller than the shear-limited Toomre mass. The goal of this model is to shed light on the conditions under which the densest structures in galaxies form, and how the local-Universe GMCs and stellar clusters may be connected to their high-redshift analogues of giant molecular clumps and globular clusters.

The structure of this paper is as follows. We present a self-consistent simple model to simultaneously predict the maximum masses of molecular clouds and stellar clusters, from local galaxies

out to the clumpy, star-forming systems observed at high redshift. We introduce the idea that the feedback time (i.e. time it takes to the stellar feedback to destroy the cloud) can be smaller than the two-dimensional free-fall time of the shear-limited region. In such a scenario, the collapsed mass will be smaller than the shear-limited Toomre mass. We present the derivation of our model in Section 2. Then we predict the maximum cloud and cluster mass for a region of the parameter space (Section 3). We then test the predictions of our model for the Milky Way, the Local Group disc galaxy M31, the grand-design spiral galaxy M83 and the high-redshift galaxy zC406690 to their observed maximum mass scales and present the results in Section 4. Finally, we present the conclusions of this work in Section 5.

2 MODEL

In this section, we derive a simple analytical model that self-consistently predicts the maximum mass scales of GMCs and stellar clusters, from local galaxies out to high redshift. We consider the situation in which the mass assembly of clouds and clusters can be limited by shear and feedback. Which of these two mechanisms ends up setting the maximum mass scales depends on whether or not the collapse of the GMC enclosed by the shear-limited area proceeds more rapidly (i.e. the free-fall time) than the time it takes stellar feedback to disperse the GMC (i.e. the feedback time).

2.1 Mass of the most massive GMC

We first determine the collapse time of a GMC enclosed by the shear-limited area. In a differentially rotating disc, Toomre (1964) explores the possibility of compensating a gravitational instability with internal kinetic energy and shear. The author finds that the random motions set a minimum scale for collapse that corresponds to the Jeans length λ_J , whereas the maximum scale is set by shear and corresponds to the Toomre length λ_T , which is set by galactic-scale quantities,

$$\lambda_T = \frac{4\pi^2 G \Sigma_g}{\kappa^2}, \quad (1)$$

where G is the gravitational constant, Σ_g is the gas surface density and κ corresponds to the epicyclic frequency. The disc is stable to perturbations with wavelengths larger than this length-scale. Toomre posits that collapse can only take place when $\lambda_J < \lambda_T$. Given that the Jeans length depends on local conditions and increases with the local velocity dispersion, the turbulent energy will dissipate even if initially $\lambda_J > \lambda_T$, thus decreasing the Jeans length and eventually meeting the instability condition. The collapse then occurs on a scale λ_T , which is therefore the largest scale on which collapse can take place in our model.

The collapse length-scale can naturally be related to an equivalent mass scale (i.e. the Toomre mass) for a given gas surface density:

$$M_T = \pi \Sigma_g \frac{\lambda_T^2}{4} = \frac{4\pi^5 G^2 \Sigma_g^3}{\kappa^4}. \quad (2)$$

The characteristic time-scale associated with the collapse of a region enclosed by shear can be determined as the two-dimensional free-fall time of the sheet of gas derived by Burkert & Hartmann (2004). They assume finite, self-gravitating sheets of gas and derive the typical infall time for a subregion within a collapsing sheet of radius r . Using numerical simulations, they demonstrate that this time-scale also describes the time it takes to the edges of the collapsing sheet to reach the centre. Using that our maximum collapsing region

has a size $r = \lambda_T/2$ and equation (1) to describe the Toomre length, we obtain a collapsing time-scale $t_{\text{ff},2\text{D}}$ inversely proportional to the epicyclic frequency,

$$t_{\text{ff},2\text{D}} = \sqrt{\frac{r}{\pi G \Sigma_g}} = \sqrt{\frac{\lambda_T}{2\pi G \Sigma_g}} = \frac{\sqrt{2\pi}}{\kappa}. \quad (3)$$

In environments of low gas surface density and low shear (i.e. low λ_T), the two-dimensional free-fall time may become larger than the time it takes massive stars to destroy the cloud (the feedback time-scale t_{fb}). In the case where $t_{\text{fb}} < t_{\text{ff},2\text{D}}$, the collapsing GMC will be destroyed by stellar feedback before it has finished the collapse, so the maximum mass of the collapsing region will be limited by the minimum time-scale.

We use equation (20) in Kruijssen (2012) to determine the feedback time-scale, that is, the time needed to achieve pressure balance between the feedback energy density and the turbulent pressure of the ISM, by setting ambient gas density equal to the mid-plane density. This leads to

$$t_{\text{fb}} = \frac{t_{\text{sn}}}{2} \left(1 + \sqrt{1 + \frac{4\pi^2 G^2 t_{\text{ff},g} Q^2 \Sigma_g^2}{\phi_{\text{fb}} \epsilon_{\text{ff}} t_{\text{sn}}^2 \kappa^2}} \right), \quad (4)$$

where $t_{\text{sn}} = 3$ Myr is the typical time of the first supernova explosion, $t_{\text{ff},g}$ is the free-fall time of the ISM, Q is the Toomre parameter, $\phi_{\text{fb}} \approx 0.16 \text{ cm}^2 \text{ s}^{-3}$ is a constant that represents the rate at which feedback injects energy into the ISM per unit stellar mass and ϵ_{ff} corresponds to the star formation efficiency (SFE) per free-fall time. We use the empirically motivated assumption that ϵ_{ff} is approximately constant from Elmegreen (2002), $\epsilon_{\text{ff}} = 0.012$ (also see Krumholz, Dekel & McKee 2012). Equation (4) shows that in high-surface density environments, it may take time for feedback to overcome the ambient pressure, whereas in low surface density environments the feedback time-scale can be shorter than global, two-dimensional free-fall time. This definition of the feedback time assumes that stars can start forming immediately once a cloud starts to collapse, which is justified because the hierarchical structure of the ISM means that locally the free-fall time is much shorter than it is globally, enabling star formation in local overdensities once the GMC has condensed out of the background.

The Toomre (1964) Q parameter is defined as

$$Q \equiv \frac{\kappa \sigma}{\pi G \Sigma_g}, \quad (5)$$

where σ corresponds to the one-dimensional velocity dispersion of the gas. This parameter is used to assess the stability of the disc against shear. The case $\lambda_J = \lambda_T$ refers to the value of $Q = 2$, which implies marginal stability. A region of the disc will collapse if its value of the parameter is $Q < 2$, which implies $\lambda_J < \lambda_T$.¹

The free-fall time of the ISM $t_{\text{ff},g}$ corresponds to the collapsing time in the vertical direction at the mid-plane density as represented in Fig. 1 and it characterizes the gravitational collapse towards star formation,

$$t_{\text{ff},g} = \sqrt{\frac{3\pi}{32G\rho_g}}, \quad (6)$$

¹ This differs from the classical $Q = 1$ condition because we are interested in the largest unstable scale rather than the most unstable scale.

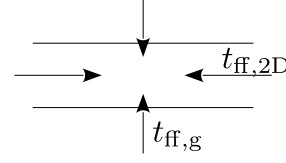


Figure 1. Schematic representation of the collapse. The two-dimensional collapsing time-scale $t_{\text{ff},2\text{D}}$ describes the collapse proceeding on the horizontal direction, whereas the vertical mid-plane free-fall time $t_{\text{ff},g}$ characterizes the gravitational collapse towards star formation, and thus, the feedback time-scale t_{fb} .

where ρ_g corresponds to the mid-plane density of the ISM and can be defined following Krumholz & McKee (2005) and assuming a disc in hydrostatic equilibrium as

$$\rho_g = \frac{\phi_p \kappa^2}{2\pi Q^2 G}, \quad (7)$$

where $\phi_p = 3$ is a constant to account for the gravity of the stars. The hydrostatic equilibrium assumption has the major advantage that the properties of the ISM can be described in terms of just three variables: the gas surface density Σ_g , the epicyclic frequency κ and the stability parameter Q .

Using equations (2) and (3), we can determine the dependence of the Toomre mass in the collapsing time-scale as $M_T \propto t_{\text{ff},2\text{D}}^4$. With that relation we can define the fraction of collapsed mass as

$$f_{\text{coll}} = \min \left(1, \frac{t_{\text{fb}}}{t_{\text{ff},2\text{D}}} \right)^4, \quad (8)$$

which will be less than unity when the stellar feedback halts collapse towards faster than the two-dimensional collapse is completed.

Thus, the maximum mass of the collapsing region can be determined from the Toomre mass and the collapsed-mass fraction as

$$M_{\text{GMC,max}} = M_T \times f_{\text{coll}} = \frac{4\pi^5 G^2 \Sigma_g^3}{\kappa^4} \times \min \left(1, \frac{t_{\text{fb}}}{t_{\text{ff},2\text{D}}} \right)^4. \quad (9)$$

Inspection of equations (3) and (6) shows that feedback dominates in regions of low epicyclic frequency and low gas surface density, whereas free-fall dominates in regions of high epicyclic frequency and/or high gas surface density. We refer to these two regimes as feedback-limited and shear-limited, respectively.

2.2 Mass of the most massive stellar cluster

Given the mass of the most massive GMC, it is possible to derive the mass of the most massive stellar cluster. We assume that cluster complexes can continue to collapse within the collapsed region of the cloud even if the stellar feedback stops the collapse of the GMC. Following Kruijssen (2014), we derive the maximum cluster mass by assuming some fraction of the GMC is converted into stars (i.e. the star formation efficiency or SFE, ϵ), of which some fraction is born in gravitationally bound stellar clusters (i.e. the cluster formation efficiency or CFE, Γ as defined by Bastian 2008), resulting in

$$M_{\text{cl,max}} = \epsilon \Gamma(\Sigma, \kappa, Q) M_{\text{GMC,max}}, \quad (10)$$

where we set $\epsilon = 0.1$ (e.g. Lada & Lada 2003; Oklopčić et al. 2017). This fiducial value is broadly consistent with the SFE of embedded clusters (0.1–0.3, Lada & Lada 2003) and nearby molecular clouds (0.03–0.06, Evans 1999). The total dynamic range of the SFE is there for a factor of three in either direction. The maximum cluster

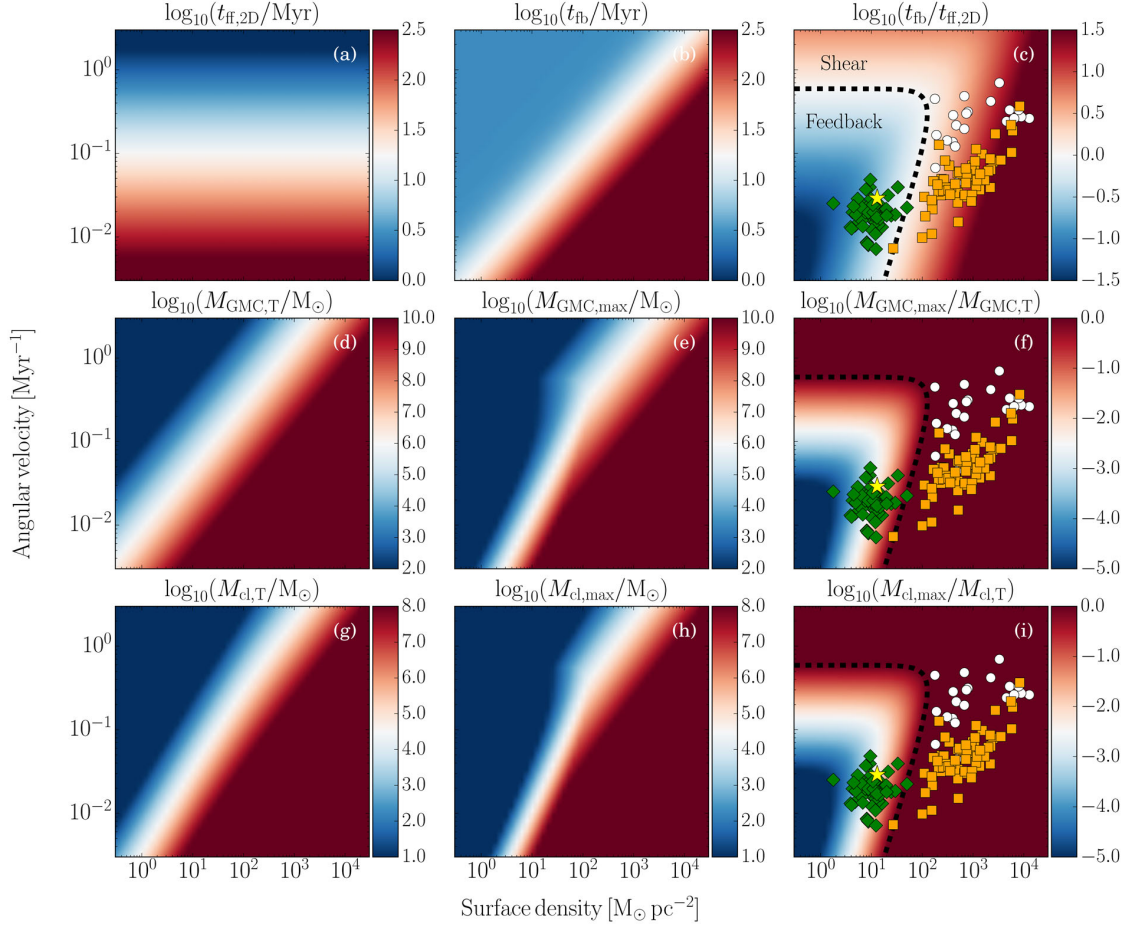


Figure 2. Predictions of our model assuming $Q = 1.5$. From left to right, the panels represent: (1st row) the two-dimensional free-fall time-scale of a GMC $t_{\text{ff},2\text{D}}$, the feedback time-scale t_{fb} and the ratio of time-scales $t_{\text{fb}}/t_{\text{ff},2\text{D}}$; (2nd row) the shear-limited Toomre mass of the cloud $M_{\text{GMC},\text{T}}$, the hybrid maximum mass of the cloud $M_{\text{GMC},\text{max}}$ and the ratio of cluster mass scales; (3rd row) the shear-limited mass of the cluster $M_{\text{cl},\text{T}}$, the hybrid maximum mass of the cluster $M_{\text{cl},\text{max}}$ and the ratio of cluster mass scales. We overplot observational data from four different environments. The values for the solar neighbourhood are represented with a yellow star. The green diamonds represent the spiral galaxies from table 1 in Kennicutt (1998), whereas the circumnuclear starbursts of their table 2 are represented by white dots. The orange squares correspond to the high-redshift galaxies from Tacconi et al. (2013).

mass scales in this paper cover a range of several orders of magnitude (see Section 4). Assuming a constant SFE is therefore a minor effect relative to the other elements in our model (such as the steep dependences on the epicyclic frequency and the surface density). The CFE $\Gamma(\Sigma, \kappa, Q)$ is evaluated at $t = t_{\text{fb}}$ using the model from Kruijssen (2012). This model predicts the naturally bound fraction of star formation f_{bound} as well as the fraction thereof that survives tidal perturbations by nearby gas clouds on a star formation time-scale (‘the cruel cradle effect’). Because we are interested in the most massive cluster that can possibly form, we adopt $\Gamma = f_{\text{bound}}$ and ignore the cruel cradle effect. For the same reason, we consider the limiting case in which the cloud undergoes complete hierarchical merging and all bound stars end up in a single cluster.

3 EXPLORING PARAMETER SPACE

Using the model derived in the previous section, we now calculate the resulting maximum GMC and cluster mass scales, and demonstrate in which part of the parameter space formed by Σ_{g} , κ and Q these are limited by feedback rather than by shear.

The model has been derived without the assumption of a flat rotation curve. In order to facilitate the comparison to observations, we now assume a flat rotation curve and change the epicyclic frequency κ in equations (3), (4), (9) and (10), following:

$$\kappa \equiv \sqrt{2} \frac{V}{R} \sqrt{1 + \frac{d \ln V}{d \ln R}} \rightarrow \sqrt{2} \Omega, \quad (11)$$

where V corresponds to the circular velocity, R corresponds to the galactocentric radius and Ω is the angular velocity, i.e. $\Omega = V/R$.

We start by setting a fiducial value of the stability parameter $Q = 1.5$ to study the predictions of our model as a function of the gas surface density and the angular velocity, and then we study the influence of the Toomre parameter on our predictions.

3.1 Influence of the gas surface density and the angular velocity

The results for a fiducial value of $Q = 1.5$ are presented in Fig. 2. From left to right and top to bottom, the panels represent the two-dimensional free-fall time-scale of the GMC ($t_{\text{ff},2\text{D}}$), the feedback

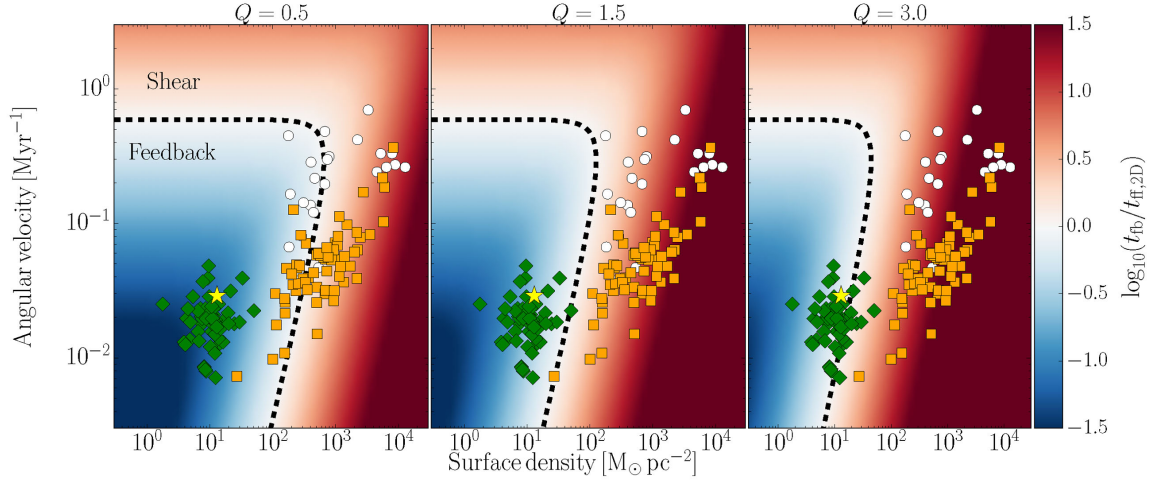


Figure 3. Influence of the stability parameter Q on the ratio of the feedback and free-fall time-scales $t_{\text{fb}}/t_{\text{ff},2\text{D}}$: (left) $Q = 0.5$, (middle) $Q = 1.5$ and (right) $Q = 3$. The dashed line indicates the change of regime from being feedback-limited ($t_{\text{ff},2\text{D}} > t_{\text{fb}}$) in the bottom-left to being shear-limited ($t_{\text{ff},2\text{D}} < t_{\text{fb}}$) in the top and/or right. We overplot observational data from four galactic environments as in Fig. 2.

time-scale (t_{fb}), the ratio of time-scales, the shear-limited GMC mass ($M_{\text{GMC},\text{T}}$), the hybrid maximum GMC mass including feedback ($M_{\text{GMC},\text{max}}$), the ratio of both GMC mass scales, the shear-limited cluster mass ($M_{\text{cl},\text{T}}$), the hybrid maximum cluster mass including feedback ($M_{\text{cl},\text{max}}$) and the ratio of both cluster mass scales.

For comparison, we also overplot the positions in parameter space of four observed galaxy samples: the solar neighbourhood, nearby spiral galaxies, circumnuclear starbursts and high-redshift galaxies. For the solar neighbourhood we use the observed values $\Sigma_{\text{g},\text{MW}} \simeq 13 M_{\odot} \text{pc}^{-2}$ (fig. 7 from Kennicutt & Evans 2012) and $\Omega_{\text{MW}} \simeq 0.029 \text{Myr}^{-1}$ (Section 6.4.2 in Bland-Hawthorn & Gerhard 2016). The nearby spiral galaxies are listed in table 1 of Kennicutt (1998), whereas the circumnuclear starburst galaxies are listed in their table 2. Lastly, the high-redshift galaxies are listed in table 2 of Tacconi et al. (2013). For these, we determine the angular velocity from the listed circular velocity and the optical half-light radius and we use their measurement of the mean molecular gas surface density within the half-mass radius.

As expected from equation (3), in panel (a) it is found that the two-dimensional free-fall time of the cloud does not depend on the gas surface density, but it is inversely proportional to the angular velocity. This dependence is especially relevant in environments with low angular velocity, as they yield very large collapsing time-scales. By contrast, the feedback time-scale depends on both parameters, as seen in panel (b). The feedback time-scale reaches its lower limit, $t_{\text{fb}} = t_{\text{sn}}$, in environments with high angular velocity and low gas surface density.

The contrast in the behaviour between the two time-scales is best visualized in panel (c), where we show the ratio of the feedback time over the two-dimensional free-fall time of the shear-limited area. The dashed line marks the separation between the shear-limited ($t_{\text{ff},2\text{D}} < t_{\text{fb}}$) and the feedback-limited ($t_{\text{ff},2\text{D}} > t_{\text{fb}}$) regimes. It can be seen that, for low angular velocity and low gas surface density, the feedback time-scale can be more than an order of magnitude less than the free-fall time-scale. This directly implies that shear cannot be setting the maximum mass scales of GMCs and clusters for an important part of parameter space.

For a fixed value of the angular velocity, the GMC mass scales [panels (d) and (e)] increase with increasing gas surface density,

whereas they decrease for increasing angular velocity and a fixed gas surface density. The hybrid GMC mass behaves like the shear-limited Toomre mass except for low angular velocity and low gas surface density, where it has lower values due to the short feedback time-scales.

The ratio between these two GMC masses is shown in panel (f) and, as expected, the parameter space affected matches the area where the feedback time is shorter than the free-fall time. The region of the parameter space affected by our model is occupied by most spiral galaxies in the local Universe (here showing the sample from Kennicutt 1998, including the solar neighbourhood). Higher density systems, such as the starburst galactic nuclei from Kennicutt (1998) and the high-redshift galaxies from Tacconi et al. (2013) are located in the shear-limited regime. This indicates that the higher GMC (or clump) masses observed in high-redshift and starburst galaxies are due to them being limited by shear instead of by stellar feedback.

Turning to maximum cluster masses in panels (g)–(i), we see that the parameter space affected by our model is still in agreement with the time-scale ratios in panel (c). Compared to the GMC mass scales, the cluster mass scales shown in panels (g) and (h) have an overall similar behaviour due to the dependence of the CFE on Σ_{g} and Ω . The differences are due to the dependence of the CFE on Σ_{g} and Ω .

3.2 Influence of the stability parameter Q

We now explore the influence of the Toomre parameter in our model. We use three values of $Q = 0.5, 1.5$ and 3 and we consider the ratio of time-scales, the shear–feedback hybrid GMC mass, the ratio of GMC mass scales, the shear–feedback hybrid cluster mass and the ratio of cluster mass scales shown in panels (c), (e), (f), (h) and (i) of Fig. 2, respectively.

In Fig. 3, we present the ratio of time-scales for the three values of the stability parameter. The region of the parameter space affected by our addition of feedback as a limiting mechanism increases as we move towards lower values of Q (from right-hand to left-hand panels). The resulting reduction of the maximum mass scales is caused by an increase of the gas surface density needed to go from the shear-limited to the feedback-limited regime, whereas the limit

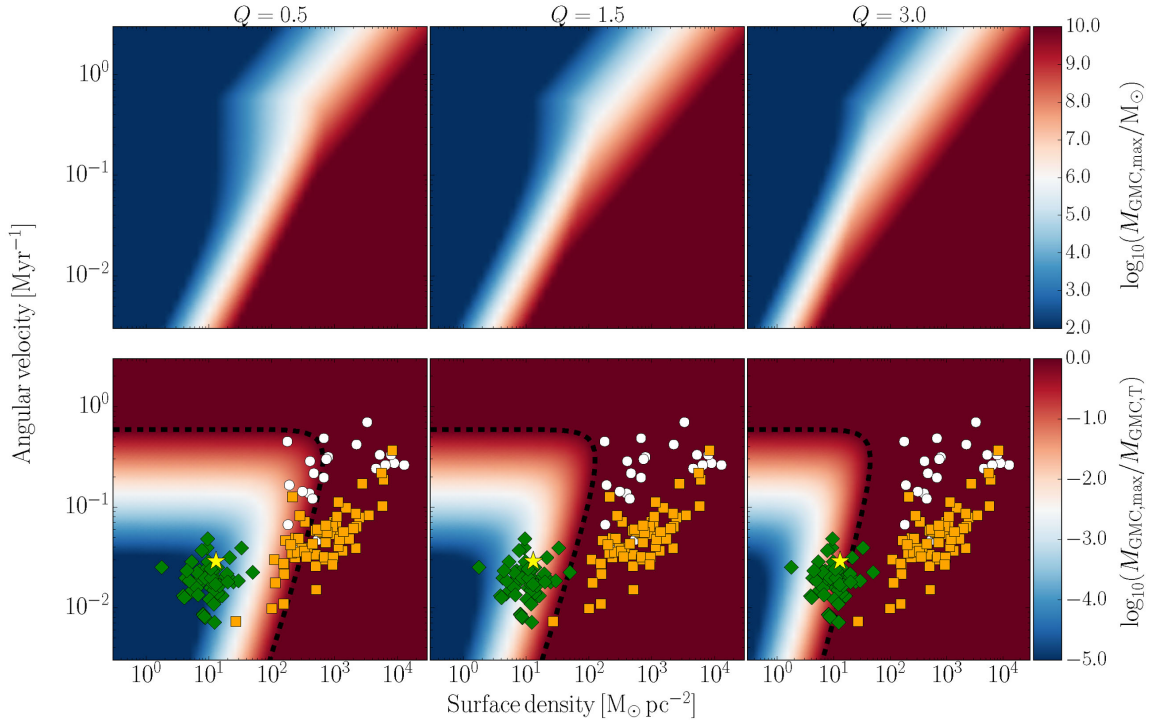


Figure 4. Influence of the stability parameter Q on (top) the maximum shear–feedback hybrid GMC mass and (bottom) the ratio of GMC mass scales: (left) $Q = 0.5$, (middle) $Q = 1.5$ and (right) $Q = 3$. The dashed line indicates the change of regime from being feedback-limited ($t_{\text{ff},2\text{D}} > t_{\text{fb}}$) in the bottom-left to being shear-limited ($t_{\text{ff},2\text{D}} < t_{\text{fb}}$) in the top and/or right. We overplot observational data from four galactic environments as in Fig. 2.

on the angular velocity does not change. This result indicates that environments with a low value of Q , which are less shear stable, are more likely to be limited by feedback rather than by shear.

The variation of Q has a similar effect on the GMC and cluster mass scales, shown in the top panels of Figs 4 and 5, respectively. The white region, corresponding to $M_{\text{GMC,max}} \sim 10^6 M_{\odot}$ and $M_{\text{cl,max}} \sim 10^{4.5} M_{\odot}$, shifts towards lower gas surface densities as we move towards larger values of Q (from left to right), thus indicating that the more shear-stable environments will have larger cloud masses compared to the unstable environments.

Leroy et al. (2008) show in their fig. 11 that nearby galaxies have an observed Toomre parameter $Q \sim 3$, which would place them in the region of the parameter space affected by our introduction of the feedback mechanism. By contrast, and despite the low value of the stability parameter of $Q \sim 1$ reported in fig. 24 in Genzel et al. (2014), the high-redshift galaxies lie in the region of the parameter space that is only limited by shear. It seems that as galaxies evolve and become less gas-rich, they move in the parameter space from the shear-limited towards the feedback-limited region.

3.3 Limitations of the model

In Section 2, we derive our model by considering a differentially rotating disc in hydrostatic equilibrium. This assumption implies the presence of some degree of shear and allows us to describe the properties of the ISM just using three variables (Σ , κ and Q). These simple assumptions yield some caveats that need to be accounted for when comparing the predictions of our hybrid model with the observed mass scales of real galaxies.

The first caveat is due to our model predicting the maximum mass scales based on the present-day properties of the gas surface density. Therefore, the predictions of the hybrid model should be compared to a cluster sample with an age range small enough such that the gas properties have not undergone significant change. Otherwise, the input gas conditions in our model will not agree with the gas conditions at birth of these clusters. A natural time-scale for changes in the gas conditions is the orbital time-scale Ω^{-1} , which is of the order of 50 Myr in nearby galaxies (Leroy et al. 2008). The second caveat comes from the fact that our hybrid shear–feedback model does not consider systematic structural morphological features that may exist in the disc, such as bars, rings or spiral arms. Such structures may induce the formation of more massive clouds than the ones predicted by our model, as the external compression from the structure would yield larger densities and thus larger mass scales that would not have been reached if shear is considered. Finally, we also need to consider the effect of dynamical friction on the most massive clusters when we apply our model to star-forming high-redshift environments. According to the cluster formation model described in Kruijssen (2015), stellar clusters may survive over a Hubble time and become the present-day GCs if they migrate towards the host galaxy halo (e.g. by hierarchical galaxy growth) before they are destroyed by impulsive shocks or dynamical friction into the centre. For the most massive clusters, the dynamical friction time-scale may be too short for the clusters to survive till migration, which would cause them to spiral in and contribute to the growth of a bulge. Given a galaxy stellar mass, it is possible to determine what is the maximum mass of clusters that will survive dynamical friction, i.e. the maximum mass that may be observed in the local Universe. We will have to correct the predictions of our model

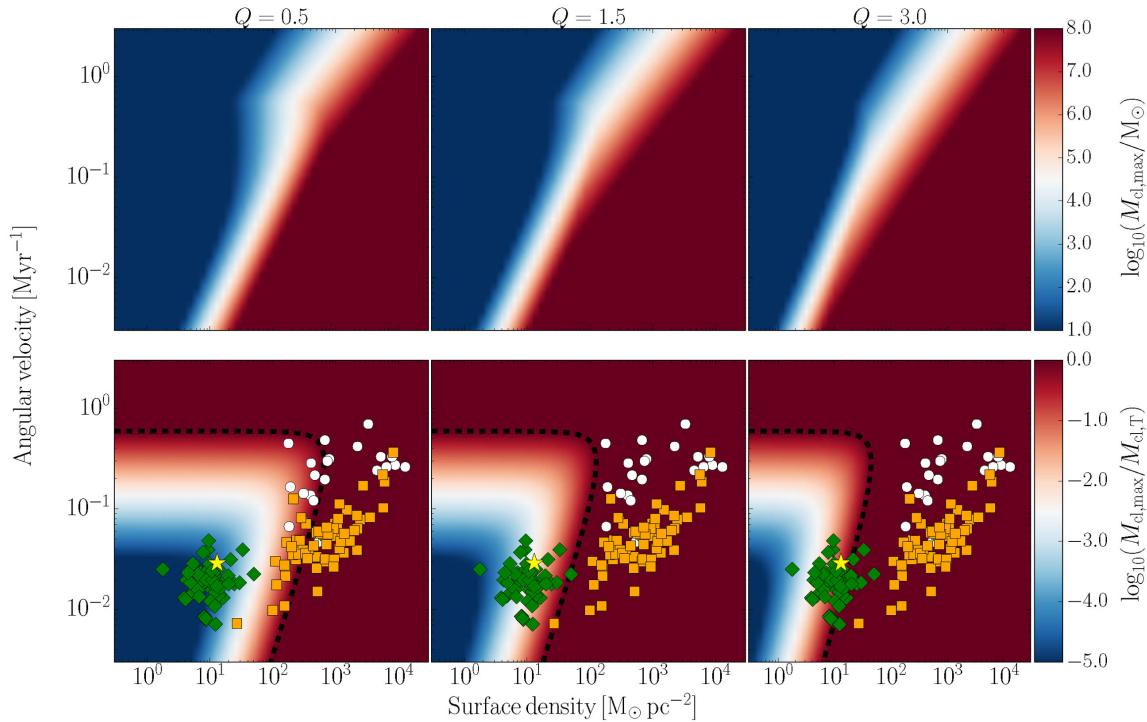


Figure 5. Influence of the stability parameter Q on (top) the maximum shear–feedback hybrid cluster mass and (bottom) the ratio of cluster mass scales: (left) $Q = 0.5$, (middle) $Q = 1.5$ and (right) $Q = 3$. The dashed line indicates the change of regime from being feedback-limited ($t_{\text{ff},2\text{D}} > t_{\text{fb}}$) in the bottom-left to being shear-limited ($t_{\text{ff},2\text{D}} < t_{\text{fb}}$) in the top and/or right. We overplot observational data from four galactic environments as in Fig. 2.

if they are larger than these dynamically limited mass scales (see Section 4.4.1).

4 COMPARISON TO OBSERVATIONS OF CLOUDS AND CLUSTERS

We now apply our shear–feedback hybrid model to observational data and compare the results with the observed GMCs and cluster masses, from local galaxies out to the clumpy, star-forming systems observed at high redshift. We choose four galactic environments as probes to test the model: the Milky Way, the disc galaxy M31, the grand-design spiral galaxy M83 and the high-redshift galaxy ZC406690. These four galaxies represent the subset of systems for which the most comprehensive observational data are available to carry out a detailed comparison and, at the same time, they have a sufficiently wide variety of properties to cover the galaxy population of interest, including different galactic stellar masses ($\sim 10^{10}$ – $10^{11} M_{\odot}$), SFR surface densities ($\sim 10^{-3}$ – $10^1 M_{\odot} \text{ kpc}^{-2} \text{ yr}^{-1}$), substructure (spiral arms, clumpy and ring-like morphologies) and gas fraction (~ 10 – 70 per cent).

4.1 Milky Way

We carry out a first test of our model by simultaneously comparing it to the most massive GMCs and stellar clusters in our Galaxy. We apply the model to two different regions of the Milky Way: the Central Molecular Zone (corresponding to $R < 0.2$ kpc, CMZ hereafter) and the disc (corresponding to $R \in [3.5, 10]$ kpc). For the CMZ, we use a gas surface density of $\Sigma_{\text{g}} \sim 10^3 M_{\odot} \text{ pc}^{-2}$ and a one-dimensional velocity dispersion of $\sigma = 5 \text{ km s}^{-1}$ (as in

Henshaw, Longmore & Kruijssen 2016) and we determine the circular velocity from the relation between the enclosed mass and the radius shown in fig. A1 in Kruijssen, Dale & Longmore (2015). For the disc of the Milky Way, we use the red rotation curve shown in fig. 16 in Bland-Hawthorn & Gerhard (2016) for a disc with a radial scale-length of $R_{\text{d}} = 2.6$ kpc. To ensure the continuity of the derivatives, we carry out a b-spline fit the rotation curve before calculating the epicyclic frequency as in equation (11). We determine the total gas surface density from the addition of the atomic and molecular gas surface densities shown in fig. 7 in Kennicutt & Evans (2012)² and we assume a fiducial constant one-dimensional velocity dispersion of $\sigma = 10 \text{ km s}^{-1}$ (cf. Heiles & Troland 2003). This allows us to determine the stability parameter Q as a function of the galactocentric radius as in equation (5).

With the values obtained, we evaluate the model of Section 2 at each galactocentric radius. We determine the free-fall and feedback time-scales, as well as the maximum GMC and cluster mass scales. We show a comparison of the two-dimensional free-fall time and the feedback time in Fig. 6, where we determine the uncertainties associated with the characteristic time-scales performing 10^6 Monte Carlo runs assuming typical uncertainties of 10 per cent and 30 per cent for the epicyclic frequency and the gas surface density, respectively. We shade the area in Fig. 6 where the feedback time-scale is smaller than the collapsing free-fall time, i.e. when the cloud masses will be feedback-limited and less massive than the Toomre

² We repeat the calculation using the gas surface density profile in fig. 9 of Miville-Deschênes, Murray & Lee (2017) and we obtain the same mass scale predictions to within the errorbars.

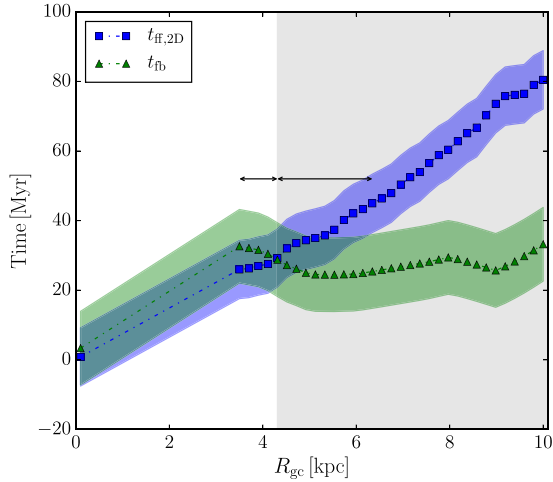


Figure 6. Predicted free-fall and feedback time-scales for GMCs in the Milky Way as a function of the galactocentric radius. The colour-shaded area indicates the uncertainties associated with the characteristic time-scales determined with 10^6 Monte Carlo runs assuming typical uncertainties for the epicyclic frequency and the gas surface density of 10 per cent and 30 per cent, respectively. The grey-shaded area corresponds to the feedback-limited regime, $t_{fb} < t_{ff,2D}$, located at $R \geq 4.3^{+2.0}_{-0.8}$ kpc. The lower errorbar is determined from the inner boundary of the data, whereas the higher one comes from the change of regime of the colour-shaded areas. Both of them are represented with black arrows.

mass. This happens at galactocentric radii $R \geq 4.3^{+2.0}_{-0.8}$ kpc due to a gradual change of the time-scales with the environment, not due to any particular (morphological) feature such as the tip of the bar. For smaller galactocentric radii, the two-dimensional free-fall time is shorter than the feedback time and the maximum cloud mass is equal to the Toomre mass.

The panels in Fig. 7 show the maximum cloud mass and the maximum cluster mass, respectively. For the sake of a better visualization, we separately show the maximum mass set by each mechanism (i.e. shear and feedback). We remind the reader that the lowest of these curves sets the maximum mass scale. With typical uncertainties of 10 per cent in the epicyclic frequency and 30 per cent in the gas surface density, the uncertainty associated with our predictions is ~ 0.4 dex. In the CMZ, the clouds are shear-limited and our prediction agrees well with the observed cloud mass of $\sim 10^5 M_\odot$ in Longmore et al. (2012). For $R \gtrsim 4.3$ kpc, the mass scales become feedback-limited, as indicated by the shaded area. In that regime, the feedback-limited GMC mass remains approximately constant at $M_{GMC,max} \sim 10^6 M_\odot$, in agreement with the most massive clouds for the solar neighbourhood reported in fig. 3 in Heyer et al. (2009).³ The predicted shear-limited cloud and cluster masses increase at large galactocentric radius (for $R > 4.3$ kpc) due to the steady drop of the epicyclic frequency. The resulting increase of the two-dimensional free-fall time implies that feedback becomes the mechanism responsible for setting the approximately constant GMC mass as a function of radius.

³ These authors first determine the ^{13}C and ^{12}C column densities from the $^{13}\text{CO}(1-0)$ emission and using a radially dependent conversion factor of $^{12}\text{C}/^{13}\text{C}$ taken from Milam et al. (2005), respectively. They then determine the H_2 column density by assuming a constant $\text{H}_2/^{12}\text{CO}$ abundance ratio of 1.1×10^4 (Frerking, Langer & Wilson 1982).

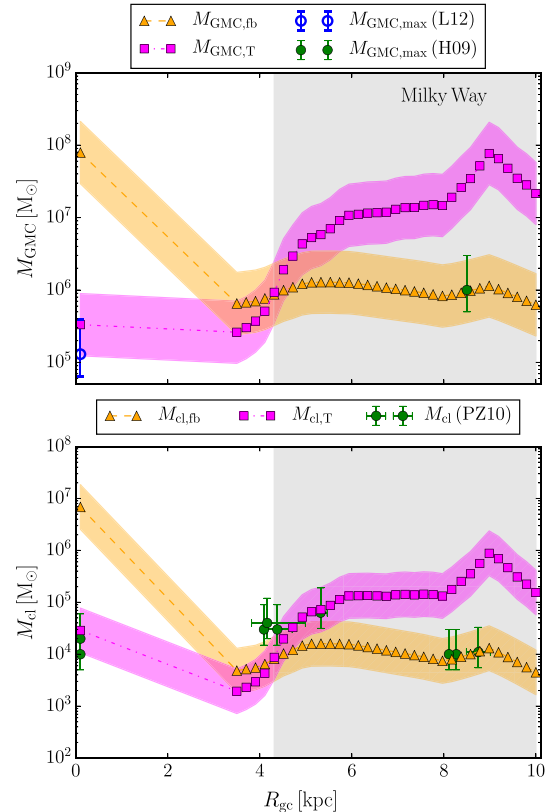


Figure 7. Result of applying our shear–feedback hybrid model to the Milky Way: (top) maximum GMC mass and (bottom) maximum cluster mass as a function of the galactocentric radius. The magenta squares correspond to the shear-limited mass scales and the orange triangles correspond to the feedback-limited mass scales. The observed maximum GMC and cluster masses are represented by the green and blue dots with error bars. The grey-shaded area corresponds to the feedback-limited regime: $t_{fb} < t_{ff,2D}$. The colour-shaded areas indicate a fiducial uncertainty range, assuming that the rotation curve and the gas surface density profile are known to an accuracy of ~ 0.04 and ~ 0.13 dex, respectively.

In the bottom panel, we show the predicted maximum cluster masses by our model. We overplot the masses of the observed clusters Arches, Quintuplet, RSGC01, RSGC02, RSGC03, Westerlund 1, Westerlund 2, Trumpler 14 and NGC 3603 reported in table 2 in Portegies Zwart, McMillan & Gieles (2010). The vertical error bars correspond to an uncertainty of ± 0.3 dex, whereas the error bars on the galactocentric radius have been propagated from the distance uncertainties in the original papers referenced by Portegies Zwart et al. (2010). Except for the clusters located at the end of the bar ($R \simeq 4$ kpc), the predicted cluster masses for the CMZ and the solar neighbourhood are in agreement with the observed cluster masses. A possible reason why the cluster masses at the end of the bar would be elevated is that the bar may be sweeping up the material, thus producing an environment in which external compression aids mass accumulation towards mass scales that otherwise would not be achieved. The data point at $R \approx 5.5$ kpc corresponds to Westerlund 1, which resides in the Scutum arm that connects to the bar. It lies just 10 Myr downstream from the bar, which means that it likely

formed through a similar compression event like we suggest for the RSG clusters (located at $R \approx 4$ kpc).

4.2 M31

We now test our model with the disc galaxy M31, the most massive galaxy in the Local Group. We apply the model in the radial range $R \in [8, 15]$ kpc in order to have measurements for all input variables. This radial range contains the 10-kpc ring of star formation, i.e. the region where cluster formation is more likely to occur (Vashevicius et al. 2009, Caldwell et al. 2009 and references therein). We use the turbulent velocity dispersion from Braun et al. (2009, fig. 19, panel f) and the rotation curve described in Corbelli et al. (2010, fig. 7 and table 1), both of them obtained with the Westerbork Synthesis Radio Telescope (WRST) H I survey of M31 described in Braun et al. (2009). We determine the gas surface density from the addition of the atomic and molecular profiles reported in Schrubba et al. (in preparation), of which the data are described by Leroy et al. (2016), and determined from observations with the WRST and the IRAM 30 m telescope, respectively.

As previously done for the Milky Way, we do not assume a flat rotation curve, but instead we determine the epicyclic frequency as in equation (11) and carrying out a b-spline fit to the rotation curve. We then determine the stability parameter Q at each galactocentric radius as in equation (5). With these values, we apply the model described in Section 2 and show the predicted cloud and cluster mass scales in Fig. 8.

In the top panel, we represent the predicted shear and feedback-limited mass scales for the GMCs. With typical uncertainties of 10 per cent for both the gas surface density⁴ and the epicyclic frequency, we determine the uncertainties associated with our predictions to be ~ 0.22 dex. As indicated by the shaded area, the maximum mass scales are feedback-limited for galactocentric radii $R \geq 8.4$ kpc, whereas they become shear-limited at smaller radii. There is a good agreement between our predictions and the observed maximum GMC mass of $M_{\text{GMC,max}} \sim 10^{5.5} M_{\odot}$ reported in Schrubba et al. (in preparation).⁵

The maximum cluster mass scales are shown in the bottom panel of Fig. 8. The symbols correspond to the prediction of our model using the current gas condition, whereas the colour-shaded area reflects a fiducial uncertainty range of ~ 0.22 dex, as well as changes in the gas surface density over the past 300 Myr, corresponding to the age range for which the cluster masses in Johnson et al. (2017) have been measured. These authors determine the observed truncation mass by fitting an exponentially truncated power law with index -2 (i.e. a Schechter 1976 function) to the mass function of a sample of 840 young clusters of ages between 10 and 300 Myr. Given this large age range, it may not be surprising that the present-day predictions of our model do not reproduce the observed maximum cluster mass scale. The 10-kpc ring is a long-lived structure with a bursty star formation history (Lewis et al. 2015), which means that the currently observed gas properties may not be representative for the conditions under which the most massive clusters in the ring formed. Indeed, figs 5 and 6 of Lewis et al. (2015) show that, over the past 300 Myr, the SFR surface density of the 10-kpc ring

⁴ This uncertainty is lower than for the Milky Way, where we assumed 30 per cent, because M31 is atomic gas-dominated.

⁵ The cloud mass is derived from CO data using the standard Galactic CO-to-H₂ conversion factor of $X_{\text{CO}} = 2 \times 10^{20} \text{ cm}^{-2} (\text{K km s}^{-1})^{-1}$ (Bolatto, Wolfire & Leroy 2013).

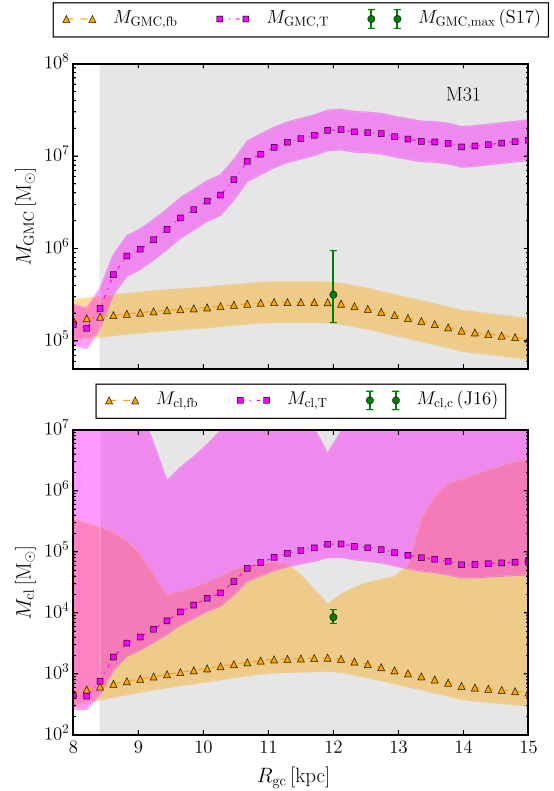


Figure 8. Result of applying our shear–feedback hybrid model to the disc galaxy M31: (top) maximum GMC mass and (bottom) maximum cluster mass as a function of the galactocentric radius. The magenta squares correspond to the shear-limited mass scales and the orange triangles correspond to the feedback-limited mass scales. The observed maximum GMC and cluster masses are represented by the green and blue dots with error bars. The grey-shaded area corresponds to the feedback-limited regime: $t_{\text{fb}} < t_{\text{ff,2D}}$. The colour-shaded areas indicate a fiducial uncertainty range, assuming that the rotation curve and the gas surface density profile are known to an accuracy of ~ 0.04 dex. It also accounts for changes in the gas surface density over the past 300 Myr, corresponding to the age range for which the cluster masses have been measured.

experienced several peaks of up to a factor of 4 higher than it is at present. This increase would correspond to a similar increase of the CFE and, hence, of the maximum cluster mass.

In order to account for the past variations of the gas surface density, we assume a linear relation between the SFR density and the gas surface density, $\Sigma_{\text{g}} \propto \Sigma_{\text{SFR}}$ (Bigiel et al. 2008, Leroy et al. 2008), and use fig. 6 in Lewis et al. (2015) to derive a radially dependent correction factor, $f(R) \equiv \max[\Sigma_{\text{SFR}}(R, 0 \leq \tau/\text{Myr} < 316)]/\Sigma_{\text{SFR}}(R, 0 \leq \tau/\text{Myr} < 25)$. This factor converts the SFR over the most recent 25 Myr, and hence, the present gas surface density, to the maximum over the past 316 Myr, as that corresponds to the true conditions when the clusters were formed. We apply our model to the past-corrected gas surface density profile and those predictions are included in the colour-shaded area. We find that the predictions based on the present-day SFR underpredict the truncation mass reported in Johnson et al. (2017) which is $M_{\text{cl,c}} = 8.5^{+2.8}_{-1.8} \times 10^3 M_{\odot}$ by a factor of 4, but when accounting for the past range of gas surface densities, we find that our prediction agrees with the observed mass.

The above considerations show that at certain times in the history of the 10-kpc ring, the maximum cluster mass scales predicted by our model would have been consistent with the observed truncation mass from Johnson et al. (2017). We can test further whether this is indeed the reason for the discrepancy by considering the ages of the most massive clusters in M31. Fouesneau et al. (2014) present a subset of the cluster sample used by Johnson et al. (2017) and show that the most massive clusters in the 0–300 Myr age range have ages exceeding 100 Myr. This corresponds to multiple dynamical times at the radius of the 10-kpc ring and matches a burst that occurred 100–150 Myr ago. We thus conclude that the discrepancy between model and observation is likely due to changes in environmental conditions since the observed clusters formed.

4.3 M83

For the third test of our model, we use the nearby grand-design spiral galaxy M83. In order to apply our model, we use the observational data reported in fig. 6 in Freeman et al. (2017): the total gas surface density curve from the top panel, the rotation curve from the middle panel obtained from the 21-cm line in Walter et al. (2008) and the velocity dispersion inferred from the Atacama Large Millimeter/submillimeter Array (ALMA) CO and THINGS 21-cm data from the bottom panel.

We compare the predictions of our model with the observed maximum masses of two observational samples. For the GMC sample, we use the cloud catalogue of Freeman et al. (2017), who present data obtained with ALMA, whereas for the clusters, we use the sample from Adamo et al. (2015), based on *Hubble Space Telescope* data.

As for the previous tests, we carry out a b-spline fit to the rotation curve to determine the epicyclic frequency κ . We determine the stability parameter Q as in equation (5) and we apply the model from Section 2 at each galactocentric radius. We determine the maximum cloud mass, the CFE and the maximum cluster mass. In order to compare with the observed masses, we calculate the mass-weighted average of the predicted quantities for each radial bin described in Adamo et al. (2015) and show the result in Fig. 9. With typical uncertainties of 10 per cent in the epicyclic frequency and 30 per cent in the gas surface density, the uncertainty associated with our predictions is ~ 0.4 dex.

In the top panel in Fig. 9, we show the GMC mass scales. We plot the mean mass for the five most massive GMCs ($M_{\text{GMC,max}}^5$) and the most massive GMC $M_{\text{GMC,max}}$ reported in Freeman et al. (2017),⁶ as well as our predicted shear and feedback-limited mass scales for the clouds. Given that the region studied is shear-limited, the predicted maximum mass by our model corresponds to the Toomre mass and they agree with the observed cloud masses, at each radial bin.

Adamo et al. (2015) determine the CFE of two groups of clusters; Γ_{1-10} for the clusters of ages between 1 and 10 Myr and Γ_{10-50} for the clusters of ages between 10 and 50 Myr. Given that for the age bin 1–10 Myr it is non-trivial to distinguish between bound clusters and unbound associations, we decide to use Γ_{10-50} to represent the CFE of the cluster population in M83.

We show the observed and predicted CFEs in the middle panel in Fig. 9. Specifically, we show the observed CFE Γ_{10-50} described in Adamo et al. (2015), the error bars correspond to the values given

⁶The cloud masses are derived from CO data using the standard Galactic CO-to-H₂ conversion factor of $X_{\text{CO}} = 2 \times 10^{20} \text{ cm}^{-2} (\text{K km s}^{-1})^{-1}$ (Bolatto et al. 2013).

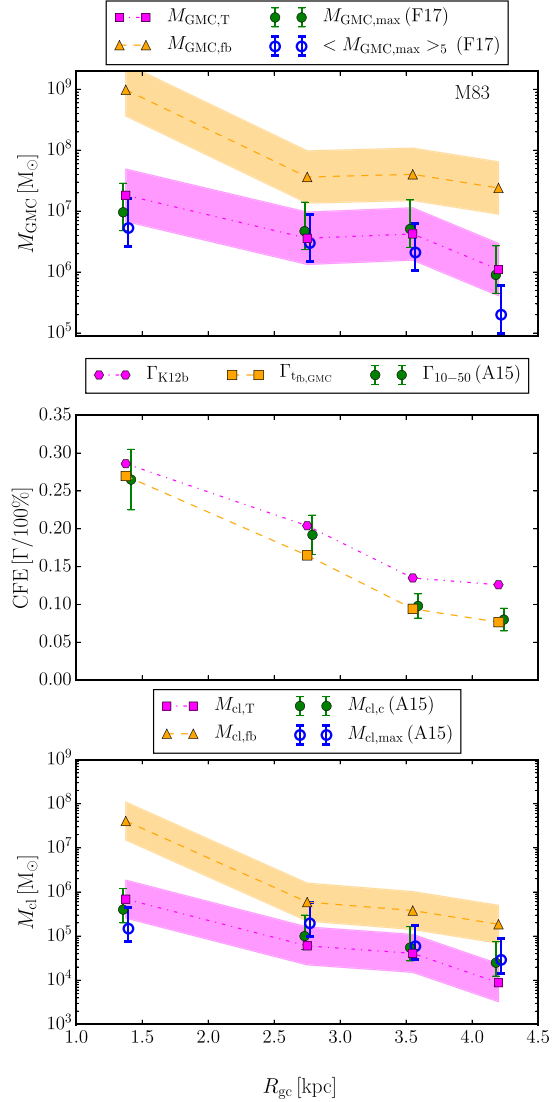


Figure 9. Result of applying our shear–feedback hybrid model to M83: (top) maximum GMC mass and (bottom) maximum cluster mass as a function of the galactocentric radius. The magenta squares correspond to the shear-limited mass scales and the orange triangles correspond to the feedback-limited mass scales. The observed maximum mass scales and CFE are represented by the green and blue dots with error bars. The colour-shaded areas indicate a fiducial uncertainty range, assuming that the rotation curve and the gas surface density profile are known to an accuracy of ~ 0.04 and ~ 0.13 dex, respectively. For more details see the text.

in their paper), the predicted CFE using the model described in Kruijssen (2012) with a time of observing the cluster population of $t = 10$ Myr and the predicted CFE using the same model but at a different time $t = t_{\text{fb}}$. Our prediction agrees well with the observational Γ_{10-50} in all the radial bins. To first order, this confirms the agreement found by Adamo et al. (2015), who carried out a similar comparison using lower resolution input data for the model. To second order, we see that evaluating the CFE predicted by Kruijssen (2012) at the feedback time yields somewhat better agreement with the observations than using the fiducial evaluation time of 10 Myr.

1292 *M. Reina-Campos and J. M. D. Kruijssen*

However, it is not immediately clear how significant this improvement is, given the intrinsic ~ 0.2 dex uncertainty in the model. Only at the largest radius does the difference between both models exceed this margin.

In the bottom panel of Fig. 9, we present the observed and predicted cluster masses. We show the maximum cluster mass $M_{\text{cl,max}}$ and the characteristic cluster mass $M_{\text{cl,c}}$ obtained when fitting an exponentially truncated power law with index -2 (i.e. a Schechter 1976 function) presented in Adamo et al. (2015), as well as our predicted shear-limited (using $M_{\text{GMC}} = M_{\text{GMC,T}}$) and feedback-limited cluster masses. As in the cloud mass scales, we predict the masses are shear-limited over the entire radial range and they closely agree with the observed masses.

The strong bar in M83 only appears to slightly affect the observed cluster masses. From the maps in Adamo et al. (2015), the bar ends at $R \sim 2.3$ kpc, which corresponds to the end of their first bin. Any influence of the bar should manifest itself in the first two radial bins. As opposed to the comparison done in Section 4.1 for the Milky Way, where we use individual masses of observed clusters, here we compare the predictions of our model with two mass scales: the characteristic mass derived from a Schechter function fit to the cluster mass function within a radial bin $M_{\text{cl,c}}$ and the maximum cluster mass within a radial bin $M_{\text{cl,max}}$. The first mass scales are averaged both azimuthally and over the bin, whereas the second ones are not, indicating they are equivalent to the individual cluster masses we use for the Milky Way. Looking into Fig. 9, there is a slight disagreement between the predictions of our model and the maximum mass scales in the first and second bin. This region is where the bar should have an effect, but given that the disagreement is within the errorbars we can conclude that cluster formation is only slightly affected by the bar.

4.4 zC406690

As a final test of our model, we use the high-redshift galaxy zC406690 ($z = 2.196$) from the zCOSMOS-SINFONI sample (see Förster Schreiber et al. 2009; Mancini et al. 2011). This choice is motivated by its average properties for a high-redshift galaxy (see e.g. Mancini et al. 2011, Tacconi et al. 2013), except for its high SFR, which is typical of a highly actively star-forming environment. Next to zC406690, there are two additional galaxies in the samples from Genzel et al. (2011) and Tacconi et al. (2013) with known clump masses and macroscopic observational parameters. However, zC406690 is the only galaxy that is classified as rotationally dominated, which rules out the other galaxies as suitable targets for the application of our model.

4.4.1 Prediction of the maximum mass scales for clumps and stellar clusters

We now compare the predictions of our model to the observed clump masses from Genzel et al. (2011) derived using $H\alpha$ data obtained as part of the SINS GTO survey (Förster Schreiber et al. 2009) and the SINS/zCOSMOS ESO Large Program (see Mancini et al. 2011) of high-redshift galaxy kinematics carried out with SINFONI at the Very Large Telescope.

In order to properly describe the host galaxy gas disc, we use the properties derived from CO data obtained in the context of the PHIBSS survey with the Plateau de Bure millimeter Interferometer (PdBI, nowadays called NOEMA) and listed in table 2 of Tacconi et al. (2013). In particular, we use the circular velocity

$V = 224 \text{ km s}^{-1}$, the optical half-mass radius $R_{1/2} = 6.3 \text{ kpc}$ and the mean molecular gas surface density contained in the half-mass radius $\Sigma_g(R \leq R_{1/2}) = 10^{2.52} M_{\odot} \text{ pc}^{-2}$.⁷ These global properties are then converted to radial profiles. In principle, Genzel et al. (2011) use the $H\alpha$ emission in conjunction with the gas depletion time to estimate a molecular gas surface density profile. However, while this method is intrinsically indirect, it also provides the *present* gas surface density profile, in which the clumps have already condensed. We are interested in the initial gas surface density profile, *before* the clumps have formed. We therefore assume that the gas initially followed an exponential profile with the same half-light radius as currently seen in the optical. The ratio between the half-mass radius and the scale radius in a two-dimensional exponential surface density profile is constant at $R_{1/2}/R_d = 1.678$, which allows us to express this profile as

$$\Sigma_g(R) = \Sigma_0 \exp(-R/R_d), \quad (12)$$

with

$$\Sigma_0 = \frac{\Sigma_g(R \leq R_{1/2})}{2} \frac{(R_{1/2}/R_d)^2}{\left[1 - \exp\left(-\frac{R_{1/2}}{R_d}\right)\left(1 + \frac{R_{1/2}}{R_d}\right)\right]}. \quad (13)$$

We assume that the rotation curve is flat at the quoted circular velocity and use a velocity dispersion of $\sigma = 50 \text{ km s}^{-1}$ to determine Q .

We thus apply the model described in Section 2 to the obtained values for a radial range out to twice the optical half-mass radius. We determine the shear and feedback-limited maximum cloud and cluster mass scales and we show them in Fig. 10. Assuming typical uncertainties of 10 per cent in the epicyclic frequency and 30 per cent in the gas surface density, the uncertainty associated with our predictions is ~ 0.4 dex.

We overplot the observed clump masses from Genzel et al. (2011) in the top panel with an error bar of a factor 3 (as indicated in their paper). We also plot the shear-limited Toomre mass determined directly from the galaxy-average properties listed in Tacconi et al. (2013). Its large discrepancy relative to the predicted mass scales using the exponential fit is due to the use of the mean surface density contained within a certain radius rather than the density at that radius, which is much lower. The predicted clump mass scales by our model correspond to the shear-limited Toomre masses, and they are of the order of the observed clump masses. Dekel & Krumholz (2013) demonstrate that stellar feedback is expected to produce steady outflows from the giant clumps in high-redshift galaxies, but they are not expected to be disrupted in the process. The authors argue that the clumps are expected to migrate to the centre to build-up the bulge in a short time-scale, although recent work suggests this process may be inhibited by short clump lifetimes (e.g. Oklopčić et al. 2017).

A consideration to be made is whether the larger mass scales observed for the high-redshift clumps than for the local-Universe GMCs are result of the observing resolution, as recent studies suggest (e.g. Behrendt, Burkert & Schartmann 2016; Dessauges-Zavadsky et al. 2017). The idea that high-redshift clumps may be analogous to the GMCs in the local Universe has already been suggested in previous studies (e.g. Oklopčić et al. 2017). The massive clumps may fragment into smaller ones, which at low spatial

⁷ The mean molecular gas surface density is determined as $\Sigma_g(R \leq R_{1/2}) = M_{\text{mol-gas}}/(\pi R_{1/2}^2)$, where the molecular mass of the cloud is derived from CO data using the standard Galactic CO-to- H_2 conversion factor of $X_{\text{CO}} = 2 \times 10^{20} \text{ cm}^{-2} (\text{K km s}^{-1})^{-1}$ (Bolatto et al. 2013).

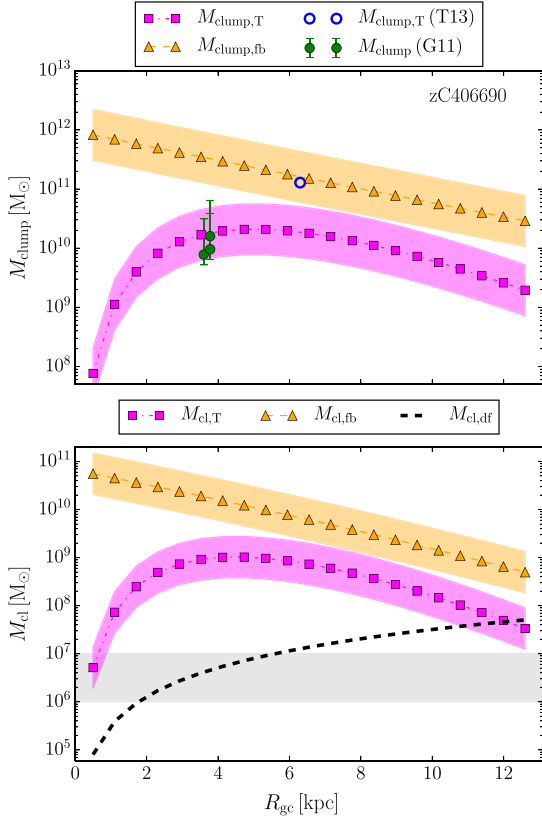


Figure 10. Result of applying our shear–feedback hybrid model to zC406690 using CO data from the PHIBSS survey: (top) maximum clump mass and (bottom) maximum cluster mass as a function of the galactocentric radius. The magenta squares correspond to the shear-limited mass scales and the orange triangles correspond to the feedback-limited mass scales. In the bottom panel, the dashed line indicates the maximum cluster mass that may survive dynamical friction over a typical major merger time-scale, i.e. before the clusters would be redistributed by mergers. The observed clump masses from Genzel et al. (2011) are represented by the green filled dots with error bars. For comparison, the blue open circle shows the predicted shear-limited mass when using the global-average properties from table 2 in Tacconi et al. (2013) rather than the radial profiles used here. The colour-shaded areas indicate a fiducial uncertainty range, assuming that the rotation curve and the gas surface density profile are known to an accuracy of ~ 0.04 and ~ 0.13 dex, respectively. The grey-shaded area in the bottom panel indicates the typical maximum mass scale of globular clusters (see the text).

resolution could appear as a single clump, but could also end up merging into a single clump. Therefore, this fragmentation is not inconsistent with our results in the context of massive clump and cluster assembly in gravitationally unstable environments, which is expected to be a two-step process around a reversal of the growth hierarchy. It starts as a top-down process, where the largest gravitationally unstable scale contracts and fragments into many smaller clumps. As time proceeds, the resulting hierarchy of smaller clumps may coalesce to form more massive clumps and clusters, thus transitioning to a bottom-up hierarchy. When defining the maximum possible clump and cluster masses as we do in this paper, one has to adopt the optimal case in which the entire hierarchy within the largest gravitationally unstable scale has merged. For these reasons, our predictions are insensitive to the recently-reported effects of

spatial resolution on resolving high-redshift clumps into smaller fragments.

The predicted cluster masses, shown in the bottom panel in Fig. 10, are much larger than any cluster mass observed at $z = 0$. We investigate the possibility of dynamical friction being the mechanism that destroys the more massive clusters. In the context of the Kruijssen (2015) globular cluster formation model, stellar clusters are disrupted by tidal shocks until they are redistributed to the halo during galaxy mergers or in accretion events (also see Kravtsov & Gnedin 2005, Prieto & Gnedin 2008, Rieder et al. 2013). Equation (18) of Kruijssen (2015) shows the minimum cluster mass that will spiral in a time-scale shorter than a galaxy merging time, and thus, it will get destroyed by dynamical friction before it can escape to the halo,

$$M_{\text{cl,df}} = 10^6 M_{\odot} \left(\frac{t_{\text{merge}}}{2 \text{ Gyr}} \right)^{-1} \left(\frac{R}{2 \text{ kpc}} \right)^2 \left(\frac{V}{200 \text{ km s}^{-1}} \right), \quad (14)$$

where t_{merge} is the galaxy merger time-scale, R is the galactocentric radius of the stellar cluster and V is the circular velocity. Given the galaxy’s stellar mass of $M_{*} \simeq 4 \times 10^{10} M_{\odot}$, we infer a halo mass at $z \simeq 2.2$ of $M_{\text{h}} \simeq 2 \times 10^{12} M_{\odot}$ through abundance matching (Moster, Naab & White 2013). For such a halo mass, we use the relations from Genel et al. (2009) to estimate that the time-scale to merge with another halo of at least 1/3 its own mass⁸ is $t_{\text{merge}} \simeq 3.5$ Gyr. We use the same flat rotation curve of $V = 224 \text{ km s}^{-1}$ and obtain an expression that only depends on the galactocentric radius of the cluster:

$$M_{\text{cl,df}} = 3.2 \times 10^5 M_{\odot} \left(\frac{R}{\text{kpc}} \right)^2. \quad (15)$$

We plot this relation in the bottom panel in Fig. 10. Only the most massive clusters on the edge of the radial range considered ($R > 12 \text{ kpc}$) may spiral in slowly enough to be ejected before they become part of the nucleus. Therefore, the minimum cluster mass for destruction by dynamical friction becomes the effective predictor for the maximum mass scales of globular clusters at $z = 0$. Indeed, the predicted mass range matches the observed truncation mass of the globular cluster mass function (GCMF) of about 10^6 – $10^7 M_{\odot}$ (e.g. Fall & Zhang 2001; Jordán et al. 2007; Kruijssen & Portegies Zwart 2009). This result is in contradiction to the finding of Jordán et al. (2007) that dynamical friction does not drive the truncation of the GCMF. However, we note that this work considers the observed conditions in real high-redshift galaxies, in which globular clusters must have formed, whereas Jordán et al. (2007) arrived at their conclusions by using the properties of the present-day galaxy population.

4.4.2 Comparison to previous work on the maximum mass scales of high-redshift clumps

This is not the first time that the shear-limited Toomre mass is calculated for high-redshift galaxies, with the goal of determining the maximum clump mass. Dekel et al. (2009) derive a simplified expression for the Toomre mass that is based on global galaxy properties, by assuming that the angular velocity traces the gravitational potential (i.e. the disc is rotation-dominated). This allows them to relate the Toomre clump mass to a fraction of the disc mass. We use

⁸ We follow the assumption of Kruijssen (2015) that this is a reasonable minimum mass ratio for driving the redistribution of the clusters.

this formalism to evaluate whether the sample from Tacconi et al. (2013) can be used to test our model.

Dekel et al. (2009) present a simple theoretical framework for massive galaxies at high redshift in which discs are considered to be self-gravitating and rotating objects subject to gravitational instabilities. Despite recent work calling into question the validity of using the linear Toomre analysis in the context of highly non-linear galaxies (Behrendt, Burkert & Schartmann 2015, Tamburello et al. 2015, Inoue et al. 2016), these concerns mainly relate to the subsequent fragmentation of the clumps. Their maximum mass scales are still largely set by the balance between self-gravity, the centrifugal force and the turbulent pressure. Thus, the larger clumps are limited by shear and correspond to the Toomre mass, to which the results of this work adds further support. Following a similar line of reasoning, Dekel et al. (2009) use the characteristic Toomre length to define the properties of the clumps. They use a number of assumptions to relate those properties with the radius and the mass of the disc component of the galaxy. We now re-evaluate these assumptions and use the high-redshift galaxies listed in Tacconi et al. (2013) to see if the parameter space studied is affected.

Dekel et al. (2009) define two quantities, δ and β , which correspond to the mass fraction of the disc and to the baryon mass fraction, respectively,

$$\delta \equiv \frac{M_d}{M_{\text{tot}}} \leq \beta \equiv \frac{M_{\text{bar}}}{M_{\text{tot}}}, \quad (16)$$

where M_d is the mass in the disc component within the disc radius R_d , M_{bar} is the mass of the baryons in the disc and bulge within R_d and M_{tot} is the total mass taking into account the dark matter, the stellar and the disc masses within R_d .

The inequality of equation (16) implies that the disc mass has to be smaller than or equal to the baryonic mass, $M_d \leq M_{\text{bar}} \equiv \beta M_{\text{tot}}$. Dekel et al. (2009) determine the total mass from the expression of the circular velocity at the disc radius R_d ,

$$(\Omega R_d)^2 = V^2 = \frac{GM_{\text{tot}}}{R_d} \rightarrow M_{\text{tot}} = \frac{\Omega^2 R_d^3}{G} \quad (17)$$

and assume a constant surface density within R_d to determine the disc mass, $M_d = \pi \Sigma_{\text{tot}} R_d^2 = \pi \Sigma_g R_d^2 / f_g$, where $f_g = M_g / (M_g + M_*)$ is the gas fraction. Assuming a bulgeless disc (i.e. $\delta = \beta$ and $M_d = M_{\text{bar}}$), this then allows Dekel et al. (2009) to write:

$$M_T \simeq \frac{\pi^2}{36} \beta^2 M_d, \quad (18)$$

with the express requirement that $0 \leq \beta \leq 1$.

By introducing the above expressions in the mass in equation (16) and again assuming $\delta = \beta$, we can define the combination of the baryon and the gas fraction with its physical range:

$$\frac{\pi \Sigma_g R_d^2}{f_g} = \beta \frac{\Omega^2 R_d^3}{G} \rightarrow 1 \geq \beta f_g = \frac{\pi G \Sigma_g}{\Omega^2 R_d} \geq 0. \quad (19)$$

To test if the simplified expression for the maximum mass scale holds, i.e. if the product of the baryon fraction and gas fraction apply, we use the high-redshift galaxies listed in Tacconi et al. (2013). We separate the galaxies into two subsamples depending on the kinematic classification done by Tacconi et al. (2013); *rotation* are galaxies with disc-like morphology and a velocity gradient in the CO data and *dispersion* are disc galaxies without a velocity gradient (*disk(A)* and *disk(B)* in their classification). We use the circular velocity V , the half-light optical radius $R_{1/2}$, the gas fraction f_g and the mean gas surface density within the half-light optical radius $\Sigma_g (r < R_{1/2})$ listed in their table 2. We determine the angular

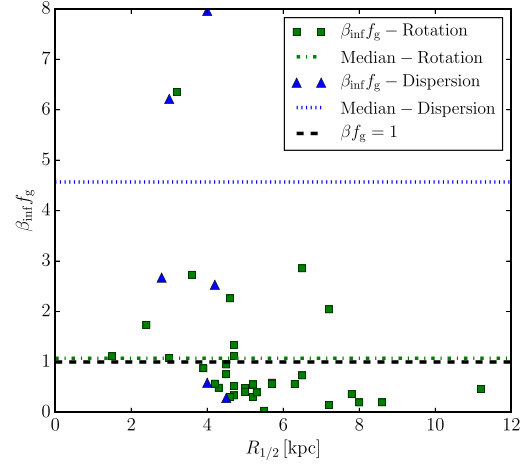


Figure 11. Product of the baryon fraction β and the gas fraction f_g that would be implied by using the simplified expression of the Toomre mass from Dekel et al. (2009) as a function of the half-light optical radius $R_{1/2}$ for two sub-samples of high-redshift galaxies from Tacconi et al. (2013), i.e. dispersion- or rotation-dominated. We overplot the median for each subsample (green line for rotation, blue line for dispersion-dominated) and the unity line (black dashed line), which represents the maximum allowed value of βf_g .

velocity at the half-light radius as $\Omega_{\text{obs}} = V/R_{1/2}$. We restrict the galaxies to be in the parameter space studied in Fig. 2.

With these values (Ω_{obs} , Σ_g , f_g and $R_{1/2}$) we determine the value of the product of the baryon and gas fraction $\beta_{\text{inf}} f_g$ required by the combination of the angular velocity and the baryonic surface density for each subsample of galaxies using equation (19). We show it as a function of the half-light radius of the galaxy in Fig. 11. We overplot the median of each subsample, as well as the maximum value for $\beta_{\text{inf}} f_g = 1$. The galaxies dominated by dispersion show a larger dispersion in βf_g , whereas the rotation-dominated galaxies have a significantly lower ratio between the gas mass and the dynamical mass, to such an extent that the median is consistent with the allowed range of $\beta f_g \leq 1$. This comparison shows that dispersion-dominated galaxies have measured values of βf_g that are well in excess of the allowed range, which means that the Dekel et al. (2009) expression for the Toomre mass from equation (18) substantially overestimates the mass if the observed inferred βf_g are used.

We emphasize that the bias induced by unphysical values of βf_g is not exclusive to the simplified Dekel et al. (2009) expression for the Toomre mass, but is more immediately obvious in their formulation. Fundamentally, the bias arises because the inferred angular velocity in dispersion-dominated systems underestimates the depth of the gravitational potential and, hence, the total galaxy mass. This underestimate of Ω affects equation (18) in the same way as it affects the formal expression in equation (2) – both effectively scale with Ω^{-4} .

With this result we can revisit the condition on $\beta f_g \leq 1$ and obtain a condition for the angular velocity that isolates the part of parameter space in which the observed galaxy properties can be used reliably as input for our model:

$$\frac{\pi G \Sigma_g}{\Omega^2 R_d} \leq 1 \rightarrow \Omega \geq \sqrt{\frac{\pi G \Sigma_g}{R_d}}, \quad (20)$$

where we use the mean galaxy size of the high-redshift sample for R_d . This is a representative radius because Fig. 11 shows that the

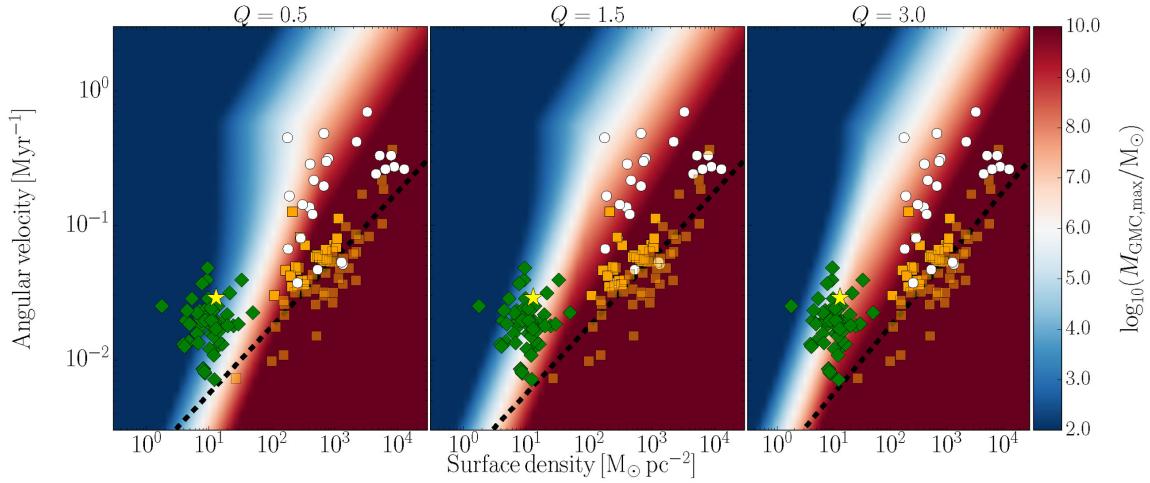


Figure 12. Maximum cloud mass as a function of the angular velocity and the surface density for three values of the stability parameter Q . We overplot observational data from four galactic environments as in Fig. 2. We shade the high-redshift galaxies that require baryon fractions larger than unity when using the simplified expression of the Toomre mass from Dekel et al. (2009). The black dashed line indicates a required baryon fraction of unity for the mean disc size in the galaxy sample of Tacconi et al. (2013).

product βf_g has no strong radius dependence. In order to visualize better this condition, we plot it in a modification of Fig. 4 that is shown in Fig. 12. We include the same galactic environments discussed in Section 3, but we shade the high-redshift galaxies for which the inferred low angular velocities imply a product of the baryon fraction and the gas fraction in excess of unity. These galaxies have gas masses exceeding the total mass needed to maintain their angular velocity.

The condition for the angular velocity clearly separates the high-redshift galaxy sample into two sub-samples; above the line, they fulfil the condition of having a gas-to-total mass fraction βf_g smaller than unity, but below the line this condition is violated. We find 44 high-redshift galaxies out of the total sample of 65 in Tacconi et al. (2013) that fall into this regime. The large implied gas-to-total mass fractions indicate that the observed angular velocity (Ω_{obs}) is smaller than the angular velocity determined from the surface density [equation (17) and assuming $M_{\text{tot}} = \pi R^2 \Sigma_g f_g$]. In view of these results, we caution that only those high-redshift galaxies with implied gas-to-total mass fractions smaller than unity should be used to test the predictions of our model.

5 CONCLUSIONS

We present a simple, self-consistent analytical model to determine the maximum mass of GMCs and stellar clusters as a function of the galactic environment. The model develops the idea that these maximum masses can be limited by shear and stellar feedback. In environments with low shear and low gas surface densities, feedback is expected to proceed more rapidly than the free-fall times of shear-limited GMCs, thus giving time to the massive stars to disrupt the cloud before the collapse has finished. Taking this into account, our model predicts smaller masses for both GMCs and stellar clusters in those environments.

We have explored the parameter space formed by Q , Σ_g and Ω and we predict that GMC and cluster masses are feedback-limited if both the galactic gas surface density $\Sigma_g \leq 100 M_\odot \text{pc}^{-2}$ and the angular velocity $\Omega \leq 0.6 \text{Myr}^{-1}$, assuming a typical $Q = 1.5$.

For larger values of gas surface density and angular velocity, the masses become shear-limited. For lower (higher) values of Q , the limit for the gas surface density shifts towards higher (lower) values ($\Sigma_g \leq 650 M_\odot \text{pc}^{-2}$ for $Q = 0.5$ and $\Sigma_g \leq 45 M_\odot \text{pc}^{-2}$ for $Q = 3$), whereas the limit for the angular velocity does not change.

We also find that the region affected by feedback in our model encompasses the solar neighbourhood and the discs of local-Universe spiral galaxies described in Kennicutt (1998). On the other hand, the high-redshift galaxies from Tacconi et al. (2013) and the circumnuclear starbursts of Kennicutt (1998) reside in the shear-limited regime. This transition between a feedback-dominated and a shear-dominated regime explains why the clumps observed in those environments have higher masses than those in local galaxies (Elmegreen & Elmegreen 2005), even beyond the environmental dependence already expected if the mass scales would only be set by the shear-limited Toomre mass.

There are a couple of limitations that should be kept in mind when applying our model. We assume a differentially rotating disc in hydrostatic equilibrium. External compression of the material caused by the presence of substructure in the disc (such as bars, arms or galaxy mergers) may yield larger mass scales than those predicted by the model. At the same time, the model bases its predictions on the current gas conditions, so the cluster sample to which it has to be compared has to correspond to an age range where the gas surface density has remained stable. Last, the predictions of the model for cluster forming in high-redshift environments carry the caveat that such massive objects may not survive until the present day due to dynamical friction towards the bulge of the galaxy.

We compare our predictions as a function of the galactocentric radius for the Milky Way, the disc galaxy M31, the grand-design spiral galaxy M83 and the high-redshift galaxy zC406690 with the observed GMC, clump and cluster masses in these galaxies. As in the numerical simulations by Oklopčić et al. (2017, see also Soto et al. 2017 for an observational study), we find that the molecular clumps become less massive with decreasing redshift; in the context of our analytical model, this happens because the galaxies become

more extended and less gas-rich, driving them into the feedback-limited regime.

For the Milky Way, the key new ingredient of our model, i.e. that the cloud can be disrupted by stellar feedback due to the feedback time-scale being smaller than the free-fall time, is applicable for galactocentric radii of $R \geq 4.3$ kpc. Observations indicate a roughly constant mass of $M_{\text{cl,max}} \sim 10^4 M_{\odot}$ across all galactocentric radii, as our model predicts. For the CMZ and the inner part of the galaxy, the GMC masses are equal to the shear-limited Toomre mass. Our hybrid mass predictions correctly reproduce the maximum observed cloud mass in the CMZ and the solar neighbourhood, as well as the observed cluster masses at all radii, except for those located at the end of the bar. The compression of the gas at the end of the bar may aid the accumulation of a larger mass reservoir than would normally have been possible against shear and feedback.

In M31, the feedback-time-scale is smaller than the two-dimensional free-fall time-scale for galactocentric radii $R \geq 8.4$ kpc. Our predictions for the maximum GMC mass agrees with the observed maximum cloud mass reported in Schrubba et al. (in preparation). However, our predictions based on the present-day gas surface density do not reproduce the truncation mass reported in Johnson et al. (2017). We use the spatially resolved star formation history of M31 to show that this discrepancy is plausibly explained by the fact that the most massive clusters are older than 100 Myr and formed under higher gas densities than currently observed. As opposed to the Milky Way and M31, the maximum mass scales in M83 fall in the shear-limited regime of our model. Again, the predicted cloud and cluster mass scales agree well with the observed masses at all galactocentric radii.

Johnson et al. (2017) have recently proposed a relation between the high-mass end of the young cluster mass function and the galaxy-averaged SFR surface density. In the context of our model, their $M_c - \Sigma_{\text{SFR}}$ relation does not account for the steep dependence of the Toomre mass on the epicyclic frequency ($M_T \propto \kappa^{-4}$). We therefore interpret the relation proposed by Johnson et al. (2017) as the result of selecting environments at similar epicyclic frequencies, which hides the κ dependence and allows the residual effect to be absorbed into Σ_{SFR} . This happens because Σ_{SFR} is covariant with κ due to the radial decrease of both quantities in nearly all galaxies. In principle, the dependence on κ should affect the maximum mass scale everywhere, but most noticeably so in shear-dominated environments like the CMZ or M83. We use the CMZ as a test case to compare the prediction from the $M_c - \Sigma_{\text{SFR}}$ relation to that of our model, as well as to the observed maximum cluster masses. We consider the CMZ within $|l| \leq 1^\circ$, corresponding to $R \leq 140$ pc, where the $\text{SFR} = 0.1 M_{\odot} \text{yr}^{-1}$ (Longmore et al. 2013; Barnes et al. 2017). With these values, we obtain a SFR surface density of $\Sigma_{\text{SFR}} = 1.6 M_{\odot} \text{yr}^{-1} \text{kpc}^{-2}$, for which the relation between M_c and Σ_{SFR} suggested by Johnson et al. (2017) yields a Schechter characteristic mass of $M_c \simeq 1 \times 10^7 M_{\odot}$. By contrast, our model predicts a shear-limited maximum cluster mass of $M_{\text{cl,max}} \simeq 3 \times 10^4 M_{\odot}$. These predictions differ by nearly three orders of magnitude. If we now compare them to the most massive clusters in the CMZ, which are the Arches and Quintuplet clusters with masses of $M \simeq 2 \times 10^4 M_{\odot}$ (Portegies Zwart et al. 2010), we find that our model agrees very well with the observed cluster mass scales, whereas the $M_c - \Sigma_{\text{SFR}}$ relation strongly overpredicts the cluster masses. This is also reflected by the maximum cloud masses observed in the CMZ – the GMCs on the 100-pc stream have masses of $\sim 10^5 M_{\odot}$ (Walker et al. 2015), well below the maximum cluster mass one would infer from the proposed $M_c - \Sigma_{\text{SFR}}$

relation.⁹ This example highlights the importance of accounting for differential rotation and shear when predicting the maximum mass scales for molecular clouds and stellar clusters.

The fact that the observed cluster masses agree with the feedback-limited cluster mass scales predicted by our model for a significant subset of local-Universe environments suggests that the most massive GMCs are gravitationally collapsing (e.g. fig. 17 in Miville-Deschênes et al. 2017). Otherwise, the clusters forming within that cloud would not be able to continue their assembly into one object after the feedback has blown out the gas. Therefore, an important implication of our results is that the formation time-scale of both GMCs and high-redshift clumps has an upper limit set by the two-dimensional free-fall time at the Toomre length (also see Jeffreson & Kruijssen, in preparation). By adding feedback to the normal Toomre analysis, we obtain a formation time set by the minimum of the two-dimensional free-fall time in equation (3) and the feedback time-scale in equation (4). We note that support against collapse by shear can significantly increase these time-scales, but only if $Q \gtrsim 3$ (Jeffreson & Kruijssen, in preparation).

The clump and cluster mass scales in the high-redshift galaxy zC406690 are also limited by shear. The predictions of our model for the maximum clump masses agree with the observed clump masses from Genzel et al. (2011). Our model predicts very large maximum cluster masses, but we demonstrate that, across the radial range covered, dynamical friction would cause these clusters to spiral into the nucleus before they might be scattered out into the halo by a major merger. Dynamical friction thus limits the maximum mass scales of long-lived globular clusters at $z = 0$. We predict globular clusters formed in zC406690 should not exceed $10^6 - 10^7 M_{\odot}$, which agrees with the observed truncation mass of the GCMF (Jordán et al. 2007; Kruijssen & Portegies Zwart 2009).

We use a commonly used, simplified expression based on macroscopic galaxy properties (Dekel et al. 2009) and find that the properties of observed, dispersion-dominated galaxies (Tacconi et al. 2013) have strongly underestimated angular velocities, which leads to gas-to-total mass fractions in excess of unity and correspondingly overestimated maximum clump masses. We use this example to illustrate that the observed properties of galaxies are sometimes inconsistent. Only those high-redshift galaxies with implied gas-to-total mass fractions smaller than unity should be used to test the predictions of our model.

⁹ One could argue that the total SFR in the CMZ is so low that the maximum cluster mass is set by the size-of-sample effect, which would mean that the physical maximum cluster mass is larger than observed. Fortunately, this effect can be quantified using fig. 1 of Gieles (2009), who show the mass of the most massive cluster given the true maximum cluster mass as a function of the total mass of the cluster population $\Gamma \times \text{SFR} \times \Delta t$, where Δt is the age range of the clusters. For the observed $\text{SFR} = 0.1 M_{\odot} \text{yr}^{-1}$, the expected CFE of $\Gamma \sim 50$ per cent (Kruijssen et al. 2014), and a putative cluster age range of $\Delta t = 10 \text{Myr}$, we find a total cluster population mass of $\Gamma \times \text{SFR} \times \Delta t = 5 \times 10^5 M_{\odot}$. For a Schechter-type initial cluster mass function with commonly adopted slope $\beta = -2$, we see that the observed masses of the most massive clusters in the CMZ imply a maximum mass scale of a few $10^4 M_{\odot}$, and certainly $< 10^5 M_{\odot}$. This result is consistent with our prediction. Note that we are ignoring the suggestion that the SFR in the CMZ was even higher when the Arches and Quintuplet clusters formed (Krumholz, Kruijssen & Crocker 2017), which would imply an underlying maximum mass even closer to the observed cluster masses. The size-of-sample effect is therefore not dominant in setting the maximum cluster masses observed in the CMZ, as expected from the fact that the clouds have masses of only $\sim 10^5 M_{\odot}$ – the material for forming more massive clusters is not available within the tidal limit.

The shear-limited clump mass scales predicted by our hybrid model for zC406690 are also confirmed by the results in Fisher et al. (2017b), which appeared while this paper was in review. They use the DYNAMO sample of low-redshift ($z \sim 0.1$) analogues to clumpy high-redshift galaxies (Green et al. 2014) to show that the clump sizes correspond roughly to the most shear-unstable scale, which corresponds to half the Toomre length. This supports the hypothesis that massive star-forming clumps in turbulent discs are the result of gravitational instabilities. In the context of our model, this result is to be expected because the DYNAMO galaxies considered by Fisher et al. (2017a) have typical surface densities and angular velocities of $\Sigma \sim 400 M_{\odot} \text{pc}^{-2}$ and $\Omega \sim 0.09 \text{Myr}^{-1}$, respectively,¹⁰ which places them firmly in the shear-limited part of parameter space in Fig. 3 for $Q > 0.5$ and on the limit between both regimes for $Q \sim 0.5$.

In the context of galaxy formation, our model predicts an evolution of the maximum GMC (or clump) and stellar cluster (or globular cluster) mass with galactic environment and thus with redshift. As galaxies grow, they become less gas rich (Tacconi et al. 2010) and less compact due to their inside-out growth (De Lucia & Helmi 2008, Allen et al. 2017), implying that, over time, galaxies evolve to the feedback-limited regime in the parameter space of our model. We demonstrate that this prediction agrees with the observed GMC and cluster masses for four different galactic environments.

It is particularly important to consider the evolution of the mass scales with the environment in galaxy formation models which are aimed at reproducing the masses of molecular clouds and stellar clusters until $z = 0$. For instance, our results imply that the simple (star) particle-tagging techniques that are commonly used to assign globular clusters to the output of galaxy formation simulations result in biased samples of candidate globular clusters. Studies aiming to model the origin of the globular cluster population, i.e. the most massive clusters in the Universe, must account for the variation with time and environment of the maximum cloud and cluster mass scales.

ACKNOWLEDGEMENTS

We thank the anonymous referee for their helpful comments and suggestions. We thank Pamela Freeman and Erik Rosolowsky for providing the data from Freeman et al. (2017) in electronic form, Andreas Schruha for providing the gas surface profiles from Schruha et al. (in preparation) and Cliff Johnson for sharing the manuscript of Johnson et al. (2017) ahead of publication, as well as for helpful discussions. We acknowledge helpful discussions with Joel Pfeffer, as well as with the members of the MUSTANG group. MRC would like to thank to the International Max Planck Research School for Astronomy and Cosmic Physics at the University of Heidelberg (IMPRS-HD) for the funding for this work. JMDK gratefully acknowledges support in the form of an Emmy Noether Research Group from the Deutsche Forschungsgemeinschaft (DFG), grant number KR4801/1-1.

REFERENCES

Adamo A., Kruijssen J. M. D., Bastian N., Silva-Villa E., Ryon J., 2015, *MNRAS*, 452, 246

¹⁰The surface density is obtained by writing $\Sigma = f_{\text{gas}} M_{\text{star}} / 2(1 - f_{\text{gas}}) \pi R_{1/2}^2$, where the stellar mass ($M_{\text{star}} \sim 3 \times 10^{10} M_{\odot}$), gas fraction ($f_{\text{gas}} \sim 0.3$) and half-light radius ($R_{1/2} \sim 2.3 \text{kpc}$) were determined for the first seven galaxies in table 1 of Fisher et al. (2017b). The angular velocity is obtained by writing $\Omega = V/R_{1/2}$, where $V \sim 210 \text{km s}^{-1}$ is taken to be the average for the same seven galaxies in table 1 of Fisher et al. (2017a).

- Allen R. J. et al., 2017, *ApJ*, 834, L11
 Barnes A. L., Longmore S. N., Battersby C. D., Bally J., Kruijssen J. M. D., Henshaw J. D., Walker D. L., 2017, *MNRAS*, preprint (arXiv:1704.03572)
 Bastian N., 2008, *MNRAS*, 390, 759
 Bastian N. et al., 2012, *MNRAS*, 419, 2606
 Behrendt M., Burkert A., Schartmann M., 2015, *MNRAS*, 448, 1007
 Behrendt M., Burkert A., Schartmann M., 2016, *ApJ*, 819, L2
 Bigiel F., Leroy A., Walter F., Brinks E., de Blok W. J. G., Madore B., Thornley M. D., 2008, *AJ*, 136, 2846
 Bland-Hawthorn J., Gerhard O., 2016, *ARA&A*, 54, 529
 Bolatto A. D., Wolfire M., Leroy A. K., 2013, *ARA&A*, 51, 207
 Braun R., Thilker D. A., Walterbos R. A. M., Corbelli E., 2009, *ApJ*, 695, 937
 Burkert A., Hartmann L., 2004, *ApJ*, 616, 288
 Caldwell N., Harding P., Morrison H., Rose J. A., Schiavon R., Kriessler J., 2009, *AJ*, 137, 94
 Colombo D. et al., 2014, *ApJ*, 784, 3
 Corbelli E., Lorenzoni S., Walterbos R., Braun R., Thilker D., 2010, *A&A*, 511, A89
 De Lucia G., Helmi A., 2008, *MNRAS*, 391, 14
 Dekel A., Krumholz M. R., 2013, *MNRAS*, 432, 455
 Dekel A., Sari R., Ceverino D., 2009, *ApJ*, 703, 785
 Dessauges-Zavadsky M., Schaerer D., Cava A., Mayer L., Tamburello V., 2017, *ApJ*, 836, L22
 Elmegreen B. G., 2002, *ApJ*, 577, 206
 Elmegreen B. G., 2010, *ApJ*, 712, L184
 Elmegreen B. G., Elmegreen D. M., 2005, *ApJ*, 627, 632
 Evans N. J., II, 1999, *ARA&A*, 37, 311
 Fall S. M., Zhang Q., 2001, *ApJ*, 561, 751
 Fisher D. B. et al., 2017a, *MNRAS*, 464, 491
 Fisher D. B. et al., 2017b, *ApJ*, 839, L5
 Förster Schreiber N. M. et al., 2009, *ApJ*, 706, 1364
 Fouesneau M. et al., 2014, *ApJ*, 786, 117
 Freeman P., Rosolowsky E., Kruijssen J. M. D., Bastian N., Adamo A., 2017, *MNRAS*, 468, 1769
 Frerking M. A., Langer W. D., Wilson R. W., 1982, *ApJ*, 262, 590
 Genel S., Genzel R., Bouché N., Naab T., Sternberg A., 2009, *ApJ*, 701, 2002
 Genzel R. et al., 2011, *ApJ*, 733, 101
 Genzel R. et al., 2014, *ApJ*, 785, 75
 Gieles M., 2009, *MNRAS*, 394, 2113
 Gieles M., Larsen S. S., Anders P., Bastian N., Stein I. T., 2006, *A&A*, 450, 129
 Green A. W. et al., 2014, *MNRAS*, 437, 1070
 Heiles C., Troland T. H., 2003, *ApJ*, 586, 1067
 Henshaw J. D., Longmore S. N., Kruijssen J. M. D., 2016, *MNRAS*, 463, L122
 Heyer M., Krawczyk C., Duval J., Jackson J. M., 2009, *ApJ*, 699, 1092
 Hughes A. et al., 2013, *ApJ*, 779, 46
 Inoue S., Dekel A., Mandelker N., Ceverino D., Bournaud F., Primack J., 2016, *MNRAS*, 456, 2052
 Johnson L. C. et al., 2017, *ApJ*, 839, 78
 Jordán A. et al., 2007, *ApJS*, 171, 101
 Kennicutt R. C., Jr, 1998, *ARA&A*, 36, 189
 Kennicutt R. C., Evans N. J., 2012, *ARA&A*, 50, 531
 Konstantopoulos I. S. et al., 2013, *AJ*, 145, 137
 Kravtsov A. V., Gnedin O. Y., 2005, *ApJ*, 623, 650
 Kruijssen J. M. D., 2012, *MNRAS*, 426, 3008
 Kruijssen J. M. D., 2014, *Class. Quantum Gravity*, 31, 244006
 Kruijssen J. M. D., 2015, *MNRAS*, 454, 1658
 Kruijssen J. M. D., Portegies Zwart S. F., 2009, *ApJ*, 698, L158
 Kruijssen J. M. D., Longmore S. N., Elmegreen B. G., Murray N., Bally J., Testi L., Kennicutt R. C., 2014, *MNRAS*, 440, 3370
 Kruijssen J. M. D., Dale J. E., Longmore S. N., 2015, *MNRAS*, 447, 1059
 Krumholz M. R., McKee C. F., 2005, *ApJ*, 630, 250
 Krumholz M. R., Dekel A., McKee C. F., 2012, *ApJ*, 745, 69
 Krumholz M. R., Kruijssen J. M. D., Crocker R. M., 2017, *MNRAS*, 466, 1213

1298 *M. Reina-Campos and J. M. D. Kruijssen*

- Lada C. J., Lada E. A., 2003, *ARA&A*, 41, 57
- Larsen S. S., 2009, *A&A*, 494, 539
- Larson R. B., 1981, *MNRAS*, 194, 809
- Leroy A. K., Walter F., Brinks E., Bigiel F., de Blok W. J. G., Madore B., Thornley M. D., 2008, *AJ*, 136, 2782
- Leroy A. K. et al., 2013, *AJ*, 146, 19
- Leroy A. K. et al., 2016, *ApJ*, 831, 16
- Lewis A. R. et al., 2015, *ApJ*, 805, 183
- Longmore S. N. et al., 2012, *ApJ*, 746, 117
- Longmore S. N. et al., 2013, *MNRAS*, 429, 987
- Longmore S. N. et al., 2014, in Beuther H., Klessen R. S., Dullemond C. P., Henning T., eds, *Protostars and Planets VI*. Univ. Arizona Press, Tucson, AZ, p. 291
- Mancini C. et al., 2011, *ApJ*, 743, 86
- Milam S. N., Savage C., Brewster M. A., Ziurys L. M., Wyckoff S., 2005, *ApJ*, 634, 1126
- Miville-Deschênes M.-A., Murray N., Lee E. J., 2017, *ApJ*, 834, 57
- Moster B. P., Naab T., White S. D. M., 2013, *MNRAS*, 428, 3121
- Murray N., 2011, *ApJ*, 729, 133
- Oklopčić A., Hopkins P. F., Feldmann R., Kereš D., Faucher-Giguère C.-A., Murray N., 2017, *MNRAS*, 465, 952
- Oort J. H., Spitzer L., Jr, 1955, *ApJ*, 121, 6
- Portegies Zwart S. F., McMillan S. L. W., Gieles M., 2010, *ARA&A*, 48, 431
- Prieto J. L., Gnedin O. Y., 2008, *ApJ*, 689, 919
- Rieder S., Ishiyama T., Langelaa P., Makino J., McMillan S. L. W., Portegies Zwart S., 2013, *MNRAS*, 436, 3695
- Schechter P., 1976, *ApJ*, 203, 297
- Schruba A. et al., 2011, *AJ*, 142, 37
- Shapiro K. L., Genzel R., Förster Schreiber N. M., 2010, *MNRAS*, 403, L36
- Solomon P. M., Rivolo A. R., Barrett J., Yahil A., 1987, *ApJ*, 319, 730
- Soto E. et al., 2017, *ApJ*, 837, 6
- Tacconi L. J. et al., 2010, *Nature*, 463, 781
- Tacconi L. J. et al., 2013, *ApJ*, 768, 74
- Tamburello V., Mayer L., Shen S., Wadsley J., 2015, *MNRAS*, 453, 2490
- Toomre A., 1964, *ApJ*, 139, 1217
- Vansevičius V., Kodaira K., Narbutis D., Stonkutė R., Bridžius A., Deveikis V., Semionov D., 2009, *ApJ*, 703, 1872
- Walker D. L., Longmore S. N., Bastian N., Kruijssen J. M. D., Rathborne J. M., Jackson J. M., Foster J. B., Contreras Y., 2015, *MNRAS*, 449, 715
- Walter F., Brinks E., de Blok W. J. G., Bigiel F., Kennicutt R. C. J., Thornley M. D., Leroy A., 2008, *AJ*, 136, 2563

This paper has been typeset from a $\text{\TeX}/\text{\LaTeX}$ file prepared by the author.

Chapter 3

A systematic analysis of star cluster disruption by tidal shocks – I. Controlled N-body simulations and a new theoretical model

Authors:

Jeremy J. Webb, Marta Reina-Campos
and J. M. Diederik Kruijssen

Published in *MNRAS* 486 (2019) 5879.

Reproduced with permission from the journal

The principal authorship of this article is split on equal footing between the coauthors. Dr. Webb and Dr. Kruijssen developed the original idea, and Dr. Webb performed the N-body simulations. Marta Reina-Campos derived the analytical model described in Sect. 3.4. Dr. Webb and Marta Reina-Campos wrote the manuscript, and all authors collaborated with corrections and suggestions to the manuscript.



A systematic analysis of star cluster disruption by tidal shocks – I. Controlled N -body simulations and a new theoretical model

Jeremy J. Webb,¹★ Marta Reina-Campos^{1b}² and J. M. Diederik Kruijssen^{1b}²

¹Department of Astronomy and Astrophysics, University of Toronto, 50 St George Street, Toronto, ON M5S 3H4, Canada

²Astronomisches Rechen-Institut, Zentrum für Astronomie der Universität Heidelberg, Mönchhofstraße 12-14, D-69120 Heidelberg, Germany

Accepted 2019 April 29. Received 2019 March 26; in original form 2018 November 26

ABSTRACT

Understanding the evolution of stellar clusters in an evolving tidal field is critical for studying the disruption of stellar clusters in a cosmological context. We systematically characterize the response of stellar clusters to tidal shocks using controlled N -body simulations of clusters with various properties that are subjected to different types of shocks. We find that the strength of the shock and the density of the cluster within the half-mass radius are the dominant properties that drive the amount of mass lost by the cluster, with the shape of the cluster profile being of minor influence. When the shock is applied as two separate sub-shocks, the amount of mass-loss during the second sub-shock is sensitive to the gap time between them. Clusters that experience successive sub-shocks separated by less than their crossing time attain the same masses and sizes at the end of the simulation. However, clusters subjected to sub-shocks separated by more than a crossing time experience different evolutionary histories. The amount of mass lost in the N -body models and its scaling with shock and cluster properties differ from that predicted by classical tidal disruption theory. We demonstrate that the discrepancy is alleviated by including a dependence on the escape time-scale of unbound stars, analogously to mass-loss driven by two-body relaxation. With our new theoretical model for shock-driven mass-loss, the predicted relative amounts of mass-loss agree with the results of the N -body simulations to ~ 0.3 dex across the full suite of simulations.

Key words: stars: kinematics and dynamics – globular clusters: general – open clusters and associations: general.

1 INTRODUCTION

The long-term evolution of a star cluster is governed by both internal and external processes. External mechanisms, which depend on the cluster's formation environment and subsequent orbit within its host galaxy, include tidal stripping, tidal shocks, and dynamical friction. Tidal shocks are well known to play an important role in the dynamical evolution of star clusters, both during formation and their long-term evolution (e.g. Spitzer 1958, 1987; Ostriker, Spitzer & Chevalier 1972; Chernoff, Kochanek & Shapiro 1986; Aguilar, Hut & Ostriker 1988; Chernoff & Weinberg 1990; Kundic & Ostriker 1995; Gieles et al. 2006; Kruijssen et al. 2011). In many (and possibly most) cases, tidal shock-driven mass-loss dominates over the other mass-loss mechanisms across a cluster's history (Lamers & Gieles 2006; Elmegreen 2010; Elmegreen & Hunter 2010; Kruijssen 2015; Miholics, Kruijssen & Sills 2017; Li & Gnedin 2018; Pfeffer et al. 2018).

Over the course of a cluster's lifetime, shocks can occur due to interactions with any form of granularity in the gravitational potential, such as giant molecular clouds (GMCs, Gieles et al. 2006; Lamers & Gieles 2006), spiral arm passages (Gieles, Athanassoula & Portegies Zwart 2007), galaxy merger-induced structure (Kruijssen et al. 2012), passages through the Galactic disc (Gnedin & Ostriker 1997; Kruijssen & Mieske 2009; Webb et al. 2014b), and perigalactic passes (Gnedin & Ostriker 1997; Baumgardt & Makino 2003; Webb et al. 2013, 2014a). A cluster orbiting in any realistic tidal field that contains substructure (as opposed to a smooth distribution of matter) will be subject to a non-negligible number of tidal shocks. Hence, obtaining a systematic understanding of how individual shocks influence cluster evolution is an important step towards understanding the distribution of cluster properties observed today throughout the Universe. Furthermore, being able to quantify the effects of tidal shocks will not only enable probing the conditions of the formation environment and birth properties of stellar clusters, but it will also allow for present-day clusters to be used as tools to study the formation and assembly history of their host galaxy (e.g. Kruijssen et al. 2019a, b).

* E-mail: webb@astro.utoronto.ca

5880 *J. J. Webb, M. Reina-Campos and J. M. Kruijssen*

The earliest framework for quantifying how clusters are affected by tidal shocks dates back to Spitzer (1958), who used the impulse approximation to explore how tidal interactions with GMCs determine a cluster's disruption time. Spitzer (1958) found that repeated GMC interactions accelerate how quickly a cluster will dissolve, with the change in energy and the amount of mass lost during an interaction dependent on cluster density and the amount of energy injected by the encounter. Aguilar & White (1985) performed a series of N -body simulations of collisionless systems to determine how well the impulse approximation predicted the changes in mass experienced by interacting spherical galaxies. The authors found that, when integrating over the entire orbital path of the perturbing galaxy, the impulse approximation could accurately predict the change in energy and mass of the primary galaxy. In fact, the mass and density evolution can be predicted given the precise details of each shocking event (Aguilar & White 1986). The authors also explored the validity of using the tidal approximation, which assumes the impact parameter is sufficiently large such that the density profile of the perturber can be ignored, which allows to determine analytically the impulse given to each star. Aguilar & White (1985) find that the change in energy of stars that remain bound after a shock and the overall change in mass could not be recovered when using the impulse and tidal approximations together. The fundamental issue with the tidal approximation is that it does not take into consideration the distribution of stellar velocities in the system being perturbed, which Aguilar & White (1985) note is what prevents the existence of a clear scaling relation between changes in mass and the properties of the two galaxies. However, when the exact details of individual shocking events are unknown, the tidal approximation is unavoidable and it is often assumed that the relative change in mass is proportional to the relative change in energy.

Gieles et al. (2006) have since updated the impulse approximation, showing that the inclusion of gravitational focusing and accounting for close encounters further adds to a GMCs ability to remove stars from a cluster. The description of shock-driven mass-loss was refined further by Kruijssen et al. (2011), who included the second-order term in the shock-driven mass-loss rate. Even more recently, Gieles & Renaud (2016) have included the cluster density evolution under the combined influence of repeated tidal shocks and two-body relaxation, enabling a better estimate of the disruption time for large statistical ensembles of shocks. Based on these works, it is possible to determine the time-scale over which a cluster is disrupted due to tidal shocks of any kind (e.g. GMCs, disc crossings, spiral arm crossings) and model the mass evolution of individual clusters along a given orbit (e.g. Ostriker et al. 1972; Gieles et al. 2007; Kruijssen & Mieske 2009). However, in each of the cases, it is necessary to assume that the local density, mass, structure, and relative velocity dispersion of the perturbing sources, as well as the fraction (f) of the injected energy that contributes to the cluster mass-loss ($\Delta M/M = f\Delta E/E$), are all identical and static in order to analytically estimate the cluster disruption time.

A more flexible method for determining the time-scale over which tidal shocks drive cluster disruption stems from extracting the tidal tensor experienced by a cluster as a function of time from galaxy simulations (Prieto & Gnedin 2008; Kruijssen et al. 2011). By integrating each element of the tidal tensor over the duration of a single shock, one can determine the integrated tidal heating experienced by the cluster, which defines its change in energy over the course of a tidal shock. By defining a 'tidal heating parameter' (Gnedin 2003) and again assuming $\Delta M/M = f\Delta E/E$, a cluster's mass-loss history can be estimated for any known tidal history.

Such an approach is ideal for modelling a single shock event or multiple events where the tidal shock sources are neither static nor uniform and the evolution of the tidal tensor can be determined. This approach is difficult to apply to clusters observed in the present-day Universe, as their complete tidal histories are typically unknown. However, in cases where the tidal tensor is known explicitly (such as in models of galaxy formation and evolution), the effects of all types of tidal shocks can be traced.

To date, no dynamically motivated framework for how individual shocks affect star clusters has been successfully tested against direct N -body simulations in cases where the tidal approximation is necessary. The need for such a model is of increasing importance as the resolution difference between large-scale cosmological simulations of galaxy formation and small-scale simulations of star cluster evolution is continually decreasing. In fact, several large-scale simulations of galaxy formation have reached the resolution scale necessary to identify sites of star cluster formation and track the location of star cluster particles as galaxies form and evolve (e.g. Kravtsov & Gnedin 2005; Maxwell et al. 2012; Li et al. 2017; Kim et al. 2018; Mandelker et al. 2018; Pfeffer et al. 2018). Since the tidal fields experienced by such clusters evolve with time and contain substructure in the form of GMCs, spiral arms, discs, and spheroids, the clusters are subject to a wide range of tidal shock strengths, frequencies, and durations over their lifetimes. Hence, a cluster's mass-loss rate cannot be estimated by assuming a single set of global properties for the perturbing source. Furthermore, since individual clusters are not directly modelled in these large-scale simulations, the full form of the impulse approximation cannot be applied either. A general framework for how clusters respond to tidal shocks is needed before the ever increasing resolution of cosmological simulations can be exploited.

Understanding how the evolution of a cluster in a cosmologically motivated tidal field compares to a cluster orbiting in a static and smooth tidal field is necessary before models of star clusters can be accurately compared to observations. An accelerated disruption time due to tidal shocks has profound implications for the evolution of the globular cluster¹ mass function (GCMF, Elmegreen 2010; Kruijssen 2015; Reina-Campos et al. 2018), the stellar mass function (MF, Vesperini & Heggie 1997; Baumgardt & Makino 2003; Kruijssen 2009; Lamers, Baumgardt & Gieles 2013; Webb et al. 2014a; Baumgardt & Sollima 2017) of individual clusters, and the distribution of cluster sizes (Webb et al. 2014a, b; Gieles & Renaud 2016). If tidal shocks have had a stronger effect on cluster evolution in the past, estimates of the initial GCMF based on the present-day distribution of cluster masses and the tidal field of the galaxy underestimate the mass and number of clusters that form in high-redshift galaxies. Furthermore, if a proper treatment of tidal shocks (e.g. from interactions with GMCs in their natal environment) results in clusters experiencing higher mass-loss rates, current estimates of initial cluster masses based on their orbit (Gnedin & Ostriker 1997; Dinescu, Girard & van Altena 1999; Baumgardt & Makino 2003) are in fact lower limits. This second point may offer an explanation for why the stellar MFs of Galactic clusters suggest they have lost a higher fraction of their initial mass than their present-day orbit indicates (Webb & Leigh 2015).

¹Note that we do not distinguish between open and globular clusters in this work. Dynamically, the tidal shock-driven mass-loss rate depends on the cluster density rather than its mass. Open and globular clusters span a similar range in densities (e.g. Krumholz, McKee & Bland-Hawthorn 2019), implying that it is not necessary to distinguish between these systems.

Finally, tidal shocks experienced by tidally underfilling clusters will result in cluster expansion as opposed to mass-loss. Hence tidal shocks may help clusters expand from compact sizes at formation to their present-day sizes, offering a potential pathway for producing extended (globular) clusters.

In this work, we present a systematic study of how individual tidal shocks and successive pairs of shocks affect stellar clusters. For this purpose, we use controlled N -body simulations in which we subject clusters to a variety of tidal shocks. Our approach specifically focuses on quantifying the amount of mass lost by the cluster due to a tidal shock, i.e. how changes in the tidal tensor along the cluster's orbit cause stars to become unbound. As previously discussed, the use of the tidal tensor offers a way of quantifying the strength of the background tidal field that does not require an analytic fit to the host galaxy's potential and it can evolve with time. A tidal tensor-based analysis is particularly useful for studies that model the evolution of stellar clusters in a cosmological context, during which interactions with GMCs dominate cluster mass-loss, as an on-the-fly determination of the tidal tensor at the location of the star cluster particles allows for a more accurate description of their evolution (e.g. Pfeffer et al. 2018).

The structure of this paper is as follows: in Section 2, we introduce the suite of simulations of star clusters that are subjected to a range of different tidal shocks. Section 3 explores the mass and size evolution of each model, including a discussion of how the mass lost by each cluster during a shock depends on the detailed evolution of the cluster's properties and of the tidal tensor over the course of the shock. In Section 4, we present a new, dynamically motivated theoretical model for cluster mass-loss due to tidal shocks, which accurately reproduces the N -body simulations. Finally, we summarize and discuss our conclusions in Section 5.

2 N -BODY SIMULATIONS

In order to explore the amount of mass lost by a stellar cluster after a tidal shock, and how this depends on the properties of the shock and the cluster itself, we perform a large number of direct N -body simulations with NBODY6TT (Aarseth 2003, 2010; Renaud, Gieles & Boily 2011) with different shock durations and strengths, as well as different cluster masses, densities, and density profiles. In order to perform a systematic and detailed study of how tidal shocks affect star clusters, the properties of both the model clusters and the shocks themselves have been idealized as much as possible to limit the number of free parameters influencing cluster evolution.

The N -body code NBODY6TT is a modified version of NBODY6 (Aarseth 2003, 2010), which models the external tidal field experienced by a stellar cluster according to a given tidal tensor. The main suite of models consists of clusters with initially 50 000 stars of equal mass $0.6 M_{\odot}$ that are evolved in isolation for 1 Myr. After that time, clusters are subjected to an extensive tidal shock of duration Δt , which is implemented by setting the first component of the tidal tensor to be positive, $T_{xx} > 0$. Because we aim to study the effects of tidal shocks on cluster evolution throughout its lifetime, individual stars do not undergo stellar evolution. Cluster expansion due to stellar evolution is only an important factor at early times ($\lesssim 100$ Myr), but would need to be accounted for when applying tidal shock theory to very young star clusters.

The simulations are run with very small force calculation time steps (of $\Delta t = 0.003$ Myr) to ensure the energy injected into each cluster by the tidal shock is modelled accurately. We summarize the characteristics of the models considered in Table 1, with the names of the models describing the details of each cluster model

and the tidal shock it undergoes. Specifically, model names reflect the shock strength (S), shock duration (L), cluster mass (M), and cluster density (D) relative to one another.

First, to probe the dependence of the amount of mass lost on the tidal shock particularities, we perform simulations of clusters with the same initial density within the half-mass radius ($\rho_{h,i} = 7.55 M_{\odot} \text{pc}^{-3}$, M1D27) that undergo a single tidal shock of different strengths, i.e. $T_{xx} = \{5.75 \times 10^{-2}, 0.29, 0.86\} \text{Myr}^{-2}$ (S1, S5, S15), and different durations, i.e. $\Delta t = \{0.5, 1\} \text{Myr}$ (L1, L2). While the purpose of our study is to explore the effects that arbitrary tidal shocks have on star clusters with a range of properties, our choice of cluster and shock properties are motivated by physical processes. Specifically, the initial range of densities $\rho_{h,i}$ is chosen to be comparable to high-density open clusters and low-density globular clusters (e.g. Portegies Zwart, McMillan & Gieles 2010; Longmore et al. 2014; Krumholz et al. 2019). The ranges in shock strengths and durations are motivated by encounters between star clusters and GMCs. On the ~ 4 pc size scale of the modelled clusters, the dynamical time for encounters with substructure in the interstellar medium is 0.2–5 Myr (Efremov & Elmegreen 1998; Bolatto et al. 2008; Kruijssen & Longmore 2013), implying that shock durations of 1 Myr accurately reflect encounters between star clusters and gas density peaks. Focusing on shock durations that are much less than the cluster's crossing time (4 Myr) has the added benefit of allowing us to consider impulsive shocks and thus ignore any correction factors accounting for the adiabatic expansion of the cluster.² Finally, the range of shock strengths that we consider ($T_{xx} = 0.06$ – 0.86Myr^{-2}) corresponds to head-on (defined as occurring within ~ 10 pc for typical GMC sizes) encounters with perturbers having central densities of $\rho_{\text{pert}} \approx 2.3$ – $34 M_{\odot} \text{pc}^{-3} \approx 40$ – 600cm^{-3} , where the second equality assumes a perturber consisting of molecular gas. For more distant encounters, the density of the perturber scales as the impact parameter of the encounter cubed. Observed GMC densities are in the range $\rho_{\text{GMC}} = 10$ – 10^4cm^{-3} (e.g. Heyer et al. 2009; Longmore et al. 2012). The above examples demonstrate that the initial conditions adopted for the simulations presented here provide an accurate representation of tidal perturbations due to encounters with substructure in the interstellar medium, which are thought to dominate cluster disruption across cosmic time (e.g. Gieles et al. 2006; Elmegreen & Hunter 2010; Kruijssen et al. 2011; Miholics et al. 2017).

We illustrate the tidal histories that we consider in Fig. 1, where we show the time evolution of the tidal tensor for a shock of strength $T_{xx} = 0.29 \text{Myr}^{-2}$; the top and middle panels show the effect of changing the shock duration ($\Delta t = 0.5 \text{Myr}$ and $\Delta t = 1 \text{Myr}$). These models represent our basic suite of simulations and are described in the first half of Table 1.

Second, we explore how a cluster's response to a tidal shock depends on its own properties. To do so, we vary a single cluster property at a time: either their initial masses $M_i = \{6, 60\} \times 10^3 M_{\odot}$ (M02, M2), their initial densities within the half-mass radius $\rho_{h,i} = \{0.29, 203.74\} M_{\odot} \text{pc}^{-3}$ (D1, D729), or their initial density profiles. The lower and higher initial densities are comparable to the densities of typical open clusters and globular clusters, respectively (see fig. 9 in Krumholz et al. 2019). All of these models are then

²We note that the relevant quantity of interest is not the shock duration itself, but the shock duration in units of the cluster crossing time, because that determines whether the shock is impulsive or drives an adiabatic response (e.g. Gnedin & Ostriker 1997).

5882 *J. J. Webb, M. Reina-Campos and J. M. Kruijssen*

Table 1. Summary of the models considered. The columns list the name of the model, the strength of the tidal shock, its duration, the initial cluster mass, the initial cluster half-mass radius, the volume density within the half-mass radius, and the initial density profile of the stellar cluster. The models in the first and second halves of the table list models with different tidal shock strengths and different cluster properties, respectively. The density profile of the cluster is only indicated in the name of the model if it differs from the default Plummer (1911) profile. Stars next to the model name indicate that it is repeated for 15 additional models that separate the shock into two sub-shocks of 0.5 Myr duration with different temporal offsets (see the text).

Name	Shock strength	Shock duration	Initial mass	Initial half-mass radius	Initial density	Density profile
	T_{xx} [Myr ⁻²]	Δt [Myr]	M_i [M _⊙]	$r_{h,i}$ [pc]	$\rho_{h,i}$ [M _⊙ pc ⁻³]	
S1L1M1D27	5.75×10^{-2}	0.5	30 000	7.8	7.55	Plummer
S1L2M1D27*	5.75×10^{-2}	1.0	30 000	7.8	7.55	Plummer
S5L1M1D27	0.29	0.5	30 000	7.8	7.55	Plummer
S5L2M1D27*	0.29	1.0	30 000	7.8	7.55	Plummer
S15L1M1D27	0.89	0.5	30 000	7.8	7.55	Plummer
S15L2M1D27*	0.89	1.0	30 000	7.8	7.55	Plummer
S5L1M02D27	0.29	0.5	6000	4.6	7.55	Plummer
S5L2M02D27	0.29	1.0	6000	4.6	7.55	Plummer
S5L1M2D27	0.29	0.5	60 000	9.8	7.55	Plummer
S5L2M2D27	0.29	1.0	60 000	9.8	7.55	Plummer
S5L1M1D729	0.29	0.5	30 000	2.6	203.74	Plummer
S5L2M1D729*	0.29	1.0	30 000	2.6	203.74	Plummer
S5L1M1D1	0.29	0.5	30 000	23.0	0.29	Plummer
S5L2M1D1*	0.29	1.0	30 000	23.0	0.29	Plummer
S5L1M1D27W5	0.29	0.5	30 000	7.8	7.55	King $W_0 = 5$
S5L2M1D27W5	0.29	1.0	30 000	7.8	7.55	King $W_0 = 5$
S5L1M1D27W7	0.29	0.5	30 000	7.8	7.55	King $W_0 = 7$
S5L2M1D27W7	0.29	1.0	30 000	7.8	7.55	King $W_0 = 7$

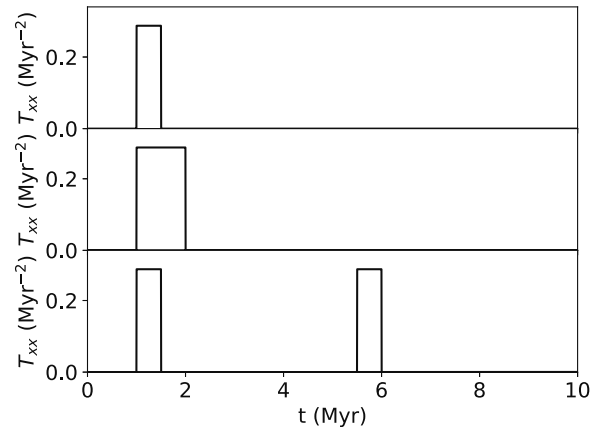


Figure 1. Time evolution of three tidal fields describing a tidal shock of strength $T_{xx} = 0.29 \text{ Myr}^{-2}$ with a duration of $\Delta t = 0.5 \text{ Myr}$ (top), $\Delta t = 1 \text{ Myr}$ (middle), and $\Delta t = 1 \text{ Myr}$ with a gap of $t_{\text{gap}} = 4 \text{ Myr}$ between the first and the second half of the shock (bottom).

evolved to undergo a tidal shock of strength $T_{xx} = 0.29 \text{ Myr}^{-2}$ and duration $\Delta t = \{0.5, 1\} \text{ Myr}$. For those models with different initial masses, their radii are adjusted to have the same initial density within the half-mass radius as our base models. For the initial density profile of the clusters, we consider King profiles (King 1966) of parameters $W_0 = \{5, 7\}$ to compare them against the Plummer profiles used in our basic suite of models. This suite of models is described in the second half of Table 1.

Finally, to explore how strongly the amount of mass-loss depends on the exact shape of the tidal shock, we repeat models S1L2M1D27, S5L2M1D27, S15L2M1D27 from Table 1, i.e. stellar clusters of initial densities within the half-mass radii $\rho_{h,i} = 7.55 \text{ M}_{\odot} \text{ pc}^{-3}$ that undergo a 1 Myr shock of strength $T_{xx} = \{5.75 \times 10^{-2}, 0.29, 0.89\} \text{ Myr}^{-2}$, respectively,

with different tidal histories. We do the same for models with different initial densities, i.e. S5L2M1D1 and S5L2M1D729. This time, the shock experienced in the above seven models is split into two equal sub-shocks separated by different ‘gap’ times t_{gap} . We explore 15 different gap times, of $t_{\text{gap}} = \{0.25, 0.5, 1, 1.5, 2, 3, 4, 6, 8, 12, 16, 20, 24, 28, 32\} \text{ Myr}$, which includes gaps smaller and larger than the cluster’s crossing time ($t_{\text{cr}} \simeq 4 \text{ Myr}$). The first component of the tidal tensor describing this type of shock with a gap time of $t_{\text{gap}} = 4 \text{ Myr}$ is illustrated in the bottom panel of Fig. 1. This suite of models is not included in the description of Table 1, but they are noted in the legend and caption of any figures in which they are used.

3 EVOLUTION OF THE MASS AND THE SIZE OF THE CLUSTER

The immediate effect of a tidal shock on the evolution of a stellar cluster is to change its mass and size. During a tidal shock, the stars in the cluster gain energy (e.g. Spitzer 1987). Stars with sufficiently high energies will become unbound from the cluster and set the amount of mass lost. Less energetic stars will migrate outwards while remaining bound, thus driving the expansion of the cluster.

Using the models described in the previous section, we now discuss the evolution of the mass and the size of the cluster during a tidal shock for different tidal shock strengths, for shocks with different gap times and for clusters with different initial properties. In this discussion, we only consider stars that are energetically bound to each other to be members of the cluster.

3.1 Dependence on the tidal shock strength

In order to understand how the shock properties influence the amount of mass lost by a stellar cluster during a tidal shock, we first consider initially identical stellar clusters that are subject to tidal shocks of varying strength and duration (described in Section 2 and summarized in the first half of Table 1).

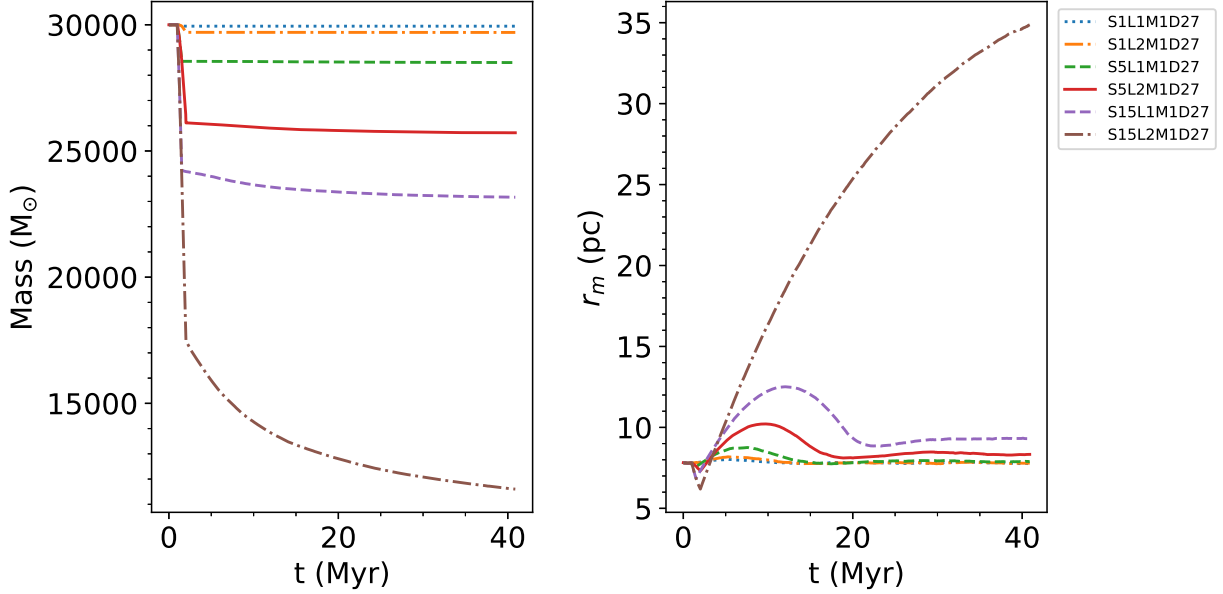


Figure 2. Time evolution of the masses and half-mass radii of stellar clusters that undergo tidal shocks of different strength ($T_{xx} = \{5.75 \times 10^{-2}, 0.29, 0.89\} \text{ Myr}^{-2}$) and duration ($\Delta t = \{0.5, 1\} \text{ Myr}$). The models are described in Section 2 and summarized in the first half of Table 1.

The time evolution of the masses and the radii of the clusters are shown in the left- and right-hand panels of Fig. 2. We find that increasing the shock strength significantly affects the evolution of the cluster. Stronger tidal shocks, like the ones modelled in S15L1M1D27 and S15L2M1D27, inject more energy into the cluster, thus increasing both the amount of mass lost and the final radius of the cluster. The left-hand panel shows that the considered shock causes the clusters to lose 5–60 per cent of their initial mass, which increases with the integral of the shock and thus with its peak value and duration. The right-hand panel of Fig. 2 shows that, immediately after a tidal shock, the cluster rapidly shrinks. This occurs because the outer stars in the cluster experience the strongest energy gain and become unbound, leading to their rapid escape and reducing the half-mass radius of the stars remaining bound to the cluster. After the tidal shock, these remaining stars undergo a net expansion, as their gain in energy causes them to migrate outwards.

3.2 Dependence on the shock interval

We now explore how the mass-loss depends on the distribution of the total amount of tidal heating over multiple shocks. To do so, we consider the idealized case of splitting the tidal shock into two sub-shocks of 0.5 Myr each, separated by a certain gap time t_{gap} . Any configuration of these shocks corresponds to the same total amount of tidal heating, which is a function of the time integral of the tidal history, but the dynamical response of the cluster during the hiatus between the two sub-shocks might modify the amount of mass lost. To address this, we use models based on S5L2M1D27, but with different gap times as described in Section 2.

The resulting time evolution of the cluster masses and half-mass radii is shown in Fig. 3. Introducing a gap in the middle of the shock affects both the amount of mass lost and the radius evolution

of the cluster. We find that those shocks with gap times smaller than the initial crossing time of the cluster, $t_{\text{gap}} \lesssim 4 \text{ Myr}$, produce a negligible effect on the evolution of the mass and the size of the cluster, reaching comparable final masses, $M \simeq 2.6 \times 10^4 M_{\odot}$, and sizes, $r_h \simeq 8.3 \text{ pc}$.

Conversely, models with tidal shocks separated by gap times longer than the cluster’s initial crossing time ($t_{\text{gap}} \gtrsim 4 \text{ Myr}$) exhibit a larger variety of final masses and sizes. In these models, the dynamical response of the cluster to the first sub-shock changes the mass and spatial structure of the cluster, such that it has a noticeably different mass, size, and density profile by the time the second sub-shock begins. Hence, the mass-loss and radius evolution caused by the second sub-shock depend on the new, evolved cluster properties, rather than on its initial mass and size.

We also find that models with tidal shocks separated by gap times in the range $t_{\text{gap}} = 8\text{--}16 \text{ Myr}$ lose more mass during the second sub-shock than the models in which the sub-shocks are separated by $t_{\text{gap}} < 8 \text{ Myr}$. This difference in the amount of mass-loss is caused by the considerable expansion of the cluster between the shocks for gap times $t_{\text{gap}} = 8\text{--}16 \text{ Myr}$, which implies a lower cluster density with a lower binding energy, making the stars more susceptible to becoming unbound during the second sub-shock. For models with gap times $t_{\text{gap}} > 16 \text{ Myr}$, the clusters have already contracted to near their original size by the time of the second sub-shock, such that their total mass-loss is comparable to the models with gap times $t_{\text{gap}} < 8 \text{ Myr}$.

In summary, these results show that for tidal shocks separated over time-scales shorter than the initial crossing time of the cluster, fluctuations of (components of) the tidal tensor can be treated as a single tidal shock. However, fluctuations that are separated by a longer time interval should be considered independently when applying tidal shock theory to determine the induced mass-loss and expansion.

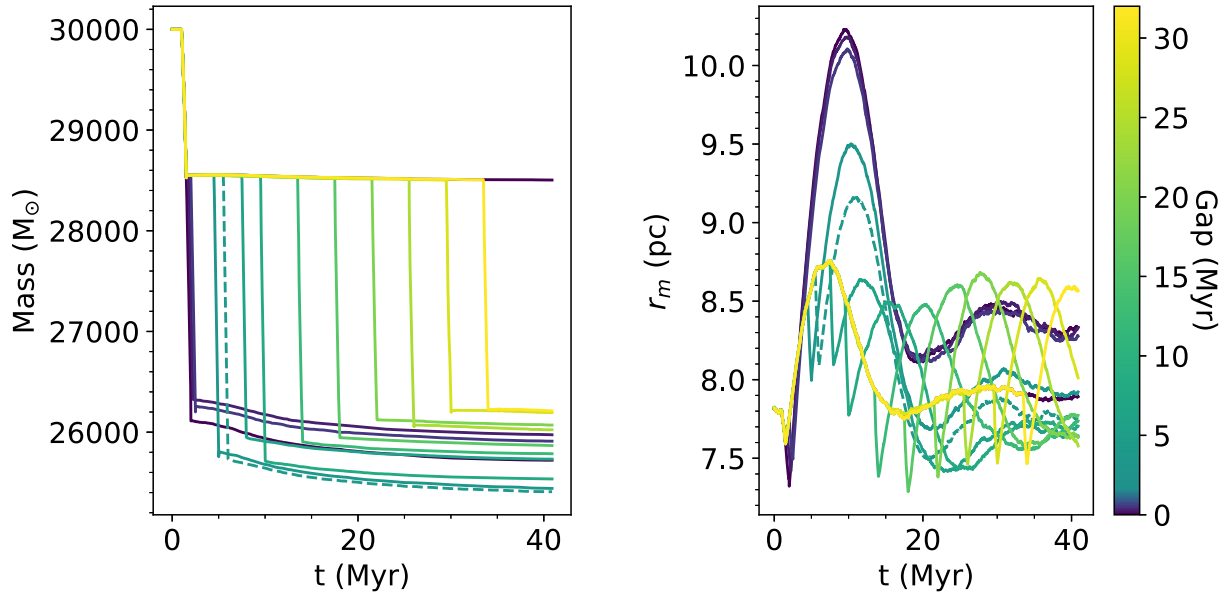
5884 *J. J. Webb, M. Reina-Campos and J. M. Kruijssen*

Figure 3. Time evolution of the masses and half-mass radii of stellar clusters that undergo two consecutive tidal sub-shocks of strength $T_{xx} = 0.29 \text{ Myr}^{-2}$ and a duration of 0.5 Myr each, which are separated by a certain time t_{gap} (indicated by the colours, with $t_{\text{gap}} = 4 \text{ Myr}$ shown as a dashed line). These models are based on S5L2M1D27 and are described in Section 2.

3.3 Dependence on the cluster properties

Finally, we turn to the influence of the initial cluster properties on its response to a tidal shock. To do so, we consider models with different initial masses, half-mass radii, or density profiles, as described in Section 2 and summarized in Table 1. These models experience a tidal shock of strength $T_{xx} = 0.29 \text{ Myr}^{-2}$ of two different durations ($\Delta t = \{0.5, 1\} \text{ Myr}$).

For cluster models with different initial masses, but identical densities as our basic models summarized in the first half of Table 1, we show the time evolution of the present-to-initial mass ratio in Fig. 4. The figure clearly shows that the response of the cluster to the tidal shock does not depend on its initial mass; the differences between some of the curves reflect different shock durations. Fig. 4 is consistent with the impulse approximation, which predicts that the change in mass is only dependent on cluster density and shock strength. Hence, we can focus solely on changing the initial densities of our model clusters to probe the effect that tidal shocks have on cluster evolution.

Fig. 5 shows clusters with the same properties as our basic set of models (see the first half of Table 1), but with initial half-mass radii of $r_{h,i} = \{2.6, 23\} \text{ pc}$, and so, different initial densities within the half-mass radius, $\rho_{h,i} = \{0.29, 203.74\} \times 10^3 \text{ M}_{\odot} \text{ pc}^{-3}$. As predicted, the mass-loss strongly depends on the cluster density. This figure reveals that low-density models lose more mass than high-density models, by up to a factor of ~ 4 for densities differing by an order of magnitude. This dependence is consistent with stars having lower binding energies in the low-density models than in the high-density models, and thus, being more susceptible to becoming unbound and escaping from the cluster due to the energy gain from the tidal shock. The higher susceptibility of low-density clusters to tidal shocks is also reflected in the evolution of their half-mass radii. While high-density clusters undergo very little expansion after a shock, the low-density models S5L1D27 and S5L2D27 expand by over a factor of 2 within $\sim 40 \text{ Myr}$, corresponding to 10 initial crossing times or 1–2 final crossing times.

Lastly, we consider the influence of the density profile of the cluster on its response to a tidal shock. We use the cluster models with the same properties as our basic set, but instead follow a King profile with parameters $W_0 = \{5, 7\}$ rather than the Plummer profile considered in the rest of this work. The shape of the profile affects the binding energies of the stars in the cluster. More concentrated profiles have more strongly bound stars that will experience less mass-loss than extended profiles.

The time evolution of the masses and half-mass radii of these models are shown in Fig. 6. At a factor of 2 level, the differences in mass-loss are subdominant relative to the density dependence shown in Fig. 5. None the less, the models confirm that clusters with more extended density profiles lose more mass and expand more than centrally concentrated clusters. These results are consistent with (Baumgardt & Makino 2003), who observed a similar trend in model clusters undergoing shocks at perigalacticon.

In conclusion, the evolution of a stellar cluster during a tidal shock is most strongly affected by the strength and duration of the shock (i.e. the integral over the tidal tensor), as well by the cluster volume density. A second-order effect comes from the density profile, whereas the initial mass of the cluster has no impact on cluster mass-loss. Across all presented models, fluctuations in the tidal tensor together constitute a single shock if they are separated by less than a crossing time, and should be considered as different shocks if they are separated by more than a crossing time.

4 DISCUSSION

4.1 Relative amount of mass lost in the N -body models

A large body of literature has studied the effect of tidal shocks on stellar clusters from an analytical perspective (e.g. Spitzer 1987; Kundic & Ostriker 1995; Gnedin, Hernquist & Ostriker 1999; Gieles et al. 2006; Prieto & Gnedin 2008; Kruijssen et al. 2011; Gieles &

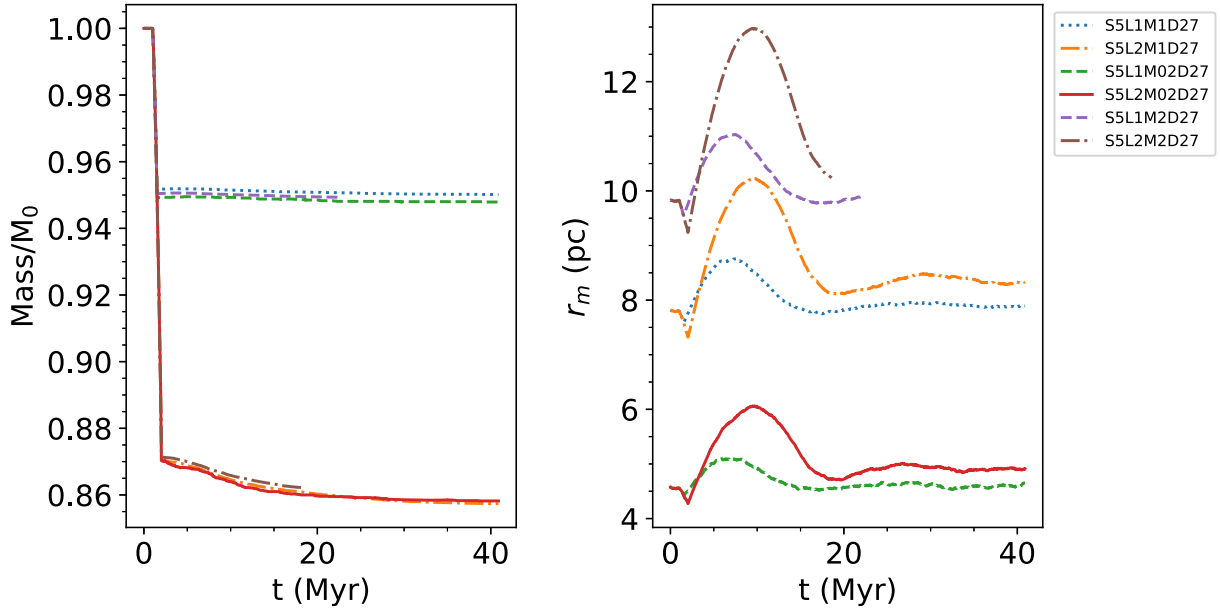


Figure 4. Time evolution of the present-to-initial mass ratios of stellar clusters with different initial masses ($M_i = \{6, 30, 60\} \times 10^3 M_\odot$), but the same volume densities, that undergo a shock of strength $T_{xx} = 0.29 \text{ Myr}^{-2}$ of different durations ($\Delta t = \{0.5, 1\} \text{ Myr}$).

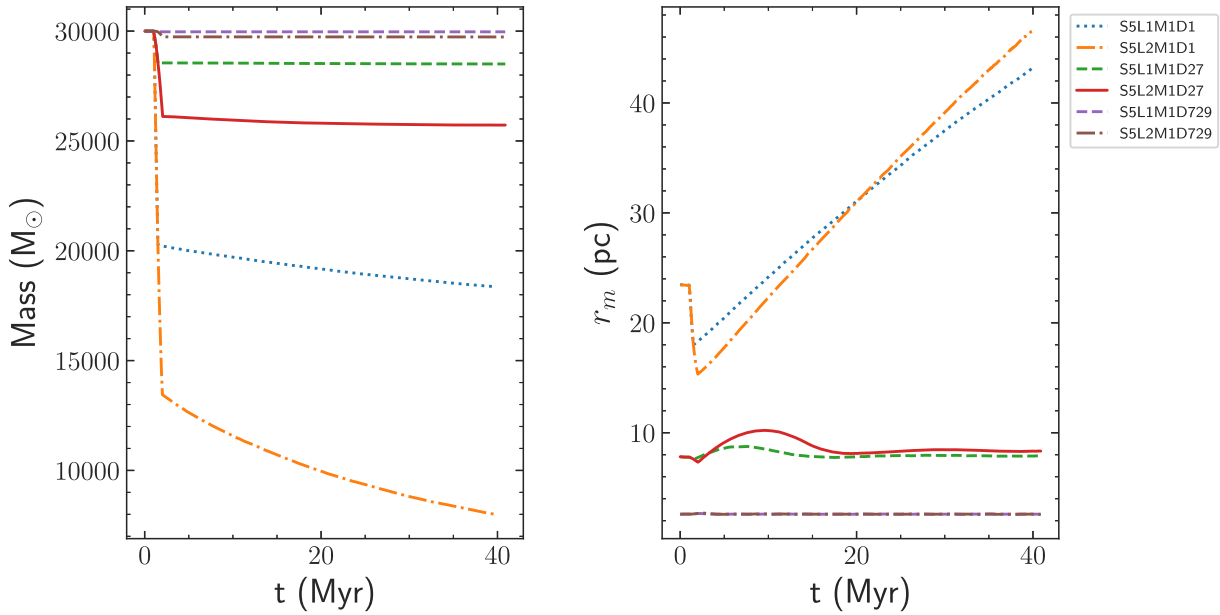


Figure 5. Time evolution of the present-to-initial mass ratios of stellar clusters with different initial densities ($\rho_{h,i} = \{0.29, 7.55, 203.74\} \times 10^3 M_\odot \text{ pc}^{-3}$) that undergo a shock of strength $T_{xx} = 0.29 \text{ Myr}^{-2}$ of different durations ($\Delta t = \{0.5, 1\} \text{ Myr}$).

Renaud 2016). The common goal in these studies is to determine the tidal shock-driven mass-loss due to various different sources. Most often, these consider the movement of a cluster in a galactic potential in which it experiences tidal shocks during the disc crossing and pericentre passage. Additional tidal histories considered include spiral arm crossings, GMC encounters, or any arbitrary history generated by the structure of the interstellar medium.

To calculate the mass-loss due to tidal shocks, classical tidal shock theory uses the approach of determining how much energy is injected into a cluster over the duration of the shock, and relating the relative energy gain to the mass fraction that remains bound to the cluster after the shock (Spitzer 1958, 1987). Given that the amount of mass lost is inversely proportional to the cluster disruption time-scale (t_{dis}), if tidal shocks are the dominant mechanism driving

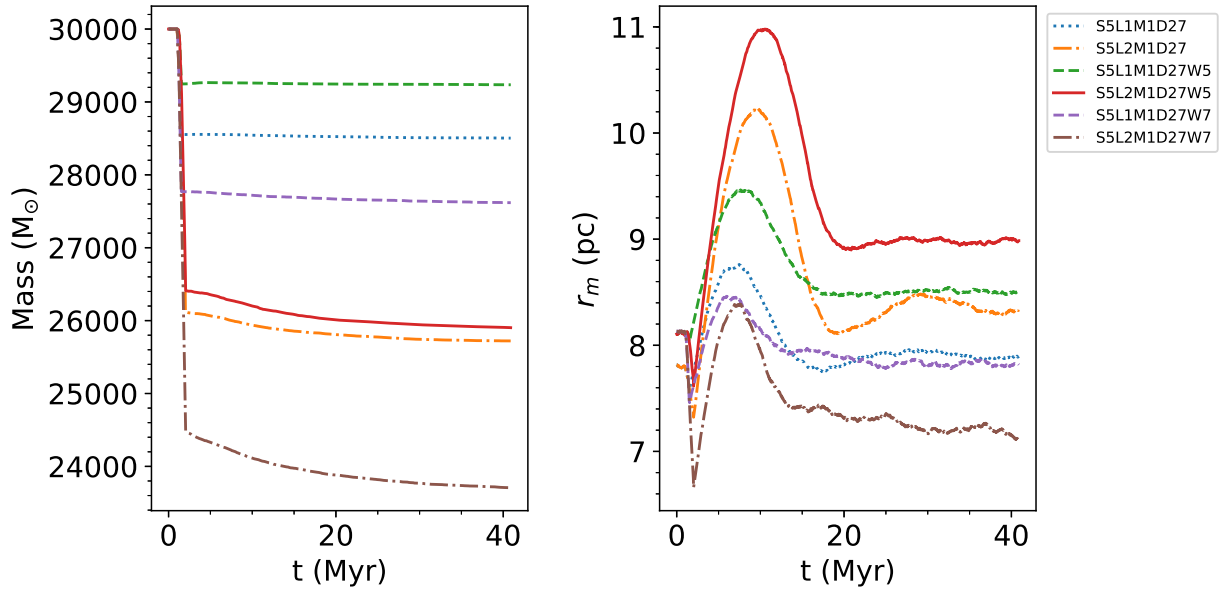
5886 *J. J. Webb, M. Reina-Campos and J. M. Kruijssen*

Figure 6. Time evolution of the masses and half-mass radii of stellar clusters characterized by different density profiles (Plummer and King with $W_0 = \{5, 7\}$) that undergo a shock of strength $T_{xx} = 0.29 \text{ Myr}^{-2}$ of different durations ($\Delta t = \{0.5, 1\} \text{ Myr}$).

cluster evolution, then the amount of mass lost is also inversely proportional to the shock-driven disruption time-scale (t_{sh}), i.e.

$$\frac{\Delta M}{\Delta t} = \frac{M}{t_{\text{dis}}} \rightarrow \frac{\Delta M}{M} = \frac{\Delta t}{t_{\text{dis}}} = \frac{\Delta t}{t_{\text{sh}}}. \quad (1)$$

Using the tidal approximation, the shock-driven disruption time-scale in this expression can be related to the properties of the cluster and the tidal history (Prieto & Gnedin 2008), i.e.

$$t_{\text{sh}} \propto \rho_h I_{\text{tid}}^{-1} = \rho_h \left(\sum_{i,j} \left(\int T_{ij} dt \right)^2 A_{w,ij} \right)^{-1}, \quad (2)$$

where ρ_h is the density of the cluster within the half-mass radius. The tidal heating parameter I_{tid} describes the increase in random motion (or heating) due to the tidal shock (Gnedin 2003), and is determined as an integration over the duration of the shock of the tidal tensor components T_{ij} . Early work by Weinberg (1994a, b, c) found that T_{ij} needs to be corrected for energy loss due to the adiabatic expansion of the cluster, which later led to Gnedin (2003) introducing the adiabatic correction terms $A_{w,ij}$. We can, however, omit this correction given that the impulsive shocks considered here are always much shorter than a crossing time. Assuming the change in cluster mass scales with the change in cluster energy, the shock-driven mass-loss follows as

$$\frac{\Delta M}{M} = -\frac{\Delta t}{t_{\text{sh}}} \propto \rho_h^{-1} \sum_{i,j} \left(\int T_{ij} dt \right)^2 \Delta t. \quad (3)$$

In this equation, the mass-loss depends on the integral of tidal tensor components over the course of the shock to the *second* power. This dependence makes it critical to properly identify individual shocks in order to correctly model their influence on the stellar cluster. For irregular tidal histories, this is highly non-trivial (see e.g. Prieto & Gnedin 2008; Kruijssen et al. 2011; Pfeffer et al. 2018,

for discussions), but our models with tidal shocks split into two sub-shocks with different gap times now enable a physically motivated definition of what constitutes a single shock.

We now compare the amount of shock-driven mass-loss in our models to the mass-loss predicted by classical tidal field theory. In order to do so, we determine the amount of mass lost relative to the mass of the cluster before the shock, $\Delta M/M_{\text{pre-shock}}$, for each of the models described in Section 2. For models that undergo a single shock, we determine the mass-loss as the difference between the mass of the cluster at $t = 40 \text{ Myr}$, by when the shock-driven mass-loss rate has become negligible, and the mass of the cluster when the shock begins at $t = 1 \text{ Myr}$, i.e. $\Delta M = M(40 \text{ Myr}) - M(1 \text{ Myr})$. However, for models where the shock is applied as two consecutive sub-shocks separated by a gap time t_{gap} , we determine the mass lost during the two sub-shocks separately. The mass-loss during the first sub-shock is always equal to the amount of mass lost by the model with a shock duration of $\Delta t = 0.5 \text{ Myr}$, which is the same for all gap times. The mass-loss during the second sub-shock is sensitive to the dynamical evolution of the cluster during the gap time. We use the mass of the cluster after the first sub-shock as its mass before the shock, $M_{\text{pre-shock}} = M(1.5 \text{ Myr})$.

For all of the models in the top half of Table 1 and the low- and high-density models that experience shocks of strength $T_{xx} = 0.29 \text{ Myr}^{-2}$ and durations of $\Delta t = \{0.5, 1\} \text{ Myr}$, the left-hand panel of Fig. 7 shows the amount of mass-loss in units of the initial mass of the cluster before the shock, as a function of the tidal heating parameter. In all cases, models that experience two consecutive shocks (of duration 0.5 Myr) as opposed to a single shock (of duration 1 Myr) are also shown. For clusters that experience the same I_{tid} , but have different initial densities, the amount of mass-loss per unit pre-shock cluster mass is shown as a function of the initial half-mass density in the right-hand panel of Fig. 7.

We perform a three-parameter power-law fit to determine the relation between the relative amount of mass-loss, the cluster

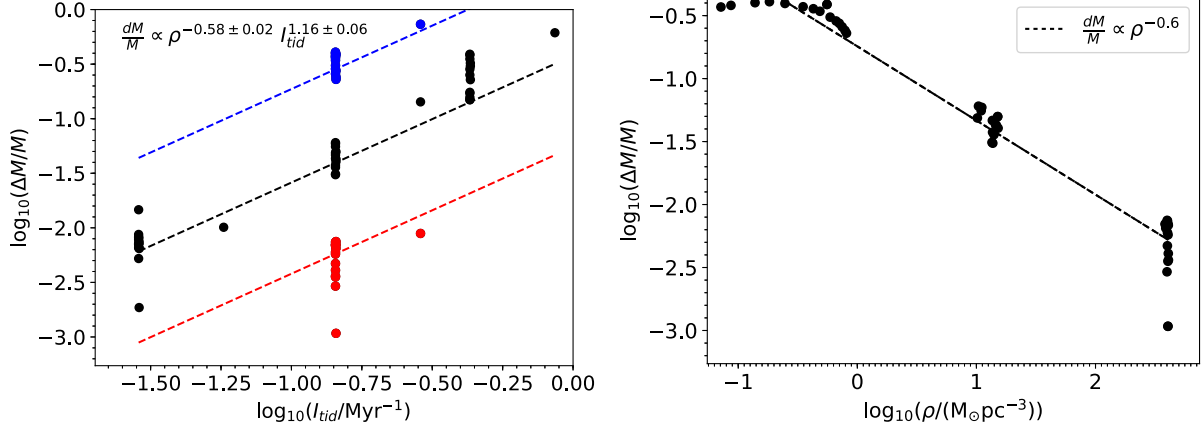


Figure 7. (Left) Amount of mass-loss in units of the pre-shock cluster mass as a function of the tidal heating parameter for the base models as well for the models with different initial densities and gap times, as described in Section 2. Models with the same initial half-mass density are shown in red, black, and blue in order of decreasing density (D729, D27, and D1, respectively). The dashed lines visualize the best-fitting power-law relation between the relative amount of mass-loss, density, and tidal heating parameter (see the legend and the text). (Right) Amount of mass-loss in units of the pre-shock cluster mass as a function of the pre-shock half-mass density for the subset of models with different initial densities that are injected the same integrated tidal heating. The black dashed line indicates the best-fitting power-law relation between the relative amount of mass-loss and the density (see the legend and the text).

density, and the tidal heating parameter as

$$\frac{\Delta M}{M_{\text{pre-shock}}} = A \left(\frac{\rho_h}{10 M_{\odot} \text{pc}^{-3}} \right)^B \left(\int \left(\frac{T_{00}}{0.1 \text{ Myr}^{-2}} \right), dt \right)^C \quad (4)$$

where we have simplified the tidal heating parameter to describe our extensive shock along the direction of the x -axis, without including the adiabatic correction. The best-fitting parameters are $A = 0.033 \pm 0.007$, $B = -0.59 \pm 0.02$, and $C = 1.16 \pm 0.06$, indicating that the results from our controlled N -body simulations differ significantly from the description considered in classical tidal field theory, for which $B = -1$ and $C = 2$ (in agreement with Aguilar & White 1985).

For a given initial half-mass density, the relative amount of mass lost depends almost linearly on the tidal heating parameter, $\Delta M/M_{\text{pre-shock}} \propto I_{\text{tid}}^{1.2}$. In addition, there is also a clear dependence on the density of the cluster – for a given amount of tidal heating, lower density clusters lose more mass than their higher density counterparts (models R9 and R1, respectively). We quantify the dependence using the models from the second half of Table 1, as they all experience a tidal shock that produces the same tidal heating. For these models, we find that the mass-loss scales with the half-mass density as $\Delta M/M_{\text{pre-shock}} \propto \rho_h^{-0.6}$.

The above dependences break down for some of the lowest and highest density models, indicating there might be additional, second-order dependences. Both at the low- and high-density ends, the models undergoing two sub-shocks separated by a long ($t_{\text{gap}} = 8\text{--}16$ Myr) gap time can expand substantially between the two-subshocks, such that their density profiles differ greatly from their initial profiles. The fact that our description breaks in these cases would indicate that their density profiles need to be taken into account as second-order dependences, as suggested by Fig. 6.

With the best-fitting description of the relative amount of mass-loss, we can briefly explore how accurately it describes the shock-induced mass-loss experienced by our models. Fig. 8 shows the relative amount of mass-loss determined from equation (4) as a function of the relative amount of mass-loss found in our N -body models. The best fit exhibits a standard deviation of $\sigma = 0.2$ relative

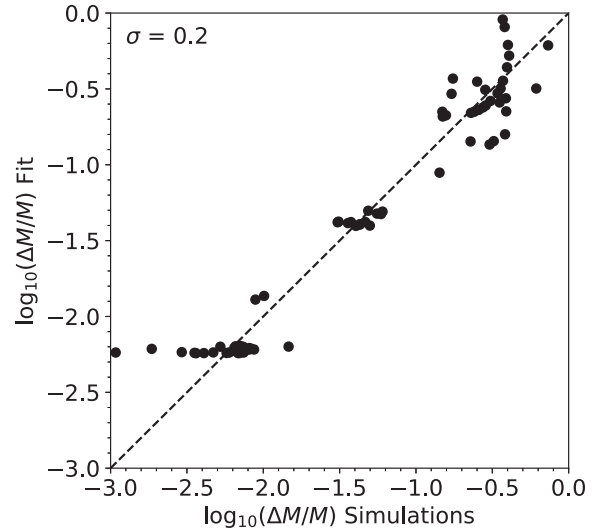


Figure 8. Relative amount of mass lost determined from our fit in equation (4) as a function of the relative amount of shock-driven mass-loss experienced in our models. The standard deviation around the 1:1 (dashed) line is indicated in the top-left corner.

to the results from the simulations. As discussed above, this scatter increases towards the larger and smaller relative amounts of mass-loss, which is due to changes in the density profiles of those clusters, indicating that the amplitude of equation (4) potentially hides a second-order dependence on the cluster density profile.

4.2 A new theoretical model for tidal shocks

The direct N -body simulations presented in this work show a clear discrepancy between the tidal shock-driven mass-loss and the amount predicted by classical tidal shock theory. Comparing equations (3) and (4), we find considerably shallower dependences

5888 *J. J. Webb, M. Reina-Campos and J. M. Kruijssen*

on the tidal heating and the cluster half-mass density than previously suggested. This discrepancy indicates that the classical theoretical description cannot reproduce the true amount of mass-loss across the full range of tidal heating parameters ($I_{\text{tid}} = 10^0 - 10^7 \text{ Gyr}^{-2}$, see e.g. Kruijssen et al. 2011; Pfeffer et al. 2018) and densities ($\rho = 10^{-1} - 10^5 \text{ M}_{\odot} \text{ pc}^3$, see Krumholz et al. 2019) expected across the full cluster population.

Importantly, classical tidal shock theory generally assumes that a star gets unbound from the cluster as soon as it attains a positive total energy. However, it was already proposed by Chandrasekhar (1942) and followed up by King (1959) that stars that have gained total positive energy can remain bound if they encounter other stars on their way out of the cluster, such that they are recaptured by further two-body interactions that decrease their energy back to a total negative energy. King (1959) concludes that the retention of unbound stars that could potentially escape from an isolated cluster lengthens its lifetime. As previously mentioned, Aguilar & White (1985) also pointed out that a star's ability to escape the cluster will also depend on the distribution of stellar velocities relative to the direction of the impulse provided by the tidal shock.

Lee & Ostriker (1987) first considered the idea that during the evolution of a cluster in a static tidal field, stars that have gained sufficient energy from two-body interactions to leave the cluster still require some time to find the region around the Lagrange points where escape is actually achieved. The time-scale for escape therefore scales linearly with the crossing time. The inclusion of this escape time lengthens the lifetime of the cluster and is relevant both for isolated clusters and clusters in tidal fields (Baumgardt 2001). The ability of individual stars to escape from the cluster depends on the distribution function of energies, which sets both the density profile and the velocity distribution of the stars; more extended clusters with higher velocity stars will get disrupted sooner as they are more loosely bound.

We suggest to introduce a dependence of the disruption time due to tidal shocks on the escape time, analogously to the argument put forward by King (1959) and Baumgardt (2001). This accounts for the 'back-scattering' of stars unbound by a tidal shock due to two-body encounters prior to their escape. The new description retains an influence on the shock strength and cluster density, as well as an additional dependence on the energy distribution function that characterizes the density profile and the velocity of the stars in the cluster. Including an escape time-scale should also alleviate the discrepancies found by Aguilar & White (1985) between tidal shock theory and N -body simulations, as the distribution of stellar velocities is accounted for when estimating an escape time-scale.

Following Baumgardt (2001), we consider two mechanisms that modify the energy of the stars in the cluster. Tidal shocks increase the energy of the stars, whereas two-body relaxation can provide or remove energy from the stars. The change of the distribution function of the energy $[N(\hat{E})]$ with time is then given by

$$\frac{dN(\hat{E})}{d\hat{E}} = \frac{k_1}{t_{\text{rh}}} \frac{d^2 N(\hat{E})}{d\hat{E}^2} + \frac{k_2}{t_{\text{sh}}} \frac{d^2 N(\hat{E})}{d\hat{E}^2} - \hat{E}^2 \frac{N(\hat{E})}{t_{\text{esc}}}, \quad (5)$$

where $\hat{E} = (E - E_{\text{crit}})/E_{\text{crit}}$ and E_{crit} is the critical energy required to escape, k_1 and k_2 indicate how efficient each mechanism is at modifying the energy distribution of the cluster, and t_{rh} , t_{sh} , and t_{esc} are the half-mass relaxation, shock disruption, and escape time-scales, respectively. Through this equation, we generalize the definition of the escape time-scale introduced by Baumgardt (2001), i.e. the time required to escape once a star attains positive energy, to also account for the energy input from tidal shocks.

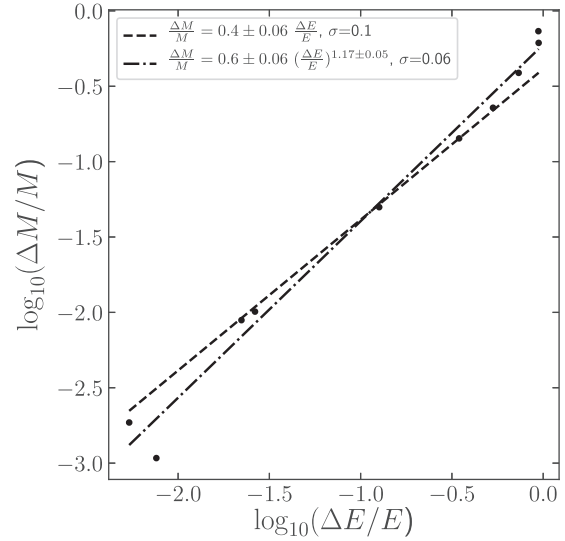


Figure 9. Amount of mass-loss in units of the pre-shock cluster mass as a function of the amount of energy loss in units of the pre-shock cluster binding energy for model clusters that undergo a single shock. The dashed line shows a fit to the data assuming $\Delta M/M$ and $\Delta E/E$ are linearly related (as classically assumed). The dash-dotted line shows a power-law fit to the data, which assumes $\Delta M/M \propto (\Delta E/E)^\alpha$, with the best-fitting exponent being $\alpha = 1.17 \pm 0.05$. In each case, the dispersion about the line of best fit is given.

Rearranging the previous equation and introducing the factor $\beta = k_1 t_{\text{sh}}/k_2 t_{\text{rh}}$, we find that the cluster disruption time-scale depends on the time-scales for shock disruption and escape as

$$t_{\text{dis}} \propto \left(\frac{t_{\text{sh}}}{k_2} \frac{1}{1 + \beta} \right)^{3/4} t_{\text{esc}}^{1/4}. \quad (6)$$

The cluster disruption time takes on different forms depending on the dominant evolution mechanism. When tidal shock-driven disruption dominates, i.e. $k_1 t_{\text{sh}} \ll k_2 t_{\text{rh}}$ and $\beta \ll 1$, the disruption time depends solely on the shock time-scale as $t_{\text{dis}} \propto t_{\text{sh}}^{3/4} t_{\text{esc}}^{1/4}$. However, when tidal shocks are subdominant, i.e. $k_1 t_{\text{sh}} \gg k_2 t_{\text{rh}}$ and $\beta \gg 1$, then we recover the solution described in Baumgardt (2001), where the disruption time depends on the half-mass relaxation time and the escape time-scale as $t_{\text{dis}} \propto t_{\text{rh}}^{3/4} t_{\text{esc}}^{1/4}$.

As previously discussed, to relate a change in the energy of the cluster to a change in mass it must be assumed that $\Delta M/M = f \Delta E/E$. To test the validity of this assumption, we show in Fig. 9 how $\Delta M/M$ is related to $\Delta E/E$ in model clusters that undergo a single shock. Over the entire range of energies we find $f \sim 0.4$ with a dispersion about the mean of $\sigma = 0.1$. Alternatively, a power-law relation has a slightly lower dispersion than the linear case ($\sigma = 0.06$), but has difficulty reproducing models with $\log_{10}(\Delta E/E) < -1.5$. Hence the assumption that $\Delta M/M$ and $\Delta E/E$ are linearly related is preferred over a power-law relation for $\log_{10}(\Delta E/E) < -0.2$. We therefore conclude that for the models considered here the best assumption is that $\Delta M/M = f \Delta E/E$. None the less, we note that for strong tidal shocks or low-density clusters, i.e. in the regime of large changes in cluster energy, the assumption starts to break down and significant scatter will be introduced when attempting to predict changes in cluster mass. This finding is again in agreement with Aguilar & White (1985), who suggest that a single scaling relation between

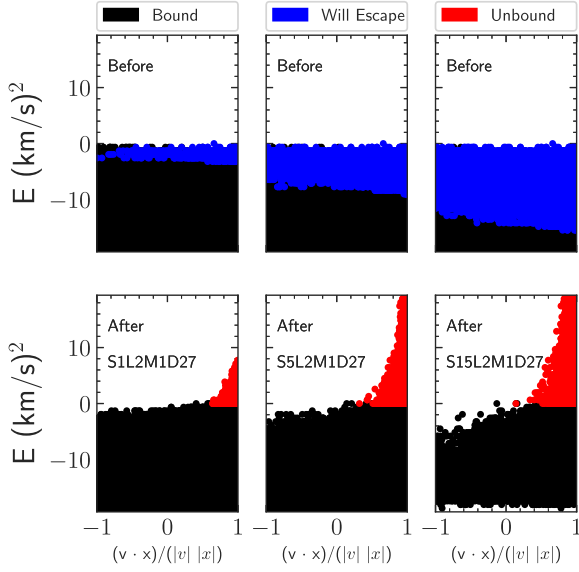


Figure 10. Orbital energy as a function of the orientation between the main direction of the shock and the velocities of the stars before (top row) and after (bottom row) the shock for three models that describe shocks of different strength: S1L2M1D27 (left), S5L2M1D27 (middle), and S15L2M1D27 (right). Bound stars are shown in black, stars that will become unbound due to the shock are marked in blue and unbound stars are shown in red.

$\Delta M/M$ and $\Delta E/E$ may not exist over the entire range of $0 < \Delta E/E < 1$.

Using equation (6) to describe the disruption time, and assuming $\Delta M/M$ and $\Delta E/E$ are linearly related, we obtain that the amount of mass-loss follows as

$$\frac{\Delta M}{M} = -\frac{\Delta t}{t_h} \propto \left(\frac{t_{sh}}{k_2} \frac{1}{1 + \beta} \right)^{-3/4} t_{esc}^{-1/4} \Delta t, \quad (7)$$

which implies a shallower dependence on the shock disruption time-scale than for the classical description in equation (3). We define the escape time-scale to be proportional to the crossing time, $t_{esc} \propto t_{cr} = \sqrt{r_h^3/GM}$, as it takes some multiple of a crossing time to change the orbital parameters of the stars in the cluster.

As first noted by Aguilar & White (1985), the amount of mass lost by a stellar population subjected to a tidal shock depends on the distribution of stellar velocities. The ability of an individual star to leave the cluster depends not only on their energy or their position within the cluster, but also on the orientation of its velocity relative to the principal direction of the tidal shock (given by the largest eigenvector of the tidal tensor, see Kruijssen et al. 2011; Pfeffer et al. 2018). Those stars with velocities parallel to the shock can escape more easily than those with velocities perpendicular or antiparallel to the shock. In addition, tidal shocks modify the velocity field of the stars by introducing a degree of anisotropy along the principal direction of the shock, resulting in a higher probability of escape for those stars with velocities that are aligned with the shock.

Fig. 10 shows the orbital energy of stars before and after a shock, as a function of the orientation between their velocities and the principal direction of the shock, for three of our models that describe identical clusters that undergo shocks of different strength. Our models are initially characterized by a Plummer profile, so the clusters are spherically symmetric and the velocities of the stars are isotropic. This set-up results in a uniform distribution

of orientations between the velocities and the shock (top row in Fig. 10). After the shock, the velocities become more parallel to its main direction, with the escaping stars having velocities that were predominantly oriented towards the direction of the shock before it occurred (bottom row in Fig. 10). In order to account for the influence of the orientation between the velocities of the stars and the main direction of the shock in the ability of stars to escape, we consider the escape time-scale to be given by

$$t_{esc} = \sqrt{\frac{r_h^3}{GM}} (1 - \overline{\cos(\theta)}), \quad (8)$$

where $\overline{\cos(\theta)}$ is the mean cosine of the angle between the velocities of the stars and the principal direction of the shock. Our models are initially virialized and isotropic, so the mean cosine of the angle is $\overline{\cos(\theta)} = 0$ and the escaping time-scale is just the crossing time. However, if a cluster undergoes several shocks in the same direction without being able to virialize in between them, the velocity field will be more anisotropic and stars will be more likely to escape. In the more common case, where the distribution of repeated tidal shocks is isotropic, any anisotropy induced by a previous shock will have little influence over how a cluster responds to a second shock unless the time between shocks is short.

In order to quantify the degree of anisotropy introduced by a tidal shock in the velocities of the stars, we first need to determine the tidal force per unit mass experienced by the stars in the cluster. Following Gnedin et al. (1999) and assuming that stars do not move significantly during the tidal shock (i.e. the impulse approximation), stars feel an acceleration (\mathbf{a}_{sh}) due to the tidal encounter of

$$\mathbf{a}_{sh} = - \left(\frac{\partial^2 \Phi}{\partial \mathbf{R} \partial \mathbf{R}} \right) \cdot \mathbf{x}, \quad (9)$$

where Φ is the potential describing the perturber causing the tidal shock, \mathbf{R} is the position vector of the centre of the cluster relative to the perturber, and \mathbf{x} is the position vector of a star relative to the centre of the cluster (note that vectors are indicated in boldface). We can rewrite this expression using the definition of the tidal tensor, ($T_{ij} = -\partial^2 \Phi / \partial R_j \partial R_i$) to obtain

$$\mathbf{a}_{sh} = \sum_{j=0}^2 x_j (T_{0j}, T_{1j}, T_{2j}), \quad (10)$$

and the velocities of the stars after the shock are

$$\begin{aligned} \mathbf{v}_{sh} &= \mathbf{v} + \Delta \mathbf{v}_{sh} \\ &= \mathbf{v} + \sum_{j=0}^2 x_j \left(\int T_{0j} dt, \int T_{1j} dt, \int T_{2j} dt \right), \end{aligned} \quad (11)$$

where we integrate the tidal force per unit mass over the duration of the shock.

The principal direction of the shock is given by the eigenvector corresponding to the largest eigenvalue of the tidal tensor, i.e. a unit vector of the form $\hat{\lambda} = (\lambda_x, \lambda_y, \lambda_z)/|\lambda|$. The anisotropy induced by the shock for a single star is then given by

$$\begin{aligned} \cos(\theta) &= \frac{\hat{\lambda} \cdot \mathbf{v}_{sh}}{|\mathbf{v}_{sh}|} \\ &= \frac{\sum_{i=0}^2 \lambda_i \left(v_i + \sum_{j=0}^2 x_j \int T_{ij} dt \right)}{\sqrt{|\mathbf{v}|^2 + 2 \sum_{i,j=0}^2 v_i x_j \int T_{ij} dt + \sum_{i=0}^2 \left(\sum_{j=0}^2 x_j \int T_{ij} dt \right)^2}}. \end{aligned} \quad (12)$$

The cluster is initially described by a density profile with a normalized distribution function $d^2 N / d\mathbf{r} d\mathbf{v}$. This allows us to integrate over

5890 *J. J. Webb, M. Reina-Campos and J. M. Kruijssen*

phase space and determine the mean angle between the velocities of the stars and the main direction of the shock as

$$\overline{\cos(\theta)} = \frac{\iint \mathrm{d}^2N}{\mathrm{d}r\mathrm{d}v} \times \frac{\sum_{i=0}^2 \lambda_i \left(v_i + \sum_{j=0}^2 x_j \int T_{ij} \mathrm{d}t \right)}{\sqrt{|\mathbf{v}|^2 + 2 \sum_{i,j=0}^2 v_i x_j \int T_{ij} \mathrm{d}t + \sum_{i=0}^2 \left(\sum_{j=0}^2 x_j \int T_{ij} \mathrm{d}t \right)^2}}. \quad (13)$$

In this work, we consider a single extensive tidal shock, such that a suitable choice of coordinates (with the shock acting along the x -axis) returns a tidal tensor that only contains a single positive component (T_{00}); all other components are zero. The principal direction vector is then given by $\hat{\lambda} = (\text{sgn}(x), 0, 0)$, where $\text{sgn}(x) = x/|x|$ indicates the sign of the position of the star along the x -axis. As the shock only breaks the spherical symmetry for the x -axis, we can consider spherical coordinates rotated such that the spatial coordinates are described by $x = r \cos(\phi)$ and $R = r \sin(\phi) = \sqrt{y^2 + z^2}$ and the velocity coordinates are $v_x = v \cos(\gamma)$ and $v_R = v \sin(\gamma) = \sqrt{v_y^2 + v_z^2}$. Here, ϕ and γ are the angles of the star's radius and velocity vectors relative to the x -axis (i.e. the principal direction of the shock), respectively, measured before the shock. With these definitions, we can rewrite equation (13) as

$$\overline{\cos(\theta)} = 4\pi^2 \iint \sin(\phi) \mathrm{d}\phi \mathrm{d}r v^2 \sin(\gamma) \mathrm{d}\gamma \frac{\mathrm{d}^2N}{\mathrm{d}r\mathrm{d}v} \times \frac{\text{sgn}[\cos(\phi)] [v \cos(\gamma) + r \cos(\phi) \int T_{00} \mathrm{d}t]}{\sqrt{v^2 + 2v \cos(\gamma) r \cos(\phi) \int T_{00} \mathrm{d}t + [r \cos(\phi) \int T_{00} \mathrm{d}t]^2}}. \quad (14)$$

Assuming a Plummer profile, its normalized distribution function can be written in terms of the energy if the cluster is spherically symmetric and isotropic (Heggie & Hut 2003), i.e.

$$\frac{\mathrm{d}N}{\mathrm{d}r\mathrm{d}v} = f(E) = \frac{3 \times 2^{7/2}}{7\pi^3} \frac{a^2}{G^5 M^5} (-E)^{7/2}, \quad (15)$$

where $E = \Phi_p(r) + v^2/2 = -GM/\sqrt{r^2 + a^2} + v^2/2$ is the total energy of a star in the cluster before the shock, $a \approx r_h/1.3$ is the Plummer radius, r_h is the half-mass radius, M is the cluster mass, and G is the gravitational constant. Substituting this into equation (14), the mean cosine angle between the velocities and the shock after a tidal shock becomes

$$\overline{\cos(\theta)} = \frac{12 \times 2^{7/2}}{7\pi} \frac{a^2}{G^5 M^5} \times \int_0^\pi \mathrm{d}\phi \int_0^\pi \mathrm{d}\gamma \int_0^\infty \mathrm{d}r \int_0^{v_{\text{esc}}(r)} \mathrm{d}v \sin(\phi) \sin(\gamma) r^2 v^2 \times \frac{\text{sgn}[\cos(\phi)] [v \cos(\gamma) + r \cos(\phi) \int T_{00} \mathrm{d}t]}{\sqrt{v^2 + 2v \cos(\gamma) r \cos(\phi) \int T_{00} \mathrm{d}t + [r \cos(\phi) \int T_{00} \mathrm{d}t]^2}} \times \left(\frac{GM}{\sqrt{r^2 + a^2}} - \frac{1}{2} v^2 \right)^{7/2}, \quad (16)$$

where $v_{\text{esc}}(r) = \sqrt{-2\Phi_p(r)} = \sqrt{2GM/(r^2 + a^2)^{1/2}}$ is the escape velocity at radius r of a Plummer sphere. By integrating up to $v_{\text{esc}}(r)$, we are only including stars that remain bound to the cluster in our calculation of $\overline{\cos(\theta)}$ as the distribution function cancels for stars with $v = v_{\text{esc}}(r)$ (i.e. for those with null energy, $E = 0$). If there is no tidal shock or if it is comparatively weak, the mean cosine angle after the shock will be similar to that before the shock, $\overline{\cos(\theta)} \simeq \overline{\cos(\gamma)} = 0$, where the equality to zero arises because we

assume isotropy prior to the shock. To obtain a simple expression for the anisotropy introduced in the velocities by the shock, we can numerically integrate equation (16) for different shocks strengths and cluster half-mass densities. We show the obtained mean cosine angles in Fig. 11 and find that the mean cosine angle is well fitted by

$$\overline{\cos(\theta)} \simeq A \left[1 + \left(\frac{\rho_h}{10 M_\odot \text{pc}^{-3}} \right)^B \right]^C \times \tanh \left(D \left(\frac{\rho_h}{10 M_\odot \text{pc}^{-3}} \right)^E \int \left(\frac{T_{00}}{0.1 \text{ Myr}^{-2}} \right) \mathrm{d}t \right), \quad (17)$$

with $A = 1.01 \pm 0.54$, $B = 0.44 \pm 1.24$, $C = -0.43 \pm 0.95$, $D = 0.16 \pm 0.12$, and $E = -0.27 \pm 0.30$. We show the quality of the fit in Fig. 12. This type of dependence for the mean cosine angle indicates that the anisotropy in the velocity field of the cluster induced by a shock of a certain strength will depend on the cluster's half-mass density, with the anisotropy increasing towards lower densities for the same shock strength. At a given density, weak shocks will induce little anisotropy to the velocity field of the stars, but the anisotropy induced increases quickly with the shock strength, with a saturation limit (i.e. $\lim_{x \rightarrow 0} \tanh x = 1$) proportional to the cluster's half-mass density. Complete anisotropy, i.e. $\overline{\cos(\theta)} \approx 1$, can only be induced for clusters with densities $\rho_h \ll 1 M_\odot \text{pc}^{-3}$ for the range of shock strengths considered in this work.

We can combine the shock time-scale (equation 2), the definition of the escape time (equation 8), and the general fit for the mean cosine angle (equation 17) to determine whether the amount of shock-induced mass-loss in a cluster is significantly affected by the introduction of the escape time-scale. In the case of our extensive tidal shock along the x -axis, the shock time-scale and the escape time depend on the density of the cluster within the half-mass radius, the integral of the tidal shock strength and the mean cosine angle, $\overline{\cos(\theta)}$, as

$$\frac{\Delta M}{M} \propto t_{\text{sh}}^{-3/4} t_{\text{esc}}^{-1/4} \propto \rho_h^{-5/8} \left(\int T_{00} \mathrm{d}t \right)^{3/2} (1 - \overline{\cos(\theta)})^{-1/4}. \quad (18)$$

Using the full suite of N -body simulations, we fit for the required proportionality constant in equation (18), resulting in

$$\frac{\Delta M}{M_{\text{pre-shock}}} = A \left(\frac{\rho_h}{10 M_\odot \text{pc}^{-3}} \right)^{-5/8} \times \left(\int \left(\frac{T_{00}}{0.1 \text{ Myr}^{-2}} \right) \mathrm{d}t \right)^{3/2} (1 - \overline{\cos(\theta)})^{-1/4}, \quad (19)$$

where the proportionality constant including its uncertainty is $A = 2.06 \pm 0.04 \times 10^{-4}$. In the left-hand panel of Fig. 13, we explore how well our new theoretical model estimates the relative amount of mass lost by each model cluster, in comparison to classical tidal shock theory. By accounting for the stellar escape time, this expression achieves a significant improvement in predicting the relative amount of tidal shock-driven mass-loss compared to classic tidal shock theory. The new theoretical model (shown in black) predicts mass-loss that is clustered around the 1:1 line, with a standard deviation around the line of $\sigma = 0.3$. This deviation is only slightly larger than the one obtained when carrying out a direct fit to the simulations (see Fig. 8 and equation 4). By contrast, classical tidal shock theory (shown in red) poorly predicts the relative amounts of mass lost by the simulations, resulting in a much larger standard deviation around the line of $\sigma = 0.6$. The largest

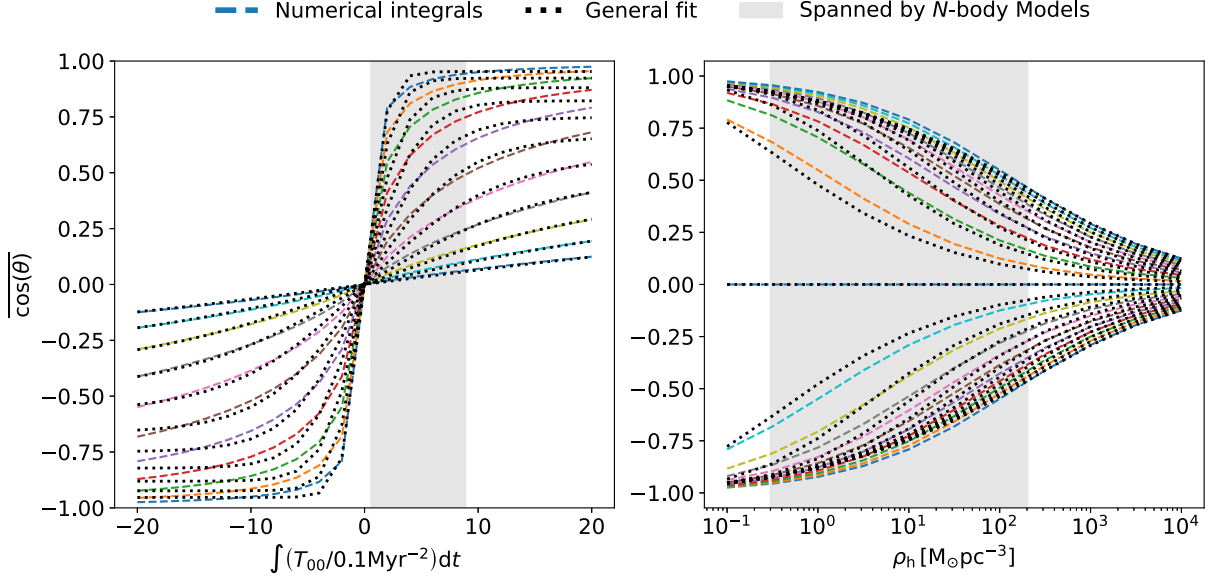


Figure 11. Mean cosine angle of the stellar velocity relative to the main direction of the shock as a function of shock strength (*left*) and cluster half-mass density (*right*). In the left- and right-hand panels, dashed lines represent the result of equation (16) at various fixed values of the cluster half-mass density and shock strength, respectively. The black dotted lines represent the general fit described in equation (17). The range in shock strengths and cluster densities considered in this work is indicated by the grey shaded regions.

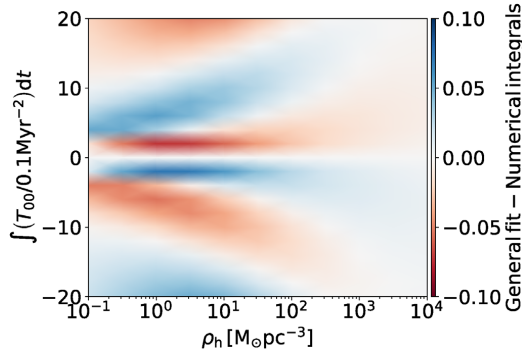


Figure 12. Absolute difference between the mean cosine angle of the stellar velocity relative to the main direction of the shock obtained as a result of equation (16) and the general fit described in equation (17). The difference is < 0.1 for all densities and shock strengths considered.

discrepancy for classical tidal shock theory arises for both the weak (S1) and strong (S15) shock models and the low (D1) and high (D729) density models. These discrepancies are a direct result of overestimating the dependences on cluster density and tidal shock strength. We thus find that the introduction of the escape time is critical to accurately reproduce the response of shock-induced mass-loss, as the discrepancy between predicted and observed mass-loss is decreased by a factor of 2.

In order to further simplify the scalings of equation (19), we restrict our analysis to the range of shock strengths and densities considered in this work (indicated in Fig. 11 as grey shaded regions). Over this regime, we can approximate equation (17) in terms of a

power law,

$$1 - \overline{\cos(\theta)} \propto \rho_h^B \left(\int T_{00} dt \right)^C \quad (20)$$

with $B \simeq 0.09\text{--}0.27$ and $C \simeq -0.52\text{--}0.00$ across the grey shaded areas in Fig. 11. For this power-law approximation, the escape time follows as

$$t_{\text{esc}} \propto \rho_h^{B-1/2} \left(\int T_{00} dt \right)^C, \quad (21)$$

with the power of the density now in the range $B - 1/2 \simeq -0.41\text{--}-0.23$. Substituting this expression along with equation (2) into equation (6) for the tidal shock-dominated case ($\beta \rightarrow 0$), the amount of mass lost by a cluster during a tidal shock can be approximated as

$$\begin{aligned} \frac{\Delta M}{M} &\propto t_{\text{sh}}^{-3/4} t_{\text{esc}}^{-1/4} \\ &\propto \rho_h^{-(5+2B)/8} \left(\int T_{00} dt \right)^{(6-C)/4}, \end{aligned} \quad (22)$$

with the slopes in the range $-(5 + 2B)/8 = -0.65\text{--}-0.69$ and $(6 - C)/4 = 1.5\text{--}1.63$. Adopting the mean slopes across these intervals, we can use the simulations to fit for the proportionality constant in equation (22), resulting in

$$\frac{\Delta M}{M_{\text{pre-shock}}} = A_{\text{approx}} \left(\frac{\rho_h}{10 \text{ M}_{\odot} \text{ pc}^{-3}} \right)^{-0.67} \left(\int \left(\frac{T_{00}}{0.1 \text{ Myr}^{-2}} \right) dt \right)^{1.57}, \quad (23)$$

where the proportionality constant in the power-law approximation is $A_{\text{approx}} = 1.74 \pm 0.03 \times 10^{-4}$. As expected, the power-law approximation exhibits shallower dependences on the cluster density and the tidal shock strength than those predicted by classical field theory (equation 3). Comparing the exponential dependences in this result ($B_{\text{new}}, C_{\text{new}}$) to the fit to our N -body models from equation (4) ($B_{\text{fit}}, C_{\text{fit}}$), the introduction of the escape time-scale reproduces the dependence on the density of the cluster (slopes of $B_{\text{new}} = -0.67$

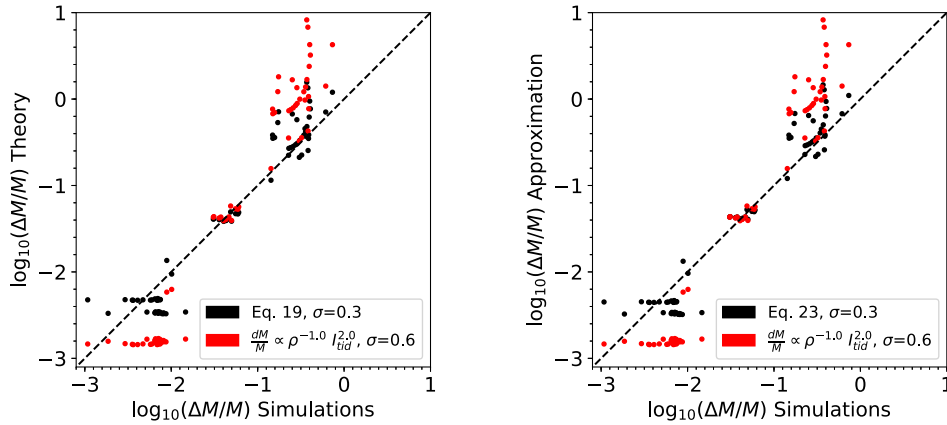
5892 *J. J. Webb, M. Reina-Campos and J. M. Kruijssen*

Figure 13. *Left:* Relative amount of mass lost determined from our new theoretical model in equation (19) (black) and classic tidal shock theory in equation (3) (red) as a function of the relative amount of shock-driven mass-loss experienced in our models. *Right:* Same as the left-hand panel, but with a power-law approximation in place of our new theoretical model (equation 23). The standard deviation from the 1:1 dashed line is noted in the legend for each method. The new model including the escape time leads to a factor of 2 less scatter when predicting the relative amount of mass-loss than classical tidal shock theory.

and $B_{\text{fit}} = -0.59$, respectively), but predicts a somewhat steeper dependence for the tidal shock strength (slopes of $C_{\text{new}} = 1.57$ and $C_{\text{fit}} = 1.16$, respectively). Both represent a clear improvement relative to the classical description.

In the right-hand panel of Fig. 13, we explore how well the power-law approximation reproduces the relative amount of mass lost by each model cluster, again in comparison to classical tidal shock theory. We find that approximating the $1 - \cos(\theta)$ term as a power-law does very little to change our new theoretical model’s ability to produce the fraction of mass lost by the model clusters. In fact, using the power-law approximation over the range in cluster densities and shock strengths covered by our models works extremely well, with the standard deviation around the one-to-one line in the right-hand panel of Fig. 13 being $\sigma = 0.3$ as in the left-hand panel. However, the power-law approximation is only valid for the range of parameters considered in this work. For a more general determination of the mean cosine angle, it is recommended to use the general fit described in equation (17) or solving the numerical integral described in equation (16).

5 CONCLUSIONS

We examine how stellar clusters evolve under the influence of tidal shocks in direct N -body simulations. We perform simulations of different model clusters subjected to evolving tidal tensors that represent different types of shocks. This approach allows us to study the influence of the properties of the shock and of the cluster on its mass and size evolution.

We find that clusters undergoing a single tidal shock react differently depending on the strength of the shock. Over a factor of 15 in shock strength, we find a factor of ~ 60 variation in shock-induced mass-loss, with stronger shocks leading to more mass-loss. When the tidal shock is applied as two sub-shocks separated by a certain gap time, the mass lost during the second sub-shock is sensitive to the dynamical evolution of the cluster during the gap time. Those clusters that encounter the second sub-shock faster than their crossing time ($t_{\text{gap}} \lesssim 4$ Myr) exhibit a similar evolution of their mass and radius by the end of the simulation. By contrast, the clusters that encounter the second sub-shock on time-scales longer than their crossing time ($t_{\text{gap}} \gtrsim 4$ Myr) exhibit a large variation

of their final masses and sizes, indicating that their evolution in between both sub-shocks affects how they respond to the second sub-shock.

The response of the models to single and consecutive shocks indicates that, within one crossing time of the cluster, a tidal shock should be defined as a single, uninterrupted injection of energy with a magnitude equal to the integral of the tidal tensor. Likewise, the cluster density can be evaluated at the beginning of the shock. Over time-scales longer than the cluster’s crossing time, energy injections should be treated as multiple tidal shock events. The appropriate cluster density must be evaluated at each of these individual events.

The initial mass of the cluster does not have a major effect on the response of the cluster to the tidal shock, but the cluster’s evolution is controlled by its density within the half-mass radius. Across a factor of ~ 700 in density, the shock-induced mass-loss varies by up to a factor of 80, with lower density clusters losing less mass. This happens because the stars in lower density clusters are more loosely bound and can escape more easily. We identify a second-order dependence on the cluster density profile, expressed in terms of the King parameter W_0 , such that less concentrated cluster profiles exhibit elevated mass-loss.

We determine the mass-loss in units of the initial cluster mass for all of our models, and find that it depends on the tidal shock strength and the cluster density as $\Delta M/M \propto \rho^{-0.59} (\int T_{00} dt)^{1.16}$. These dependences are considerably shallower than those predicted by classical tidal shock theory, which predicts $\Delta M/M \propto \rho^{-1} (\int T_{00} dt)^2$ when using the tidal approximation. In order to explain this discrepancy, we propose that stars require a certain time to escape the cluster once their energy has become positive due to the shock, analogously to the model of Baumgardt (2001) for mass-loss driven by two-body relaxation. We define an escape time-scale proportional to the crossing time and a factor accounting for the orientation of the velocities of the stars in the cluster relative to the principal direction of the shock. The introduction of this time-scale lengthens the cluster’s lifetime and correctly predicts the amount of shock-induced mass-loss over a range of shock strengths and cluster densities via equation (19). The relation is an accurate method for predicting mass-loss due to tidal shocks, while still using the tidal approximation, instead of having to know the details of each tidal shock event (i.e. the density profile and orbit of the perturber).

Approximating this new formalism for shock-induced mass-loss as a power-law for the range of shock strengths and densities considered in this work, we obtain $\Delta M/M \propto \rho^{-0.67} (\int T_{00} dt)^{1.57}$, which is also in considerably better agreement with our simulations than the classical prediction.

Incorporating a dependence on the stellar escape time into tidal shock theory significantly improves our ability to predict the shock-induced mass-loss. This new model is able to correctly predict the relative amounts of mass-loss ($\Delta M/M$) found in the simulations with a standard deviation of $\sigma = 0.3$. This amount of scatter is similar to that obtained when fitting the results of our simulations for the power-law dependence on density and shock strength ($\sigma = 0.2$). Hence, the new model provides an excellent description of the simulations. Without a dependence on the escape time, we instead obtain a dispersion of $\sigma = 0.6$ and are unable to retrieve the absolute amount of mass-loss over the full range of model cluster densities and tidal shock strengths. Our new model also accounts for the identified second-order dependence on the cluster density profile. In order to determine the degree of anisotropy of the stellar velocity distribution induced by the tidal shock, we consider a Plummer profile (equation 16), but a similar derivation for a King model could be easily done by replacing the appropriate description in equation (14).

Developing an accurate model for the impact of tidal shocks on the evolution of stellar clusters is an important step, because studies of cluster evolution continue to move away from static, smooth potentials, and instead model the evolution of clusters in a cosmological context. Over the course of a cluster's lifetime (and especially at early times), tidal shocks represent the dominant source of dynamical mass-loss. Therefore, being able to predict shock-driven mass-loss rate is critical for describing the formation and evolution of stellar cluster populations. By accounting for shock-driven mass-loss in a cosmological context (as is now being pursued, see Pfeffer et al. 2018), the present-day properties of globular cluster populations may be connected to those at the time of their formation. In turn, this will enable the use of globular clusters as direct tracers of the formation and evolution of their host galaxy (e.g. Kruijssen et al. 2019b).

ACKNOWLEDGEMENTS

JW acknowledges financial support through a Natural Sciences and Engineering Research Council of Canada (NSERC) Postdoctoral Fellowship and additional financial support from NSERC (funding reference number RGPIN-2015-05235) and an Ontario Early Researcher Award (ER16-12-061). MRC is supported by a Fellowship from the International Max Planck Research School for Astronomy and Cosmic Physics at the University of Heidelberg (IMPRS-HD). MRC and JMDK gratefully acknowledge funding from the European Research Council (ERC) under the European Union's Horizon 2020 research and innovation programme via the ERC Starting Grant MUSTANG (grant agreement number 714907). JMDK gratefully acknowledges funding from the German Research Foundation (DFG) in the form of an Emmy Noether Research Group (grant number KR4801/1-1). This work was made possible in part by the facilities of the Shared Hierarchical Academic Research Computing Network (SHARCNET: www.sharcnet.ca) and Compute/Calcul Canada, in part by Lilly Endowment, Inc., through its support for the Indiana University Pervasive Technology Institute, and in part by the Indiana METACyt Initiative. The Indiana METACyt Initiative at IU is also supported in part by Lilly Endowment, Inc. We thank Gonzalo Alonso-Álvarez, Sarah

Jeffreson, and Benjamin Keller for helpful discussions, as well as Mark Gieles, Oleg Gnedin, and Simon White for feedback on the original version of this paper.

REFERENCES

- Aarseth S. J., 2003, *Gravitational N-Body Simulations*, Cambridge Univ. Press, Cambridge
- Aarseth S. J., 2010, *Gravitational N-Body Simulations*, Cambridge Univ. Press, Cambridge
- Aguilar L., Hut P., Ostriker J. P., 1988, *ApJ*, 335, 720
- Aguilar L. A., White S. D. M., 1985, *ApJ*, 295, 374
- Aguilar L. A., White S. D. M., 1986, *ApJ*, 307, 97
- Baumgardt H., 2001, *MNRAS*, 325, 1323
- Baumgardt H., Makino J., 2003, *MNRAS*, 340, 227
- Baumgardt H., Sollima S., 2017, *MNRAS*, 472, 744
- Bolatto A. D., Leroy A. K., Rosolowsky E., Walter F., Blitz L., 2008, *ApJ*, 686, 948
- Chandrasekhar S., 1942, *Principles of Stellar Dynamics*, The University of Chicago Press, Chicago, IL
- Chernoff D. F., Weinberg M. D., 1990, *ApJ*, 351, 121
- Chernoff D. F., Kochanek C. S., Shapiro S. L., 1986, *ApJ*, 309, 183
- Dinescu D. I., Girard T. M., van Altena W. F., 1999, *AJ*, 117, 1792
- Efremov Y. N., Elmegreen B. G., 1998, *MNRAS*, 299, 588
- Elmegreen B. G., 2010, *ApJ*, 712, L184
- Elmegreen B. G., Hunter D. A., 2010, *ApJ*, 712, 604
- Gieles M., Renaud F., 2016, *MNRAS*, 463, L103
- Gieles M., Portegies Zwart S. F., Baumgardt H., Athanassoula E., Lamers H. J. G. L. M., Sipior M., Leenaarts J., 2006, *MNRAS*, 371, 793
- Gieles M., Athanassoula E., Portegies Zwart S. F., 2007, *MNRAS*, 376, 809
- Gnedin O. Y., 2003, *ApJ*, 582, 141
- Gnedin O. Y., Ostriker J. P., 1997, *ApJ*, 474, 223
- Gnedin O. Y., Hernquist L., Ostriker J. P., 1999, *ApJ*, 514, 109
- Heggie D., Hut P., 2003, *The Gravitational Million-Body Problem: A Multidisciplinary Approach to Star Cluster Dynamics*. Cambridge Univ. Press, Cambridge, p. 372
- Heyer M., Krawczyk C., Duval J., Jackson J. M., 2009, *ApJ*, 699, 1092
- Kim J.-h. et al., 2018, *MNRAS*, 474, 4232
- King I., 1959, *AJ*, 64, 351
- King I. R., 1966, *AJ*, 71, 64
- Kravtsov A. V., Gnedin O. Y., 2005, *ApJ*, 623, 650
- Kruijssen J. M. D., 2009, *A&A*, 507, 1409
- Kruijssen J. M. D., 2015, *MNRAS*, 454, 1658
- Kruijssen J. M. D., Longmore S. N., 2013, *MNRAS*, 435, 2598
- Kruijssen J. M. D., Mieske S., 2009, *A&A*, 500, 785
- Kruijssen J. M. D., Pelupessy F. I., Lamers H. J. G. L. M., Portegies Zwart S. F., Icke V., 2011, *MNRAS*, 414, 1339
- Kruijssen J. M. D., Pelupessy F. I., Lamers H. J. G. L. M., Portegies Zwart S. F., Bastian N., Icke V., 2012, *MNRAS*, 421, 1927
- Kruijssen J. M. D., Pfeffer J. L., Crain R. A., Bastian N., 2019a, *MNRAS*, 486, 3134
- Kruijssen J. M. D., Pfeffer J. L., Reina-Campos M., Crain R. A., Bastian N., 2019b, *MNRAS*, 486, 3180
- Krumholz M. R., McKee C. F., Bland-Hawthorn J., 2019, *ARA&A*, preprint (arXiv:1812.01615)
- Kundic T., Ostriker J. P., 1995, *ApJ*, 438, 702
- Lamers H. J. G. L. M., Gieles M., 2006, *A&A*, 455, L17
- Lamers H. J. G. L. M., Baumgardt H., Gieles M., 2013, *MNRAS*, 433, 1378
- Lee H. M., Ostriker J. P., 1987, *ApJ*, 322, 123
- Li H., Gnedin O. Y., 2018, *MNRAS*, 486, 4030
- Li H., Gnedin O. Y., Gnedin N. Y., Meng X., Semenov V. A., Kravtsov A. V., 2017, *ApJ*, 834, 69
- Longmore S. N. et al., 2012, *ApJ*, 746, 117
- Longmore S. N. et al., 2014, *Protostars and Planets VI*, Univ. Arizona Press, Tucson, 291
- Mandelker N., van Dokkum P. G., Brodie J. P., van den Bosch F. C., Ceverino D., 2018, *ApJ*, 861, 148

5894 *J. J. Webb, M. Reina-Campos and J. M. Kruijssen*

- Maxwell A. J., Wadsley J., Couchman H. M. P., Mashchenko S., 2012, *ApJ*, 755, L35
- Miholics M., Kruijssen J. M. D., Sills A., 2017, *MNRAS*, 470, 1421
- Ostriker J. P., Spitzer Jr. L., Chevalier R. A., 1972, *ApJ*, 176, L51
- Pfeffer J., Kruijssen J. M. D., Crain R. A., Bastian N., 2018, *MNRAS*, 475, 4309
- Plummer H. C., 1911, *MNRAS*, 71, 460
- Portegies Zwart S. F., McMillan S. L. W., Gieles M., 2010, *ARA&A*, 48, 431
- Prieto J. L., Gnedin O. Y., 2008, *ApJ*, 689, 919
- Reina-Campos M., Kruijssen J. M. D., Pfeffer J., Bastian N., Crain R. A., 2018, *MNRAS*, 481, 2851
- Renaud F., Gieles M., Boily C. M., 2011, *MNRAS*, 418, 759
- Spitzer L., Jr., 1958, *ApJ*, 127, 17
- Spitzer L., 1987, *Dynamical Evolution of Globular Clusters*, Princeton University Press, Princeton, NJ
- Vesperini E., Heggie D. C., 1997, *MNRAS*, 289, 898
- Webb J. J., Leigh N. W. C., 2015, *MNRAS*, 453, 3278
- Webb J. J., Harris W. E., Sills A., Hurley J. R., 2013, *ApJ*, 764, 124
- Webb J. J., Leigh N., Sills A., Harris W. E., Hurley J. R., 2014a, *MNRAS*, 442, 1569
- Webb J. J., Sills A., Harris W. E., Hurley J. R., 2014b, *MNRAS*, 445, 1048
- Weinberg M. D., 1994a, *AJ*, 108, 1398
- Weinberg M. D., 1994b, *AJ*, 108, 1403
- Weinberg M. D., 1994c, *AJ*, 108, 1414

This paper has been typeset from a \TeX/L\TeX file prepared by the author.

Part II

Globular clusters in a cosmological context

Chapter 4

Formation histories of stars, clusters, and globular clusters in the E-MOSAICS simulations

Authors:

Marta Reina-Campos, J. M. Diederik Kruijssen,
Joel L. Pfeffer, Nate Bastian and Robert A. Crain

Published in *MNRAS* 486 (2019) 5838.

Reproduced with permission from the journal

Marta Reina-Campos is the principal author of this article. The original idea was developed by all coauthors, and Marta Reina-Campos performed the analysis of the simulations. All authors collaborated in a weekly discussion on the project and Marta Reina-Campos produced all the figures and wrote the manuscript. All authors collaborated with corrections and suggestions to the manuscript, and Marta Reina-Campos performed the last improvements during the review process.



Formation histories of stars, clusters, and globular clusters in the E-MOSAICS simulations

Marta Reina-Campos¹,¹★ J. M. Diederik Kruijssen¹,¹ Joel L. Pfeffer²,² Nate Bastian² and Robert A. Crain²

¹Astronomisches Rechen-Institut, Zentrum für Astronomie der Universität Heidelberg, Mönchhofstraße 12-14, D-69120 Heidelberg, Germany

²Astrophysics Research Institute, Liverpool John Moores University, 146 Brownlow Hill, Liverpool L3 5RF, UK

Accepted 2019 April 30. Received 2019 April 28; in original form 2018 October 30

ABSTRACT

The formation histories of globular clusters (GCs) are a key diagnostic for understanding their relation to the evolution of the Universe through cosmic time. We use the suite of 25 cosmological zoom-in simulations of present-day Milky Way-mass galaxies from the E-MOSAICS project to study the formation histories of stars, clusters, and GCs, and how these are affected by the environmental dependence of the cluster formation physics. We find that the median lookback time of GC formation in these galaxies is ~ 10.73 Gyr ($z = 2.1$), roughly 2.5 Gyr earlier than that of the field stars (~ 8.34 Gyr or $z = 1.1$). The epoch of peak GC formation is mainly determined by the time evolution of the maximum cluster mass, which depends on the galactic environment and largely increases with the gas pressure. Different metallicity subpopulations of stars, clusters, and GCs present overlapping formation histories, implying that star and cluster formation represent continuous processes. The metal-poor GCs ($-2.5 < [\text{Fe}/\text{H}] < -1.5$) of our galaxies are older than the metal-rich GC subpopulation ($-1.0 < [\text{Fe}/\text{H}] < -0.5$), forming 12.13 Gyr and 10.15 Gyr ago ($z = 3.7$ and $z = 1.8$), respectively. The median ages of GCs are found to decrease gradually with increasing metallicity, which suggests different GC metallicity subpopulations do not form independently and their spatial and kinematic distributions are the result of their evolution in the context of hierarchical galaxy formation and evolution. We predict that proto-GC formation is most prevalent at $2 \lesssim z \lesssim 3$, which could be tested with observations of lensed galaxies using JWST.

Key words: stars: formation – globular clusters: general – galaxies: evolution – galaxies: formation – galaxies: star clusters: general.

1 INTRODUCTION

Globular clusters (GCs) are often considered to be old (ages > 10 Gyr), relatively metal-poor ($[\text{Fe}/\text{H}] < 0$), massive ($M \simeq 10^4$ – $10^6 M_{\odot}$) stellar clusters with multiple stellar populations (i.e. light elements abundance spreads) that have remained gravitationally bound until the present time. Even though exceptions exist for this classical definition, like the extremely young GC population of ages 0.1–1 Gyr observed by Schweizer & Seitzer (1998), their overall old ages make them compelling candidates to provide insights into the physics of the early Universe (e.g. Harris 1991; Forbes, Brodie & Grillmair 1997; Brodie & Strader 2006; Kruijssen 2014; Forbes et al. 2018).

Nevertheless, obtaining absolute measurements of GC ages is extremely challenging and several methods have been used over the years to determine them. The GC population of the Milky Way is

the best suited to obtain age measurements based on their resolved colour–magnitude diagrams (CMDs), either by fitting the turn-off point of the main sequence or by using the luminosity cooling function of white dwarfs. The former is the most common method, and 64 GCs in the Milky Way have age measurements based on deep CMDs observed with the ACS of the *Hubble Space Telescope* (Marín-Franch et al. 2009), though absolute measurements are sensitive to the uncertainties in the stellar evolution models, the intrinsic abundance variations, foreground dust corrections, the assumed helium content, and the object’s distance. By contrast, the latter method is insensitive to the metallicity of the cluster, but it requires going deeper in their CMDs and it has only been performed for a handful of GCs in the Milky Way (e.g. 47 Tuc in Hansen et al. 2013). In the case of extragalactic GCs, an extensive body of the literature uses age determination methods based on spectroscopically inferred properties, such as spectral indices (e.g. Strader et al. 2005; Beasley et al. 2008), colour–metallicity relations (Usher et al. 2012) or metallicities (Forbes et al. 2015).

* E-mail: reina.campos@uni-heidelberg.de

Despite the differences between the methods used to determine GC ages, they paint a similar picture: GC populations are typically older than field stars, as they mostly formed before the peak of the cosmic star formation history ($z \simeq 2$, Madau & Dickinson 2014), and metal-poor GCs seem to have formed coevally to or earlier than the metal-rich ones. In the Milky Way, the population of massive ($M > 10^5 M_{\odot}$) GCs with metallicities $-2.5 < [\text{Fe}/\text{H}] < -0.5$ is $\simeq 12.2$ Gyr old ($z \sim 4$, Kruijssen et al. 2019a, based on measurements from Forbes & Bridges 2010; Dotter et al. 2010; Dotter, Sarajedini & Anderson 2011; VandenBerg et al. 2013), which is older than the inferred mean star formation time based on the star formation history of the Milky Way, $\tau_f = 10.5 \pm 1.5$ Gyr (Snaith et al. 2014). Despite the relatively large uncertainties (~ 1 Gyr), several studies find an age–metallicity relation among the GCs in the Milky Way, with metal-poor GCs being the oldest and younger objects having higher metallicities. The exact age offset between both subpopulations depends on the catalogue considered and the metallicity range, but overall metal-poor GCs are found to be coeval to or older (by up to ~ 1.25 Gyr) than the metal-rich subpopulation within the uncertainties (considering $[\text{Fe}/\text{H}] \gtrsim -1.2$ between the metal-poor and metal-rich subpopulations; Dotter et al. 2010; Forbes & Bridges 2010; Dotter et al. 2011; VandenBerg et al. 2013). Subsamples of GCs in different metallicity intervals are also observed to have radial age gradients, as seen in M31 (Beasley et al. 2005) and in 11 early-type galaxies from the SLUGGS survey (Forbes et al. 2015). The implied differences in formation epoch have been proposed to explain the observed differences in spatial distributions and kinematics between these metallicity GC subpopulations (Brodie & Strader 2006), and some authors also suggest they indicate different formation mechanisms (Griffen et al. 2010).

The formation mechanism of GCs is still under debate (see Forbes et al. 2018 for a recent review). The striking differences between open clusters and GCs in the Milky Way (ages, masses, densities) encouraged early work on the topic to invoke special conditions in the early Universe to form GCs (e.g. Peebles & Dicke 1968; Fall & Rees 1985). However, the discovery of young super star clusters in the local Universe (e.g. Holtzman et al. 1992) with similar properties to the observed GC populations fueled the hypothesis that GCs could be the relics of massive cluster formation during the epoch of peak star formation activity in the Universe (e.g. Ashman & Zepf 1992). Several models in the current literature have been suggested to explain the formation of GCs: some invoke exotic formation mechanisms at extremely high redshift (such as GC formation in dark matter mini haloes, e.g. Griffen et al. 2010; Trenti, Padoan & Jimenez 2015), whereas others consider the premise of regular cluster formation at high redshift producing massive clusters that remain gravitationally bound until the present day (e.g. Ashman & Zepf 1992; Elmegreen 1997; Fall & Zhang 2001; Kravtsov & Gnedin 2005; Kruijssen 2015; Li et al. 2017; Kim et al. 2018). Despite the very different formation mechanisms considered, these models predict that the bulk of GC formation should happen before the peak of cosmic star formation ($z \simeq 2$, Madau & Dickinson 2014). However, the former family of models places the bulk of metal-poor GC formation at $z > 6-10$, whereas the prediction of the latter lies at later times, $z \sim 2-10$, depending on the exact physics considered. Therefore, the ages of different populations of GCs are essential to establish their relation to galaxy formation and evolution, and to test different GC formation models.

A variety of papers has used the age distribution of GCs in the Milky Way to test GC formation models (e.g. Beasley et al. 2002; Muratov & Gnedin 2010; Griffen et al. 2013; Renaud, Agertz & Gieles 2017; Choksi & Gnedin 2018; Li & Gnedin 2018; El-

Badry et al. 2019). These models combine a description of cluster formation (and in some cases also cluster mass-loss due to stellar evolution and evaporation) with a hierarchical description of galaxy assembly to study the buildup of GC populations, as well as the formation times of the metal-poor and metal-rich subpopulations. Overall, these models predict that GC formation happens before the peak of the cosmic star formation rate ($z \simeq 2$, Madau & Dickinson 2014), with the exact range in cosmic time depending on the details of each model (i.e. the GC formation times found can range between $2 \lesssim z \lesssim 14$).

In this work, we study the cosmic history of formation of stars, clusters, and GCs,¹ as well as the influence of the environmental dependence of the cluster formation physics in the context of the E-MOSAICS simulations (Pfeffer et al. 2018; Kruijssen et al. 2019b). This project combines the sub-grid model for stellar cluster formation and evolution MOSAICS (MOdelling Star cluster population Assembly In Cosmological Simulations, Kruijssen et al. 2011; Pfeffer et al. 2018), with the EAGLE (Evolution and Assembly of GaLaxies and their Environments, Crain et al. 2015; Schaye et al. 2015) galaxy model, a set of state-of-the-art hydrodynamical simulations of galaxy formation in the Λ CDM cosmogony. For the first time, we can study self-consistently how galaxies and stellar clusters form and co-evolve through cosmic time. Several papers using the E-MOSAICS simulations demonstrate that self-consistent modelling of cluster formation and evolution in a galaxy formation context allows to reproduce a wide variety of properties of galaxy and GC populations (Pfeffer et al. 2018; Usher et al. 2018; Hughes et al. 2019; Kruijssen et al. 2019b,a).

We first describe the cluster formation and evolution model used in E-MOSAICS in Section 2. With the aim of studying the formation histories of stars, clusters, and GCs in a cosmological context and assessing the role of the cluster formation physics, we use the 10 cosmological zoom-in simulations of present-day Milky Way-mass galaxies from the E-MOSAICS simulations described by Pfeffer et al. (2018) (MW00–MW09, Sections 3 and 4). We expand this to the full sample of 25 galaxy simulations described by Kruijssen et al. (2019b) to consider the formation histories of different metallicity subsamples of stars, clusters, and GCs and investigate how the median age of GCs is predicted to vary with metallicity (Section 5). In Section 6, we compare our results with those of previous works. We conclude with a summary of our results in Section 7.

2 THE E-MOSAICS PROJECT

We use the formation histories of stars, clusters, and GCs in the 25 cosmological zoom-in present-day Milky Way-mass galaxies from the E-MOSAICS simulations (Pfeffer et al. 2018; Kruijssen et al. 2019b) to determine when GCs form relative to the field stars. We define our GC population as massive ($M > 10^5 M_{\odot}$) stellar clusters that survive until the present time, whereas our cluster population corresponds to all surviving clusters. The E-MOSAICS simulations allow the self-consistent study of the formation and co-evolution of stellar clusters and their host galaxies through cosmic time and it has been demonstrated to reproduce a wide variety of properties of the galaxy and GC populations. We briefly summarize here the elements of the model considered in the simulations that are relevant for this work.

¹The definition of GC used in this work corresponds to those clusters that survive with masses $M > 10^5 M_{\odot}$ until the present time.

The EAGLE galaxy formation model uses a modified version of the N -body TreePM smoothed particle hydrodynamics code GADGET-3 (last described by Springel 2005). The key modifications are to the time-step criteria, the hydrodynamical algorithm, and the inclusion of numerous sub-grid routines to describe the baryonic physics at scales smaller than the resolution. Most significant for this work are the routines modelling radiative cooling and photoionization (Wiersma, Schaye & Smith 2009a) in the presence of a redshift-dependent UV background (Haardt & Madau 2001), stochastic star formation that by construction reproduces the Kennicutt–Schmidt relation (Schaye & Dalla Vecchia 2008), the chemical enrichment of 11 species (H, He, and nine metal species, Wiersma et al. 2009b), the feedback associated with star formation (Dalla Vecchia & Schaye 2012), and the growth of black holes (Booth & Schaye 2009; Schaye et al. 2015). For further details we refer the reader to Schaye et al. (2015) and Crain et al. (2015). The galaxies are identified using the friends-of-friends (Davis et al. 1985) and SUBFIND algorithms (Springel et al. 2001; Dolag et al. 2009), following the description in Schaye et al. (2015).

In the fiducial model of E-MOSAICS, stellar clusters are formed according to the local gas properties at the time of their formation as a sub-grid component of the newly born star particles. We describe cluster formation with two physical models. First, we consider the cluster formation efficiency (CFE; Bastian 2008), which determines the fraction of star formation occurring in bound clusters. We use the model described by Kruijssen (2012), in which the CFE increases with the gas density or pressure [and indirectly with the star formation rate (SFR) surface density], such that the densest gas environments form greater fractions of the stellar mass in bound stellar clusters. This model reproduces the observed trends in actively star-forming galaxies in the local Universe (e.g. Adamo et al. 2015; Johnson et al. 2016). Our second ingredient considered is the initial cluster mass function (ICMF), which we assume to be a Schechter function, that is a power law of slope $\alpha = -2$ with an exponential high-mass truncation (Schechter 1976). We model the upper mass scale of the mass function according to Reina-Campos & Kruijssen (2017), where the competition between centrifugal forces and stellar feedback sets the maximum cloud mass from which the most massive cluster forms. In this model, the cloud (and cluster) truncation masses correlate with gas pressure, so the highest pressure environments are more likely to form massive stellar clusters that can survive for a Hubble time. Such a description simultaneously explains the constant upper mass scales of molecular clouds and clusters in nearby galaxies (Reina-Campos & Kruijssen 2017; Messa et al. 2018), as well as the higher molecular clump masses observed at high redshift (e.g. Genzel et al. 2011). The combination of these ingredients implies that higher pressure environments, like those within high-redshift galaxies or merging galaxies in the local Universe, are more likely to form a larger fraction of their mass in bound stellar clusters that will extend to higher cluster masses.

The evolution of the gas properties as galaxies form and evolve implies that the environmental dependence of the cluster formation physics considered in E-MOSAICS also implies a time dependence; as the Universe expands, haloes virialize at a lower density and gas inflow rates decline (e.g. Correa et al. 2015), so that gas pressures decrease, less mass is turned into stellar clusters, and their maximum cluster mass scale decreases. The evolution of the cluster formation ingredients across cosmic time is shown in figs 6 and 8 of Pfeffer et al. (2018) across a sample of 10 galaxies for the CFE and the maximum cluster mass scale, respectively. Among the galaxy sample, high-redshift environments have high median

CFEs of $\Gamma \sim 5$ –50 per cent up until $z \sim 1$ –2, after which they decrease sharply to $\Gamma \sim 1$ –10 per cent at the present time. The upper mass scale of the ICMF exhibits a similar behaviour, up until $z \simeq 1$ galaxies have median truncation masses of a few $10^5 M_{\odot}$, but they decrease steeply to $\sim 10^3 M_{\odot}$ at the present time. Due to this time dependence, the bulk of GC formation in present-day Milky Way-mass galaxies is expected to occur at high redshift with little GC formation nowadays. It is worth noting that massive cluster formation is not restricted to early cosmic times, as interacting or starbursting galaxies can host the high-pressure environments that lead to the formation of these objects by means of dramatically increased values of the CFE and upper mass scales (similar to the average high-redshift Milky Way progenitors).

Once the cluster populations are formed, they are evolved alongside their host galaxies according to four disruption mechanisms. The main source of cluster mass-loss is due to tidal shocking with the cold interstellar medium (ISM) (e.g. Gieles et al. 2006; Kruijssen et al. 2011; Miholics, Kruijssen & Sills 2017; Pfeffer et al. 2018). We model the amount of mass lost in these interactions using an on-the-fly calculation of the tidal tensor at the position of the cluster (Spitzer 1958), which allows us to track the disruptive ‘power’ of the different environments clusters may reside in during their lifetimes. As described by Pfeffer et al. (2018), the lack of a cold ISM treatment in EAGLE causes tidal shocks to be underestimated in low-pressure environments ($P/k_B < 10^7 \text{ K cm}^{-3}$), but shocks are the main disruption mechanism in high-pressure environments. We also consider mass-loss due to two-body interactions between the stars in the cluster, which becomes relevant in low-density environments where the ISM is not as disruptive (Gieles 2009; Kruijssen et al. 2011). Thirdly, clusters lose mass due to stellar evolution (Wiersma et al. 2009b). Finally, we consider the effect of dynamical friction in removing the most massive inner clusters in post-processing. The combination of these disruption mechanisms affects mostly low-mass clusters (Reina-Campos et al. 2018), indicating that massive clusters are more likely to survive until the present time, and thus, to be identified as GCs (i.e. stellar clusters more massive than $10^5 M_{\odot}$ at the present time).

In order to study how the environmental dependence of cluster formation influences the formation of stellar clusters and GCs relative to the field stellar population, we consider four cluster formation scenarios with different degrees of environmental dependence that are summarized in Table 1 and described below. For each of these scenarios, we reran 10 galaxies (MW00–MW09, described by Pfeffer et al. 2018) out of our sample of 25 present-day Milky Way-mass simulations in E-MOSAICS (Kruijssen et al. 2019b).

In our second cluster formation model we maintain the CFE model, but switch off the environmental dependence of the upper mass scale of the ICMF. Instead, we assume the ICMF to be a pure power law of slope $\alpha = -2$. In this scenario, massive clusters can form throughout cosmic time, but the stellar mass formed in bound clusters varies between environments with different gas pressures. For our third model, we maintain the upper mass scale model, but switch off the environmental dependence of the CFE by assuming a constant value of $\Gamma = 10$ per cent. We expect the least prevalent formation of GCs in this scenario, as the upper mass scale of the ICMF correlates strongly with gas pressure, indicating that only the highest pressure environments will be able to form massive clusters, and only a small constant fraction of stellar mass is formed into clusters. In our last model, we switch off all the environmental dependences of the cluster formation physics; the ICMF is assumed to be a power law of slope $\alpha = -2$ and the CFE is fixed at 10 per cent throughout cosmic time. This scenario thus resembles those studies

Table 1. Cluster formation models considered in this work. From left to right, columns contain the name of the cluster formation scenario and the description used for the CFE and the ICMF, respectively.

Name	CFE	ICMF
Fiducial	$\Gamma(\Sigma, Q, \kappa)$ Kruijssen (2012)	Schechter function $M_{\text{cl, max}}(\Sigma, Q, \kappa)$ Reina-Campos & Kruijssen (2017)
$\alpha = -2$	$\Gamma(\Sigma, Q, \kappa)$ Kruijssen (2012)	Power law of slope $\alpha = -2$
$\Gamma = 10\%$	$\Gamma = 10\%$	Schechter function $M_{\text{cl, max}}(\Sigma, Q, \kappa)$ Reina-Campos & Kruijssen (2017)
No formation physics	$\Gamma = 10\%$	Power law of slope $\alpha = -2$

that identify GCs in their simulations tagging particles that meet certain criteria such as metallicity, position, mass, kinematics, etc. (e.g. Tonini 2013; Renaud et al. 2017).

Pfeffer et al. (2018) and Kruijssen et al. (2019b) show that the variety of formation and assembly histories among the galaxy sample from the E-MOSAICS simulations covers a wide range of conditions for cluster formation and evolution. This makes them an ideal sample to study how clusters and GCs form relative to the stars.

3 FORMATION HISTORIES OF STARS, CLUSTERS, AND GLOBULAR CLUSTERS

We study how stars, clusters, and GCs form across cosmic time and whether the environmental dependence of the cluster formation physics affects their formation histories. To do that, we determine the median formation rates of these objects over the sample of 10 present-day Milky Way-mass zoom-in simulations from the E-MOSAICS simulations described in Pfeffer et al. (2018) in each cluster formation scenario described in Section 2.

To determine the formation histories of stars, stellar clusters, and GCs, we only consider those objects that belong to the central galaxy in the simulations (i.e. all objects within the virial radius at the present time) and, in the case of the clusters and GCs, we restrict our analysis to the observed metallicity range of GCs with measured ages in the Milky Way, $[\text{Fe}/\text{H}] \in (-2.5, -0.5]$.² Both the SFR and the cluster formation rate (CFR) are determined from the initial masses of stars and clusters, respectively, whereas the GC formation rate (GCFR) corresponds to the formation history of the observed, massive ($M > 10^5 M_{\odot}$) stellar clusters at the present time. Given that L^* galaxies like the Milky Way contain most of the GCs in the Universe (Harris 2016), this rate is roughly proportional to the GCFR of the Universe across all galaxies. According to these definitions, the SFR (CFR) gives us information on the initial conditions of star (cluster) formation, whereas the GCFR is affected by cluster mass-loss and represents the formation rate of stars that remain gravitationally bound in massive clusters at the present time.³

²This metallicity range also mitigates against the overproduction of young metal-rich clusters that do not get disrupted by the lack of cold ISM modelling in the EAGLE model (see discussion in Section 2).

³The instantaneous formation of massive clusters ($M > 10^5 M_{\odot}$) at any given epoch may differ from the GCFR curve, as their survival to the present time is required to be identified as a GC.

We present the median formation histories of the 10 galaxies in Fig. 1, with the shaded areas indicating the 25th–75th percentiles. As observed for the cosmic SFR (Madau & Dickinson 2014) and for the SFR of the Milky Way (Snaith et al. 2014), our median SFRs also peak at $z \sim 2$ (~ 10 Gyr ago). Only L^* galaxies, like the Milky Way, are expected to reproduce the cosmic SFR density evolution, as most of the stellar mass at the present time lies in these type of galaxies. More and less massive galaxies are instead expected to peak before and after $z \approx 2$, respectively (Qu et al. 2017). The cluster and GC formation histories present a similar peak regardless of the cluster formation physics considered, as their formation depends on that of stars. Despite the similarity of the peak epoch of the formation histories, the behaviour shown by the cluster and GC formation histories at early and late epochs differ from one formation scenario to another.

We now discuss the evolution of the formation histories from high to low redshift. In the fiducial model (top-left panel in Fig. 1), both the SFR and the CFR present a steady increase up to $z \sim 2$. At later times, the SFR barely decreases, whereas the CFR declines with a considerably steeper slope. This decline is produced by two factors. First, the metallicity cut imposed on the clusters to replicate the observed Milky Way range disregards the latest cluster formation, which proceeds at near-solar metallicity. Secondly, the CFR indicates the initial mass formed as bound stellar clusters per unit time, hence, it is highly sensitive to the CFE (i.e. the stellar mass reservoir from which stellar clusters can be formed). The CFE presents a steep decline at $z \sim 1-2$ for our galaxy sample (see discussion in Section 2), indicating that at late epochs the stellar mass reservoir for clusters is smaller and so less mass is initially formed as bound clusters.

The formation of the surviving, massive ($M > 10^5 M_{\odot}$) clusters identified as GCs at the present time in our fiducial model occurs between $z \simeq 1-7$ (between ~ 8 and 13 Gyr ago). The GCFR rises steadily up to $z \sim 3$ (~ 11.7 Gyr ago), but it abruptly declines after $z \sim 2$ (~ 10.5 Gyr ago) and completely stops by $z \simeq 1$ (8 Gyr ago). There are three factors affecting the behaviour of the GCFR. First, our Milky Way-like metallicity cut neglects the youngest GC formation at solar metallicities. Secondly, the formation and survival of massive clusters depend on the upper mass scale of their ICMF (i.e. more massive clusters are more likely to survive), so the GCFR is sensitive to the time evolution of the cluster truncation mass. The median cluster truncation masses over our 10 galaxies drop below $10^5 M_{\odot}$ already at $z \sim 1-2$, so the formation of massive clusters at late epochs becomes highly unlikely (see discussion in Section 2 and fig. 8 in Pfeffer et al. 2018). Finally, the normalization of the GCFR is given by the time evolution of the CFE; a larger reservoir

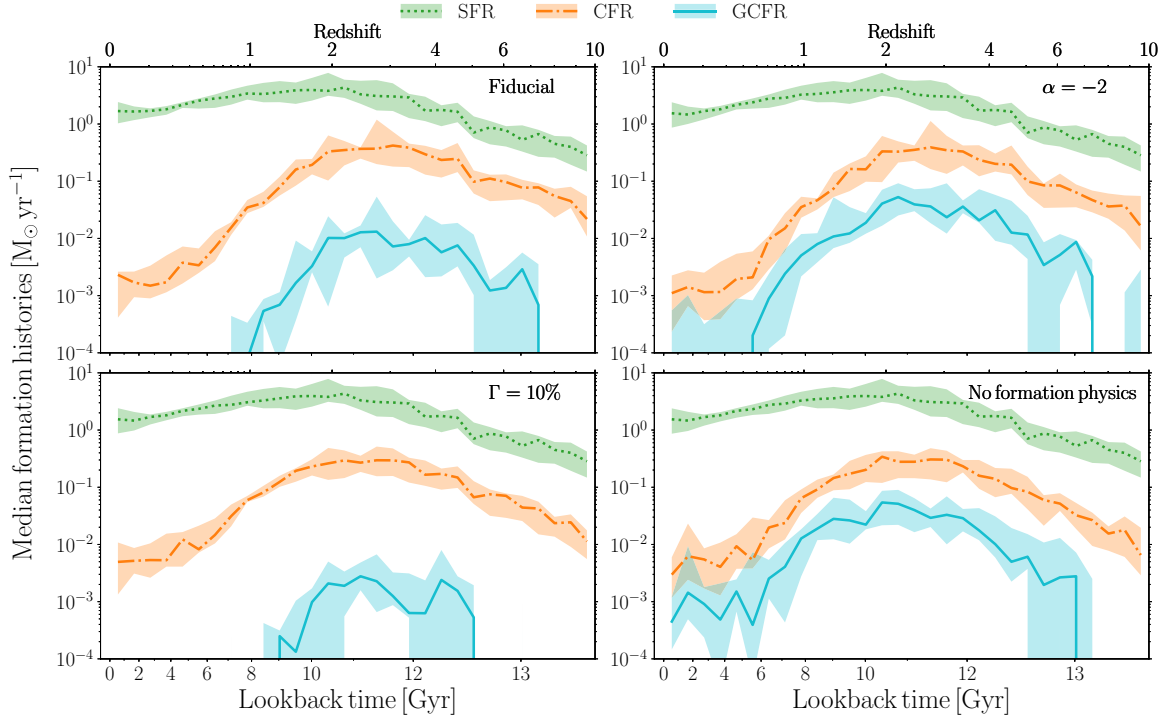


Figure 1. Median formation histories of stars, clusters, and GCs over a sample of 10 galaxies from the E-MOSAICS simulations (MW00–MW09) for each cluster formation physics scenario: fiducial model with full environmental dependence (*top left*), semi-universal formation model with a constant power-law ICMF (*top right*), semi-universal formation model with a constant CFE (*bottom left*), universal formation model with no environmental dependence (*bottom right*). We restrict all populations to reside in the central galaxy of the simulations, and we restrict our cluster and GC populations to metallicities $[\text{Fe}/\text{H}] \in (-2.5, -0.5]$ (see the text). The shaded regions correspond to the 25th–75th percentiles.

of mass to be formed as stellar clusters implies that a larger number of massive ones can be formed. The combination of these factors predicts a rather abrupt end of GC formation at late epochs in our fiducial model.

We can use the mean ages of the five⁴ youngest, massive ($M > 10^5 M_{\odot}$) GCs in the Milky Way with metallicities $-2.5 < [\text{Fe}/\text{H}] < -0.5$ to place a lower limit on GC formation epoch across all of its progenitors. Their formation $10.4 \pm 0.1 \pm 0.8$ Gyr ago (statistical and systematic uncertainties, respectively; $z \simeq 1.92$; NGC 1261, NGC 1851, NGC 6544, NGC 6712, and NGC 6864, Kruijssen et al. 2019a) implies that shortly afterwards the GC formation with $[\text{Fe}/\text{H}] < -0.5$ in the Milky Way ceased, as predicted by our fiducial model. Another constraint can be placed by comparing the total surviving GC mass in the Milky Way to that in our simulations. We use the implied masses from the absolute visual magnitudes in Harris (1996)⁵ of those massive ($M > 10^5 M_{\odot}$) clusters in our metallicity range ($[\text{Fe}/\text{H}] \in (-2.5, -0.5]$) and obtain that the total mass in GCs is $M \sim 2.8 \times 10^7 M_{\odot}$. In our simulated galaxies, we can determine the total GC mass by integrating the median GCFR over cosmic time, which results in a surviving GC mass of $\sim 2.7 \times 10^7 M_{\odot}$ (9.5×10^6 – $6.4 \times 10^7 M_{\odot}$ for percentiles 25–75th,

respectively). Therefore, our fiducial model reproduces both the late epoch inefficiency of GC formation and the total mass of surviving GCs in the Milky Way.

We can now study how the environmental dependence of the cluster formation physics affects the way clusters and GCs form in our galaxy sample. To do so, we compare the cluster formation models with different degrees of environmental dependence (described in Table 1) to our fiducial model. We start by considering our second model, where we only switch off the environmental dependence of the upper mass scale and instead adopt a power-law ICMF with slope $\alpha = -2$ (top-right panel in Fig. 1). Only the GCFR presents significant differences with respect to the fiducial cluster formation model. Keeping a constant ICMF through cosmic time implies that a large fraction of the clusters are forming massive enough so that they survive as massive ($M > 10^5 M_{\odot}$) clusters at the present time, which extends the formation of GCs until the present time and produces ~ 4.3 times the surviving GC mass in the fiducial model. According to this formation model, the formation of clusters with masses $M > 10^5 M_{\odot}$ and metallicities $-2.5 < [\text{Fe}/\text{H}] < -0.5$ should be commonplace in the progenitors of Milky Way-mass galaxies until recently ($z \sim 0.4$ or ~ 5.5 Gyr ago).

In our third model, where we assume a constant CFE of $\Gamma = 10$ per cent (bottom-left panel in Fig. 1), the CFR presents a steeper (shallower) slope at early (late) epochs relative to the fiducial scenario, but the peaks coincide. The GCFR also resembles its counterpart from the fiducial model, but halted at early and late cosmic times. The similar epoch of peak GC formation relative to the fiducial model means that it is mainly determined by the truncation

⁴We have verified that changing this number in the range 3–7 does not significantly change the numbers quoted here.

⁵We assume an absolute visual magnitude for the Sun of $M_{V, \odot} = 4.83$ and a constant mass-to-light ratio of $M/L_V = 2 M_{\odot} L_{\odot}^{-1}$ to determine the cluster masses.

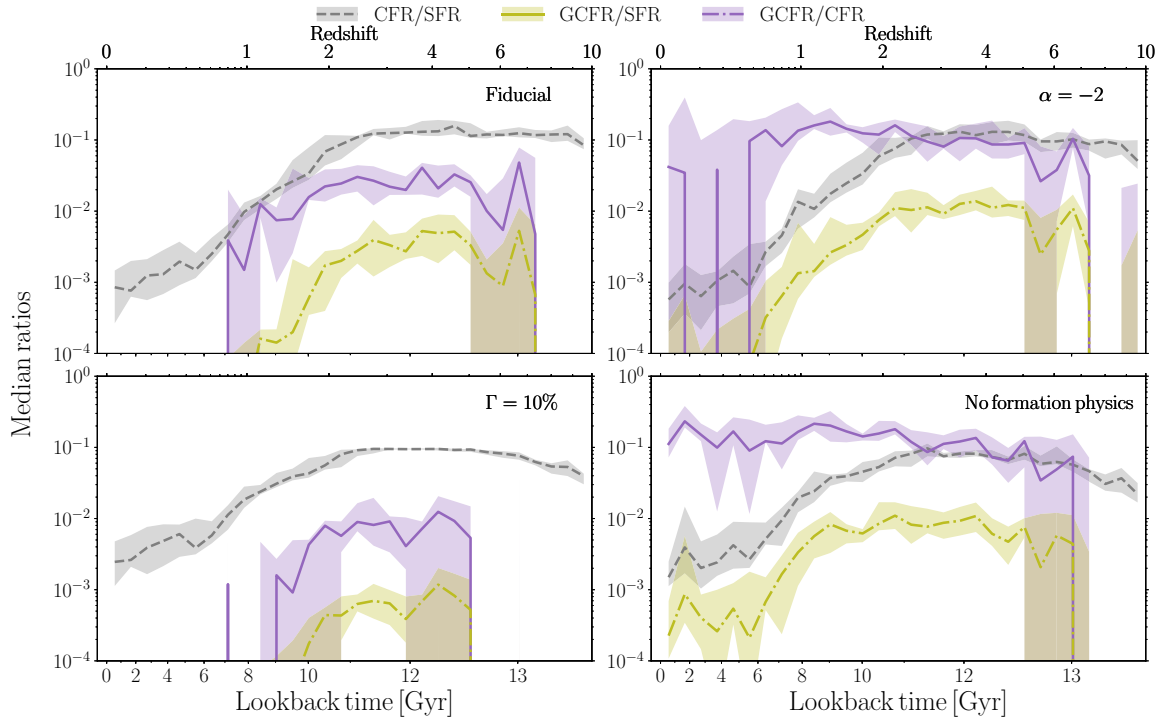


Figure 2. Median relative formation histories of stars, clusters, and GCs over a sample of 10 galaxies from the E-MOSAICS simulations (MW00–MW09) for each cluster formation physics scenario: fiducial model with full environmental dependence (*top left*), semi-universal formation model with a constant power-law ICMF (*top right*), semi-universal formation model with a constant CFE (*bottom left*), universal formation model with no environmental dependence (*bottom right*). We restrict all populations to reside in the central galaxy of the simulations, and we restrict our cluster and GC samples to metallicities $[\text{Fe}/\text{H}] \in (-2.5, -0.5]$ (see the text). The shaded regions correspond to the 25th–75th percentiles.

mass of the ICMF. Maintaining a universal fraction of star formation in bound clusters avoids the abrupt drop of cluster formation towards the present time, but overall it produces 70 per cent of the total mass initially in clusters and 20 per cent of the total mass in surviving GCs relative to the fiducial model. In this semi-universal scenario, the constant low amount of mass formed in stellar clusters and the environmental dependence of the upper mass scale combine to form a small fraction of surviving GCs.

By contrast, the combination of a constant CFE and a power-law ICMF in our ‘no formation physics’ model (*bottom-right panel* in Fig. 1) produces the formation of a significant number of GCs throughout cosmic evolution, resulting in a factor of ~ 5.5 more mass residing in surviving GCs than in the fiducial model. The GC formation extends until the present time, which implies on-going massive ($M > 10^5 M_{\odot}$) cluster formation should be commonplace in Milky Way-mass galaxies if this formation model were correct.

We can study in more detail the relative formation histories between stars, clusters, and GCs to better understand the influence of the environmental dependence of cluster formation physics. We determine the relative formation histories of clusters and GCs with respect to stars, and of GCs with respect to clusters in our galaxy sample for each cluster formation scenario. The ratio of the CFR to the SFR indicates the mass initially formed in stellar clusters relative to the initial stellar population mass, which effectively corresponds to the CFE model considered. By contrast, the GCFR to CFR ratio describes the fraction of initial cluster mass that forms and survives as massive ($M > 10^5 M_{\odot}$) clusters at the present time and is mainly determined by the ICMF considered and cluster evolution. Lastly,

the ratio of the GCFR to the SFR corresponds to the fraction of initial stellar mass that ends up in GCs at the present time. We expect this ratio to be affected by both the CFE and the ICMF models describing cluster formation. We present the median relative formation histories over our sample of 10 galaxies in Fig. 2 with the shaded areas indicating the 25th–75th percentiles.

Roughly ~ 10 per cent of the initial stellar mass forms as clusters until $z \sim 2$ (~ 10.5 Gyr ago) in our fiducial model (*top-left panel* of Fig. 2), which then drops to less than 0.1 per cent at the present time. The difference between this result and the few per cent at the present time in fig. 6 in Pfeffer et al. (2018) is due to the metallicity range of the clusters. As discussed before, the typical gas pressure peaks at around $z \sim 2$, after which it declines as cosmic expansion starts to dominate over collapse, so that lower gas pressures are attained at later epochs and a smaller fraction of stars is born in clusters. Together with the metallicity cut considered, it produces the drop in the CFR to SFR ratio at late cosmic times. Out of the initial cluster mass formed, until $z \sim 2$ approximately 2–3 per cent forms in massive clusters that survive as GCs, but then their formation drops and stops at $z \sim 0.8$ (7 Gyr ago). The shape is driven by the time evolution of the upper-mass scale model; the decrease of the gas pressure with cosmic time implies less massive clusters can form. Higher pressure environments are also more disruptive and destroy the oldest massive clusters, explaining why the GCFR-to-CFR ratio does not continue to the highest redshifts. The evolution of the CFE and the ICMF truncation mass imply that merely ~ 0.4 per cent of the initial stellar mass forms in surviving GCs at high redshift ($z \geq 2.5$).

5844 *M. Reina-Campos et al.*

Changing the ICMF to be constant in time (top-right panel of Fig. 2) implies that the high-mass end of the cluster mass function can be reached throughout cosmic evolution, which increases the fraction of initial cluster mass that survives as GCs to be roughly constant at ~ 15 per cent at high redshift ($z \geq 2$). The slight decrease towards early epochs is caused by cluster evolution disrupting the oldest clusters. A similar enhancement relative to the fiducial model is also seen in the fraction of initial stellar mass surviving as GCs, which increases to ~ 1 per cent at high redshift ($z \geq 2$). If instead we change the CFE model to be constant at $\Gamma = 10$ per cent (bottom-left panel of Fig. 2), the ratio of the CFR to the SFR should correspond to that value. It presents some deviations at early and late epochs that are caused by the metallicity range chosen, which excludes the earliest ($[\text{Fe}/\text{H}] < -2.5$) and latest ($[\text{Fe}/\text{H}] > -0.5$) cluster formation. The fractions of both the initial stellar and cluster mass surviving as GCs present a similar shape as in the fiducial model, but reach smaller values. Only ~ 0.06 per cent and ~ 0.8 per cent of the total initial stellar and cluster mass, respectively, survive as GCs in this scenario between $z \simeq 2-5$, a factor ~ 6 and 2.5 smaller than in the fiducial model.

Disabling the environmental dependence of the cluster formation physics (bottom-right panel of Fig. 2) produces large fractions of initial stellar and cluster mass surviving as GCs until the present time. The lack of young, massive GCs in the Milky Way with metallicities $-2.5 < [\text{Fe}/\text{H}] < -0.5$ (Forbes & Bridges 2010; Dotter et al. 2011; VandenBerg et al. 2013) precludes those models predicting present-day massive cluster formation. Likewise, the underprediction of the total GC surviving mass in our third model discards it as a suitable representation of the cluster formation physics. Hence, environmentally dependent cluster formation physics (as in our fiducial model) are required in order to reproduce the observed formation history of the GC population of the Milky Way. This agrees with earlier E-MOSAICS papers (e.g. Pfeffer et al. 2018), and here we identify that the environmental variation of the high-mass end of the ICMF is the controlling factor.

4 MEDIAN AGES OF STARS, CLUSTERS, AND GCs

The ages of GCs are a key observable to evaluate their relation to galaxy formation and evolution across cosmic time and to test different GC formation models. Hence, in this section we investigate when stellar clusters and GCs form relative to the field stellar population, and whether that depends on the environmental dependence of the cluster formation model.

We present the median cumulative formation histories of stars, clusters, and GCs over the 10 present-day Milky Way-mass galaxies described by Pfeffer et al. (2018) for our fiducial and ‘no formation physics’ models in Fig. 3 (top), as well as the median ages of GCs relative to field stars for the galaxies in our sample in Fig. 3 (bottom). As stated above, the ‘no formation physics’ model corresponds to the particle tagging technique that is frequently employed in galaxy formation models without a physical GC formation model (e.g. Tonini 2013; Renaud et al. 2017). In both formation scenarios half of the stellar mass is in place ~ 8 Gyr ago ($z \simeq 1$), whereas both clusters and GCs form half their masses at earlier cosmic times. Snaith et al. (2014) report that the formation of the thick disc in the Milky Way happened between 9 and 12.5 Gyr ago ($z = 1.5-4.5$) during the maximum star formation activity in the Universe. During that period, our sample of galaxies form between a few to ~ 40 per cent of their stellar mass, indicating the Milky Way underwent a rapid phase of formation and assembly, as suggested

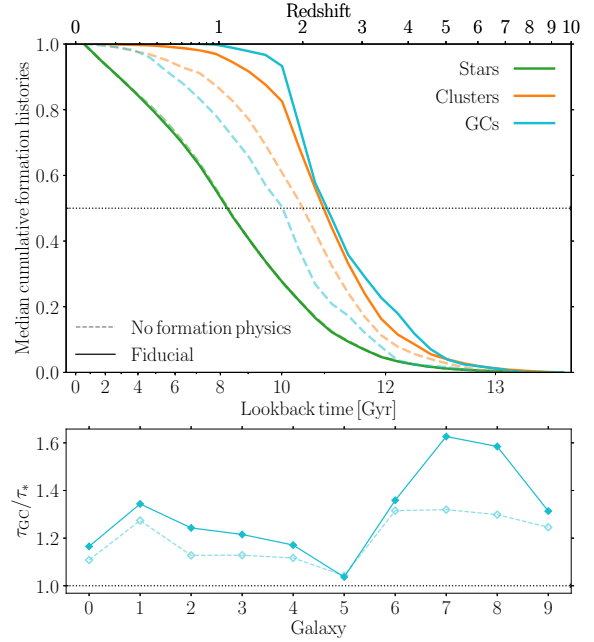


Figure 3. Comparison between the fiducial and the no cluster formation physics scenarios over a sample of 10 galaxies: median cumulative formation histories of stars, clusters, and GCs (top), median ages of GCs relative to those of all field stars across our galaxy sample (bottom).

in other studies (e.g. Haywood et al. 2013; Snaith et al. 2014, 2015; Mackereth et al. 2018; Kruijssen et al. 2019a). The cluster and GC populations form half their mass faster than field stars over our galaxy sample, indicating that the conditions in the early Universe were more favourable for (massive) cluster formation. The clusters in the fiducial model form earlier than those in the ‘no formation physics’ model, due to the larger CFEs attained at the elevated gas pressures typical of the environments present at early epochs.

On the other hand, the GCs in the fiducial and ‘no formation physics’ models are older and younger than the total cluster population, respectively, and they are consistently older than field stars on a galaxy-to-galaxy basis (Fig. 3, bottom panel). In our fiducial model, the most favourable conditions to form massive clusters exist in high-gas pressure environments, which are typical at high redshift (or in interacting or starburst galaxies at the present time), so that the bulk of GC formation takes place predominantly at early epochs. By contrast, the constant ICMF used in the ‘no formation physics’ model allows the formation of massive clusters through cosmic time, and cluster disruption is responsible for shifting the median cumulative GC formation history to a later time relative to clusters.

We can use the time when half the mass of the median GC population has formed as a proxy for their median ages. Using this metric, GCs form on average 11.1 and 10.0 Gyr ago ($z = 2.38$ and $z = 1.72$) in the fiducial and ‘no formation physics’ models, respectively, with 25th–75th percentile ages of 10.4–12.1 Gyr ($z = 1.90-3.58$) for the fiducial model and 8.4–11.2 Gyr ($z = 1.12-2.49$) for the ‘no formation physics’ model. We can compare these ages with the median age of the massive ($M > 10^5 M_{\odot}$) GC population in the Milky Way, $\tau_{\text{GC}} = 12.2 \pm 0.1 \pm 0.8$ Gyr (statistical and systematic uncertainties, respectively, Kruijssen et al. 2019a). This age is determined from a combination of different age-

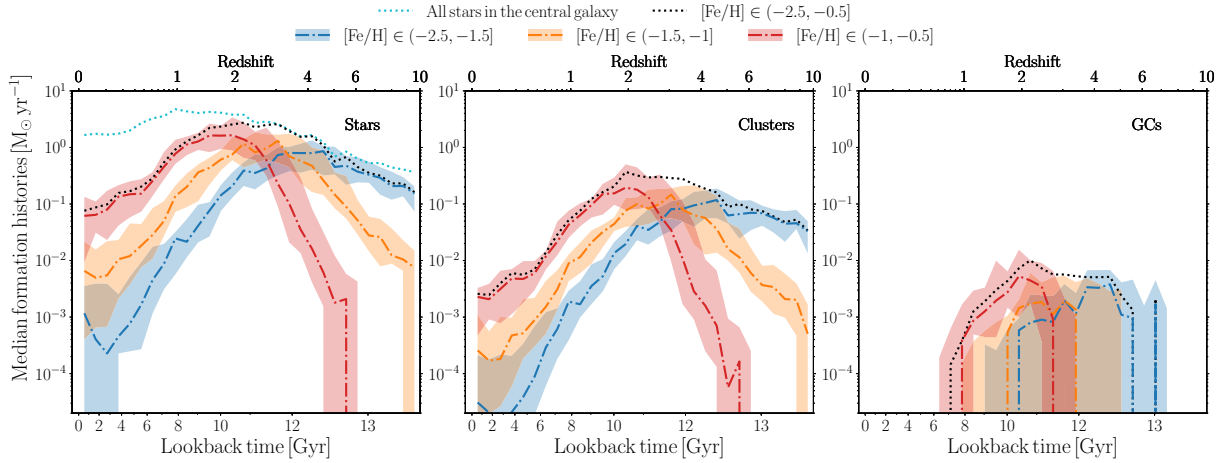


Figure 4. Median formation histories of stars, clusters, and GCs over the 25 galaxies from the E-MOSAICS simulations for the fiducial model. We restrict all populations to reside in the central galaxy of each simulation, and for clusters and GCs we consider the metallicity range $[\text{Fe}/\text{H}] \in (-2.5, -0.5)$. We subdivide each population into three metallicity subsamples: blue or metal-poor ($[\text{Fe}/\text{H}] \in (-2.5, -1.5)$), intermediate ($[\text{Fe}/\text{H}] \in (-1.5, -1)$), and red or metal-rich ($[\text{Fe}/\text{H}] \in (-1, -0.5)$). The shaded regions correspond to the 25th–75th percentiles. For reference, we also include the median formation history of all stars in the central galaxy in the left-hand panel.

metallicity samples (Forbes & Bridges 2010; Dotter et al. 2010, 2011; VandenBerg et al. 2013) to reduce the systematic errors between the samples. The ‘no formation physics’ scenario predicts a GC population that is considerably too young relative to the GCs in the Milky Way, in addition to its poor agreement with the observables discussed in Section 3 (i.e. the total mass surviving in GCs and the existence of on-going massive [$M > 10^5 M_\odot$] cluster formation in Milky Way-mass galaxies). By contrast, the fiducial formation model produces GC populations that are compatible with the observed ages to within one standard deviation (even though the Milky Way GC system likely formed early relative to that of the typical Milky Way-mass galaxy). This again demonstrates that the environmental dependence of the cluster formation physics is crucial in order to reproduce the GC population observed in the Milky Way.

5 FORMATION HISTORIES OF METALLICITY SUBSAMPLES OF STARS, CLUSTERS, AND GCs

In the previous sections, we determined the crucial role of the environmental dependence of the cluster formation physics in reproducing the observed GC populations in the local Universe. Previous works find evidence of a possible trend between the ages of GCs in the Milky Way and their metallicities, with the metal-poor objects being coeval to or older than their metal-rich counterparts within the uncertainties (e.g. Forbes & Bridges 2010; Dotter et al. 2010, 2011; VandenBerg et al. 2013; Forbes et al. 2015). The seemingly different ages of the metallicity subpopulations of GCs have been advanced as explanations for their different spatial distributions and kinematics (Brodie & Strader 2006), and some authors suggest they might indicate different formation scenarios. For instance, Griffen et al. (2010) suggest a scenario in which metal-poor GCs would have formed from the collapse of gas clouds with temperatures exceeding 10^4 K, whereas metal-rich GCs would be the result of star formation triggered by mergers. With the aim of investigating these suggestions, we now evaluate the formation

histories of different metallicity subsamples of stars, clusters, and GCs using our complete volume-limited sample of 25 present-day Milky Way-mass galaxies from the E-MOSAICS simulations described by Kruijssen et al. 2019b.

We define the *parent* sample of stars, clusters, and GCs following the same criteria as in Section 3: we consider all objects that belong to the central galaxy in each of our 25 simulated galaxies and we restrict the cluster and GC populations to have Milky Way GC-like metallicities in the range $[\text{Fe}/\text{H}] \in (-2.5, -0.5)$. In order to facilitate comparison, we also consider a *cluster-like* sample of stars with metallicities in the same metallicity range. As for our metallicity subsamples, we consider three metallicity bins: *blue* or metal-poor, *intermediate*, and *red* or metal-rich with metallicities $[\text{Fe}/\text{H}] \in (-2.5, -1.5)$, $(-1.5, -1)$ and $(-1, -0.5)$, respectively. As gas requires some time to enrich within a galaxy, we expect an age difference between these subsamples, with the metal-rich ones being the youngest.

We present the median formation histories of each metallicity subsample described above of stars, clusters, and GCs over our 25 simulated galaxies in Fig. 4 with the shaded region indicating the 25th–75th percentiles. The cluster-like sample of stars follows the complete sample of stars only between $3 < z < 5$, indicating that the metallicity range considered neglects the earlier ($[\text{Fe}/\text{H}] < -2.5$) and later ($[\text{Fe}/\text{H}] > -0.5$) star and cluster formation.

The median formation histories of the metallicity subsamples of stars, clusters, and GCs describe a continuous process of star and cluster formation, where the parent sample is dominated by different metallicity subsamples as cosmic time advances. As Milky Way-mass galaxies evolve, first the blue (metal-poor) objects peak at $z \simeq 4$ (~ 12 Gyr ago), then the intermediate subsample peaks at $z \simeq 3$ (~ 11 Gyr ago) and finally the red (metal-rich) subsample peaks at $z \simeq 2$ (~ 10 Gyr ago). Thus, there exists a relation between the age of the peak formation rate and the metallicity of the subsample, which indicates that considering a certain metallicity subsample implies sampling a different epoch within the parent formation history, which will offset the median ages relative to those of the parent sample.

Table 2. Total mass in surviving GCs (clusters more massive than $M > 10^5 M_{\odot}$ at the present time) across our sample of 25 present-day Milky Way-mass galaxies and in the Milky Way. From left to right, the columns contain the total mass of GCs in the parent, blue, intermediate, and red metallicity ranges ($[\text{Fe}/\text{H}] \in \{(-2.5, -0.5], (-2.5, -1.5], (-1.5, -1.0], (-1.0, -0.5]\}$). We also list the minimum, median, maximum, and IQR of each column at the bottom of the table, as well as the observed values in the Milky Way.

Name	M_{GC} $\times 10^7 M_{\odot}$	$M_{\text{GC, b}}$ $\times 10^7 M_{\odot}$	$M_{\text{GC, i}}$ $\times 10^7 M_{\odot}$	$M_{\text{GC, r}}$ $\times 10^7 M_{\odot}$
MW00	2.23	0.59	0.68	0.96
MW01	2.77	0.36	0.98	1.44
MW02	10.29	1.87	1.79	6.63
MW03	4.11	0.81	1.03	2.27
MW04	4.35	0.66	0.98	2.71
MW05	10.76	1.57	1.79	7.41
MW06	6.82	0.67	0.64	5.51
MW07	2.11	0.37	0.51	1.23
MW08	1.62	0.14	0.83	0.65
MW09	2.76	0.43	0.59	1.74
MW10	11.04	1.71	1.57	7.76
MW11	2.70	0.56	0.46	1.67
MW12	8.51	1.95	1.31	5.24
MW13	3.18	1.06	1.05	1.08
MW14	3.89	0.60	1.08	2.22
MW15	1.99	0.30	0.23	1.46
MW16	7.23	2.11	1.57	3.56
MW17	2.90	0.69	0.81	1.40
MW18	2.27	1.20	0.80	0.26
MW19	1.46	0.28	0.16	1.01
MW20	2.89	0.28	0.89	1.72
MW21	3.68	1.17	0.78	1.73
MW22	8.53	2.05	1.42	5.06
MW23	12.84	1.94	2.46	8.44
MW24	1.66	0.25	0.39	1.02
Minimum	1.46	0.14	0.16	0.26
Median	3.18	0.67	0.89	1.73
Maximum	12.84	2.11	2.46	8.44
IQR	4.97	1.19	0.67	3.83
Milky Way	2.83	1.48	1.00	0.36

It is worth noting that the bulk of cluster and GC formation is dominated by the intermediate and metal-rich subsamples, indicating that the parent samples are better described by those subpopulations. A word of caution is warranted, as the lack of a treatment for the cold ISM discussed in Section 2 leads to the underdisruption of clusters in low-pressure environments, and thus, to an artificially high survival rate of the more metal-rich clusters. The metallicity range considered mitigates against that to some extent, but spurious contamination might still exist.

Using our metallicity subsample definitions, the Milky Way has $\sim 1.5 \times 10^7$, $\sim 1 \times 10^7$, and $\sim 3.6 \times 10^6 M_{\odot}$ in metal-poor, intermediate, and metal-rich GCs,⁶ respectively, which indicates that the early stages of cluster formation were more efficient at forming massive clusters that remained gravitationally bound for a Hubble time. Across our 25 present-day Milky Way-mass simulations, we form a median of $\sim 6.7 \times 10^6 M_{\odot}$ in metal-poor GCs, $\sim 8.9 \times 10^6 M_{\odot}$ in intermediate-metallicity GCs, and $\sim 1.7 \times 10^7 M_{\odot}$ in metal-rich GCs. The range of total GC masses

⁶We determine the cluster masses using the absolute visual magnitudes from Harris (1996), an assumed absolute visual magnitude for the Sun of $M_{V, \odot} = 4.83$ and a constant mass-to-light ratio of $M/L_V = 2 M_{\odot} L_{\odot}^{-1}$.

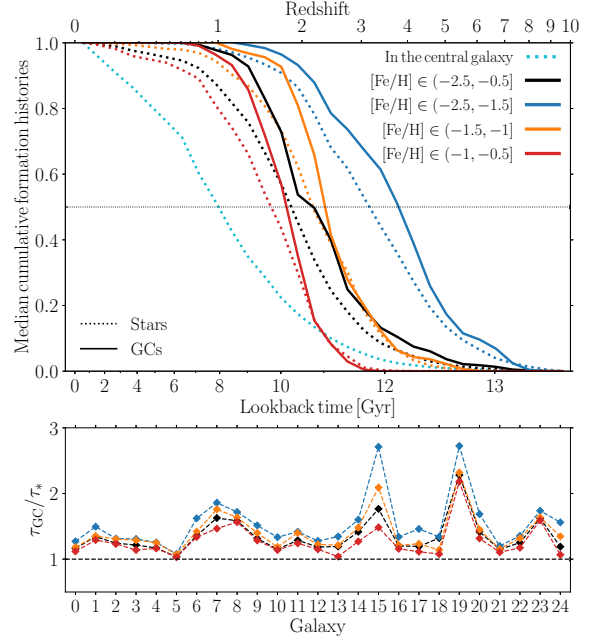


Figure 5. Comparison between different metallicity subsamples over our sample of 25 simulations: median cumulative formation histories of stars and GCs (*top*), median ages of GCs relative to those of all field stars across our galaxy sample (*bottom*).

at the present day in our simulations encompasses that of the Milky Way for all metallicity bins. Compared to our simulations, the metal-poor Milky Way GCs lie towards the top end of our total surviving masses, whereas the intermediate Milky Way GCs are well represented by our median total surviving mass and the metal-rich Milky Way GCs lie at the lower end (all values are listed in Table 2). As discussed before, our overprediction of the metal-rich GC mass is partially caused by the underdisruption of the youngest metal-rich GCs. At the same time, our galaxy sample encompasses a large variety of galaxy formation and assembly histories (Pfeffer et al. 2018; Kruijssen et al. 2019b), so our under- and overpredictions of the metallicity subsamples may also indicate that the metal-poor and intermediate (metal-rich) GC formation in the Milky Way was simply more (less) efficient than the metal-poor and intermediate (metal-rich) median GC formation of the typical galaxies in our galaxy sample.

In order to determine the median ages of the different metallicity subsamples, we determine the median cumulative formation histories of the different metallicity subsamples of stars and GCs over our sample of 25 galaxies (Fig. 5 top). As previously discussed, the different metallicity subsamples describe a continuum of star and cluster formation, where increasingly more metal-rich subsamples form later in time. Metal-poor GCs form half their mass ~ 12.1 Gyr ago ($z \simeq 4$), around 1 Gyr older than the intermediate and parent GC samples and ~ 2 Gyr older than the metal-rich subsample. Recent work predicts formation epochs for metal-poor and metal-rich GCs of $3 < z < 5$ and $1.7 < z < 2.1$, respectively, consistent with our results but obtained using a more simplistic description of galaxy and GC formation and evolution (Choksi, Gnedin & Li 2018). Fig. 5 shows that, in our simulations, the parent sample of GCs is dominated at early epochs ($3 < z < 4$) by the intermediate metallicity subsample, such that their half-mass formation times

Table 3. Median ages of the stars, clusters, and different GC subsamples across our sample of 25 Milky Way-mass galaxies for the fiducial cluster formation physics. From left to right, the columns describe the median ages of all stars belonging to the central galaxy, of clusters and GCs with metallicities in the range $[\text{Fe}/\text{H}] \in (-2.5, -0.5]$, of blue GCs, intermediate and red GCs ($[\text{Fe}/\text{H}] \in (-2.5, -1.5], (-1.5, -1.0], (-1.0, -0.5]$), relative ages of the general, blue, intermediate, and red GC subsamples over the stellar population, and the relative ages of blue over red GCs. All ages refer to lookback times in Gyr. We also include the minimum, median, maximum, and IQR of each column at the bottom.

Name	τ_* [Gyr]	τ_{cl} [Gyr]	τ_{GC} [Gyr]	$\tau_{\text{GC, b}}$ [Gyr]	$\tau_{\text{GC, i}}$ [Gyr]	$\tau_{\text{GC, r}}$ [Gyr]	τ_{GC}/τ_*	$\tau_{\text{GC, b}}/\tau_*$	$\tau_{\text{GC, i}}/\tau_*$	$\tau_{\text{GC, r}}/\tau_*$	$\tau_{\text{GC, b}}/\tau_{\text{GC, r}}$
MW00	9.37	10.64	10.92	11.92	11.08	10.49	1.17	1.27	1.18	1.12	1.14
MW01	8.10	10.45	10.88	12.11	10.95	10.46	1.34	1.49	1.35	1.29	1.16
MW02	9.27	10.42	11.52	12.17	12.10	11.42	1.24	1.31	1.31	1.23	1.07
MW03	9.14	10.39	11.10	11.95	11.77	10.41	1.22	1.31	1.29	1.14	1.15
MW04	9.76	10.81	11.43	12.25	12.20	11.37	1.17	1.25	1.25	1.16	1.08
MW05	11.49	11.85	11.91	12.41	12.32	11.83	1.04	1.08	1.07	1.03	1.05
MW06	7.58	10.21	10.30	12.30	10.77	10.15	1.36	1.62	1.42	1.34	1.21
MW07	6.55	8.83	10.65	12.17	11.52	9.59	1.63	1.86	1.76	1.47	1.27
MW08	7.56	8.95	11.97	12.98	12.36	11.82	1.58	1.72	1.64	1.56	1.10
MW09	7.83	9.98	10.28	11.85	10.94	10.06	1.31	1.51	1.40	1.29	1.18
MW10	8.80	10.11	10.13	11.74	10.43	10.03	1.15	1.33	1.19	1.14	1.17
MW11	8.34	8.17	10.73	11.82	11.68	10.34	1.29	1.42	1.40	1.24	1.14
MW12	8.86	10.28	10.49	11.32	10.85	10.19	1.18	1.28	1.22	1.15	1.11
MW13	9.31	10.32	11.10	12.51	11.28	9.67	1.19	1.34	1.21	1.04	1.29
MW14	7.36	9.41	10.43	11.78	10.89	9.34	1.42	1.60	1.48	1.27	1.26
MW15	4.47	7.12	7.90	12.13	9.36	6.64	1.77	2.71	2.09	1.48	1.83
MW16	9.20	9.87	11.06	12.32	11.15	10.65	1.20	1.34	1.21	1.16	1.16
MW17	7.73	9.09	9.22	11.28	9.52	8.60	1.19	1.46	1.23	1.11	1.31
MW18	9.42	9.70	12.45	12.63	10.74	10.15	1.32	1.34	1.14	1.08	1.24
MW19	4.27	7.60	9.73	11.62	9.89	9.30	2.28	2.72	2.32	2.18	1.25
MW20	7.20	8.67	10.19	12.15	10.45	9.48	1.42	1.69	1.45	1.32	1.28
MW21	10.27	11.20	11.80	12.33	11.86	11.35	1.15	1.20	1.16	1.11	1.09
MW22	8.36	9.53	10.46	11.32	11.03	9.81	1.25	1.35	1.32	1.17	1.15
MW23	6.96	9.92	11.29	12.08	11.38	11.08	1.62	1.74	1.64	1.59	1.09
MW24	7.86	9.20	9.36	12.27	10.60	8.39	1.19	1.56	1.35	1.07	1.46
Minimum	4.27	7.12	7.90	11.28	9.36	6.64	1.04	1.08	1.07	1.03	1.05
Median	8.34	9.92	10.73	12.13	11.03	10.15	1.25	1.42	1.32	1.17	1.16
Maximum	11.49	11.85	12.45	12.98	12.36	11.83	2.28	2.72	2.32	2.18	1.83
IQR	1.71	1.30	1.01	0.48	0.94	1.06	0.23	0.31	0.24	0.20	0.15

almost coincide. However, at later epochs, red GCs are the dominant GC subsample. Looking at the relative ages of the GC metallicity subsamples with respect to all field stars across our galaxy sample (Fig. 5 bottom), we find the expected relation between median age and subsample metallicity on a galaxy-to-galaxy basis, with metal-poor GCs being the oldest and the metal-rich GCs being the youngest. Across our sample, metal-poor GCs can be up to ~ 3 times older than the field stars, with significant variation between galaxies. Similar relations between GC age and metallicity have been extensively described in the literature (e.g. Brodie & Strader 2006; Beasley et al. 2008; Forbes & Bridges 2010; Dotter et al. 2011; VandenBerg et al. 2013; Forbes et al. 2015).

A commonly made assumption is that GCs are good tracers of the star formation history of spheroids, in the sense that major star-forming episodes are typically accompanied by significant GC formation (e.g. Brodie & Strader 2006). Given that most of the stellar mass in the local Universe lies in spheroids (Fukugita, Hogan & Peebles 1998), GCs are then considered to trace the bulk of star formation history in the Universe (Brodie & Strader 2006). Over our galaxy sample, we find that the parent GC sample only traces the parent stellar sample at very high redshift ($z \geq 6$), whereas for a given metallicity subsample, GCs trace their stellar counterpart until 20–40 per cent of their mass has formed (see Fig. 5). This would indicate that GCs better trace the very early stages of star formation rather than the bulk of it, implying that the conditions of

the early Universe are more favourable to GC formation than those at lower redshift. Note that this does not require any special physical mechanism for GC formation, but in E-MOSAICS arises due to the gradual change of the initial cluster demographics as a function of their natal galactic environment across cosmic time.

We determine the median ages of each population in all of our galaxies and list these quantities in Table 3. It is worth noting the large variety of ages in the GC metallicity subsamples of our galaxy sample; we find galaxies with coeval GC subsamples, but also galaxies with extended GC formation of up to ~ 6 Gyr between their blue and red subsamples. The former corresponds to MW05, a galaxy quenched ~ 11 Gyr ago with coeval populations of stars and the different GC metallicity subsamples, whereas the latter corresponds to MW15, a galaxy with increasing formation histories through its evolution, forming stars, and (increasingly more metal-rich) GCs until the present time. Its formation histories of stars, clusters, and GCs present a late ($z \simeq 0.2$ or ~ 1.6 Gyr ago) peak due to a merger, which causes this galaxy to have the youngest populations across our entire galaxy sample, except for the metal-poor GCs.

As discussed in Section 4, the median age of the massive ($M > 10^5 M_{\odot}$) GCs in the Milky Way within our parent metallicity range is 12.2 Gyr, which lies towards the old end of the range of parent GC ages, and there is only one galaxy in our sample which forms the parent GC sample earlier than the Milky Way. This again indicates

5848 *M. Reina-Campos et al.*

that the Milky Way assembled very early compared to the galaxies in our sample (e.g. Haywood et al. 2013; Snaith et al. 2014, 2015; Mackereth et al. 2018; Kruijssen et al. 2019a).

If we now focus on the interquartile ranges (IQRs) of the median ages across our galaxy sample, we find that the median ages of stars have the largest dispersion, indicating a large variety of star formation histories among our galaxy sample. By contrast, among the GC subsamples the metal-poor (metal-rich) have the smallest (largest) IQRs. Contrary to red GCs, blue, massive, surviving GCs form in a relatively narrow range of cosmic time, making them a suitable population for being used as a time reference. Forbes et al. (2015) determine GC ages over a sample of 11 early-type galaxies from the SLUGGS survey (Brodie et al. 2014). They find that the ages of metal-poor GC populations exhibit little scatter, which they argue indicates more uniformly old formation ages, whereas the ages of their metal-rich GC populations have a larger scatter, probably due to a range of formation histories. Our fiducial cluster model reproduces the observed scatter in the median ages of metal-poor and metal-rich GCs, but our median ages lie in the low end of their predictions. This is expected given that their more massive galaxies are expected to have formed and assembled earlier than Milky Way-mass galaxies like those in our sample.

The relative ages of the different GC metallicity subsamples (columns 8–11 in Table 3) imply a closer formation epoch of the red and the parent GC samples to the stellar population than the blue or intermediate GC subsamples. Therefore, metal-rich GCs ($-1 < [\text{Fe}/\text{H}] < -0.5$) are better tracers of the ages of field stars. We also quantify the age offset between the metal-poor and metal-rich GC subsamples (last column in Table 3). Blue GCs are, overall, a factor of 1.16 older than their red counterparts (corresponding to ~ 2 Gyr), and the galaxies in our sample range from nearly coeval GC subsamples to blue GCs being a factor of 1.83 older than their red counterparts. Given that blue GCs form roughly at the same moment in time across our galaxy sample, a range in these relative ages primarily reflects a range in formation epochs of red GCs. The formation of the red GC subsample requires a certain enrichment of the gas from which it forms, so older ages of this subpopulation trace a faster enrichment of the star-forming gas in the galaxy.

Following this idea, we can compare the median ages of our GCs subsamples with the slopes of the age–metallicity relations determined by Kruijssen et al. (2019b). They use the galaxy sample from E-MOSAICS to study how galaxy formation and evolution shape the age–metallicity distributions of GCs and consider the same metallicity range for GCs as in this work, so a direct comparison is possible. We find that those galaxies with large blue-to-red relative ages (i.e. a large age difference between metal-poor and metal-rich GCs) tend to have shallower slopes, whereas galaxies with small relative ages (age differences of ~ 1 Gyr) tend to have steeper age–metallicity slopes, thus confirming that relative ages between GC subsamples provide information about the enrichment of the gas in their host galaxies. Additionally, the relative age offset between blue and red GCs may potentially be used to trace the formation and assembly history of the host galaxy in the same way as the age–metallicity relations from Kruijssen et al. (2019b).

To explore in greater detail the relation between the median GC age and the subsample metallicity, we determine the median ages of GCs across our galaxy sample in overlapping bins of width 0.5 dex over our metallicity range $[\text{Fe}/\text{H}] \in (-2.5, -0.5]$ and present them as a function of their bin centre metallicities in Fig. 6. We show the 25th–75th percentiles as a shaded area and also show the median ages of massive ($M > 10^5 M_\odot$) Milky Way GCs in two metallicity bins.

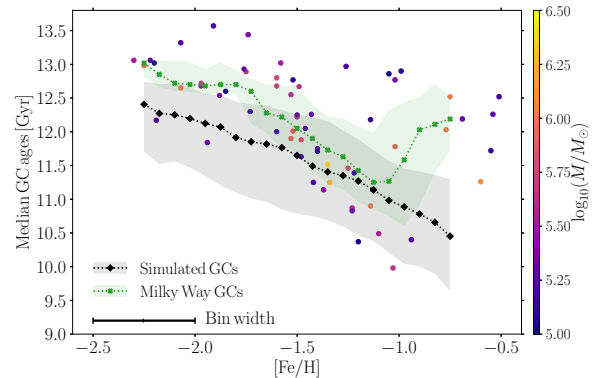


Figure 6. Median ages of different GC metallicity subsamples across our sample of 25 Milky Way-mass galaxies in overlapping metallicity bins. We use bins of 0.5 dex (black error bar in the legend) to contiguously scan the metallicity range between $[\text{Fe}/\text{H}] \in (-2.5, -0.5]$. We also show the ages of massive GCs ($M > 10^5 M_\odot$) in the Milky Way with metallicities $-2.5 < [\text{Fe}/\text{H}] < -0.5$, as well as their median ages in the same overlapping metallicity bins. The shaded regions correspond to the 25th–75th percentiles.

As we increase the GC metallicity centroid from $[\text{Fe}/\text{H}] = -2.25$ to $[\text{Fe}/\text{H}] = -0.75$, the median ages of the massive ($M > 10^5 M_\odot$) clusters surviving until the present time decrease from ~ 12.5 to ~ 10.5 Gyr. The dispersion in ages at each metallicity bin ranges between ~ 1 and 2 Gyr, indicating the rich variety of GC formation histories contained in our galaxy sample. The simulated GC populations reproduce the decreasing trend of the median ages of Milky Way GCs for metallicities $[\text{Fe}/\text{H}] < -1.0$, with the simulated median ages being ~ 0.5 Gyr younger than the Galactic GCs. This implies that the GC system in the Milky Way is most consistent with fast GC formation at early epochs. Similarly, the ages of metal-poor Galactic GCs agree better with the simulated GC populations than those of metal-rich ones ($[\text{Fe}/\text{H}] > -1.0$), indicating red GCs in the Milky Way formed earlier than the bulk of red GCs in our galaxy sample. This offset towards older ages supports the idea that the Milky Way formed and assembled at early cosmic times (e.g. Haywood et al. 2013; Snaith et al. 2014, 2015; Mackereth et al. 2018; Kruijssen et al. 2019a). Thus, the median ages of GC metallicity subsamples can be used to explore the continuous process of cluster formation across cosmic time.

An extensive body of current literature explores the idea that (metal-poor) GC formation is somehow related (or restricted) to the epoch of reionization (e.g. Moore et al. 2006; Griffen et al. 2010; Spitler et al. 2012; Corbett Moran, Teyssier & Lake 2014; Boylan-Kolchin 2018). These models populate dark matter-only haloes with GCs in a phenomenological fashion, and generally neither provide any demonstration that GC formation is related to reionization nor they include GC disruption in their analysis. We evaluate the role of reionization in (metal-poor) GC formation using the E-MOSAICS simulations, which have the advantage of populating galaxies with GCs in a self-consistent fashion and also including a model for their disruption, both of which are crucial for reproducing the observed GC population in the local Universe (see Section 3; Pfeffer et al. 2018; Usher et al. 2018; Hughes et al. 2019; Kruijssen et al. 2019b; Pfeffer et al. 2019a). During the epoch of reionization suggested by observations ($6 \lesssim z \lesssim 10$, Robertson et al. 2015), merely ~ 10 per cent of the metal-poor GC mass has formed across the 25 present-day Milky Way-mass galaxies present in our sample. By contrast, almost half the mass of the metal-poor GCs has formed

by $z \simeq 4$, and ~ 90 per cent by the peak of cosmic star formation ($z \simeq 2$, Madau & Dickinson 2014). Furthermore, GC formation extends to $z \simeq 1$ across our galaxy sample, long after the end of reionization. This result is in agreement with observational studies indicating that reionization preceded the bulk of GC formation (e.g. Forbes et al. 2015). Likewise, the agreement of the median ages of (metal-poor) GCs across our galaxy sample with those from the Milky Way reinforces the idea that metal-poor GC formation continued well after the end of reionization. We note that EAGLE implements a simplified version of reionization at $z = 11.5$ for hydrogen (Schaye et al. 2015), so even though it is modelled, GC formation occurs in galaxies where this extra heating is not relevant, indicating reionization plays no role in the formation of (metal-poor) GCs.⁷

6 COMPARISON TO PREVIOUS WORKS

This work is not the first to use the GCFR or GC ages as proxies to test GC formation models. Previous studies also consider this topic, but their methodology for populating galaxies with clusters differs from the one used in the E-MOSAICS simulations. Here we briefly highlight the differences and similarities relative to these studies.

Regarding the way in which galaxies are populated with clusters, previous studies can be divided into three categories. First, some studies insert GCs in dark matter-only simulations that are semi-analytically post-processed to include baryons (e.g. Beasley et al. 2002; Muratov & Gnedin 2010; Griffen et al. 2013; Choksi & Gnedin 2018; Choksi et al. 2018; El-Badry et al. 2019). These studies consider a simple description of cluster formation and a partial description of cluster evolution due to evaporation (except for Beasley et al. 2002 and El-Badry et al. 2019, which do not consider disruption). One limitation of these models is the lack of spatial information, which requires making additional assumptions to describe the influence of the cosmological environment on the cluster population. Secondly, some studies identify possible sites of GC formation in hydrodynamical cosmological simulations (e.g. Renaud et al. 2017). These studies often consider a phenomenological description of GC formation, and despite the detailed spatial information available in these simulations, they tend to disregard cluster disruption. Lastly, high-resolution simulations are capable of resolving the cold gas flows within galaxies that lead to massive cluster formation (Kim et al. 2018; Li, Gnedin & Gnedin 2018), but their tremendous numerical cost limits the cosmic time these simulations can reach, which complicates the interpretation of the age distributions obtained. However, the major advantage of these simulations is that they can resolve the ISM and the destructive tidal perturbations that it causes in great detail.

Compared to those studies, the E-MOSAICS simulations populate the star particles with a sub-grid cluster population generated with a cluster formation model that reproduces the observed properties of young massive clusters in the local Universe (Adamo et al. 2015; Reina-Campos & Kruijssen 2017; Pfeffer et al. 2018; Kruijssen et al. 2019b; Pfeffer et al. 2019a). Using the three-dimensional spatial information of the distribution of matter around each star particle, we then track cluster disruption due to tidal shocks and two-body relaxation as the cluster population forms and evolves across cosmic time. The subgrid approach of E-MOSAICS enables

studying the formation and evolution of the entire cluster population. We find that GCs emerge self-consistently after having evolved over a Hubble time in a cosmological environment (Pfeffer et al. 2018; Kruijssen et al. 2019b).

In agreement with observations, previous models predict that GC form before the peak of cosmic star formation rate ($z \simeq 2$ or ~ 10 Gyr ago, Madau & Dickinson 2014), although the exact range in cosmic time depends on the details of the model. Semi-analytical descriptions of cluster formation with no or a simple description of cluster disruption predict that the cosmic GC formation rate peaks at $4 \lesssim z \lesssim 6$ (~ 12.3 – 12.9 Gyr ago, Muratov & Gnedin 2010) or at $3 \lesssim z \lesssim 5$ (~ 11.7 – 12.6 Gyr ago, e.g. Choksi & Gnedin 2018; El-Badry et al. 2019), respectively. These models also predict a systematic age offset between the GC metallicity subpopulations, with metal-poor GCs being older than the metal-rich subpopulation by 2–4 Gyr across the halo-mass range considered ($\sim 2 \times 10^{11}$ – $10^{14} M_{\odot}$, Choksi et al. 2018).

By tagging star particles to assign massive ($M > 10^5 M_{\odot}$) GC-like objects to a hydrodynamical zoom-in simulation,⁸ Renaud et al. (2017) obtain mean ages of 11.4 Gyr. The authors also obtain an age offset between the GC metallicity subpopulations, with the mean ages being 11.1 and 11.8 Gyr for the metal-poor and metal-rich GCs, respectively. These results should be interpreted with some caution, as Renaud et al. (2017) select as GCs only those clusters with ages > 10 Gyr at $z = 0$. This causes a bias towards older ages, as the mean age of all tagged particles in their simulations is just 7.9 Gyr.

In this work, we use the 25 present-day Milky Way-mass galaxies from the E-MOSAICS simulations to study how stars, clusters, and GCs form relatively to each other across cosmic time. We find that massive ($M > 10^5 M_{\odot}$) cluster formation with metallicities $[\text{Fe}/\text{H}] \in (-2.5, -0.5]$ peaks at $2 \lesssim z \lesssim 5$, and we also find that a natural age offset between the different GC metallicity subsamples arises from the gradual enrichment of the ISM from which GCs form, with its exact range depending on the assembly history of the host galaxy (Kruijssen et al. 2019b). These results are consistent with previous studies in which massive cluster formation is correlated with star formation (e.g. Choksi & Gnedin 2018; El-Badry et al. 2019). In addition, we find that the main mechanism driving the peak of massive ($M > 10^5 M_{\odot}$) cluster formation at high-redshift is the time evolution of the upper mass scale of the ICMF (see discussion in Section 3).

7 CONCLUSIONS

We explore the formation histories of stars, clusters, and GCs and how these are influenced by the environmental dependence of the cluster formation physics in the context of the E-MOSAICS simulations (Pfeffer et al. 2018; Kruijssen et al. 2019b). For that, we use the 10 galaxies described in Pfeffer et al. (2018) from the volume-limited galaxy sample of 25 present-day Milky Way-mass galaxies, using cluster formation models with a differing dependence on the environment (described in Section 2 and summarized in Table 1).

The median GC (here defined as $M > 10^5 M_{\odot}$ and $-2.5 < [\text{Fe}/\text{H}] < -0.5$) formation histories in all cluster formation models peaks at $z \simeq 2$ – 3 , roughly corresponding to the peak of cosmic

⁷For a more detailed discussion on whether GCs can be the sources of reionization in the context of the E-MOSAICS simulations, we refer the reader to Pfeffer et al. (2019b).

⁸This method of inserting GCs in a cosmological context is equivalent to the ‘no formation physics’ model considered in this work, which has been shown not to reproduce the observed properties of the Galactic GC population (this paper Pfeffer et al. 2018; Usher et al. 2018).

star formation history ($z \simeq 2$, Madau & Dickinson 2014). This implies that proto-GC formation sites are more likely to be easily observable in lensed galaxies at $z \simeq 2-3$ than at higher redshifts. However, the exact shape of the GCFR changes greatly between the different formation models. In those models with a fixed ICMF, more mass is contained in surviving massive ($M > 10^5 M_\odot$) clusters than in those where we consider the environmental dependence of the upper mass scale of the ICMF. Additionally, those models with a fixed CFE continue to form GCs until the present day, whereas those with an environmentally dependent CFE stop forming GCs with $[\text{Fe}/\text{H}] < -0.5$ at $z \simeq 1$. The combination of both effects causes our fiducial model to be the only one which reproduces both the total GC mass in the Milky Way and its lack of massive cluster formation with $[\text{Fe}/\text{H}] < -0.5$ at the present time.

Out of the cluster formation models considered, the ‘no formation physics’ model, in which both the CFE and the ICMF are fixed throughout cosmic time, is approximately equivalent to those studies that use ‘particle-tagging’ techniques to identify GCs in cosmological simulations (e.g. Tonini 2013; Renaud et al. 2017). We find that this cluster formation model continues to form GCs at a vigorous rate until the present time, which implies it overproduces the total GC mass in the Milky Way by a factor 5.5 relative to the mass formed in the fiducial model. Likewise, the continued formation of GCs in this model predicts the on-going formation of massive ($M > 10^5 M_\odot$) clusters with $[\text{Fe}/\text{H}] < -0.5$ should be observed in Milky Way-mass galaxies at $z = 0$. For these reasons, an environmentally independent cluster formation description is not compatible with observations.

The time evolution of the gas properties of galaxies implies a time evolution of the environmentally dependent cluster formation physics considered in our fiducial model. That is, as galaxies evolve and their inflow rates decline, they become less gas-rich, so a smaller fraction of stars is born in clusters that, in turn, are less likely to be massive or remain gravitationally bound over a Hubble time. For that reason, we expect the GC formation in our fiducial model to proceed mostly at earlier epochs, when high-gas pressure star-forming environments were more common.⁹ Indeed, GCs in our fiducial model form earlier than clusters and stars, both across our entire galaxy sample and on a galaxy-to-galaxy basis, with median ages that encompasses that of the GCs in the Milky Way (7.90–12.45 Gyr, Table 3). Similar ages have been obtained for nearby galaxies (e.g. Beasley et al. 2005 in M31 and Beasley et al. 2008 in NGC 5128). Therefore, the full environmental dependence of the CFE and upper mass scale of the ICMF considered in our fiducial model is crucial to reproduce the observed GC population in the local Universe. We find that the epoch of peak GC formation is predominantly determined by the time evolution of the ICMF truncation mass.

In order to evaluate the formation histories of GCs in different metallicity subsamples, we use the complete volume-limited sample of 25 Milky Way-mass galaxies from the E-MOSAICS simulations described by Kruijssen et al. (2019b). We find that GCs in non-overlapping, consecutive metallicity subsamples do not form isolated in time, but rather sample the continuous process of star and cluster formation. These subsamples exhibit a relation between their age of peak GC formation and subsample metallicity, with

⁹However, massive cluster formation in our fiducial model is not restricted to early cosmic times; starburst or interacting galaxies can host the high-gas pressure environments that lead to the formation of these massive objects (e.g. Schweizer & Seitzer 1998; Whitmore et al. 1999).

metal-poor GCs being the oldest ($z \simeq 4$ or ~ 12 Gyr ago) and metal-rich GCs being the youngest ($z \simeq 2$ or 10–11 Gyr ago). Similar age differences between the metal-poor and metal-rich GCs subsamples have been long determined in the literature (e.g. Brodie & Strader 2006; Hansen et al. 2013; Forbes et al. 2015) and, in combination with other observables (spatial distributions and kinematics), have been argued to indicate different formation mechanisms for these subsamples (e.g. Santos 2003; Griffen et al. 2010; Trenti et al. 2015). In this work we reproduce the observed ages of GCs in different metallicity subsamples without the need for different formation mechanisms.

We briefly explore the possible relation between (metal-poor) GCs and reionization, which has been invoked in the literature to drive the formation of the metal-poor GCs, and thus, explain their old ages (e.g. Moore et al. 2006; Griffen et al. 2010; Spitler et al. 2012; Corbett Moran et al. 2014; Boylan-Kolchin 2018; Creasey et al. 2018). By the end of reionization ($z = 6$), merely 10 per cent of the mass in metal-poor GCs has formed across our 25 Milky Way-mass simulations, indicating that reionization does not play a role in halting their formation in our models. Despite not having included an ad hoc mechanism to stop their formation, we reproduce the old ages of metal-poor GCs as well as the observed trend of ages with metallicities, where metal-poor GCs are the oldest and metal-rich GCs are the youngest.

We find that our sample of metal-poor GCs has a relatively narrow range of formation epochs, with a median age of 12.1 Gyr and an IQR of 0.5 Gyr, such that it can be used as an absolute reference time. Comparing them to the metal-rich GC subsample, we obtain significant scatter in their relative ages, indicating a large variety of metal-rich GC formation histories. From our metallicity subsamples, the metal-rich GCs best trace the ages of field stars across our simulations. This link between metal-rich GCs and field stars is consistent with extragalactic observations (e.g. M31: Jablonka et al. 2000, and NGC 1399: Forte, Faifer & Geisler 2005).

We predict how the ages of GCs vary with metallicity by determining the median ages of all GCs across our galaxy sample in overlapping metallicity bins of 0.5 dex in width. We find that choosing a metallicity for the GC population implies sampling a different moment of the GC formation history, and hence, the corresponding age measurement will be offset relative to the median age of the complete GC sample. The GCs contained in our most metal-poor bin ($[\text{Fe}/\text{H}] = -2.25$) are around ~ 2 Gyr older than those in our most metal-rich one ($[\text{Fe}/\text{H}] = -0.75$; the ages decrease from ~ 12.5 to ~ 10.5 Gyr). The GC ages within each metallicity bin have a scatter of 1–2 Gyr, which illustrates the large variety of GC formation histories contained in our galaxy sample. The offset between the median ages of metal-rich GCs in the Milky Way and the GCs contained in our metal-rich bins indicate the Milky Way formed and assembled its metal-rich population faster than the median present-day Milky Way-mass galaxy in our sample. Previous studies have also concluded that the Milky Way formed and assembled relatively quickly (e.g. Haywood et al. 2013; Snaith et al. 2014, 2015; Mackereth et al. 2018; Kruijssen et al. 2019a).

The ages of GCs have long been discussed as a key observable for understanding their relation with galaxy formation and evolution across cosmic time. Current observational age measurements carry large uncertainties (~ 1 Gyr in the Milky Way, several Gyr in other galaxies) due to caveats in the methods used, as well as technical limitations that currently complicate the further expansion of GC populations with age measurements. Future work is urgently required to overcome this problem and hopefully provide insight

into the co-formation and evolution of galaxies and their GC populations.

ACKNOWLEDGEMENTS

MRC is supported by a Fellowship from the International Max Planck Research School for Astronomy and Cosmic Physics at the University of Heidelberg (IMPRS-HD). MRC and JMDK gratefully acknowledge funding from the European Research Council (ERC) under the European Union's Horizon 2020 research and innovation programme via the ERC Starting Grant MUSTANG (grant agreement number 714907). JMDK gratefully acknowledges funding from the German Research Foundation (DFG) in the form of an Emmy Noether Research Group (grant number KR4801/1-1). JP and NB gratefully acknowledge funding from the ERC under the European Union's Horizon 2020 research and innovation programme via the ERC Consolidator Grant Multi-Pop (grant agreement number 646928). NB and RAC are Royal Society University Research Fellows. This work used the DiRAC Data Centric system at Durham University, operated by the Institute for Computational Cosmology on behalf of the STFC DiRAC HPC Facility (www.dirac.ac.uk). This equipment was funded by BIS National E-infrastructure capital grant ST/K00042X/1, STFC capital grants ST/H008519/1 and ST/K00087X/1, STFC DiRAC Operations grant ST/K003267/1, and Durham University. DiRAC is part of the National E-Infrastructure. The work also made use of high performance computing facilities at Liverpool John Moores University, partly funded by the Royal Society and LJMU's Faculty of Engineering and Technology. This work has made use of Numpy (van der Walt, Colbert & Varoquaux 2011) and Scipy (Jones et al. 2001), and all figures have been produced with the Python library Matplotlib (Hunter 2007). We thank an anonymous referee for a helpful report that improved the paper.

REFERENCES

Adamo A., Kruijssen J. M. D., Bastian N., Silva-Villa E., Ryon J., 2015, *MNRAS*, 452, 246
 Ashman K. M., Zepf S. E., 1992, *ApJ*, 384, 50
 Bastian N., 2008, *MNRAS*, 390, 759
 Beasley M. A., Baugh C. M., Forbes D. A., Sharples R. M., Frenk C. S., 2002, *MNRAS*, 333, 383
 Beasley M. A., Brodie J. P., Strader J., Forbes D. A., Proctor R. N., Barmby P., Huchra J. P., 2005, *AJ*, 129, 1412
 Beasley M. A., Bridges T., Peng E., Harris W. E., Harris G. L. H., Forbes D. A., Mackie G., 2008, *MNRAS*, 386, 1443
 Booth C. M., Schaye J., 2009, *MNRAS*, 398, 53
 Boylan-Kolchin M., 2018, *MNRAS*, 479, 332
 Brodie J. P. et al., 2014, *ApJ*, 796, 52
 Brodie J. P., Strader J., 2006, *ARA&A*, 44, 193
 Choksi N., Gnedin O. Y., 2018, *MNRAS*, 486, 331
 Choksi N., Gnedin O. Y., Li H., 2018, *MNRAS*, 480, 2343
 Corbett Moran C., Teyssier R., Lake G., 2014, *MNRAS*, 442, 2826
 Correa C. A., Wytthe J. S. B., Schaye J., Duffy A. R., 2015, *MNRAS*, 452, 1217
 Crain R. A. et al., 2015, *MNRAS*, 450, 1937
 Creasey P., Sales L. V., Peng E. W., Sameie O., 2019, *MNRAS*, 482, 219
 Dalla Vecchia C., Schaye J., 2012, *MNRAS*, 426, 140
 Davis M., Efstathiou G., Frenk C. S., White S. D. M., 1985, *ApJ*, 292, 371
 Dolag K., Borgani S., Murante G., Springel V., 2009, *MNRAS*, 399, 497
 Dotter A. et al., 2010, *ApJ*, 708, 698
 Dotter A., Sarajedini A., Anderson J., 2011, *ApJ*, 738, 74
 El-Badry K., Quataert E., Weisz D. R., Choksi N., Boylan-Kolchin M., 2019, *MNRAS*, 482, 4528

GC formation histories in E-MOSAICS 5851

Elmegreen B. G., 1997, in Franco J., Terlevich R., Serrano A., eds, *Revista Mexicana de Astronomia y Astrofisica Conference Series Vol. 6*. p. 165
 Fall S. M., Rees M. J., 1985, *ApJ*, 298, 18
 Fall S. M., Zhang Q., 2001, *ApJ*, 561, 751
 Forbes D. A., Bridges T., 2010, *MNRAS*, 404, 1203
 Forbes D. A., Brodie J. P., Grillmair C. J., 1997, *AJ*, 113, 1652
 Forbes D. A., Pastorello N., Romanowsky A. J., Usher C., Brodie J. P., Strader J., 2015, *MNRAS*, 452, 1045
 Forbes D. A. et al., 2018, *Proc. R. Soc. A*, 474, 20170616
 Forte J. C., Faifer F., Geisler D., 2005, *MNRAS*, 357, 56
 Fukugita M., Hogan C. J., Peebles P. J. E., 1998, *ApJ*, 503, 518
 Genzel R. et al., 2011, *ApJ*, 733, 101
 Gieles M., 2009, *MNRAS*, 394, 2113
 Gieles M., Portegies Zwart S. F., Baumgardt H., Athanassoula E., Lamers H. J. G. L. M., Sipiør M., Leenaarts J., 2006, *MNRAS*, 371, 793
 Griffen B. F., Drinkwater M. J., Thomas P. A., Helly J. C., Pimblet K. A., 2010, *MNRAS*, 405, 375
 Griffen B. F., Drinkwater M. J., Iliev I. T., Thomas P. A., Mellema G., 2013, *MNRAS*, 431, 3087
 Haardt F., Madau P., 2001, in Neumann D. M., Tran J. T. V., eds, *Clusters of Galaxies and the High Redshift Universe Observed in X-rays*. p. 64
 Hansen B. M. S. et al., 2013, *Nature*, 500, 51
 Harris W. E., 1991, *ARA&A*, 29, 543
 Harris W. E., 1996, *AJ*, 112, 1487
 Harris W. E., 2016, *AJ*, 151, 102
 Haywood M., Di Matteo P., Lehnert M. D., Katz D., Gómez A., 2013, *A&A*, 560, A109
 Holtzman J. A. et al., 1992, *AJ*, 103, 691
 Hughes M. E., Pfeffer J., Martig M., Bastian N., Crain R. A., Kruijssen J. M. D., Reina-Campos M., 2019, *MNRAS*, 482, 2795
 Hunter J. D., 2007, *Comput. Sci. Eng.*, 9, 90
 Jablonka P., Courbin F., Meylan G., Sarajedini A., Bridges T. J., Magain P., 2000, *A&A*, 359, 131
 Johnson L. C. et al., 2016, *ApJ*, 827, 33
 Jones E. et al., 2001, *SciPy: Open source scientific tools for Python*
 Kim J.-h. et al., 2018, *MNRAS*, 474, 4232
 Kravtsov A. V., Gnedin O. Y., 2005, *ApJ*, 623, 650
 Kruijssen J. M. D., 2012, *MNRAS*, 426, 3008
 Kruijssen J. M. D., 2014, *Class. Quantum Gravity*, 31, 244006
 Kruijssen J. M. D., 2015, *MNRAS*, 454, 1658
 Kruijssen J. M. D., Pelupessy F. I., Lamers H. J. G. L. M., Portegies Zwart S. F., Icke V., 2011, *MNRAS*, 414, 1339
 Kruijssen J. M. D., Pfeffer J. L., Reina-Campos M., Crain R. A., Bastian N., 2019a, *MNRAS*, 486, 3180
 Kruijssen J. M. D., Pfeffer J. L., Crain R. A., Bastian N., 2019b, *MNRAS*, 486, 3134
 Li H., Gnedin O. Y., 2018, *ApJ*, 486, 4030
 Li H., Gnedin O. Y., Gnedin N. Y., 2018, *ApJ*, 861, 107
 Li H., Gnedin O. Y., Gnedin N. Y., Meng X., Semenov V. A., Kravtsov A. V., 2017, *ApJ*, 834, 69
 Mackereth J. T., Crain R. A., Schiavon R. P., Schaye J., Theuns T., Schaller M., 2018, *MNRAS*, 477, 5072
 Madau P., Dickinson M., 2014, *ARA&A*, 52, 415
 Marín-Franch A. et al., 2009, *ApJ*, 694, 1498
 Messa M. et al., 2018, *MNRAS*, 477, 1683
 Miholics M., Kruijssen J. M. D., Sills A., 2017, *MNRAS*, 470, 1421
 Moore B., Diemand J., Madau P., Zemp M., Stadel J., 2006, *MNRAS*, 368, 563
 Muratov A. L., Gnedin O. Y., 2010, *ApJ*, 718, 1266
 Peebles P. J. E., Dicke R. H., 1968, *ApJ*, 154, 891
 Pfeffer J., Kruijssen J. M. D., Crain R. A., Bastian N., 2018, *MNRAS*, 475, 4309
 Pfeffer J., Bastian N., Kruijssen J. M. D., Reina-Campos M., Crain R. A., Usher C., 2019a, *MNRAS*, submitted
 Pfeffer J., Bastian N., Crain R. A., Kruijssen J. M. D., Hughes M. E., Reina-Campos M., 2019b, *MNRAS*, submitted
 Qu Y. et al., 2017, *MNRAS*, 464, 1659
 Reina-Campos M., Kruijssen J. M. D., 2017, *MNRAS*, 469, 1282

5852 *M. Reina-Campos et al.*

- Reina-Campos M., Kruijssen J. M. D., Pfeffer J., Bastian N., Crain R. A., 2018, *MNRAS*, 481, 2851
- Renaud F., Agertz O., Gieles M., 2017, *MNRAS*, 465, 3622
- Robertson B. E., Ellis R. S., Furlanetto S. R., Dunlop J. S., 2015, *ApJ*, 802, L19
- Santos M. R., 2003, *Extragalactic Globular Cluster Systems*, Springer-Verlag, p. 348
- Schaye J. et al., 2015, *MNRAS*, 446, 521
- Schaye J., Dalla Vecchia C., 2008, *MNRAS*, 383, 1210
- Schechter P., 1976, *ApJ*, 203, 297
- Schweizer F., Seitzer P., 1998, *AJ*, 116, 2206
- Snaith O., Haywood M., Di Matteo P., Lehnert M. D., Combes F., Katz D., Gómez A., 2015, *A&A*, 578, A87
- Snaith O. N., Haywood M., Di Matteo P., Lehnert M. D., Combes F., Katz D., Gómez A., 2014, *ApJ*, 781, L31
- Spitler L. R., Romanowsky A. J., Diemand J., Strader J., Forbes D. A., Moore B., Brodie J. P., 2012, *MNRAS*, 423, 2177
- Spitzer Jr. L., 1958, *ApJ*, 127, 17
- Springel V., 2005, *MNRAS*, 364, 1105
- Springel V., White S. D. M., Tormen G., Kauffmann G., 2001, *MNRAS*, 328, 726
- Strader J., Brodie J. P., Cenarro A. J., Beasley M. A., Forbes D. A., 2005, *AJ*, 130, 1315
- Tonini C., 2013, *ApJ*, 762, 39
- Trenti M., Padoan P., Jimenez R., 2015, *ApJ*, 808, L35
- Usher C. et al., 2012, *MNRAS*, 426, 1475
- Usher C., Pfeffer J., Bastian N., Kruijssen J. M. D., Crain R. A., Reina-Campos M., 2018, *MNRAS*, 480, 3279
- VandenBerg D. A., Brogaard K., Leaman R., Casagrande L., 2013, *ApJ*, 775, 134
- van der Walt S., Colbert S. C., Varoquaux G., 2011, *Comput. Sci. Eng.*, 13, 22
- Whitmore B. C., Zhang Q., Leitherer C., Fall S. M., Schweizer F., Miller B. W., 1999, *AJ*, 118, 1551
- Wiersma R. P. C., Schaye J., Smith B. D., 2009a, *MNRAS*, 393, 99
- Wiersma R. P. C., Schaye J., Theuns T., Dalla Vecchia C., Tornatore L., 2009b, *MNRAS*, 399, 574

This paper has been typeset from a \TeX/L\AA\TeX file prepared by the author.

Chapter 5

Dynamical cluster disruption and its implications for multiple population models in the E-MOSAICS simulations

Authors:

Marta Reina-Campos, J. M. Diederik Kruijssen,
Joel L. Pfeffer, Nate Bastian and Robert A. Crain

Published in *MNRAS* 481 (2018) 2851.

Reproduced with permission from the journal

Marta Reina-Campos is the principal author of this article. The original idea was discussed between Marta Reina-Campos and Dr. Kruijssen, and Marta Reina-Campos developed it and performed the analysis of the simulations. All authors collaborated in a weekly discussion on the project and Marta Reina-Campos produced all the figures and wrote the manuscript. All authors collaborated with corrections and suggestions to the manuscript, and Marta Reina-Campos performed the last improvements during the review process.



Dynamical cluster disruption and its implications for multiple population models in the E-MOSAICS simulations

M. Reina-Campos,¹★ J. M. D. Kruijssen¹,¹ J. Pfeffer,² N. Bastian² and R. A. Crain²

¹Astronomisches Rechen-Institut, Zentrum für Astronomie der Universität Heidelberg, Mönchhofstraße 12-14, D-69120 Heidelberg, Germany

²Astrophysics Research Institute, Liverpool John Moores University, 146 Brownlow Hill, Liverpool L3 5RF, UK

Accepted 2018 September 3. Received 2018 September 3; in original form 2018 May 31

ABSTRACT

Several models have been advanced to explain the multiple stellar populations observed in globular clusters (GCs). Most models necessitate a large initial population of unenriched stars that provide the pollution for an enriched population, and which are subsequently lost from the cluster. This scenario generally requires clusters to lose >90 per cent of their birth mass. We use a suite of 25 cosmological zoom-in simulations of present-day Milky Way mass galaxies from the E-MOSAICS project to study whether dynamical disruption by evaporation and tidal shocking provides the necessary mass-loss. We find that GCs with present-day masses $M > 10^5 M_{\odot}$ were only 2–4 times more massive at birth, in conflict with the requirements of the proposed models. This factor correlates weakly with metallicity, gas pressure at birth, or galactocentric radius, but increases towards lower GC masses. To reconcile our results with observational data, either an unphysically steep cluster mass-size relation must be assumed, or the initial enriched fractions must be similar to their present values. We provide the required relation between the initial enriched fraction and cluster mass. Dynamical cluster mass-loss cannot reproduce the high observed enriched fractions nor their trend with cluster mass.

Key words: stars: formation – globular clusters: general – galaxies: evolution – galaxies: formation – galaxies: star clusters: general.

1 INTRODUCTION

Over the past decades, both photometric and spectroscopic studies have indicated chemical anomalies in the stellar populations of globular clusters (GCs). The presence of multiple main sequences in the optical colour–magnitude diagrams of GCs (e.g. Bedin et al. 2004; Piotto et al. 2007; Milone et al. 2012; Piotto et al. 2015) suggest differences in helium content, whereas spectroscopic studies (e.g. Carretta et al. 2009; Gratton, Carretta & Bragaglia 2012; Carretta et al. 2015) have revealed anticorrelations in the chemical abundances of light-element species (Al, Na, N, C, and Mg). Most models aiming to explain the prevalence of multiple populations in GCs assume the formation of a first generation of stars, which rapidly pollute the clusters residual gas, from which a second generation of stars is born. The mechanism through which the medium is enriched is a question of ongoing debate and depends on the model considered. Some authors suggest AGB stars are the polluters (e.g. D’Ercole et al. 2008), whereas others consider stellar winds from fast rotating massive stars (FRMS; e.g. Krause et al. 2013), supermassive stars (SMSs; Denissenkov &

Hartwick 2014), or massive binaries (de Mink et al. 2009) to be the source of the medium enrichment. See Bastian & Lardo (2018) for a review.

These models encounter many observational challenges, but we will focus on two of them here. First, the proposed polluting stars make up only a small fraction of a standard stellar population due to the stellar initial mass function (IMF). However, the median observed fraction of enriched stars is ~64 per cent (Milone et al. 2017). Hence, in order to work, the models require that GCs were originally much more massive than today, and have lost >90–95 per cent of their initial masses. This is known as the *mass budget* problem and we will refer to the affected models as mass budget-limited (MBL). Secondly, we expect the fraction of the GC mass lost to be strongly environmentally dependent. However, observed fractions of enriched stars only increase with the GC mass and show no or little correlation with other quantities (Carretta et al. 2010; Conroy 2012; Bastian & Lardo 2015; Kruijssen 2015; Milone et al. 2017).

In this paper, we study whether dynamical cluster disruption mechanisms provide the mass-loss necessary to reproduce the observed enriched fractions and its variation with GC properties, and compare it to observational data. We also use our results to reverse-engineer what the initial enriched fraction must have been in order to reproduce the observed enriched fractions at the present day.

* E-mail: reina.campos@uni-heidelberg.de

2852 *M. Reina-Campos et al.*

2 DEPENDENCE OF CLUSTER MASS-LOSS ON THE GALACTIC ENVIRONMENT

We probe the dependence of cluster mass-loss on the galactic environment using the 25 cosmological zoom-in simulations from the E-MOSAICS project which focuses on the evolution of present-day Milky Way mass galaxies (defined by the halo mass range $11.86 < \log(M_{200}/M_{\odot}) < 12.38$; Kruijssen et al. 2018; Pfeffer et al. 2018). The E-MOSAICS project couples MOSAICS (MODelling Star cluster population Assembly In Cosmological Simulations; Kruijssen et al. 2011), a subgrid model for stellar cluster formation and evolution, to the EAGLE (Evolution and Assembly of GaLaxies and their Environments; e.g. Crain et al. 2015; Schaye et al. 2015) galaxy formation model. EAGLE is a suite of hydrodynamical simulations of galaxy formation in the Λ CDM cosmogony, evolved using a modified version of the N -body TreePM smoothed particle hydrodynamics (SPH) code GADGET-3 (Springel 2005). The suite of galaxies from the E-MOSAICS project are the first simulations to describe self-consistently the formation and evolution of stellar clusters in a cosmological context. In this project, stellar clusters are formed as a subgrid component of the stellar particles following an environmentally dependent cluster formation efficiency (Kruijssen 2012) and initial cluster mass function (Reina-Campos & Kruijssen 2017). The stellar clusters then lose mass due to stellar evolution (Wiersma et al. 2009), tidal shocking, and evaporation (Kruijssen et al. 2011). In addition, we apply destruction of the most massive GCs by dynamical friction in post-processing (see Kruijssen et al. 2018 and Pfeffer et al. 2018 for further details of the simulations). The philosophy behind E-MOSAICS is to describe the formation and evolution of GCs using the physical constraints obtained from observations of star formation, young massive clusters (YMCs), and GCs from low to high redshift.

Observations, theory, and simulations together show that the amount of cluster mass-loss is expected to depend on several factors (see Kruijssen 2015 for a detailed discussion). First, we expect a strong dependence on the cluster mass, i.e. massive clusters lose less mass than low-mass clusters. Secondly, three other factors have significant, but weaker effects. We expect a dependence on the gas pressure at birth, because higher pressure environments imply larger gas density contrasts (e.g. Vazquez-Semadeni 1994; Padoan et al. 2017), so stronger tidal interactions are expected that will generally lead to more efficient mass-loss due to tidal shocks. We also expect a dependence on galactocentric radius, because the tidal field strengths and gas pressure both decrease outwards. Finally, we expect a dependence on metallicity, because it traces the host galaxy mass (albeit with large scatter) and more massive galaxies are generally characterized by stronger tidal fields and higher gas pressures. The emergence of these dependencies is modelled self-consistently in E-MOSAICS.

The absence of an explicit model for the cold, dense phase of the interstellar medium in EAGLE, which is predicted to dominate the disruptive power of galaxies, implies an underestimation of cluster disruption in our simulations. Though this could present a major caveat for their use to estimate the true mass-loss of star clusters, Pfeffer et al. (2018) show that we obtain a reasonable estimate of disruption in high-pressure environments ($P k_B^{-1} > 10^6 \text{ K cm}^{-3}$). Therefore, we focus our analysis on old ($\tau > 6 \text{ Gyr}$) GCs born in these high-gas pressure environments, for which disruption is expected to be strongest and E-MOSAICS provides a good approximation of the total amount of mass-loss.

We determine the initial-to-present mass ratio of all stellar clusters with Milky Way-like metallicities ($[\text{Fe}/\text{H}] \in [-2.5, 0.5]$) that survive to the present time in each of our 25 galaxies, and we show

the results as a function of the present cluster mass in Fig. 1. At fixed cluster mass, we also determine the median mass ratio as a function of present galactocentric radius, cluster metallicity, and gas pressure at birth to investigate secondary dependencies. The hard cut at low masses in the top left-hand panel results from the minimum initial cluster mass ($M_{\text{cl}} \geq 5 \times 10^3 M_{\odot}$) adopted in E-MOSAICS for explicitly modelling the evolution of individual clusters.

Fig. 1 shows a steeply decreasing trend of the initial-to-present mass ratio as a function of the cluster mass for clusters more massive than $\gtrsim 10^4 M_{\odot}$, and weak trends in the expected direction with galactocentric radius, cluster metallicity, and gas pressure at birth for intermediate mass (10^3 – $10^5 M_{\odot}$) clusters. For the massive clusters ($M > 10^5 M_{\odot}$), the lack of a trend between the median initial-to-present mass ratio and all cluster properties other than its mass arises because these clusters lose little mass, of the order of a factor 2–5, as the relative mass-loss rate is inversely proportional to the cluster mass for a constant radius. As a result, most of the mass in high-mass clusters is lost due to stellar evolution. MBL multiple population models require a minimum initial-to-present mass ratio of $M_{\text{cl}}^{\text{init}}/M_{\text{cl}}^{\text{present}} \gtrsim 10$ to solve the mass budget problem. Given this constraint, only clusters with $M_{\text{cl}} < 10^5 M_{\odot}$ should exhibit the high observed enriched fractions (also see Kruijssen 2015), whereas observed enriched fractions increase with cluster mass (e.g. see fig. 2, left-hand panel in Milone et al. 2017).

3 OBSERVED FRACTION OF ENRICHED STARS

From the cluster mass-loss derived in the previous section, we can determine the fraction of enriched stars present in the cluster following two assumptions. First, the initial amount of enriched material predicted by stellar evolution is considered to be in the range $f_{\text{en}}^{\text{init}} \simeq 5$ –10 per cent (see Bastian & Lardo 2018). The exact value depends on the type of polluters, the stellar IMF, and the mass range considered. We assume it to be $f_{\text{en}}^{\text{init}} = 5$ per cent, but augmenting the value does not produce major differences. In order to solve the mass budget problem, MBL multiple population models assume that all cluster mass-loss is in the form of unenriched stars. With the aim of being conservative, we use the same assumption to determine the fraction of enriched stars in each of our surviving stellar clusters. To do that, we correct the initial-to-present mass ratio determined in the previous section for stellar evolutionary mass-loss, as it affects both populations equally if they have the same IMF. We examine the dependence of the fraction of enriched stars on galactic environment and compare it to recent observations.

Assuming both populations have the same IMF, we determine the fraction of enriched stars as

$$f_{\text{en}} = \frac{f_{\text{en}}^{\text{init}}}{(1 - f_{\text{en}}^{\text{init}}) (f_* M_{\text{cl}}^{\text{init}}/M_{\text{cl}})^{-1} + f_{\text{en}}^{\text{init}}}, \quad (1)$$

where $M_{\text{cl}}^{\text{init}}$ and M_{cl} are the initial and present cluster masses, $f_* = M_*/M_*^{\text{init}} \approx 0.4$ is a factor to correct for stellar evolutionary mass-loss for our adopted Chabrier IMF using $t = 10 \text{ Gyr}$, and $f_{\text{en}}^{\text{init}} = 5$ per cent is the assumed initial enriched fraction.

We present the obtained enriched fractions as a function of the cluster mass, and their medians at fixed cluster mass as a function of present galactocentric radius and metallicity in Fig. 2. In the left-hand panel, we include the observed relation from Milone et al. (2017). The authors determine the fraction of unenriched stars for 43 clusters and show them against the photometric cluster masses from

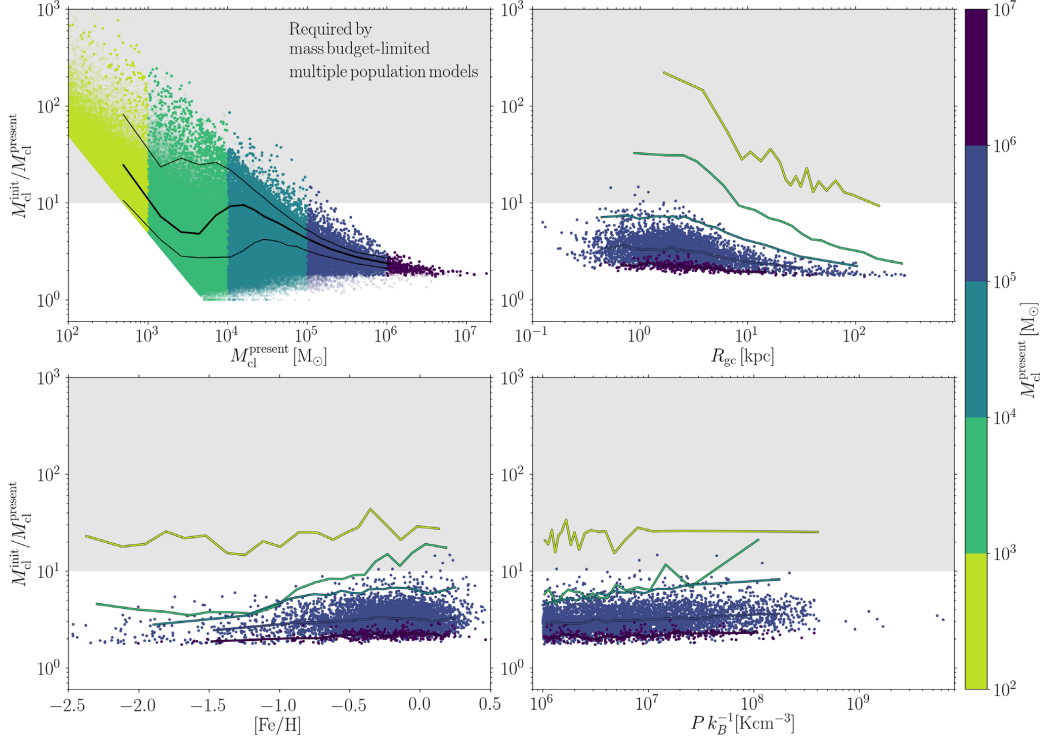


Figure 1. Initial-to-present cluster mass ratio as a function of present cluster mass (*top left*), present galactocentric radius (*top right*), cluster metallicity (*bottom left*), and gas pressure at birth (*bottom right*). All clusters with Milky Way-like metallicities ($[Fe/H] \in [-2.5, 0.5]$) that survive to the present time in our 25 haloes are included in the top left-hand panel, but only the most massive clusters ($M > 10^5 M_{\odot}$) are shown in the rest of panels. We emphasize the old ($\tau > 6$ Gyr) clusters born in high-pressure environments ($P k_B^{-1} > 10^6 K cm^{-3}$) in all the panels with opaque data points, whereas the rest are transparent and only appear in the top left-hand panel. The thick and thin solid lines in the top left-hand panel correspond to the median and the 1σ dispersion of the opaque data, whereas the solid lines in the rest of panels represent the fit obtained from Milone et al. (2017). The grey area indicates the mass-loss required by MBL multiple population models for solving the mass budget problem.

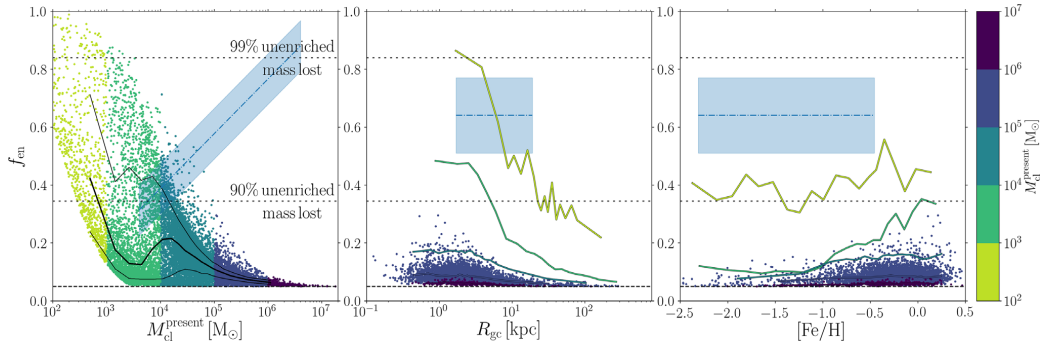


Figure 2. Fraction of enriched stars (equation 1) as a function of present cluster mass (*left*), present galactocentric radius (*middle*), and cluster metallicity (*right*). Data points and lines have the same meaning as in Fig. 1. The blue dash-dotted line and blue-shaded area in the left-hand panel correspond to a fiducial observed relation and the 1σ dispersion around the fit obtained from Milone et al. (2017), $f_{en} = 0.189 \log(M/MM_{\odot dot}) - 0.367$, whereas the blue dash-dotted line and blue-shaded area in the middle and right-hand panels correspond to the median enriched fraction and the 1σ dispersion around the median for the same cluster sample, respectively. The black dashed line corresponds to the initial enriched fraction $f_{en}^{init} = 5$ per cent typically assumed by MBL multiple population models. The upper and lower dotted black line corresponds to a 99 and 90 per cent mass-loss, respectively, in the form of unenriched stars.

2854 *M. Reina-Campos et al.*

McLaughlin & van der Marel (2005).¹ The GC sample of Milone et al. (2017) shows no trends of the enriched fraction with galactocentric radius or metallicity (see also Bastian & Lardo 2015 and Kruijssen 2015). The enriched fractions under the influence of dynamical mass-loss obtained from E-MOSAICS differ strongly from the observations, both in an absolute sense and in terms of its relation to the GC mass. The enriched fraction steeply declines with the present cluster mass and exhibits the expected trends with galactocentric radius and metallicity for intermediate mass (10^3 – $10^5 M_\odot$) clusters. Our derived enriched fractions rule out cluster mass-loss as the driving mechanism behind the observed trend; we find typical enriched fractions of 5–30 per cent, whereas observations find 50–75 per cent. In addition, the decreasing enriched fraction with increasing cluster mass predicted by MBL models contradicts the observed positive trend. The largest disagreement occurs at masses $M_{cl} \gtrsim 10^6 M_\odot$. These are observed to contain ~ 80 per cent of enriched stars, which would require them having lost ~ 99 per cent of their mass in the form of unenriched stars, but they lose less than a factor 2 in mass by dynamical disruption mechanisms.

4 RECONCILING MODELS AND OBSERVATIONS

The lack of agreement between the modelled and observed enriched fractions suggests changes to the current models for GC formation and evolution of the origin of multiple populations are needed to reconcile models and observations. First of all, we discuss whether the consideration of other cluster disruption mechanisms might provide the sufficient mass-loss to reproduce the (or lack of) observational trends. Alternatively, looking at equation (1), there are two possible ways in which the modelled and observed fractions may be reconciled. First, we consider whether the amount of mass lost in E-MOSAICS may not be correct. The main uncertainty in the mass-loss predicted by the E-MOSAICS disruption model is posed by the assumption of a constant cluster radius. Because mass-loss driven by tidal shocks depends on the cluster density, we can change the amount of mass-loss experienced by modifying the assumed mass-radius relation. Secondly, the adopted initial enriched fraction from stellar nucleosynthesis might be incorrect. We can use our results to derive what the initial amount of enriched material should be to match to the observational data. We now explore these possibilities.

4.1 Other cluster disruption mechanisms

A large body of literature explores which mechanisms influence cluster evolution, and finds that the dominant driver of mass-loss are tidal shocks with the substructure of the interstellar medium (e.g. Gieles et al. 2006; Kruijssen et al. 2011; Miholics, Kruijssen & Sills 2017; Pfeffer et al. 2018). In addition, in weaker tidal fields, clusters are mostly affected by two-body relaxation (Lamers, Baumgardt & Gieles 2010), so we consider these two mechanisms, along with stellar evolution and dynamical friction, as the sources of cluster mass-loss in E-MOSAICS.

In addition to the above, other disruption mechanisms have been invoked to solve the mass budget problem, with stellar evolution-driven expansion being the preferred mechanism. D’Ercole et al.

(2008) argue that only early mass-loss due to the expansion associated with supernovae would lead to a strong preferential loss of the unenriched population in massive ($M = 10^7 M_\odot$) stellar clusters. However, the efficiency of this mechanism depends on the cluster structure, IMF, and the initial degree of mass segregation. Tidally filling stellar clusters are mostly affected by stellar evolution-driven expansion mass-loss if they have a high degree of mass segregation, as stellar evolutionary mass-loss then lead to an enhanced flow of stars over the tidal boundary (Vesperini, McMillan & Portegies Zwart 2009). The amount of mass lost is roughly inversely proportional to the galactocentric radius, with a steeper dependence for primordially mass segregated clusters (Haghi et al. 2014), and presents a similar dependence as the one found for evaporation-driven mass-loss (Baumgardt & Makino 2003). The lack of a self-consistent model for this mechanism in the literature prevents its implementation in E-MOSAICS, but we can compare the relation between the expected mass-loss and galactocentric radius to our numerical results. Looking at the middle panel of Fig. 2, the addition of the mass lost due to stellar evolution-driven expansion would increase and steepen the enriched fractions, thus making the modelled fractions more incompatible with the constant observed fractions. Furthermore, in appendix D in Pfeffer et al. (2018) we test the amount of cluster disruption in our simulations and we find that compact ($r_h = 2.2$ pc) clusters with adiabatic expansion due to stellar evolution can double their sizes ($r_h = 3$ – 4 pc) in a short time-scale. This implies that, under the disruption mechanisms included in E-MOSAICS, these expanded clusters undergo the same mass-loss as clusters that are equally extended at birth, suggesting that adiabatic, stellar evolution-driven expansion is indistinguishable from the regular evolution of an already extended cluster. This indicates that stellar evolution-driven expansion is not the remaining mechanism that could help explain the required mass-loss to match observations.

4.2 Mass-radius relation required by the observations

The fiducial model in E-MOSAICS considers all clusters to have a constant half-mass radius of $r_h = 4$ pc, which means that the cluster density is solely controlled by its mass. From the dynamical disruption mechanisms considered in our model (i.e. evaporation and tidal shocking), the latter is dominant (e.g. Miholics et al. 2017; Pfeffer et al. 2018). Tidal shocks are inversely proportional to the cluster’s density (Spitzer 1958), so, at fixed mass, extended clusters are expected to lose more mass than their compact counterparts.

From our sample of 25 present-day Milky Way mass simulations, we run the halo MW05 with different cluster sizes that do not evolve with time ($r_h = 2, 4, 8, 16, 32,$ and 64 pc). We discard the simulations with radii of 32 and 64 pc, as disruption is so efficient that in total only 56 and 3 clusters are left, respectively. We show the maximum enriched fraction (which is analogous to the upper envelope in the left-hand panel of Fig. 2) of the old clusters born in a high-pressure environment as a function of the present cluster mass in Fig. 3 (left). Changing the cluster radii indeed affects the enriched fraction as expected; for a given cluster mass, extended clusters lose more mass, resulting in a higher enriched fraction.

Using the modelled enriched fractions for different radii and their intersection with the observed relation between the enriched fraction and the cluster mass in Fig. 3 (left), we derive the cluster mass-radius relation needed to reproduce the observed relation through cluster mass-loss. We show this mass-size relation in Fig. 3

¹Using the photometric rather than the dynamical cluster masses underestimates masses below $M_{cl} < 10^4 M_\odot$ due to dynamical effects (e.g. Kruijssen 2008). Changing to the dynamical cluster masses produces no effect in the observed trend.

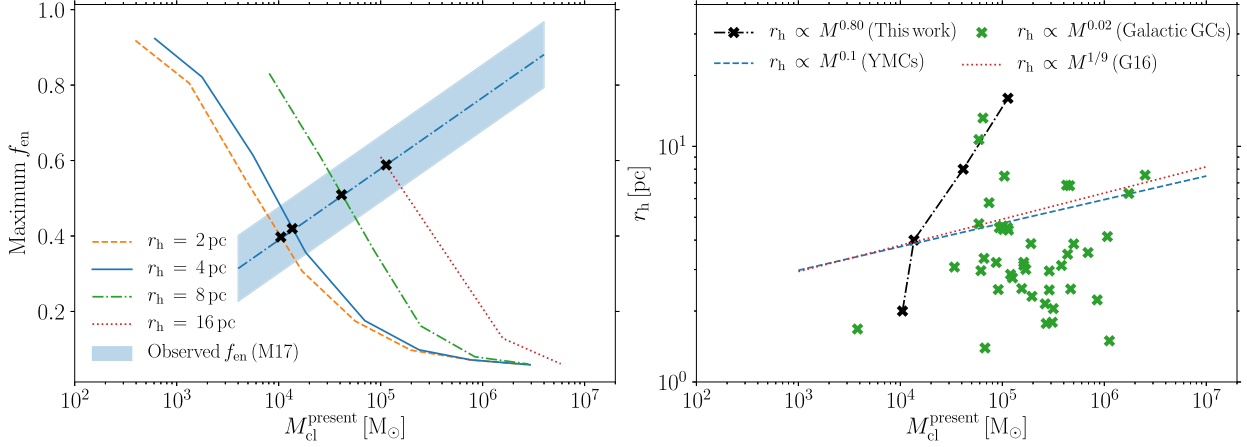


Figure 3. *Left:* Maximum enriched fraction of old clusters born in high-pressure environments as a function of the present cluster mass for simulations with different cluster sizes, assuming an initial enriched fraction of 5 per cent. As in Fig. 2 (a), the blue dash-dotted line and area are the fiducial relation and 1σ deviation from Milone et al. (2017). *Right:* Half-mass radius versus present cluster mass. The black dash-dotted line is our derived mass-radius relation needed to reproduce the observed relation in the left-hand panel through cluster mass-loss, whereas the dashed blue line is the mass-radius relation found for YMCs in Larsen (2004) and the green crosses represent the same GCs as in the Milone et al. (2017) sample (Harris 1996, McLaughlin & van der Marel 2005). The red dotted line represents the analytical mass-radius relation derived in Gieles & Renaud (2016) for the Galactic disc. All proportionalities are indicated in the legend.

(right), along with the observed mass-size relations for YMCs from Larsen (2004), for the GC sample in Milone et al. (2017) using the cluster sizes from Harris (1996) and the photometric cluster masses from McLaughlin & van der Marel (2005), and the theoretical relation from Gieles & Renaud (2016). The required mass-size relation has a much steeper slope than is supported by the observations. If we extrapolate this relation, a cluster of mass $M_{cl}^{present} = 10^6 M_{\odot}$ should have a half-mass radius of $r_h \sim 96$ pc, which is not observed.

Vanzella et al. (2017) observe a candidate proto-GC of mass $2-4 \times 10^6 M_{\odot}$ and effective radius $\simeq 20$ pc at $z = 6.145$, but this radius is likely overestimated due to protoclusters forming in larger structures (e.g. Longmore et al. 2014), that may be unresolved. Its size is an order of magnitude smaller than the half-mass radius required for cluster mass-loss to lead to the high observed enriched fractions, $r_h \sim 166-289$ pc.

The disproportionate sizes of massive clusters required to match the observed enriched fractions indicate that changing the cluster radii does not enable us to reconcile our results with the observations. This implies that cluster mass-loss is not responsible for the relation between enriched fraction and cluster mass.

4.3 Initial fraction of enriched stars

Current multiple population models assume an initial enriched fraction of 5–10 per cent (e.g. see section 5.4 in Bastian & Lardo 2018). The exact fraction depends on the polluter and the IMF, and assumes that all the polluted material is later on used to form enriched stars (i.e. 100 per cent efficiency in recycling the polluted material).

To explore whether we can reconcile the initial-to-present GC mass ratios from E-MOSAICS with the observed enriched fraction as a function of GC mass, we invert equation (1) to determine the

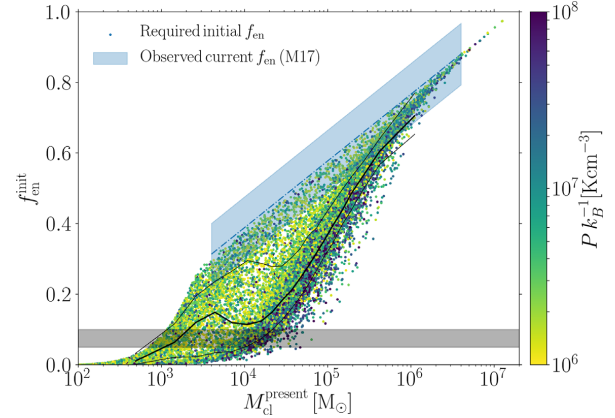


Figure 4. Required initial fraction of enriched stars as a function of the present cluster mass. Data points correspond to old ($\tau > 6$ Gyr) clusters born in high-pressure environments ($P k_B^{-1} > 10^6 \text{ K cm}^{-3}$), coloured by their gas pressure at birth. The grey area corresponds to the commonly assumed initial enriched fraction range of 5–10 per cent (Bastian & Lardo 2018).

required initial enriched fraction given the modelled mass-loss as,

$$f_{en}^{init} = \frac{f_{en}}{f_{en}(1 - f_{*}M_{cl}^{init}/M_{cl}) + f_{*}M_{cl}^{init}/M_{cl}}, \quad (2)$$

where f_{en} is the fiducial fit to the observed enriched fraction obtained from Milone et al. (2017). Fig. 4 shows the required initial enriched fraction as a function of the present cluster mass. Given the cluster mass-loss implied by E-MOSAICS, the commonly adopted initial enriched fraction of 5–10 per cent is only consistent with the observed enriched fraction for clusters with masses in

2856 *M. Reina-Campos et al.*

the range 10^3 – $10^4 M_{\odot}$. By contrast, the required initial enriched fraction for more massive clusters correlates with present cluster mass. This indicates that clusters with masses 10^5 – $10^6 M_{\odot}$ require initial enriched fractions of $f_{\text{en}}^{\text{init}} = 0.4$ – 0.7 to reproduce the relation from Milone et al. (2017) after their subsequent dynamical mass-loss. This range represents an order of magnitude departure from the commonly adopted initial enriched fractions in MBL models.

The disparity between the commonly used range and our results indicates that either different polluters have to be considered (i.e. that produce greater amounts of ejected material per unit cluster mass, e.g. SMSs, see Gieles et al. 2018) or some yet-to-be-understood physical processes in stellar evolution and/or star formation lead to the large (>0.4) enriched fractions.

5 DISCUSSION

We investigate whether dynamical mass-loss from GCs under realistic conditions satisfies the requirements from current multiple population models for reproducing the observed fractions of enriched stars in GCs. To do so, we use all surviving clusters present in the 25 present-day Milky Way mass galaxy simulations from the E-MOSAICS project (Kruijssen et al. 2018; Pfeffer et al. 2018). We determine the initial-to-present cluster mass ratios and study their dependence on cluster properties in Fig. 1. We find a steep decrease of the amount of mass lost with present cluster mass. For intermediate mass (10^3 – $10^5 M_{\odot}$) clusters, we also find significant trends of increasing mass-loss towards smaller galactocentric radii, higher gas pressures at birth, and higher cluster metallicities. More massive clusters show no dependence between their median mass ratio and these quantities due to their small amount of mass lost.

Assuming all dynamical mass-loss is in the form of unenriched stars, as posited by current multiple population models, we determine the enriched fraction of our stellar clusters. We study its dependence on cluster mass, metallicity, and galactocentric radius and compare it to observed enriched fractions from Milone et al. (2017) in Fig. 2. These mirror the dependencies found for the amount of mass-loss and fall below the observed fractions by a factor of 2–20, with an opposite dependence on GC mass. These severe discrepancies rule out cluster mass-loss as the driving mechanism behind the high observed enriched fractions.

In order to reconcile our results with observations, we consider what can be changed in models to match the observed enriched fractions. The addition of stellar evolution-driven expansion mass-loss, which is the preferred disruption mechanism suggested in the literature to solve the mass budget problem, predicts an even steeper trend between the numerical enriched fractions and galactocentric radius, in clear contrast with observations. These can only be reproduced if we consider an unphysically steep cluster mass-size relation, which indicates dynamical disruption mechanisms cannot account for the amount of mass-loss required by current multiple population models. We determine the initial amount of polluted material required to match our results with the observations. The commonly adopted range of $f_{\text{en}}^{\text{present}} = 5$ – 10 per cent is only valid for clusters with masses $M_{\text{cl}}^{\text{present}} \lesssim 10^3$ – $10^4 M_{\odot}$. At higher masses, initial enriched fractions of $f_{\text{en}} = 10$ – 80 per cent are required. We conclude that dynamical cluster disruption mechanisms are not capable of explaining the high-enriched fractions observed in GCs nor their positive trend with cluster mass. Hence, the present-day enriched fractions likely reflect their initial values, fundamentally

challenging most self-enrichment scenarios which are incapable of producing fractions above 10–20 per cent.

ACKNOWLEDGEMENTS

We thank the anonymous referee for their helpful comments and suggestions. MRC is supported by a PhD Fellowship from the International Max Planck Research School at the University of Heidelberg (IMPRS-HD). MRC and JMDK acknowledge funding from the European Research Council (ERC-StG-714907, MUSTANG). JMDK acknowledges funding from the German Research Foundation (DFG - Emmy Noether Research Group KR4801/1-1). NB and JP gratefully acknowledge financial support from the European Research Council (ERC-CoG-646928, Multi-Pop). This work used the DiRAC Data Centric system at Durham University, operated by the Institute for Computational Cosmology on behalf of the STFC DiRAC HPC Facility. This equipment was funded by BIS National E-infrastructure capital grant ST/K00042X/1, STFC capital grants ST/H008519/1 and ST/K00087X/1, STFC DiRAC Operations grant ST/K003267/1, and Durham University. DiRAC is part of the National E-Infrastructure. The work also made use of high performance computing facilities at Liverpool John Moores University, partly funded by the Royal Society and LJMU's Faculty of Engineering and Technology.

REFERENCES

- Bastian N., Lardo C., 2015, *MNRAS*, 453, 357
 Bastian N., Lardo C., 2018, *ARA&A*, 56
 Baumgardt H., Makino J., 2003, *MNRAS*, 340, 227
 Bedin L. R., Piotto G., Anderson J., Cassisi S., King I. R., Momany Y., Carraro G., 2004, *ApJ*, 605, L125
 Carretta E., Bragaglia A., Gratton R., Lucatello S., 2009, *A&A*, 505, 139
 Carretta E., Bragaglia A., Gratton R. G., Recio-Blanco A., Lucatello S., D'Orazi V., Cassisi S., 2010, *A&A*, 516, A55
 Carretta E. et al., 2015, *A&A*, 578, A116
 Conroy C., 2012, *ApJ*, 758, 21
 Crain R. A. et al., 2015, *MNRAS*, 450, 1937
 D'Ercole A., Vesperini E., D'Antona F., McMillan S. L. W., Recchi S., 2008, *MNRAS*, 391, 825
 de Mink S. E., Pols O. R., Langer N., Izzard R. G., 2009, *A&A*, 507, L1
 Denissenkov P. A., Hartwick F. D. A., 2014, *MNRAS*, 437, L21
 Gieles M., Renaud F., 2016, *MNRAS*, 463, L103
 Gieles M., Portegies Zwart S. F., Athanassoula E., Lamers H. J. G. L. M., Sipiør M., Leenaarts J., 2006, *MNRAS*, 371, 793
 Gieles M. et al., 2018, *MNRAS*, 478, 2461
 Gratton R. G., Carretta E., Bragaglia A., 2012, *A&AR*, 20, 50
 Haghi H., Hoseini-Rad S. M., Zonoozi A. H., Küpper A. H. W., 2014, *MNRAS*, 444, 3699
 Harris W. E., 1996, *AJ*, 112, 1487
 Krause M., Fierlinger K., Diehl R., Burkert A., Voss R., Ziegler U., 2013, *A&A*, 550, A49
 Kruijssen J. M. D., 2008, *A&A*, 486, L21
 Kruijssen J. M. D., 2012, *MNRAS*, 426, 3008
 Kruijssen J. M. D., 2015, *MNRAS*, 454, 1658
 Kruijssen J. M. D., Peluupessy F. I., Lamers H. J. G. L. M., Portegies Zwart S. F., Icke V., 2011, *MNRAS*, 414, 1339
 Kruijssen J. M. D., Pfeffer J. L., Crain R. A., Bastian N., 2018, *MNRAS*
 Lamers H. J. G. L. M., Baumgardt H., Gieles M., 2010, *MNRAS*, 409, 305
 Larsen S. S., 2004, *A&A*, 416, 537
 Longmore S. N. et al., 2014, *Protostars and Planets VI*. University of Arizona Press, Tucson, p. 291
 McLaughlin D. E., van der Marel R. P., 2005, *ApJS*, 161, 304
 Miholics M., Kruijssen J. M. D., Sills A., 2017, *MNRAS*, 470, 1421

Dynamical cluster mass-loss in E-MOSAICS 2857

- Milone A. P. et al., 2012, ApJ, 744, 58
Milone A. P. et al., 2017, MNRAS, 464, 3636
Padoan P., Haugbølle T., Nordlund Å., Frimann S., 2017, ApJ, 840, 48
Pfeffer J., Kruijssen J. M. D., Crain R. A., Bastian N., 2018, MNRAS, 475, 4309
Piotto G. et al., 2007, ApJ, 661, L53
Piotto G. et al., 2015, AJ, 149, 91
Reina-Campos M., Kruijssen J. M. D., 2017, MNRAS, 469, 1282
Schaye J. et al., 2015, MNRAS, 446, 521
Spitzer L., Jr, 1958, ApJ, 127, 17
Springel V., 2005, MNRAS, 364, 1105
Vanzella E. et al., 2017, MNRAS, 467, 4304
Vazquez-Semadeni E., 1994, ApJ, 423, 681
Vesperini E., McMillan S. L. W., Portegies Zwart S., 2009, ApJ, 698, 615
Wiersma R. P. C., Schaye J., Theuns T., Dalla Vecchia C., Tornatore L., 2009, MNRAS, 399, 574

This paper has been typeset from a $\text{\TeX}/\text{\LaTeX}$ file prepared by the author.

Chapter 6

The mass fraction of halo stars contributed by the disruption of globular clusters in the E-MOSAICS simulations

Authors:

Marta Reina-Campos, Meghan E. Hughes,
J. M. Diederik Kruijssen, Joel L. Pfeffer, Nate Bastian,
Robert A. Crain, Andreas Koch and Eva K. Grebel

Published in *MNRAS* 493 (2020) 3422.

Reproduced with permission from the journal

Marta Reina-Campos is the principal author of this article. The original idea was developed between Marta Reina-Campos and Dr. Kruijssen, and Marta Reina-Campos performed the calculations using the simulations. Most authors collaborated in a weekly discussion on the project. Dr. Bastian provided the comparison to observational data and Marta Reina-Campos produced all the figures and wrote the manuscript. All authors collaborated with corrections and suggestions to the manuscript, and Marta Reina-Campos performed the last improvements during the review process.



The mass fraction of halo stars contributed by the disruption of globular clusters in the E-MOSAICS simulations

Marta Reina-Campos¹,^{*} Meghan E. Hughes^{2,3}, J. M. Diederik Kruijssen¹,
Joel L. Pfeffer², Nate Bastian², Robert A. Crain², Andreas Koch¹
and Eva K. Grebel¹

¹*Astronomisches Rechen-Institut, Zentrum für Astronomie der Universität Heidelberg, Mönchhofstraße 12-14, D-69120 Heidelberg, Germany*

²*Astrophysics Research Institute, Liverpool John Moores University, 146 Brownlow Hill, Liverpool L3 5RF, UK*

³*European Southern Observatory, Karl-Schwarzschild-Straße 2, D-85748 Garching, Germany*

Accepted 2020 February 14. Received 2020 February 10; in original form 2019 October 10

ABSTRACT

Globular clusters (GCs) have been posited, alongside dwarf galaxies, as significant contributors to the field stellar population of the Galactic halo. In order to quantify their contribution, we examine the fraction of halo stars formed in stellar clusters in the suite of 25 present-day Milky Way-mass cosmological zoom simulations from the E-MOSAICS project. We find that a median of 2.3 and 0.3 per cent of the mass in halo field stars formed in clusters and GCs, defined as clusters more massive than 5×10^3 and $10^5 M_{\odot}$, respectively, with the 25–75th percentiles spanning 1.9–3.0 and 0.2–0.5 per cent being caused by differences in the assembly histories of the host galaxies. Under the extreme assumption that no stellar cluster survives to the present day, the mass fractions increase to a median of 5.9 and 1.8 per cent. These small fractions indicate that the disruption of GCs plays a subdominant role in the build-up of the stellar halo. We also determine the contributed halo mass fraction that would present signatures of light-element abundance variations considered to be unique to GCs, and find that clusters and GCs would contribute a median of 1.1 and 0.2 per cent, respectively. We estimate the contributed fraction of GC stars to the Milky Way halo, based on recent surveys, and find upper limits of 2–5 per cent (significantly lower than previous estimates), suggesting that models other than those invoking strong mass loss are required to describe the formation of chemically enriched stellar populations in GCs.

Key words: stars: formation – globular clusters: general – galaxies: evolution – galaxies: formation – galaxies: star clusters: general.

1 INTRODUCTION

Understanding the formation and evolution of massive, compact stellar clusters, also known as globular clusters (GCs), allow the reconstruction of the assembly history of their host galaxies (e.g. Forbes et al. 2018; Myeong et al. 2018; Kruijssen et al. 2019b; Massari, Koppelman & Helmi 2019). Over the past decade, several studies have used the presence of light-element abundance variations in GCs (characterized by a depletion in C, O, and Mg and an enhancement in N, Na, Al; e.g. Carretta et al. 2009; Piotto et al. 2015), along with a chemical-tagging technique, to identify stars in our Galaxy as candidates that may have formed in stripped or dissolved GCs. This technique has been applied to the inner Galaxy (Schiavon et al. 2017), as well as to halo field stars to reconstruct

the build-up of our Galaxy (e.g. Martell & Grebel 2010; Martell et al. 2011; Carollo et al. 2013; Martell et al. 2016; Koch, Grebel & Martell 2019). These latter studies find that ~ 1.4 – 2.6 per cent of halo field stars exhibit light-element abundance patterns resembling those of GCs. This suggests that, if GCs are the unique formation sites of chemically distinct stellar populations,¹ an upper limit of ~ 11 – 47 per cent of halo stars have originated in GCs, with the exact number depending on the details of the GC formation and evolution model, as well as the fraction of enriched-to-unenriched stars considered (Carretta 2016; Martell et al. 2016; Koch et al. 2019).

¹We use the terms ‘chemically distinct’ or ‘enriched’ stars interchangeably to refer to stars exhibiting the light-element abundance patterns resembling those of GCs, and we will refer to the stellar population without these chemical features as ‘unenriched’ or ‘primordial’.

* E-mail: reina.campos@uni-heidelberg.de

These fractions would imply that a considerable fraction of the stellar halo originated in disrupted or surviving GCs. However, recent observational studies suggest a different scenario for the formation of the Galactic stellar halo. By comparing the high blue straggler-to-blue horizontal branch stellar ratio in the stellar halo to the low ratios observed in GCs, Deason, Belokurov & Weisz (2015) argue that the different population ratios favour a scenario in which the Galactic stellar halo has been built up by a few, relatively massive dwarf galaxies. In addition, a large number of studies using data from the *Gaia* mission suggest that a large fraction of the inner Galactic stellar halo was contributed by a single satellite of mass $\sim 10^9 M_{\odot}$ that was accreted ~ 9 – 10 Gyr ago (*Gaia*-Enceladus/Sausage; e.g. Belokurov et al. 2018; Helmi et al. 2018; also see Kruijssen et al. 2019b). Recently, Conroy et al. (2019) find that the bulk of the stellar halo splits in discrete features in the orbital-chemical space, indicating that the majority of halo stars have assembled from tidally disrupted dwarf galaxies.

In a companion paper, we look at the mass contribution of GCs to the bulge in the suite of 25 present-day Milky Way-mass galaxies from the E-MOSAICS simulations (Pfeffer et al. 2018; Kruijssen et al. 2019a). We find that the disruption of GCs contributes between 0.3–14 percent of the bulge mass, in agreement with recent observational estimates (Hughes et al. 2020). With the aim of determining whether the disruption of GCs plays a prominent role in the build-up of stellar haloes, in this work we quantify the total mass contribution of clusters and GCs, as well as that of chemically enriched stars, to the stellar halo in the 25 Milky Way-mass galaxies from the E-MOSAICS suite, which we then compare with results obtained from recent observational studies.

2 SUMMARY OF THE E-MOSAICS SIMULATIONS

In order to determine the contribution of the dynamically disrupted mass from clusters and GCs to the build-up of the stellar halo, we use the 25 cosmological zoom-in simulations of present-day Milky Way-mass galaxies that are part of the E-MOSAICS suite. The MODelling Star cluster population Assembly In Cosmological Simulations (MOSAICS, Kruijssen et al. 2011; Pfeffer et al. 2018) within EAGLE (Evolution and Assembly of Galaxies and their Environments, Schaye et al. 2015, Crain et al. 2015) project combines a subgrid description of bound stellar cluster formation and evolution with a state-of-the-art galaxy formation model within the Λ -cold dark matter cosmogony. This enables a self-consistent study of the formation and co-evolution of galaxies and their stellar cluster populations, in which GCs emerge from the cluster population after a Hubble time of evolution. For a detailed description of the physical models adopted in E-MOSAICS and details of the simulations, we refer the reader to Pfeffer et al. (2018) and Kruijssen et al. (2019a). Here, we briefly summarize the most relevant prescriptions used.

Our description of cluster formation and evolution is as follows. Whenever a gas particle is converted to a stellar particle ($\sim 2.25 \times 10^5 M_{\odot}$), a cluster population forms within the stellar particle in a subgrid fashion. The properties of the cluster population are governed by the fraction of stellar mass forming in bound clusters (i.e. the cluster formation efficiency, Bastian 2008) and the shape of the initial cluster mass function. The cluster formation efficiency is determined using the model of Kruijssen (2012), which predicts a strong correlation with gas pressure that is also observed in nearby extragalactic systems (Adamo et al. 2015; Johnson et al.

2016). The initial cluster mass function is assumed to be a Schechter function with an environmentally dependent upper mass scale. This truncation mass is also predicted to increase with gas pressure (Reina-Campos & Kruijssen 2017), and it is found to reproduce observations of young massive clusters in the local Universe (Reina-Campos & Kruijssen 2017; Messa et al. 2018; Trujillo-Gomez, Reina-Campos & Kruijssen 2019). Once formed, the clusters are evolved alongside their host galaxies in a cosmological context. The stellar clusters lose mass due to stellar evolution (Wiersma et al. 2009), tidal shocks, two-body relaxation (Kruijssen et al. 2011), and dynamical friction (Pfeffer et al. 2018), the latter being necessarily applied in post-processing. Such a description for cluster formation and evolution has been found to reproduce a wide variety of observed cluster populations (Pfeffer et al. 2018, 2019b; Usher et al. 2018; Kruijssen et al. 2019a), as well as to predict links between the cluster population and its host galaxy (Kruijssen et al. 2019a; Hughes et al. 2019; Pfeffer et al. 2019a; Reina-Campos et al. 2019). For a comparison of the properties of the simulated GCs to those of the observed Galactic GC system, we refer the reader to fig. 2 in Kruijssen et al. (2019a).

3 MASS FRACTION OF HALO STARS FORMED IN GCs

In order to define the stellar halo of the central galaxy in our zoom-in simulations, we follow the same criteria described by Zolotov et al. (2009, see their section 2.1). Using the present-day information in our simulations, we first determine the angular momentum in the z -direction (i.e. perpendicular to the disc), J_z , of all stellar particles, and discard those that belong to the thin and thick discs, $J_z/J_{\text{circ}} \geq 0.5$ (Sales et al. 2012),² i.e. with angular momentum resembling that of a corotating circular orbit with similar orbital energy, J_{circ} . Once we select all stellar particles belonging to the spheroid ($J_z/J_{\text{circ}} < 0.5$), we distinguish between bulge and halo stars by considering a distance cut based on the half-mass stellar radius of each galaxy, $R_{1/2,*}$, which span between 2.78–10.22 kpc. Stars lying farther away than this radius and within 50 kpc, $R_{1/2,*} < r < 50$ kpc,³ are considered to belong to the halo and we determine its mass from the halo field stellar population. According to this definition, we measure stellar halo masses of a median $\sim 3.4 \times 10^9 M_{\odot}$ among our suite of galaxies, which decreases by a factor ~ 6 when restricted to a metallicity range typically used in chemical-tagging studies ($[\text{Fe}/\text{H}] \in [-1.8, -1.3]$, e.g. Koch et al. 2019). These masses are lower limits, as the EAGLE model is known to underpredict the peak of the ratio of stellar mass to halo mass of central galaxies (Crain et al. 2015).

With the aim of comparing our results with those obtained through the chemical-tagging technique, we define our cluster and GC populations to resemble those in which chemically-distinct stellar populations have been observed. Hence, we define stellar clusters to be more massive than $m_{\text{cl}}^{\text{init}} \geq 5 \times 10^3 M_{\odot}$ at birth,⁴ older than 2 Gyr (Martocchia et al. 2018), more metal-rich than

²Modifying this criterion to discard stars with $J_z/J_{\text{circ}} \geq 0.3$ to avoid the contamination of heated disc stars does not affect our estimate of the mass contributed by clusters and GCs to the stellar halo, thus implying that such contamination is negligible in our simulations.

³This outer limit is chosen in order to facilitate the comparison with observational studies (e.g. Koch et al. 2019).

⁴To reduce memory requirements, in E-MOSAICS we consider that stellar clusters less massive will experience short disruption timescales (shorter than 1 Gyr) and can be safely discarded at formation.

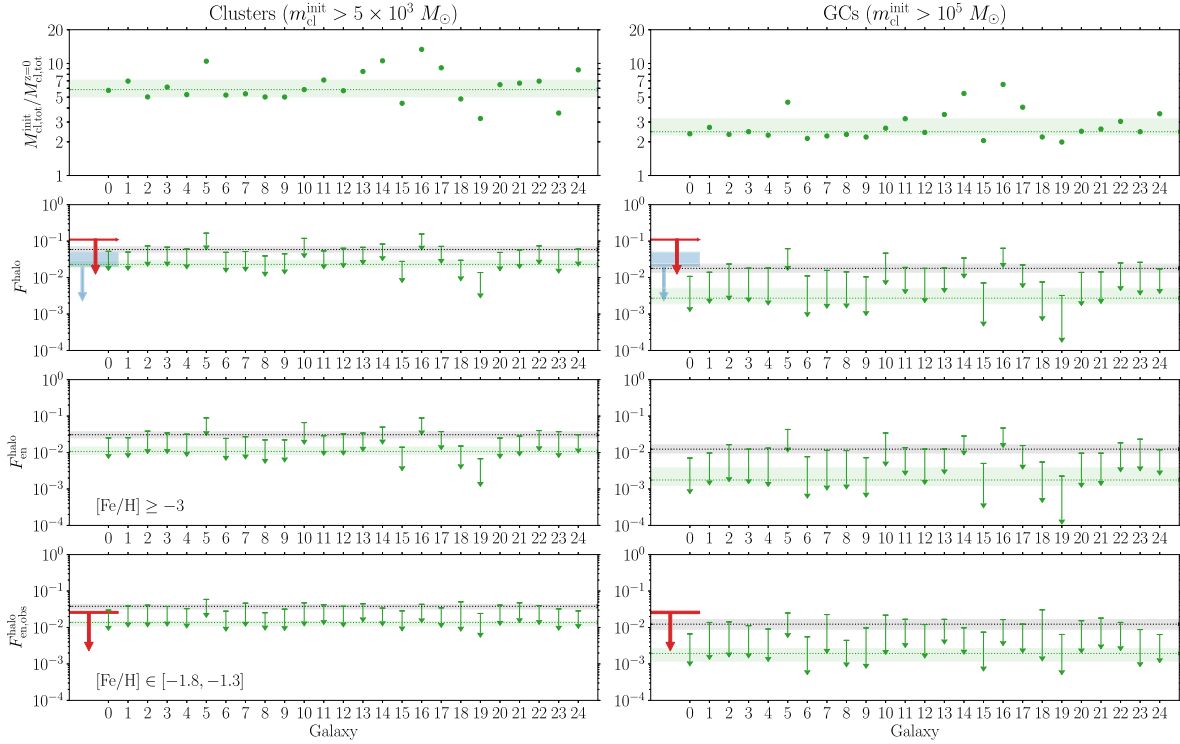


Figure 1. Total initial-to-present mass ratios of clusters and GCs (first row), mass fraction of halo stars contributed by clusters and GCs (second row), mass fraction of halo stars contributed by chemically distinct stars from clusters and GCs (third row), and mass fraction of halo stars contributed by chemically distinct stars from clusters and GCs matching the metallicity range of Koch et al. (2019) (fourth row) in each of our 25 present-day Milky Way-mass simulations. We define the stellar halo as described in the text, and define the cluster population to be older than 2 Gyr, more metal-rich than $[\text{Fe}/\text{H}] > -3$ dex, and part of the stellar halo. The GC population is also restricted to be more massive than $m_{\text{cl}}^{\text{init}} \geq 10^5 M_{\odot}$ at birth. In order to mimic observations, we restrict the metallicity range in the fourth row to $[\text{Fe}/\text{H}] \in [-1.8, -1.3]$ for the cluster and GC populations, and for the halo field stars. The upper limits correspond to the extreme case in which no cluster or GC survive to the present day. The horizontal dotted lines and the shaded regions indicate the median and the 25th–75th percentiles, respectively, of the arrow bases (top) and arrow heads (bottom), for each population over our galaxy sample. The red line and downward arrow shown in the second and fourth rows mark the derived upper limit of the mass fraction of halo stars contributed by GCs of ~ 11 per cent from Koch et al. (2019), and the observationally inferred fraction of chemically distinct stars in the Galactic halo (2.6 ± 0.2 per cent, Koch et al. 2019), respectively, whereas the blue box and downward arrow shown in the second row correspond to the revised observational upper limit of 2–5 per cent calculated in this work (see Section 4).

$[\text{Fe}/\text{H}] > -3$ dex and part of the halo as described above. In addition to that, we restrict the GC population to be more massive than $m_{\text{cl}}^{\text{init}} \geq 10^5 M_{\odot}$ at birth (Kruijssen 2015).

Our cluster and GC populations are affected by dynamical friction, which we apply in post-processing. We assume that *ex situ* objects disrupted by dynamical friction in their host dwarf galaxies contribute to the build-up of the stellar halo of the central galaxy when their host galaxy is accreted. On the contrary, *in situ* objects that disrupt due to dynamical friction are assumed to sink into the centre of the central galaxy, and their disrupted mass does not contribute to the build-up of the halo.

We determine the total final and initial masses in the cluster and GC populations for each of our simulations, and we show the resulting total initial-to-present mass ratios in the top row of Fig. 1. We find that the total numerically resolved cluster populations are a median ~ 5.8 times more massive at birth, but when restricting to massive clusters, the total initial GC populations are only a median ~ 2.5 times more massive than at the present day, in agreement with our earlier findings (Reina-Campos et al. 2018).

We then calculate the mass fraction of halo field stars contributed by clusters and by GCs as the relative contribution of the dynamically

disrupted mass to the mass of the stellar halo,

$$F^{\text{halo}} = \frac{\sum_i^{N_*} (M_{\text{cl},i}^{\text{init}} f_{*,i} - M_{\text{cl},i}^{z=0})}{M^{\text{halo}}}, \quad (1)$$

where $M_{\text{cl},i}^{\text{init}}$ and $M_{\text{cl},i}^{z=0}$ correspond to the total initial and final masses of the cluster population contained in the stellar particle i , $f_* = M_*/M_*^{\text{init}} \approx 0.4$ is a factor to correct for stellar evolutionary mass loss for our adopted Chabrier initial mass function using $t = 10$ Gyr, and M^{halo} corresponds to the total mass of the halo field stars. Due to the lack of an explicit model for the cold, dense gas of the interstellar medium in EAGLE, which is predicted to dominate the disruptive power of galaxies, cluster disruption is underestimated in E-MOSAICS (Pfeffer et al. 2018). This underdisruption occurs at all gas densities, but it is particularly important at high metallicities ($[\text{Fe}/\text{H}] > -1$ dex) since those clusters do not migrate from their birth environment (see appendix D in Kruijssen et al. 2019a). This implies that the mass fractions calculated using the dynamically disrupted mass from clusters and GCs are a lower limit, and we consider as an upper limit the extreme case in which no cluster or GC survives to the present day, i.e. all the initial mass in clusters and GCs is disrupted and contributes to the build-up of the halo. We

Table 1. Summary of the logarithm of the median mass fractions contributed to the stellar halo by clusters and GCs in the E-MOSAICS simulations shown in Fig. 1 as green dotted lines. From top to bottom, the rows correspond to the median mass fraction of halo stars contributed by clusters and GCs, the median mass fraction of halo stars contributed by chemically distinct stars from clusters and GCs, and the median mass fraction of halo stars contributed by chemically distinct stars from clusters and GCs matching the metallicity range of Koch et al. (2019) among our 25 present-day Milky Way-mass simulations. We also indicate the 25th–75th percentiles as lower and upper scripts, respectively.

	Clusters ($m_{\text{cl}}^{\text{init}} \geq 5 \times 10^3 M_{\odot}$)	GCs ($m_{\text{cl}}^{\text{init}} \geq 10^5 M_{\odot}$)
$\log_{10} F^{\text{halo}}$	$-1.64_{-1.73}^{-1.52}$	$-2.57_{-2.72}^{-2.29}$
$\log_{10} F_{\text{en}}^{\text{halo}}$	$-1.97_{-2.06}^{-1.85}$	$-2.75_{-2.91}^{-2.40}$
$\log_{10} F_{\text{en,obs}}^{\text{halo}}$	$-1.86_{-1.96}^{-1.82}$	$-2.71_{-2.93}^{-2.58}$

show these fractions for each of our simulations in the second row of Fig. 1.

We find that clusters contribute a median 2.3 per cent of mass to the stellar halo, whereas the GC populations present in our suite of simulations contribute a median 0.3 per cent of the mass in the stellar halo (with the 25–75th percentiles spanning 1.9–3.0 and 0.2–0.5 per cent, respectively, first row in Table 1). The mass fractions of halo stars contributed from clusters or GCs increase to a median 5.9 and a median 1.8 per cent among our suite of galaxies under the extreme assumption that no clusters survive to the present day, respectively, with the 25–75th percentiles spanning 4.9–7.6 and 1.4–2.4 per cent.

The scatter in the halo mass fraction contributed by GCs among our sample is caused by the differences in the formation and assembly history of each host galaxy. Two particularly noteworthy examples are galaxies MW16 and MW19, as they represent two very distinct cases. MW16 undergoes a rich history of mergers, as it is assembled from 38 distinct resolved progenitors with stellar masses $\gtrsim 4 \times 10^6 M_{\odot}$ (see table A.3 in Kruijssen et al. 2019a), and exhibits a peak in its GC formation rate and a steep GC age–metallicity relation, which lead to a GC population that is more massive than the median among our galaxy sample, both initially and at the present day. Its rich merger history also leads to a high degree of dynamical disruption. Although the stellar halo of this galaxy is the most massive among our galaxy sample, $M^{\text{halo}} \sim 10^{10} M_{\odot}$, the mass fraction of halo stars that formed in GCs in this galaxy is the highest among our suite of simulations, $F^{\text{halo}} \simeq 2$ –7 per cent for our two bracketing cases. By contrast, galaxy MW19 forms its stars primarily *in situ* and exhibits a shallower age–metallicity relation, and no significant peak in its GC formation rate (Kruijssen et al. 2019a). This leads to a GC population that is significantly less massive than the median, and a smaller mass fraction of halo stars that formed in GCs, about 0.02 per cent, which increases to 0.3 per cent under the extreme assumption that no GCs survive to the present day in the halo.

We can now use the observed relation between the fraction of chemically enriched stars and cluster mass from Milone et al. (2017) to predict the mass fraction of enriched stars contributed by clusters and GCs to the stellar haloes in our suite of simulations. Reina-Campos et al. (2018) suggest that, given the dynamical disruption mechanisms considered in E-MOSAICS, which are postulated to dominate cluster evolution, the observed positive correlation between the enriched fraction and cluster mass likely signifies the initial relation at the time the cluster was born. We thus assume that

the observed positive trend describes the initial enriched fraction in our clusters,

$$f_{\text{en}} = 0.189 \log_{10}(m/M_{\odot}) - 0.367, \quad (2)$$

with $m = m_{\text{cl}}^{\text{init}}$ being the initial cluster mass and calculate the total fraction of chemically distinct mass contributed by our cluster and GC populations to the stellar halo, $F_{\text{en}}^{\text{halo}}$, which we show in the third row of Fig. 1. We assume there is no preferential mass loss of the unenriched stellar population relative to the chemically enriched stars within the cluster, so both populations are lost at the same rate.⁵ We find that the cluster and GC populations in our suite of galaxies contribute a median 1.1 and 0.2 per cent of chemically distinct mass to the stellar halo, respectively, with the 25–75th percentiles ranging between 0.9–1.4 and 0.1–0.4 per cent (second row in Table 1).

We now restrict our cluster and GC populations, as well as our stellar haloes, to the same metallicity range typically used in chemical tagging studies ($[\text{Fe}/\text{H}] \in [-1.8, -1.3]$, e.g. Koch et al. 2019) and recalculate the total mass fraction of chemically distinct stars contributed by clusters and GCs to the stellar halo, $F_{\text{en,obs}}^{\text{halo}}$, which we show in the bottom row of Fig. 1 (the median values are listed in the bottom row of Table 1). We find that the medians of the recalculated fraction of chemically distinct stars do not change significantly relative to the metallicity-unrestricted case ($[\text{Fe}/\text{H}] > -3$ dex, third row in Fig. 1), but the scatter among our galaxy sample decreases.

In order to investigate the influence of the metallicity scale used in EAGLE in setting this result, as well as the decrease in the scatter, we explore the dependence of the mass fractions of chemically distinct halo stars contributed by clusters on the metallicity range considered in Fig. 2. To mimic observational studies, we consider the same metallicity range for both the cluster and GC populations and for the halo field stars. We find that, as the metallicity considered increases, the median mass fractions of chemically distinct halo stars among our suite of galaxies decrease, whereas the scatter in each metallicity bin increases. We also find that an offset of ± 0.3 dex in the metallicity scale of the EAGLE model would not change the metallicity-limited fractions (fourth row of Fig. 1); at metallicities of $[\text{Fe}/\text{H}] \leq -1$ dex, the mass fractions of chemically distinct stars in the halo exhibit a normalized interquartile range of ~ 0.4 , which increase to an order of magnitude larger at higher metallicities. Lastly, we find that the increase of the scatter towards large metallicities is caused by the age limit used to define our cluster and GC populations (ages older than 2 Gyr), which neglects the most recent star formation in the galaxy, in combination with lower values of CFE at high metallicities (fig. 3 in Pfeffer et al. 2018) that lead to a more stochastic process of cluster formation. As a result, if the observed fraction of enriched stars in the halo is made at the low end of the GC metallicity range, this can lead to an overestimation of the total mass contributed by GCs to the stellar halo.

4 COMPARISON TO THE MILKY WAY

Following our calculations of the mass fractions of halo stars contributed by clusters and by GCs, we now consider the suitability of the assumptions used by comparing our simulated fractions

⁵If there is preferential mass loss of the unenriched population, the mass fractions should be corrected by the ratio of chemically distinct-to-unenriched mass-loss rates, which would further decrease the simulated mass fractions.

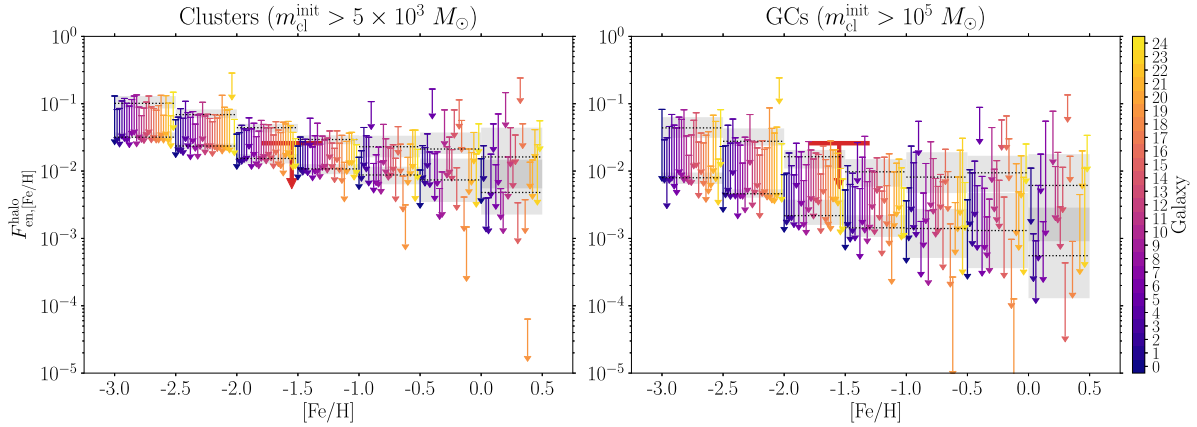


Figure 2. Mass fractions of halo stars contributed by chemically distinct stars from clusters (left-hand panel) and GCs (right-hand panel), as a function of metallicity in each of the 25 present-day Milky Way-mass galaxies of the E-MOSAICS simulations. In order to mimic observational studies, we consider the same metallicity range for both the cluster and GC populations and for the halo field stars. The upper limits correspond to the extreme case in which no cluster or GC survives in the stellar halo. For each metallicity bin, the dotted black lines and grey shaded regions indicate the median and 25–75th percentiles, respectively of the arrow bases (top) and arrow heads (bottom). The red lines and downward arrows correspond to the observationally inferred fraction of chemically distinct stars in the Galactic halo (2.6 ± 0.2 per cent, Koch et al. 2019).

with the observationally determined fraction of chemically enriched stars (e.g. Martell et al. 2016; Koch et al. 2019). In addition, we also explore the assumptions generally considered in observational studies to determine the total contribution of GCs to the stellar halo.

Observational studies work under the assumption that GCs are a unique site for the formation of chemically distinct stellar populations, and use the chemical signature observed (characterized by a depletion in C, O, and Mg as well as an enhancement in N, Na, and Al, e.g. Bastian & Lardo 2018) to estimate the mass fraction contributed by GCs (either currently still bound or fully disrupted) to the stellar halo of the Milky Way (e.g. Martell & Grebel 2010; Martell et al. 2011, 2016; Koch et al. 2019). A number of surveys have looked for stars with anomalous chemistry in samples of halo stars, mainly through either N or Na enhancement. Such an estimate naturally only corresponds to the contribution to the halo from clusters that host multiple populations, the presence of which appears to be related to the initial mass of the cluster, near $\sim 10^5 M_\odot$ (Kruijssen 2015; Reina-Campos et al. 2018). The results of these different approaches have been quite consistent, with authors finding between 1.4–2.6 per cent of halo stars showing N or Na-enhancement (e.g. Martell & Grebel 2010; Carretta et al. 2010; Koch et al. 2019).

Given that low-mass stars dominate the Chabrier stellar initial mass function used in E-MOSAICS by number, and assuming that the mean stellar mass of the unenriched and enriched stellar populations are the same, we convert the obtained mass fractions to number fractions by assuming that they are identical and compare our results with those obtained using the chemical-tagging technique. This way, we find that the metallicity-limited fractions of chemically distinct stars in the halo contributed by disrupted GCs (bottom right panel in Fig. 1) estimated in this work are consistent with the observational estimates (e.g. Martell et al. 2016; Koch et al. 2019), although perhaps a bit low. In contrast, assuming that chemically distinct stars can also form in low-mass stellar clusters (more massive than $5 \times 10^3 M_\odot$ at birth), we find that the mass fraction of chemically distinct stars in the halo exhibit better agreement with the observational results (bottom left panel in Fig. 1). This suggests that fully disrupted low-mass stellar clusters

might also exhibit stars with light-element inhomogeneities that are contributed to the stellar halo when the cluster dissolves.

In order to find the total contribution of GCs to the stellar halo, the observationally determined fraction of chemically distinct halo stars (e.g. Martell et al. 2016; Koch et al. 2019) needs to be corrected for the unseen primordial or unenriched stars with field-like abundances that are not detectable in such chemical-tagging surveys. In earlier works, this was done by adopting the heavy mass loss invoked in multiple population formation models (e.g. D’Ercole et al. 2008; Schaerer & Charbonnel 2011) in order to solve the ‘mass budget problem’ (see Bastian & Lardo 2018 for a recent review). This correction factor was largely unconstrained, resulting in estimates between 17–40 per cent for the mass fraction contribution of GC stars to the halo.

Koch et al. (2019) adopt a more physically motivated formalism to estimate the correction factor, using the constraint that GCs were (on average) only a factor 2 more massive than at present, as derived through comparisons of the index of the low-mass stellar mass function within GCs with cluster disruption models (e.g. Kruijssen & Mieske 2009; Webb & Leigh 2015). The authors also assume that all of the chemically enriched stars present in the halo are contributed from fully disrupted GCs, so that the existing GC population only lost unenriched stars to the halo. In addition, the authors assume that all GCs, regardless of their metallicity and orbit, contribute to the stellar halo. Under these assumptions, the authors estimate an upper limit of 11 per cent of the stellar halo is made up of stars formed originally in GCs.

However, Forbes et al. (2018) have estimated the total mass in existing GCs in the stellar halo, $2.6 \times 10^7 M_\odot$ (see also Kruijssen & Portegies Zwart 2009), as well as the total mass lost by each of these GCs ($2.5 \times 10^5 M_\odot$ on average, and a total of $2.5 \times 10^7 M_\odot$ for the ~ 100 halo GCs considered). They compared that to the total mass of the Galactic stellar halo ($1.5 \pm 0.4 \times 10^9 M_\odot$; Deason, Belokurov & Sanders 2019) and found that the total mass of enriched stars presently in GCs is $\sim 1.3 \times 10^7 M_\odot$ (assuming an enriched-to-total fraction of 50 per cent; this increases slightly if more realistic values, $f_{\text{en}} = 0.67$, are used). The fact that this is very close to the observed mass in halo field enriched stars ($1.4\text{--}2.6$ per cent $\times (1.5 \pm 0.4) \times$

$10^9 M_{\odot} = 1.5\text{--}4.9 \times 10^7 M_{\odot}$) suggests that the amount of mass loss from existing GCs is enough to explain the observed number of enriched stars in the halo under the assumption that both unenriched and enriched stars are lost at similar rates (also see Kruijssen 2015). This suggests that the original number of GCs was of the similar order of magnitude as the current one.

Such a conclusion is also supported by studies that have found that the present day fraction of enriched stars in GCs is representative of the initial fraction (e.g. Larsen, Strader & Brodie 2012; Bastian & Lardo 2015; Reina-Campos et al. 2018). If each present-day GC had a factor of 2–4 times more unenriched stars at birth than they currently do, this would represent a drastic difference from their present-day values and would be inconsistent with a number of observations and expectations (e.g. Bastian & Lardo 2018).

Under the assumption that the current population ratio, i.e. enriched-to-unenriched, is similar to the initial one, we would only need to correct the observed fraction of chemically distinct stars in the halo (1.4–2.6 per cent) for the population ratio between unenriched and enriched stars. Adopting a 50/50 ratio leads to 2.8–5.2 per cent, while adopting an enriched fraction of $f_{\text{en}} = 0.67$ (Milone et al. 2017) leads to fractions of 2.1–3.9 per cent of the Galactic stellar halo being contributed by GCs.⁶ This estimate remains unchanged if one posits that disrupted GCs (as opposed to dissolving GCs that still exist) are the main contributor of GC stars to the halo, as long as the enriched-to-unenriched ratio was similar in these clusters to that of existing GCs.

Finally, we note, following Koch et al. (2019), that these estimates are upper limits, as other processes (e.g. binary evolution) can lead to normal stars appearing as enriched stars. Hence, the likely contribution of GCs to the stellar halo is lower than the 2–5 per cent estimated here.

We can now compare these observational estimates to the mass fractions of halo stars dynamically lost from clusters and GCs in the E-MOSAICS simulations, which are shown in the second row of Fig. 1. We find that the simulated fractions of halo stars contributed by GCs are consistent with the revised observational upper limits of 2–5 per cent of the Galactic halo stars originating in GCs, implying that GCs play a subdominant role in the build-up of stellar haloes.

This result is in agreement with recent observational studies that suggest that the bulk of the Galactic stellar halo is assembled from tidally disrupted dwarf galaxies. Deason et al. (2015) argue that the relatively high ratio of blue stragglers to blue horizontal branch stars in the stellar halo is inconsistent with the low ratios observed in GCs, and suggests a scenario in which massive dwarfs are the dominant building blocks of the Galactic stellar halo. Moreover, a large number of studies using data from the *Gaia* mission suggest that the accretion of a single massive ($M \sim 10^9 M_{\odot}$) satellite $\sim 9\text{--}10$ Gyr ago could be the origin of the inner Galactic stellar halo (*Gaia*-Enceladus/Sausage; e.g. Belokurov et al. 2018; Helmi et al. 2018; also see Kruijssen et al. 2019b). In addition, recent observations of the Galactic halo find that the majority of the halo is composed by discrete features in orbital-chemical space, indicating that the bulk of the halo (or specifically ~ 70 per cent, see Mackereth & Bovy 2019) has assembled from the accretion of tidally disrupted dwarf galaxies (Conroy et al. 2019). Thus, the small fractions of halo stars contributed by GCs calculated in this

work using the E-MOSAICS simulations would also favour this formation scenario of the Galactic stellar halo.

5 SUMMARY

We use the 25 present-day Milky Way-mass cosmological zoom simulations from the E-MOSAICS project to quantify the total mass fraction, as well as the chemically distinct mass fraction, contributed to the stellar halo by clusters and GCs, and compare the results with recent observations.

We define our cluster and GC populations to resemble those in which light-element abundance variations have been observed. Thus, the halo cluster populations are defined to be older than 2 Gyr and more metal-rich than $[\text{Fe}/\text{H}] > -3$ dex. In order to reduce memory requirements in E-MOSAICS, only clusters initially more massive than $m_{\text{cl}}^{\text{init}} \geq 5 \times 10^3 M_{\odot}$ are evolved and considered in the numerically resolved cluster populations. In addition to these criteria, we consider as halo GCs those clusters more massive than $m_{\text{cl}}^{\text{init}} \geq 10^5 M_{\odot}$ at birth.

We find that the stellar haloes in our central galaxies contain a median 2.3 and 0.3 per cent of mass that formed as part of a cluster or a GC, with the 25–75th percentiles spanning 1.9–3.0 and 0.2–0.5 per cent, respectively. The scatter among our galaxy sample can be traced to differences in the assembly histories of the host galaxies (see Section 3). Using the observed positive correlation between the fraction of enriched stars and their cluster mass from Milone et al. (2017), we determine the mass fraction of the stellar halo contributed from disrupted clusters and GCs that would exhibit light-element abundance variations. We find that among our suite of galaxies, there is a median 1.1 and 0.2 per cent of mass in the stellar halo that is chemically enriched contributed by clusters and GCs, respectively. These small fractions imply that clusters and GCs play a subdominant role in the build-up of the stellar halo. This result is in agreement with recent studies that suggest that the Galactic stellar halo has assembled from tidally disrupted dwarf galaxies (e.g. Deason et al. 2015; Belokurov et al. 2018; Helmi et al. 2018; Conroy et al. 2019; Kruijssen et al. 2019b).

We also find that the mass fraction of chemically enriched stars in the halo contributed by clusters and GCs depends on the metallicity range considered, with decreasing fractions towards higher metallicity bins. As a result, if the observed fraction of enriched stars in the halo is made at the low end of the GC metallicity range, this can lead to an overestimation of the total mass contributed by GCs to the stellar halo.

Comparing our results to recent observational surveys, which use a chemical-tagging technique to identify chemically distinct stars in the halo and find typical upper limits between 1.4–2.6 per cent (e.g. Martell et al. 2016; Koch et al. 2019), we find that our predicted fractions of chemically distinct stars in the halo contributed by GCs are consistent with observations, although perhaps a bit low (fourth row in Fig. 1). This suggests that the amount of mass loss from surviving GCs is enough to explain the observed number of enriched stars in the halo under the assumption that both unenriched and enriched stars are lost at similar rates. Previous works have generally found good agreement between the properties of observed cluster populations and those simulated in E-MOSAICS (Pfeffer et al. 2018, 2019b; Usher et al. 2018; Kruijssen et al. 2019a). In this paper, we show that E-MOSAICS reproduces the observed fraction of chemically distinct stars in the Galactic halo, but only requires moderate mass loss from GCs to achieve this, with GCs having been 2–4 times more massive at birth (Reina-Campos et al. 2018). This suggests that models other than those requiring strong mass

⁶Defined as stellar clusters that host multiple populations, which we assume are those older than 2 Gyr, more metal-rich than $[\text{Fe}/\text{H}] > -3$ dex and more massive than $m_{\text{cl}}^{\text{init}} \geq 10^5 M_{\odot}$ at birth.

loss of unenriched stars are required to describe the formation of chemically enriched stellar populations in GCs.

ACKNOWLEDGEMENTS

MRC is supported by a Fellowship from the International Max Planck Research School for Astronomy and Cosmic Physics at the University of Heidelberg (IMPRS-HD). MRC and JMDK gratefully acknowledge funding from the European Research Council (ERC) under the European Union's Horizon 2020 research and innovation programme via the ERC Starting Grant MUSTANG (grant agreement number 714907). JMDK gratefully acknowledges funding from the German Research Foundation (DFG) in the form of an Emmy Noether Research Group (grant number KR4801/1-1). JP and NB gratefully acknowledge funding from the ERC under the European Union's Horizon 2020 research and innovation programme via the ERC Consolidator Grant Multi-Pop (grant agreement number 646928). NB and RAC are Royal Society University Research Fellows. EKG and AK acknowledge financial support from the Sonderforschungsbereich SFB 881 'The Milky Way System' (subprojects A03, A05, and A08) of the DFG with the Project-ID 138713538. This work used the DiRAC Data Centric system at Durham University, operated by the Institute for Computational Cosmology on behalf of the STFC DiRAC HPC Facility (www.dirac.ac.uk). This equipment was funded by BIS National E-infrastructure capital grant ST/K00042X/1, STFC capital grants ST/H008519/1 and ST/K00087X/1, STFC DiRAC Operations grant ST/K003267/1, and Durham University. DiRAC is part of the National E-Infrastructure. The work also made use of high performance computing facilities at Liverpool John Moores University, partly funded by the Royal Society and LJMU's Faculty of Engineering and Technology.

REFERENCES

Adamo A., Kruijssen J. M. D., Bastian N., Silva-Villa E., Ryon J., 2015, *MNRAS*, 452, 246
 Bastian N., 2008, *MNRAS*, 390, 759
 Bastian N., Lardo C., 2015, *MNRAS*, 453, 357
 Bastian N., Lardo C., 2018, *ARA&A*, 56, 83
 Belokurov V., Erkal D., Evans N. W., Koposov S. E., Deason A. J., 2018, *MNRAS*, 478, 611
 Carollo D., Martell S. L., Beers T. C., Freeman K. C., 2013, *ApJ*, 769, 87
 Carretta E., 2016, in Bragaglia A., Arnaboldi M., Rejkuba M., Romano D., eds, *IAU Symp. Vol. 317, The General Assembly of Galaxy Halos: Structure, Origin and Evolution*. Kluwer, Dordrecht, p. 97
 Carretta E., Bragaglia A., Gratton R., Lucatello S., 2009, *A&A*, 505, 139
 Carretta E., Bragaglia A., Gratton R. G., Recio-Blanco A., Lucatello S., D'Orazi V., Cassisi S., 2010, *A&A*, 516, A55
 Conroy C., Naidu R. P., Zaritsky D., Bonaca A., Cargile P., Johnson B. D., Caldwell N., 2019, *ApJ*, 887, 237
 Crain R. A. et al., 2015, *MNRAS*, 450, 1937
 D'Ercole A., Vesperini E., D'Antona F., McMillan S. L. W., Recchi S., 2008, *MNRAS*, 391, 825
 Deason A. J., Belokurov V., Weisz D. R., 2015, *MNRAS*, 448, L77
 Deason A. J., Belokurov V., Sanders J. L., 2019, *MNRAS*, 490, 3426
 Forbes D. A. et al., 2018, *Proc. R. Soc. Lond. Ser. A*, 474, 20170616

Helmi A., Babusiaux C., Koppelman H. H., Massari D., Veljanoski J., Brown A. G. A., 2018, *Nature*, 563, 85
 Hughes M. E., Pfeffer J., Martig M., Bastian N., Crain R. A., Kruijssen J. M. D., Reina-Campos M., 2019, *MNRAS*, 482, 2795
 Hughes M. E., Pfeffer J. L., Martig M., Reina-Campos M., Bastian N., Crain R. A., Kruijssen J. M. D., 2020, *MNRAS*, 491, 4012
 Johnson L. C. et al., 2016, *ApJ*, 827, 33
 Koch A., Grebel E. K., Martell S. L., 2019, *A&A*, 625, A75
 Kruijssen J. M. D., 2012, *MNRAS*, 426, 3008
 Kruijssen J. M. D., 2015, *MNRAS*, 454, 1658
 Kruijssen J. M. D., Mieske S., 2009, *A&A*, 500, 785
 Kruijssen J. M. D., Portegies Zwart S. F., 2009, *ApJ*, 698, L158
 Kruijssen J. M. D., Pelupessy F. I., Lamers H. J. G. L. M., Portegies Zwart S. F., Icke V., 2011, *MNRAS*, 414, 1339
 Kruijssen J. M. D., Pfeffer J. L., Crain R. A., Bastian N., 2019a, *MNRAS*, 486, 3134
 Kruijssen J. M. D., Pfeffer J. L., Reina-Campos M., Crain R. A., Bastian N., 2019b, *MNRAS*, 486, 3180
 Larsen S. S., Strader J., Brodie J. P., 2012, *A&A*, 544, L14
 Mackereth J. T., Bovy J., 2019, *MNRAS*, 492, 3631
 Martell S. L., Grebel E. K., 2010, *A&A*, 519, A14
 Martell S. L., Smolinski J. P., Beers T. C., Grebel E. K., 2011, *A&A*, 534, A136
 Martell S. L. et al., 2016, *ApJ*, 825, 146
 Martocchia S. et al., 2018, *MNRAS*, 473, 2688
 Massari D., Koppelman H. H., Helmi A., 2019, *A&A*, 630, L4
 Messa M. et al., 2018, *MNRAS*, 477, 1683
 Milone A. P. et al., 2017, *MNRAS*, 464, 3636
 Myeong G. C., Evans N. W., Belokurov V., Sanders J. L., Koposov S. E., 2018, *ApJ*, 863, L28
 Pfeffer J., Kruijssen J. M. D., Crain R. A., Bastian N., 2018, *MNRAS*, 475, 4309
 Pfeffer J., Bastian N., Crain R. A., Diederik Kruijssen J. M., Hughes M. E., Reina-Campos M., 2019a, *MNRAS*, 487, 4550
 Pfeffer J., Bastian N., Kruijssen J. M. D., Reina-Campos M., Crain R. A., Usher C., 2019b, *MNRAS*, 490, 1714
 Piotto G. et al., 2015, *AJ*, 149, 91
 Reina-Campos M., Kruijssen J. M. D., 2017, *MNRAS*, 469, 1282
 Reina-Campos M., Kruijssen J. M. D., Pfeffer J., Bastian N., Crain R. A., 2018, *MNRAS*, 481, 2851
 Reina-Campos M., Kruijssen J. M. D., Pfeffer J. L., Bastian N., Crain R. A., 2019, *MNRAS*, 486, 5838
 Sales L. V., Navarro J. F., Theuns T., Schaye J., White S. D. M., Frenk C. S., Crain R. A., Dalla Vecchia C., 2012, *MNRAS*, 423, 1544
 Schaerer D., Charbonnel C., 2011, *MNRAS*, 413, 2297
 Schaye J. et al., 2015, *MNRAS*, 446, 521
 Schiavon R. P. et al., 2017, *MNRAS*, 466, 1010
 Trujillo-Gomez S., Reina-Campos M., Kruijssen J. M. D., 2019, *MNRAS*, 488, 3972
 Usher C., Pfeffer J., Bastian N., Kruijssen J. M. D., Crain R. A., Reina-Campos M., 2018, *MNRAS*, 480, 3279
 Webb J. J., Leigh N. W. C., 2015, *MNRAS*, 453, 3278
 Wiersma R. P. C., Schaye J., Theuns T., Dalla Vecchia C., Tornatore L., 2009, *MNRAS*, 399, 574
 Zolotov A., Willman B., Brooks A. M., Governato F., Brook C. B., Hogg D. W., Quinn T., Stinson G., 2009, *ApJ*, 702, 1058

This paper has been typeset from a \LaTeX file prepared by the author.

Part III

Stellar clusters in a cold and dense cosmic environment

Chapter 7

Modelling the co-formation and evolution of stellar clusters and their host galaxies in *EMP-Pathfinder*

Authors:

Marta Reina-Campos, J. M. Diederik Kruijssen,
Benjamin W. Keller, Jindra Gensior,
Sebastian Trujillo-Gomez, Sarah M. R. Jeffreson
and Joel L. Pfeffer

Excerpt from Reina-Campos et al. (in prep.)

Despite the great success achieved by the E-MOSAICS project (Pfeffer et al., 2018; Kruijssen et al., 2019a) at linking GC populations with their natal sites, the lack of a model describing the cold gas in the ISM implies that stellar clusters disrupt too slowly (see appendix D by Kruijssen et al., 2019a). This prevents these simulations from extending the predictions to the entire cluster population.

This chapter addresses this issue. Following the setup introduced by the E-MOSAICS project, we develop the *EMP-Pathfinder* simulations, in which we study the formation and evolution of stellar cluster populations alongside their host galaxies in a cold, dense cosmic environment. These simulations represent the initial framework of the EMP galaxy formation model (Kruijssen et al. in prep., Keller et al. in prep.). This galaxy formation model will explore the influence of an empirically-motivated description of star formation

and stellar feedback in setting the baryonic lifecycle within galaxies. The following pages correspond to an excerpt from a paper in preparation that introduces these simulations.

This chapter is organized as follows. The methods and physical models used in the simulations are described in Section 7.1. In Section 7.2, we discuss the two sets of initial conditions of Milky-Way mass galaxies considered in this work: the low resolution isolated disk from the AGORA project (Kim et al., 2014, 2016), and the cosmological zoom-in halo MW09 used in the E-MOSAICS project (Pfeffer et al., 2018; Kruijssen et al., 2019a). We present some preliminary results of the potential of this new approach using the isolated galaxy initial conditions in Section 7.3, and we demonstrate the good behaviour of the numerical methods used to calculate the gas surface density and the epicyclic frequency in the appendices (Section 7.4).

7.1 Stellar clusters and their host galaxies in *EMP-Pathfinder*

In this section we discuss in detail the physical models used in *EMP-Pathfinder* to simulate the formation and evolution of stellar clusters alongside their host galaxies across cosmic time. These simulations use the moving-mesh, hydrodynamical code **AREPO** (Sect. 7.1.1), with a new suite of baryonic physics that model the hierarchical nature of the ISM and are part of the *EMP-Pathfinder* galaxy formation model (Sect. 7.1.2). In addition, they include an improved sub-grid model of the formation and evolution of stellar clusters (MOSAICS, Sect. 7.1.3).

7.1.1 Simulation code

We implement the *EMP-Pathfinder* galaxy formation model in the moving-mesh, hydrodynamical code **AREPO** (Springel, 2010; Weinberger et al., 2019). **AREPO** solves the hydrodynamical equations on an unstructured mesh generated from a Voronoi tessellation using a second-order accurate unsplit Godunov solver, and it treats the collisionless elements, i.e. stars and dark matter, using a Lagrangian formulation.

A particularity of this code is that the hydrodynamical component of the simulation is Galilean invariant. This is achieved by allowing the mesh generating points to move with the fluid flow velocity. The mesh can be reconstructed at any point in time, and its construction ensures that every cell has a roughly constant target mass m_{target} . In addition to the mesh movement, **AREPO** solves the hydrodynamical equations on the mesh faces. This hybrid approach allows it to overcome issues of both standard Eulerian mesh-based codes, such as their lack of Galilean invariance, as well as eliminating limitations of smoothed particle hydrodynamics methods, like artificial viscosity.

The details regarding the calculation of the gravitational interactions change slightly depending on the initial conditions considered (see Section 7.2). In the case of the isolated disk simulation, we compute the gravitational forces with a hierarchical multipole expansion that uses an oct-tree algorithm (Barnes and Hut, 1986). As the tree is traversed for each particle, multiple moments are calculated for each tree node recursively, and then used to approximate the gravitational forces. For the evolution of the cosmological zoom-in

simulations, the gravitational interactions are calculated using a TreePM algorithm (e.g. Springel, 2005), in which the long range contributions are calculated solving the Fourier transform of the Poisson equation and the short range contributions are obtained from the hierarchical oct-tree (Barnes and Hut, 1986). Additionally, we include a second mesh to compute the long range contributions at a higher resolution in the regions where particles are concentrated.

Gravitational interactions are softened on a scale ϵ in N -body simulations of collisionless systems to prevent close encounters of particles leading to divergences in the gravitational force. This softening limits the maximum force that a particle can cause (see e.g. Power et al., 2003, for a discussion on the choice of the optimal scale). To calculate the gravitational interactions of the gas cells, we use an adaptive gravitational softening scheme (Price and Monaghan, 2007), $\epsilon_{\text{gas}} = f r_{\text{cell}} = f(3V/4\pi)^{1/3}$, that is proportional to the cell radius r_{cell} of a sphere of equal volume. We choose the factor to be $f = 2.8$ and we use 64 softening levels logarithmically-spaced by 1.2 dex. Further details on the gravitational softenings used for the other particle types are given in Section 7.2.

Due to the mesh-based algorithm employed to solve the hydrodynamical equations, the entire simulated volume is filled with mesh generating points and their corresponding gas cells. For the isolated galaxy simulation, the disk is surrounded by a periodic grid of cells, whose only role is to improve the construction of the mesh. These grid cells have extremely low densities, and their evolution is inexpensive. In the case of the cosmological zoom-in simulations, most of the volume is covered with cells that are spawned from the low- and medium-resolution dark matter particles during the setup of the simulation. These cells only cover the region outside the Lagrangian volume of the halo. Thus, in order to avoid computational expense, we only allow gas cells that have been spawned from the high-resolution dark matter particles to refine. Additionally, those cells that are not allowed to refine are evolved adiabatically, and are not eligible for star formation.

7.1.2 The EMP-*Pathfinder* galaxy formation model

The EMP-*Pathfinder* model is a first step towards an empirically-motivated description of the physical processes that shape the baryonic lifecycle in galaxies, the EMP galaxy formation model (Kruijssen et al. in prep., Keller et al. in prep.). In this first generation of cosmological zoom-in simulations, we include the physics of the cold gas phase of the ISM (Sect. 7.1.2.1), and evaluate the effects of different prescriptions for star formation in the cold ISM (Sect. 7.1.2.2). We also include feedback effects, namely the mass, metals, yields, energy and momentum ejecta from AGB stars, SNII and SNIa (Sect. 7.1.2.3).

7.1.2.1 Chemistry and cooling network

We determine the thermodynamic state of the gas using the **Grackle** chemistry and cooling library (Smith et al., 2017)¹. This library is based on the work of Abel et al., (1997) and Anninos et al., (1997), and offers a non-equilibrium chemistry network for six to twelve primordial species.

¹We use the version 3.1. of the **Grackle** library, which is described in <https://grackle.readthedocs.io/>.

We use the six species network, which means that the chemical evolution, radiative cooling and heating for H, H⁺, He, He⁺ and He⁺⁺ are calculated with a non-equilibrium solver. In particular, this network accounts for collisional excitation and ionization, recombination, and Bremsstrahlung cooling rates, as well as Compton cooling and heating due to the cosmic microwave background. In addition to these rates, we also consider the photoionization heating rates and photoionization rates from the spatially-uniform, redshift-dependent UV background described by Haardt and Madau, (2012). Lastly, we consider the cooling and heating rates due to line emission from metals. With the aim of avoiding the computational expense of running a very large chemical reaction network, the **Grackle** library provides tabulated rates of metal cooling and heating for all elements heavier than He and up to Zn.

The **Grackle** library allows the input of external constant heating sources to be accounted for during the integration of energies. We use this functionality to include the thermal heating from stellar winds, SNII and SNIa feedback (see Sect. 7.1.2.3), and hence, to self-consistently integrate the chemistry and energy evolution.

The more complex chemistry networks in the **Grackle** library also include the reactions for H₂, which is a critical element for star formation (e.g. Kennicutt, 1998; Bigiel et al., 2008). However, accurately modelling the chemistry of molecular hydrogen requires a description for the self-shielding of the gas, as otherwise the ionizing radiation field can easily dissociate it. We lack the self-consistent treatment of the self-shielding from the UV background, which would require full radiative transfer and is computationally very expensive for the resolution achieved in our simulations. This prevents us from using the more complex chemistry networks that include H₂ cooling. Due to this limitation, gas in our simulations can only cool below 10⁴ K after the first stars have formed and enriched their surroundings with metals.

In order to prevent artificial fragmentation due to the presence of cold gas, we use the criterium suggested by Truelove et al., (1997). This criterium requires the local Jeans scale to be at least a factor of 4 larger than the resolution scale Δx . The local Jeans scale can be calculated as

$$\lambda_J = \sqrt{\frac{\pi c_s^2}{G\rho}}, \quad (7.1.1)$$

where G is the gravitational constant, and ρ is the density of the gas cell. The local sound speed is $c_s = \sqrt{\gamma P/\rho}$, where $\gamma = 5/3$ is the adiabatic index of the simulated gas, and P is the pressure of the gas cell. We reformulate this criterium to impose a Jeans floor on the pressure that does not affect the thermal structure of the gas,

$$P = \max\left(P_{\text{th}}, \frac{16\Delta x^2 G \rho^2}{\pi\gamma}\right), \quad (7.1.2)$$

where P_{th} is the thermal pressure calculated by the **Grackle** library. We calculate this floor at the scale of the gravitational softening, $\Delta x = 2\epsilon_{\text{gas}}$.

7.1.2.2 Star formation

Star formation proceeds on scales that are much smaller than our resolution element, which we consider to be defined by our gravitational softening. Because of that, we model star

formation as a sub-grid physical process in our simulations (e.g. Cen and Ostriker, 1992; Katz, 1992). The star formation rate is calculated as

$$\frac{d\rho_\star}{dt} = \epsilon_{\text{ff}} \frac{\rho}{t_{\text{ff}}}, \quad (7.1.3)$$

where ϵ_{ff} is the star formation efficiency per free-fall time, ρ is the density of the gas cell and $t_{\text{ff}} = \sqrt{3\pi/(32G\rho)}$ is the local gas free-fall timescale. We consider that a gas cell is eligible for star formation when its density exceeds a threshold n_{th} , and it is colder than T_{th} . The value of these thresholds changes depending on the initial conditions considered in order to reproduce the current star formation activity of the Milky Way and its cosmic evolution. For the isolated galaxy simulation, we set the thresholds to be $n_{\text{th}} = 1 \text{ H/cm}^3$ and $T_{\text{th}} = 5 \times 10^3 \text{ K}$, whereas these numbers increase slightly for the cosmological zoom-in simulations, $n_{\text{th}} = 10 \text{ H/cm}^3$ and $T_{\text{th}} = 1.5 \times 10^4 \text{ K}$. These criteria are chosen to mimic the fact that stars only form in the cold, dense ISM (e.g. Wong and Blitz, 2002; Bigiel et al., 2008). In order to avoid spurious star formation at high redshift, we also require gas cells to have overdensities larger than $\delta_{\text{th}} = \rho/(\Omega_b \rho_c) = 57.7$, where Ω_b is the density parameter of baryons. The critical density for a flat Friedmann universe, $\rho_c = 3H^2/(8\pi G)$, is calculated in terms of the Hubble parameter H .

We consider two different descriptions of the star formation process to evaluate the effects of different star formation prescriptions in setting the evolution of galaxies. These prescriptions assume different star formation efficiencies per free-fall time ϵ_{ff} , i.e. the fraction of gas that forms stars per free-fall time. Firstly, we consider a scenario in which star formation proceeds at a constant efficiency of $\epsilon_{\text{ff}} = 5$ per cent. In this scenario, the star formation rate depends only on the gas density (Eq. 7.1.3), i.e. higher density gas cells are more likely to form stars.

Secondly, we consider an environmentally-dependent description in which the star formation efficiency is set by galactic dynamics. In particular, we assume it to be proportional to the virial parameter of the gas overdensity (Padoan et al., 2012; Padoan et al., 2017; Gensior et al., 2020),

$$\epsilon_{\text{ff}} = \epsilon_{\text{wind}} \exp(-1.6\sqrt{\alpha_{\text{vir}}}), \quad (7.1.4)$$

where $\epsilon_{\text{wind}} = 0.4$ is a numerical normalization based on proto-stellar feedback (Padoan et al., 2017). We calculate the virial parameter as described in Gensior et al., (2020),

$$\alpha_{\text{vir}} = 1.35 \left(\sqrt{\frac{3\pi}{32G\rho_{\text{cl}}}} 2\sigma \left| \frac{\nabla\rho_{\text{cl}}}{\rho_{\text{cl}}} \right| \right)^2, \quad (7.1.5)$$

where the gas velocity dispersion $\sigma = \sqrt{\sigma_{\text{cl}}^2 + c_s^2}$ combines the resolved ‘cloud-scale’ velocity dispersion σ_{cl} with the thermal sound speed of the gas, $c_s = \sqrt{\gamma P_{\text{th}}/\rho}$. In order to calculate the virial parameter on the cloud-scale, we iterate over neighbouring gas cells until an overdensity is identified, effectively performing an on-the-fly cloud identification. Within the gas overdensity, we calculate a weighed gas density ρ_{cl} and its variation $\nabla\rho_{\text{cl}}$ over the scale h_{cl} , which defines its size (l_{TW} , see fig. 1 in Gensior et al. 2020).

Using a suite of isolated disk galaxies with different bulge sizes, Gensior et al., (2020) demonstrate that these star formation prescriptions lead to significant differences in the structure of the ISM in the inner part of the bulge-dominated galaxies. Only in galaxies with a dynamics-dependent description of star formation is fragmentation inhibited and the gas settles into a smooth, dense disc at the centre of the galaxy, as observed in the centres of elliptical galaxies (e.g. North et al., 2019). Similarly, the observed suppression of star formation in early-type galaxies (e.g. Kennicutt, 1989; Davis et al., 2014) is only fully reproduced with a dynamics-dependent sub-grid model.

For each star formation eligible gas cell, star formation is treated stochastically assuming a Poisson distribution. We calculate the probability for a given gas cell to turn into a star as

$$P_{\text{SF}} = \frac{m_{\text{gas}}}{m_{\text{star}}} \left[1 - \exp\left(-\frac{d\rho_{\star}}{dt} \Delta t\right) \right], \quad (7.1.6)$$

where m_{gas} and m_{star} are the gas and target stellar masses, respectively, and the probability is evaluated over the timestep Δt . A stellar particle is only added to the simulation if a randomly drawn, uniformly distributed number is smaller than this probability. In order to keep roughly similar stellar masses, AREPO allows for two channels for star formation. For gas cells more massive than twice the target mass, it spawns a single stellar particle of mass $m_{\text{star}} = 2m_{\text{target}}$, and the cell mass is accordingly decreased. On the other hand, for less massive cells, the entire gas cell is converted to a star particle of mass $m_{\text{star}} = m_{\text{gas}}$. The resulting stellar populations in our simulations have initial masses between $\sim 0.5\text{--}2 \times m_{\text{target}}$.

Every time a stellar particle is added to our simulations, we keep track of a variety of properties describing their natal environments. These include its initial position and velocity, mass and formation time, as well as some of the parent gas cell properties such as its density, thermal pressure, temperature, specific internal energy, and metallicity and chemical yields mass fractions. In addition to that, we keep track of the properties of the overdensity in which the newborn star forms, i.e. its size, turbulent velocity dispersion, virial parameter and weighed density. We use these quantities to characterize the environments that lead to the formation of stars and stellar clusters in our simulations.

7.1.2.3 Stellar feedback

Once a star forms, it continuously ejects mass, metals and energy back into the ISM during its lifetime. In order to account for those feedback processes, we assume that our stellar particles of $\sim 10^5 M_{\odot}$ are well described by stellar populations from a fully sampled initial mass function (IMF)². We thus describe the stellar populations using a Chabrier 2005 IMF (Chabrier, 2005), and use a tabulated description of their evolution from the SNAIL stellar library.

We generate this tabulated description with the ‘Stochastically Lighting Up Galaxies’ multicode library (SLUG; da Silva et al., 2012, 2014; Krumholz et al., 2015). With this code, we simulate the evolution of individual stellar clusters of mass $10^6 M_{\odot}$ as a function

²At these masses, stochasticity from sampling the stellar IMF only produces a variance of about 10 per cent on the ejected quantities.

of the metallicity using the Padova stellar evolution tracks that include pulsating AGB stars (Vassiliadis and Wood, 1993; Girardi et al., 2000). We then tabulate their evolution in terms of their age and metallicity describing the ejected quantities, i.e. number of SNII and mass ejected, as fractions relative to the initial mass of the cluster. We also follow the mass in metals and in individual elements, for which AGB winds and SNII are relevant nucleosynthetic channels (Doherty et al., 2014; Karakas and Lugaro, 2016; Sukhbold et al., 2016). These correspond to 103 different isotopes between Li and Zn, which allow us to study the evolution of the chemical enrichment of the ISM and of stellar populations over cosmic history.

This description allows us to scale the feedback ejecta for our stars, and we consider objects more massive than our stellar particles to minimize the effects of stochastically sampling the IMF. We divide the evolution in 5000 logarithmically-spaced age intervals between 10^5 – 1.5×10^{10} years, which allows us to accurately describe the early stages of stellar evolution. We also use the same five bins in metallicity space used in SLUG, and interpolate between them to avoid jumps in the ejected quantities.

Using the precomputed SNAIL stellar evolution library, at every timestep the stellar feedback algorithm proceeds as follows:

1. Each star particle computes the mass, metals, yields and energy ejected at the timestep Δt from AGB winds, SNII and SNIa. For that, we first evaluate the contribution of SNII. The number of SNII exploding during the timestep is calculated in terms of the initial mass of the stellar particle $m_{\text{star}}^{\text{init}}$, its age τ and its mass fraction in metals Z ,

$$N_{\text{SNII}} = \text{floor} \left[\max \left(m_{\text{star}}^{\text{init}} f_{\text{SNII}}(\tau, Z) - N_{\text{SNII}}^{\text{tot}}, 0 \right) \right], \quad (7.1.7)$$

where $f_{\text{SNII}}(\tau, Z)$ is the total fraction of SNII exploding per solar mass from the precomputed SNAIL table, and $N_{\text{SNII}}^{\text{tot}}$ is the total number of SNII that have exploded until the current time. We balance the total number of SNII by adding events stochastically with the appropriate probability throughout the lifetime of the stellar particle. The energy ejecta by SNII is calculated as

$$E_{\text{SNII}} = N_{\text{SNII}} \times e_{\text{SN}}, \quad (7.1.8)$$

where $e_{\text{SN}} = 1.7 \times 10^{51}$ ergs corresponds to the energy ejected by each SN event. Because of the use of precomputed tables by the SLUG library, the timescale and the number of SNII are fixed. In order to account for the effects of a different stellar IMF or minimum mass for the SN progenitor on the total SNII counts, the variable e_{SN} can be modified. Thus, a value of $e_{\text{SN}} = 1.7 \times 10^{51}$ ergs is equivalent to a Chabrier IMF with a minimum SN progenitor mass of $8 M_{\odot}$, and it corresponds to 1.1 SN event per $100 M_{\odot}$.

Then, we calculate the total energy ejected in the form of stellar winds at the current

age of the stellar particle (Agertz et al., 2013),

$$E_{\text{winds}} = \begin{cases} e_1 \left(\frac{m_{\text{star}}^{\text{init}}}{M_{\odot}} \right) \left(\frac{2Z}{Z_{\odot}} \right)^{e_2} \left(\frac{\tau}{6.5 \text{ Myr}} \right) & \text{if } \tau < 6.5 \text{ Myr,} \\ e_1 \left(\frac{m_{\text{star}}^{\text{init}}}{M_{\odot}} \right) \left(\frac{2Z}{Z_{\odot}} \right)^{e_2} & \text{if } \tau > 6.5 \text{ Myr,} \end{cases} \quad (7.1.9)$$

where $e_1 = 1.9 \times 10^{48}$ ergs and $e_2 = 0.38$. In order to obtain the energy ejected at that timestep, we compute the difference between this total energy and the accumulated energy up to the last time t_0 at which the star ejected feedback,

$$\Delta E_{\text{winds}} = E_{\text{winds}}(m_{\text{star}}^{\text{init}}, Z, \tau) - E_{\text{winds}}(m_{\text{star}}^{\text{init}}, Z, t_0). \quad (7.1.10)$$

The contributions to the mass, metals and individual yields ejected from stellar winds and SNII are calculated using the precomputed tables from the SNAIL library. Due to the design of the SLUG library, there is no metal ejection until the first SN event, and so, stars can ‘destroy’ metals by forming from metal-enriched gas but only ejecting primordial gas initially. In order to prevent that, we require the mass ejected in metals to be, at least, the stellar metallicity times the ejecta mass.

After this, we calculate the number of SNIa exploding at that timestep,

$$N_{\text{SNIa}} = 1 \text{ if } \mathcal{X} < P_{\text{SNIa}}; \quad N_{\text{SNIa}} = 0 \text{ otherwise,} \quad (7.1.11)$$

by comparing a random uniformly-generated number \mathcal{X} to the probability of having a SNIa explosion. This probability is calculated as

$$P_{\text{SNIa}} = 1 - \left(\frac{\tau}{t_0} \right)^{-4 \times 10^{-4} m_{\text{star}}^{\text{init}}} \quad (7.1.12)$$

for a stellar particle of initial mass $m_{\text{star}}^{\text{init}}$ between its current age τ and the time t_0 at which this probability was last evaluated. The energy ejecta by SNIa is described as

$$E_{\text{SNIa}} = N_{\text{SNIa}} \times e_{\text{SN}}, \quad (7.1.13)$$

where we assume that supernovae of type Ia output the same energy as those of type II. The mass and metals ejected by SNIa are thus calculated as

$$m_{\text{SNIa}} = 1.4 M_{\odot} \times N_{\text{SNIa}}; \quad m_{\text{SNIa}}^Z = 1.4 M_{\odot} \times N_{\text{SNIa}}, \quad (7.1.14)$$

and the mass for the individual yields are obtained similarly using the table from Seitzzahl et al., (2013).

The total contribution to the mass, metals, momentum³ and energy ejected by AGB winds and SNII at that timestep is thus computed for each star particle i as

$$\begin{aligned} \Delta m_i &= m_{\text{winds},i} + m_{\text{SNII},i}, \\ \Delta m_i^Z &= m_{\text{winds},i}^Z + m_{\text{SNII},i}^Z, \\ \Delta \mathbf{p}_i &= \Delta m_i \mathbf{v}_i, \\ \Delta E_i &= \Delta E_{\text{winds},i} + E_{\text{SNII},i}. \end{aligned} \quad (7.1.15)$$

³In this thesis, we follow the standard convention of denoting vectors in bold font.

2. Then, each star particle looks for the nearest gas cell neighbour. The gas cell j collects the ejecta quantities from all the stellar particles i for which j is their nearest neighbour,

$$\begin{aligned}
\Delta m_j &= \sum_i \Delta m_i, \\
\Delta m_j^Z &= \sum_i \Delta m_i^Z, \\
\Delta \mathbf{p}_j &= \sum_i \Delta \mathbf{p}_i, \\
\Delta E_j &= \sum_i \Delta E_i + \frac{1}{2} \sum_i \frac{|\Delta \mathbf{p}_i|^2}{\Delta m_i} - \frac{1}{2} \frac{|\sum_i \Delta \mathbf{p}_i|^2}{\sum_i \Delta m_i},
\end{aligned} \tag{7.1.16}$$

and it applies the ejecta from SNIa onto itself,

$$\begin{aligned}
m'_j &= m_j + \sum_i m_{\text{SNIa},i}, \\
m_j^{Z'} &= m_j^Z + \sum_i m_{\text{SNIa},i}^Z, \\
\mathbf{p}'_j &= \mathbf{p}_j + \sum_i m_{\text{SNIa},i} \mathbf{v}_i, \\
E'_j &= E_j + \sum_i E_{\text{SNIa},i}.
\end{aligned} \tag{7.1.17}$$

With this strategy, we avoid injecting momentum to distant gas cells in the rare situations when the entire galaxy is surrounded by one or several large Voronoi cells, e.g. after a merger-induced starburst ejects most of the gas in the ISM.

3. Every cell that has collected ejecta from its neighbouring stars then distributes it over its neighbouring faces. For that, we follow the mechanical feedback coupling algorithm described by Hopkins et al., (2018). Assuming that the gas cell j has collected feedback output, it injects the ejecta (i.e. mass, metals, yields, energy, and momentum) to its neighbouring cell k via their shared face $j \rightarrow k$. The corresponding fraction to be injected is given by the ratio of the surface area of the face $j \rightarrow k$ to the sum of all the surface area of the faces defining the gas cell j ,

$$w_k = \frac{A_{j \rightarrow k}}{\sum_i A_{j \rightarrow i}}. \tag{7.1.18}$$

Using this weight, the new mass of the gas cell k is

$$\begin{aligned}
m'_k &= m_k + \Delta m_k, \\
\Delta m_k &= w_k \Delta m_j.
\end{aligned} \tag{7.1.19}$$

We calculate the terminal momentum of the SNII shell using the model from Blondin et al., (1998),

$$\frac{p_t}{M_\odot \text{km s}^{-1}} = 3 \times 10^{10} \left(\frac{\Delta E_j}{10^{51} \text{ergs}} \right)^{16/17} \left(\frac{n_k}{\text{cm}^{-3}} \right)^{-2/7} f, \tag{7.1.20}$$

where n_k is the number density of the gas cell k , and the factor f depends on the mass fraction of metals as

$$f = \begin{cases} 1.905 & \text{if } Z/0.012 < 0.01, \\ (Z/0.012)^{-0.14} & \text{if } Z/0.012 > 0.01. \end{cases} \quad (7.1.21)$$

We apply a momentum kick to the neighbouring gas cell k as

$$\begin{aligned} \mathbf{p}'_k &= \mathbf{p}_k + \Delta\mathbf{p}_k, \\ \Delta\mathbf{p}_k &= p_{\text{fb}} \frac{\mathbf{r}_{j \rightarrow k}}{|\mathbf{r}_{j \rightarrow k}|} + w_k \Delta\mathbf{p}_j, \end{aligned} \quad (7.1.22)$$

where p_{fb} is the minimum between the energy-conserving momentum and the terminal momentum,

$$p_{\text{fb}} = \min \left(\sqrt{2(m_k + w_k \Delta m_j) w_k \Delta E_j}, w_k p_t \right). \quad (7.1.23)$$

Lastly, we update the total energy of the neighbouring gas cell k as

$$\begin{aligned} E'_k &= E_k + \Delta E_k, \\ \Delta E_k &= \frac{|\mathbf{p}_k + \Delta\mathbf{p}_k|^2}{2(m_k + \Delta m_k)} - \frac{|\mathbf{p}_k|^2}{2m_k}. \end{aligned} \quad (7.1.24)$$

4. Finally, to ensure the conservation of mass, momentum and energy, we apply any residual mass and momentum to the central cell j ,

$$\begin{aligned} m'_j &= m_j + \left(1 - \sum_k w_k \right) \Delta m_j, \\ \mathbf{p}'_j &= \mathbf{p}_j - \sum_k \Delta\mathbf{p}_k. \end{aligned} \quad (7.1.25)$$

We store the heating energy that should be applied to the central gas cell j ,

$$E_{\text{th},j} = \Delta E_j - \sum_k \left(\Delta E_k - \frac{1}{2} \frac{w_k |\Delta\mathbf{p}_j|^2}{\Delta m_j} \right) + \frac{1}{2m_j} (|\mathbf{p}_j|^2 - |\mathbf{p}'_j|^2), \quad (7.1.26)$$

in a separate variable such that we can use it as an input to the cooling library `Grackle` to be applied while solving the cooling equations. This method allows us to evolve the thermal heating alongside the cooling rates, rather than dumping the heat on the central cell. Given that the cooling timesteps are smaller than the hydrodynamical timesteps, this implies that the heating and cooling of the cell are self-consistently solved for during the cooling integration.

The continuous ejection of feedback quantities requires the steps to be repeated every time a stellar particle produces mass or energy to be distributed. To minimize the computational expense from finding the nearest gas cell and injecting the feedback through its faces, we discretize the feedback ejection in time. Hence, once the star particle is older than 50 Myr and most of its stellar evolution is over, it only ejects mass, metals and yields after accumulating an amount equivalent to 0.1 per cent of its current stellar mass.

7.1.3 MOSAICS: stellar cluster formation and evolution

Observations of YMC populations in starbursting galaxies in the local Universe (e.g. Holtzman et al., 1992; Whitmore and Schweizer, 1995; Holtzman et al., 1996; Whitmore et al., 1999; Zepf et al., 1999) fostered the idea that cluster formation is a high-pressure extension of the normal mode of star formation, in which the formation and evolution of these objects in a cosmic environment would be responsible for shaping their properties (e.g. Ashman and Zepf, 1992; Elmegreen and Efremov, 1997; Shapiro et al., 2010; Kruijssen, 2015; Krumholz et al., 2019). In this scenario, the observed old and massive GC populations would be the relics of regular cluster formation at high redshift that could survive to the present day. Under this assumption, it becomes critical to self-consistently model the stellar cluster populations alongside their host galaxies in order to properly reproduce their demographics.

Modelling resolved stellar clusters in cosmological simulations requires resolving the cold gas flows within galaxies leading to cluster formation (Li et al., 2017; Kim et al., 2018; Li et al., 2018; Lahén et al., 2019; Ma et al., 2020a), which greatly increases the computational cost of the simulation. By using a sub-grid description for the formation and evolution of the stellar cluster populations, we aim to reduce the computational cost needed to resolve individual stellar clusters, while at the same time benefiting from resolving the galactic environment, which determines the properties of stellar cluster populations. As mentioned in the introduction, this approach has already been used with great success in the E-MOSAICS project (Pfeffer et al., 2018; Kruijssen et al., 2019a), from which this work draws inspiration and which it aims to improve and expand.

In order to describe the formation and evolution of stellar clusters over cosmic history, we implement an improved description of the MODelling Star cluster population Assembly In Cosmological Simulations (MOSAICS; Kruijssen et al. 2011; Pfeffer et al. 2018) model into the EMP-*Pathfinder* galaxy formation model (Kruijssen et al. in prep., Keller et al. in prep.). Relative to the description included in the E-MOSAICS project (Pfeffer et al., 2018; Kruijssen et al., 2019a), in this work we implement four main modifications to the models describing the formation and evolution of stellar clusters. Those are: *(i)* that the hierarchical structure of the ISM in which clusters form can lead to a narrower initial cluster mass function (ICMF) in higher gas pressure environments (Trujillo-Gomez et al., 2019), which results in an enhancement in the number of GCs per galaxy stellar mass in certain environments, *(ii)* an environmentally-dependent description for the initial half-mass radius (Choksi and Kruijssen, 2019), and its implications for the survivability of the stellar cluster populations, *(iii)* a phenomenological description of cluster disruption due to tidal shocks based on N -body simulations (Webb et al., 2019a) that predicts a more disruptive effect compared to analytical derivations (e.g. Prieto and Gnedin, 2008), and *(iv)* the effects of accounting for both cluster mass and size evolution. We provide below further details on each of these new models considered.

One of the goals of this work is to study the effects of assuming different scenarios for cluster formation and evolution on the stellar cluster populations. For that, we make use of the fact that the sub-grid stellar clusters are inert⁴ and implement a framework

⁴The sub-grid stellar clusters do not contribute to the baryonic lifecycle of the simulated galaxies because

that allows us to run multiple parallel stellar cluster populations, each governed by their own formation and evolution models. In addition to reducing the computational expense of these simulations, this parallel implementation is interesting as it enables to fix the baryonic physics affecting cluster populations, and so to highlight the differences between formation and evolution scenarios.

Given the sub-grid nature of the stellar cluster populations, our clusters inherit their phase space properties (i.e. their positions and kinematics), as well as their metallicities and chemical abundances, from their host stellar particles. However, we consider that the formation and the evolution of the cluster populations within the star particle is solely governed by the galactic environment, which we self-consistently model alongside the clusters. Here we proceed to describe the models considered for the formation and the evolution of the stellar cluster populations.

7.1.3.1 Cluster formation

In our sub-grid description, every time a stellar particle is formed from a gas cell, we assume that a fraction of its mass forms in a bound clustered fashion. This mass corresponds to the total mass budget for the stellar cluster population within that stellar particle. From this budget mass, we form stellar clusters with masses distributed according to an assumed ICMF, with sizes that are either constant or environmentally-dependent, and with ages equal to the ages of the host star particle. We assume that the remaining mass forms in unbound stars or unbound associations that immediately disperse into the field.

The fraction of star formation that goes into bound stellar clusters is the cluster formation efficiency (CFE, Γ , Bastian, 2008), which we describe using an environmentally-dependent model (Kruijssen et al., 2012). This model uses the hierarchical nature of the ISM to predict a steeply increasing bound fraction towards environments with higher gas pressures, as observed in the local Universe (e.g. Adamo et al., 2015; Johnson et al., 2016; Adamo et al., 2020). The pressure dependence of this description of the CFE implies that high-redshift galaxies, which typically have larger gas pressures than low-redshift galaxies (Tacconi et al., 2013), produce higher fractions of star formation in bound clusters (Pfeffer et al., 2018). The cosmic evolution of this model reproduces observations of YMCs in the local Universe (Pfeffer et al., 2019b).

Contrary to the E-MOSAICS project (Pfeffer et al., 2018; Kruijssen et al., 2019a), the inclusion of the cold phase of the ISM in our models prevents us from assuming that the local gas cell properties are a good description of the global state of the gas, i.e. that the local gas pressure and density approximately describe the mid-plane pressure and density, respectively. Because of that, we use the global formalism of the CFE model, $\Gamma(\Sigma_g, \kappa, Q)$, which depends on the gas surface density Σ_g , the epicyclic frequency κ and the Toomre parameter Q . As we treat cluster disruption explicitly (Section 7.1.3.2), we exclude the ‘cruel-craddle effect’ from the formulation of the CFE, i.e. the disruption of clusters due to their natal environment (Kruijssen, 2012), such that the cluster formation efficiency is set only by the gravitationally-bound cluster formation fraction, $\Gamma(\Sigma_g, \kappa, Q) = f_{\text{bound}}$.

the feedback ejecta is calculated based on the host stellar particle properties (see Sect. 7.1.2.3).

We describe here briefly how we determine these global gas quantities at runtime using local properties of the gas cells (more details can be found in appendices 7.4.1 and 7.4.2). In order to calculate the gas surface density, we find that a neighbour-weighted turbulent pressure is a good description of the mid-plane pressure of a disk in hydrostatic equilibrium (Elmegreen, 1989; Krumholz and McKee, 2005),

$$\Sigma_g = \sqrt{\frac{2P_{\text{ngbs}}}{\pi G \phi_P}}, \quad (7.1.27)$$

where ϕ_P is a constant that accounts for the contribution of stars to gravity. We calculate it over the same volume as the neighbour-weighted pressure as (e.g. Elmegreen, 1989; Krumholz and McKee, 2005)

$$\phi_P = 1 + \frac{\sigma_{\text{gas}}}{\sigma_{\text{stars}}} \left(\frac{1}{f_{\text{gas}}} - 1 \right), \quad (7.1.28)$$

where σ_{gas} and σ_{stars} are the gas and stellar velocity dispersions, respectively, and $f_{\text{gas}} = M_{\text{gas}}/(M_{\text{gas}} + M_{\text{stars}})$, M_{gas} , and M_{stars} are the gas fraction, and the gas and stellar masses within the volume, respectively. If no stars are found within the volume, the gas fraction and ϕ_P are both set to one.

Then, we use the Poisson equation to relate the spatial variation of the potential at the location of the newborn star with the angular velocity and the epicyclic frequency at the location of the stellar particle. We describe the spatial variation of the gravitational potential Φ in terms of a tidal tensor

$$T_{ij} = -\frac{\partial^2 \Phi}{\partial x_i \partial x_j}, \quad (7.1.29)$$

which is generally described in terms of its eigenvalues and corresponding eigenvectors. These vectors represent the principal axes of the action of the tidal field, and its eigenvalues λ_i correspond to the magnitude of the force gradient along them. Due to the inclusion of the cold gas in our simulations, the local tidal tensors at the location of newborn stars are heated due to the presence of the star-forming overdensity which dominates the gravitational potential locally. To correct for that, we compute a neighbour-weighted tidal tensor within the same volume as for the gas surface density, but avoiding the natal overdensity. With the eigenvalues of these neighbour-weighted tensors, we compute the angular velocity, Ω , and the epicyclic frequency, κ , as

$$\Omega^2 = -\frac{1}{3} \sum_i \lambda_i; \quad \kappa^2 = 3\Omega^2 - \lambda_1, \quad (7.1.30)$$

with λ_1 being the largest eigenvalue of the tidal tensor.

Finally, we calculate the Toomre parameter as

$$Q = \frac{\kappa \sigma_{\text{gas}}}{\pi G \Sigma_g}, \quad (7.1.31)$$

where G is the gravitational constant, and σ_{gas} corresponds to the neighbour-weighted isotropic turbulent gas velocity dispersion calculated over the same volume as the gas surface density. With these global gas quantities (i.e. the gas surface density, the epicyclic frequency and the Toomre parameter) calculated for each star particle, the CFE and the ICMF are fully determined for its cluster population.

To describe the initial distribution of masses of the stellar cluster populations, we consider three different cases. Firstly, we use a single power-law distribution to describe the ICMF,

$$\frac{dN}{dm} \propto m^\alpha, \quad (7.1.32)$$

with a slope $\alpha = -2$. This shape was suggested by early observations of YMCs (e.g. Zhang and Fall, 1999), and it has been argued to be produced by the fragmentation of clouds due to the balance between the gravitational collapse and turbulence (Elmegreen, 2011). In our model, this ICMF is kept constant in time and space, thus reproducing the suggested mechanism of constant cluster formation relative to stars (e.g. Chandar et al., 2015, 2017).

However, recent observations of YMCs in nearby starbursts suggest that their ICMF can be well described by an exponentially-truncated power-law distribution (e.g. Portegies Zwart et al., 2010; Adamo et al., 2020), in which the exponential cut-off is found to increase with star formation activity (Larsen, 2009; Adamo et al., 2015; Johnson et al., 2017; Messa et al., 2018). This distribution corresponds to a Schechter function (Schechter, 1976), which we describe as

$$\frac{dN}{dm} \propto m^\alpha \exp\left(-\frac{m}{M_{\text{cl,max}}}\right), \quad (7.1.33)$$

with a power-law slope of $\alpha = -2$ and an environmentally-dependent upper mass scale $M_{\text{cl,max}}$. The truncation mass is assumed to be related to the maximum molecular cloud mass from which stellar clusters can form (Kruijssen, 2014),

$$M_{\text{cl,max}}(\Sigma_{\text{g}}, \kappa, Q) = \epsilon \times \Gamma \times M_{\text{GMC,max}}(\Sigma_{\text{g}}, \kappa, Q), \quad (7.1.34)$$

where $\epsilon = 0.1$ is the star formation efficiency integrated over the molecular cloud (Lada and Lada, 2003; Oklopčić et al., 2017; Chevance et al., 2020). The maximum molecular cloud mass $M_{\text{GMC,max}}$ is calculated by considering the interplay between the gravitational collapse of the largest centrifugally-unstable region (defined by the Toomre length) and the stellar feedback from the newborn stars within the region (Reina-Campos and Kruijssen, 2017, and Chapter 2). In this model, the maximum molecular cloud mass can be described in terms of global gas quantities as

$$M_{\text{GMC,max}} = M_{\text{T}} \times f_{\text{coll}}, \quad (7.1.35)$$

where M_{T} is the mass enclosed in the largest gravitationally-unstable region to centrifugal forces (i.e. the Toomre mass),

$$M_{\text{T}} = \frac{4\pi^5 G^2 \Sigma_{\text{g}}^3}{\kappa^4}. \quad (7.1.36)$$

The collapse fraction f_{coll} indicates whether the unstable region collapses before stellar feedback can stop its collapse,

$$f_{\text{coll}} = \min \left(1, \frac{t_{\text{fb}}}{t_{\text{ff},2\text{D}}} \right)^4, \quad (7.1.37)$$

where t_{fb} is the feedback timescale, and $t_{\text{ff},2\text{D}} = \sqrt{2\pi}/\kappa$ is the two-dimensional free-fall timescale for the largest gravitationally unstable region. If stellar feedback can halt the collapse of the unstable region ($t_{\text{fb}} < t_{\text{ff},2\text{D}}$)⁵, then the maximum cloud mass is feedback-limited and corresponds to a fraction of what it would have been if the entire region had collapsed. This regime is found to be typical of galactic outskirts ($\Sigma_{\text{g}} \leq 100 \text{ M}_{\odot} \text{pc}^{-2}$ and $\kappa \leq 0.8 \text{ Myr}^{-1}$ for $Q = 1.5$), thus explaining the observed constant radial profile of the upper mass scales of clouds and clusters (Reina-Campos and Kruijssen, 2017; Messa et al., 2018).

Following eq. (18) in Kruijssen, (2012), we define the feedback timescale as the time required to reach pressure equilibrium between the stellar feedback and the surrounding interstellar gas,

$$t_{\text{fb}} = \frac{t_{\text{sn}}}{2} \left(1 + \sqrt{1 + \frac{4\pi^2 G^2 t_{\text{ff},\text{ISM}} Q^2 \Sigma_{\text{g}}^2}{\phi_{\text{fb}} \epsilon_{\text{ff}} t_{\text{sn}}^2 \kappa^2}} \right), \quad (7.1.38)$$

where $t_{\text{sn}} = t_{\text{sn},0} = 3 \text{ Myr}$ is the typical time for the first SN to explode (e.g. Ekström et al., 2012), $t_{\text{ff},\text{ISM}} = \sqrt{32\pi/(G\rho_{\text{ISM}})}$ is the free-fall timescale of the ISM, $\phi_{\text{fb}} \approx 0.16 \text{ cm}^2 \text{ s}^{-3}$ is a constant that represents the rate at which feedback injects energy into the ISM per unit stellar mass for a single stellar population with a normal stellar IMF, and $\epsilon_{\text{ff}} = 0.012$ is the star-formation efficiency per free-fall time (e.g. Elmegreen, 2002; Utomo et al., 2018). The mid-plane density of the ISM ρ_{ISM} can be calculated as (eq. 34 in Krumholz and McKee 2005)

$$\rho_{\text{ISM}} = \frac{\phi_{\text{P}} \kappa^2}{2\pi Q^2 G}, \quad (7.1.39)$$

assuming a gas disk in hydrostatic equilibrium.

The last model for the ICMF that we consider is exponentially-truncated both at the upper and lower mass scales. Considering the hierarchical nature of the ISM, Trujillo-Gomez et al., (2019) suggest a model for the minimum cluster mass that remains gravitationally bound after gas expulsion. In their model, the initial cluster mass distribution is represented by a double Schechter mass function of slope $\alpha = -2$,

$$\frac{dN}{dm} \propto m^{\alpha} \exp \left(-\frac{M_{\text{cl},\text{min}}}{m} \right) \exp \left(-\frac{m}{M_{\text{cl},\text{max}}} \right), \quad (7.1.40)$$

with environmentally-dependent truncation mass-scales, $M_{\text{cl},\text{min}}$ and $M_{\text{cl},\text{max}}$. Galactic environments with high gas surface densities are predicted to lead to narrower mass functions than lower gas densities environments, which reproduces the narrower cluster mass function

⁵These short timescales are not resolved in the simulations as they correspond to just a few Myrs. Because of this, they are computed sub-grid.

observed in the Central Molecular Zone of the Milky Way relative to the one observed in the Solar Neighbourhood.

This model hinges on the stellar feedback from supernovae to halt the star formation process, so the supernova timescale t_{sn} used in eq. (7.1.38) needs to be modified to account for the sampling of the stellar IMF in low-mass clouds,

$$t_{\text{sn}} = t_{\text{sn},0} + \frac{m_{\text{OB}} t_{\text{ff}}}{\epsilon_{\text{ff}} m_{\text{c}}}, \quad (7.1.41)$$

where m_{c} is the molecular cloud mass and m_{OB} is the minimum stellar mass needed such that the cloud forms at least one massive star ($m > 8 M_{\odot}$), which for a Chabrier, (2003) stellar IMF is $m_{\text{OB}} = 99 M_{\odot}$.

In low mass clouds, the maximum cluster mass $M_{\text{cl,max}}$ is calculated as a modified version of the model described in Reina-Campos and Kruijssen, (2017), with the consideration that the stellar IMF sampling may delay the timescale for the first supernova to explode (eq. 7.1.41). The minimum cluster mass $M_{\text{cl,min}}$ is then calculated as

$$M_{\text{cl,min}} = \epsilon_{\text{bound}} \epsilon_{\text{core}} m_{\text{th}}, \quad (7.1.42)$$

where $\epsilon_{\text{bound}} \approx 0.4$ is the minimum fraction of the cloud that must condense into molecular cores to form a bound cluster (Baumgardt and Kroupa, 2007), and $\epsilon_{\text{core}} \approx 0.5$ is the limiting efficiency of star formation within protostellar cores (Enoch et al., 2008). The threshold cloud mass below which all stars must hierarchically merge into a bound cluster m_{th} is calculated solving the implicit equation (eq. 28 in Trujillo-Gomez et al., 2019)

$$\epsilon_{\text{bound}} \epsilon_{\text{core}} = \epsilon_{\text{SF}} = \epsilon_{\text{ff}} \frac{t_{\text{SF}}}{t_{\text{ff}}}, \quad (7.1.43)$$

in which the timescale for star formation can be determined as

$$t_{\text{SF}} = \frac{t_{\text{sn}}}{2} \left[1 + \sqrt{1 + \sqrt{\frac{\pi^{1/2}}{8G} \frac{8\pi^{1/2} \phi_{\text{P}} G \Sigma_{\text{g}}^2 m_{\text{th}}^{3/4}}{3\phi_{\text{fb}} \epsilon_{\text{ff}} t_{\text{sn}}^2 \Sigma_{\text{c}}^{9/4}}}} \right], \quad (7.1.44)$$

where Σ_{c} is the cloud gas surface density.

Once we determine the total mass budget for the sub-grid stellar cluster population as Γm_{star} , and the ICMF is fully characterized, we calculate the mean mass of the ICMF as

$$\overline{M}_{\text{cl}} = \int_{100 M_{\odot}}^{10^8 M_{\odot}} m \frac{dN}{dm} dm, \quad (7.1.45)$$

and then the expected number of stellar clusters to be formed is $N_{\text{exp}} = \Gamma m_{\text{star}} / \overline{M}_{\text{cl}}$, with m_{star} being the mass of the stellar particle. The actual number of clusters to be formed N_{tot} is stochastically-drawn from a Poisson distribution with $\lambda = N_{\text{exp}}$, such that in most cases stars will form no stellar clusters, and in a small fraction of the cases there will be too much mass in stellar clusters relative to the stellar particle mass. On average, the drawn mass is equal to the desired $N_{\text{exp}} \overline{M}_{\text{cl}} = \Gamma m_{\text{star}}$.

This stochastically-drawn number N_{tot} corresponds to the total number of clusters to be formed. We then determine the properties of the individual stellar clusters within our populations. For each cluster to be formed, we stochastically draw its mass from the chosen ICMF, and only add it to the resolved cluster population if the mass is larger than $M_{\text{min,evolve}} = 5 \times 10^3 M_{\odot}$. This is done to reduce memory requirements, as we consider that clusters less massive than $5 \times 10^3 M_{\odot}$ will experience dissolution time-scales \ll Gyr, and so they can be safely discarded at formation and their masses are then contributed to the field star population.

Lastly, we assign an initial half-mass radius to the sub-grid individual stellar clusters. Observationally, stellar clusters more massive than $5 \times 10^3 M_{\odot}$ have half-mass radii between ~ 1 – 10 pc (e.g. see fig. 9 in Krumholz et al., 2019), with a slight dependence on their mass. Given that most disruption mechanisms depend on the cluster density, setting this quantity to be fixed or environmentally-dependent is likely to have consequences on the rate of disruption that stellar clusters experience. To investigate this effect, we consider two cases for the initial half-mass radius.

Firstly, we assume that all stellar clusters have constant initial half-mass radius of $r_{\text{h}}^{\text{init}} = 4$ pc, thus simplifying the interpretation of their evolution. Secondly, we use the environmentally-dependent model by Choksi and Kruijssen, 2019 to calculate their initial half-mass radius,

$$r_{\text{h,env}}^{\text{init}} = f_{\text{acc}} \frac{\alpha_{\text{vir}}}{5\epsilon_{\text{c}}^{3/2}} \frac{\phi_{\rho}}{\phi_{\bar{P}}} \sqrt{\frac{m}{\Sigma_{\text{g}}}}, \quad (7.1.46)$$

where $f_{\text{acc}} = 0.5$ is a constant of order unity, $\epsilon_{\text{c}} \approx 0.5$ – 1 is the integrated star formation efficiency in the clump, and $\phi_{\bar{P}}$ and ϕ_{ρ} are the relative mean cloud pressures and densities with respect to the ISM, respectively. For a disk in hydrostatic equilibrium, Krumholz and McKee, (2005) demonstrate that the pressure ratio can be estimated as

$$\phi_{\bar{P}} \approx (10 - 8f_{\text{GMC}}), \quad (7.1.47)$$

with the fraction of all gas locked in giant molecular clouds being

$$f_{\text{GMC}} \approx \left[1 + 0.025 (\Sigma_{\text{g}}/100 M_{\odot} \text{ pc}^{-2})^{-2} \right]^{-1}. \quad (7.1.48)$$

In turn the ratio of densities can be calculated as

$$\phi_{\rho} = \left(\frac{375}{2\pi^2} \right)^{1/4} \left(\frac{\phi_{\bar{P}}}{\phi_{\text{P}}\alpha_{\text{vir}}} \right)^{1/4}, \quad (7.1.49)$$

where α_{vir} is the virial parameter of the natal overdensity (Eq. 7.1.5). We limit this initial size to an upper value of 30 per cent of the tidal radius of the cluster (Alexander et al., 2014),

$$r_{\text{t}} = \left(\frac{Gm}{T} \right)^{1/3}, \quad (7.1.50)$$

where T is the tidal field strength. We then use this environmentally-dependent initial half-mass radius to center a log-normal distribution of 0.2 dex in scatter from which we stochastically draw an initial radius for each resolved stellar cluster in the newborn sub-grid population.

7.1.3.2 Cluster evolution

As clusters orbit within their host galaxies, several physical mechanisms can affect their properties. In our model, stellar cluster populations are considered to evolve through stellar evolution as well as through dynamical processes. These include two-body interactions and the evolution due to tidal shocks. The effect of dynamical friction in the most massive clusters is accounted for in post-processing. Besides their mass evolution, we also consider the influence of the environment on the size evolution of the sub-grid clusters, and the subsequent effects that such evolution has on the survivability of cluster populations.

We assume that our sub-grid stellar clusters are well described by a King profile of parameter $W_0 = 5$, and we follow their disruption until their masses are below $100 M_\odot$, with the aim of tracking the entire evolution of massive clusters. Given that part of the mechanisms considered in this work are already discussed by Kruijssen et al., (2011) and Pfeffer et al., (2018), we briefly summarize them here and provide a discussion of the new ingredients of the model.

We describe the total cluster mass evolution as a function of time as a combination of stellar evolution, two-body relaxation and tidal shocks,

$$\left(\frac{dm}{dt}\right)_{\text{dis}} = \left(\frac{dm}{dt}\right)_{\text{ev}} + \left(\frac{dm}{dt}\right)_{\text{rlx}} + \left(\frac{dm}{dt}\right)_{\text{sh}}. \quad (7.1.51)$$

Here, the first term describes the mass loss due to stellar evolution, and the second and third terms describe the evolution due dynamical processes, i.e. relaxation and tidal shocks, respectively. We self-consistently calculate the mass loss due to stellar evolution of stars within the cluster assuming a Chabrier IMF using the SNAIL stellar library (see Sect. 7.1.2.3), and using the Padova stellar evolutionary tracks that include pulsating AGB stars (Vassiliadis and Wood, 1993; Girardi et al., 2000). After accounting for dynamical evolution, we apply the stellar evolution disruption term as a fractional variation of the cluster mass, which is given by the ratio of the stellar particle mass at the current time relative to the previous timestep. Finally, we return the mass lost due to dynamical processes to the sub-grid field component within the host stellar particle.

Dynamical mass loss is governed by the local tidal field, which we calculate as a tensor at the location of the host stellar particle (Eq. 7.1.29). This tensor represents the change of the gravitational potential over a certain spatial scale, and we use the forward difference approximation to evaluate the first-order numerical derivative of the gravitational acceleration at the position of the host star. We evaluate it over a spatial interval of 2.5 per cent of the gravitational stellar softening, $\Delta x = 0.025 \times 175 \text{ pc} = 4.4 \text{ pc}$, which roughly corresponds to the initial half-mass radius of our stellar clusters. We discuss the optimal spatial scale to recover the gravitational potential in Appendix 7.4.3, together with the effect of evaluating the tidal tensor on larger scales.

The tidal field strength that sets the tidal radius of stellar clusters on circular orbits is $T = -\partial^2\Phi/\partial r^2 + \Omega^2$ (King, 1962; Renaud et al., 2011), which can be approximated using the maximal eigenvalue of the tidal tensor as

$$T = \max(\lambda_i) + \Omega^2, \quad (7.1.52)$$

where the angular velocity is relevant to account for the effect of the orbit (see Renaud et al. 2011, and appendix C in Pfeffer et al. 2018).

Two-body interactions among stars within stellar clusters lead to a slow, but continuous disruption of the cluster (e.g. Ambartsumian, 1938; Spitzer, 1940; Hénon, 1961; Lamers et al., 2005b). In our model, we consider that relaxation mass loss is well described as a combination of the cluster mass loss in an isolated regime and the evolution in a tidal field,

$$\left(\frac{dm}{dt}\right)_{\text{rlx}} = \left(\frac{dm}{dt}\right)_{\text{rlx,st}} + \left(\frac{dm}{dt}\right)_{\text{rlx,tid}}. \quad (7.1.53)$$

In an isolated regime, the mass evolution of a stellar cluster can be described as (e.g. Spitzer, 1987)

$$\left(\frac{dm}{dt}\right)_{\text{rlx,st}} = -\frac{\xi_0 m}{t_{\text{rh}}}, \quad (7.1.54)$$

where $\xi_0 = 0.0074$ is the probability of one star evaporating over a relaxation time-scale t_{rh} (Spitzer, 1987; Gieles and Baumgardt, 2008). The relaxation time-scale at the cluster half-mass radius can be described as (Spitzer and Hart, 1971; Giersz and Heggie, 1994)

$$t_{\text{rh}} = \frac{0.138\sqrt{N}r_{\text{h}}^{3/2}}{\sqrt{MG \ln(0.11N)}}, \quad (7.1.55)$$

where $N = m/\bar{M}$ is the mean number of stars in the cluster, r_{h} is the half-mass radius of the cluster, and $\bar{M} = 0.41 M_{\odot}$ is the mean stellar mass in a Chabrier, (2005) IMF integrated in the range $0.08 \leq m/M_{\odot} \leq 120$.

In order to describe the mass loss due to two-body interactions for clusters in a tidal field, we adopt the model by Lamers et al., (2005b), in which the mass loss rate is proportional to the cluster mass and the tidal field strength,

$$\left(\frac{dm}{dt}\right)_{\text{rlx,tid}} = -\frac{m}{t_{\text{dis}}} = -\frac{M_{\odot}}{t_{0,\odot}} \left(\frac{m}{M_{\odot}}\right)^{1-\gamma} \left(\frac{T}{T_{\odot}}\right)^{1/2}, \quad (7.1.56)$$

where $\gamma = 0.62$ and $t_{0,\odot} = 21.3$ Myr is the dissolution time-scale in a logarithmic potential at the galactocentric position of the Sun for a cluster described by a King profile with $W_0 = 5$. The tidal field strength at the same radius is $T_{\odot} \approx 7.01 \times 10^2 \text{ Gyr}^{-2}$ for a circular velocity of 220 km s^{-1} . If the cluster is in a fully compressive field, i.e. if the three eigenvalues are negative, we consider that there is only disruption from the isolated regime term.

Sudden tidal shocks from perturbations of the gravitational potential can lead to an increase in the energy of the stars (e.g. Prieto and Gnedin, 2008). These interactions can occur when eccentric orbits bring clusters through the galactic disk and bulge (e.g. Aguilar et al., 1988), or early in the lifetime of the cluster due to strong shocks with the cold, clumpy ISM (e.g. Gieles et al., 2006; Elmegreen and Hunter, 2010; Kruijssen et al., 2011). The disruption caused by a given tidal shock can be analytically derived for a stellar cluster

with a King profile (Kruijssen et al., 2011). To first and second order, the mass-loss rate is proportional to the cluster half-mass radius and the strength of the shock,

$$\left(\frac{dm}{dt}\right)_{\text{sh}} = -\frac{m}{t_{\text{sh}}} = \frac{-20.4 M_{\odot}}{\text{Myr}} \left(\frac{r_{\text{h}}}{4 \text{ pc}}\right)^3 \left[\sum_{ij} \left| \frac{\int T_{ij} dt}{10^2 \text{ Gyr}^{-1}} \right|^2 A_{\text{w},ij} \right] \left(\frac{\Delta t_{\text{sh}}}{10 \text{ Myr}}\right)^{-1}, \quad (7.1.57)$$

where t_{sh} corresponds to the disruption time for stellar shocks, Δt_{sh} is the shock duration, and $A_{\text{w},ij}$ are the Weinberg correction factors that describe the amount of injected energy lost due to adiabatically expanding the cluster (Weinberg, 1994a,b,c; Gnedin, 2003). For each stellar particle containing a cluster population, we follow the time evolution of their tidal tensors, and we integrate over the full duration of the shock for each tidal tensor component. For a given tidal shock, the appropriate amount of tidal heating is only applied when a valid minimum is identified, i.e. when it is smaller than 0.88 times the value of the last maximum, in any of the components of the tidal tensor.

In this formalism, the ratio of the shock-timescale to the shock duration can be written in terms of the cluster mass, the half-mass radius and the strength of the tidal shock as

$$\left(\frac{t_{\text{sh}}}{\Delta t_{\text{sh}}}\right)_{\text{K11}} = 49.18 \left(\frac{m}{10^4 M_{\odot}}\right) \left(\frac{r_{\text{h}}}{4 \text{ pc}}\right)^{-3} \left(\sum_{ij} \left| \frac{\int T_{ij} dt}{10^2 \text{ Gyr}^{-1}} \right|^2 A_{\text{w},ij} \right)^{-1}. \quad (7.1.58)$$

For a given stellar cluster, this ratio indicates how disruptive a shock is regardless of its duration.

Alternatively, we also consider the formalism for the mass-loss rate due to tidal shocks introduced by Webb et al., (2019a) (and Chapter 3). The authors study the tidal shock-induced disruption in a suite of N-body simulations of stellar clusters characterized by a Plummer profile, and provide a best fit description of the mass-loss rate,

$$\left(\frac{dm}{dt}\right)_{\text{sh}} = \frac{-22.85 M_{\odot}}{\text{Myr}} \left(\frac{m}{10^4 M_{\odot}}\right)^{0.41} \left(\frac{r_{\text{h}}}{4 \text{ pc}}\right)^{1.77} \left[\sum_{ij} \left| \frac{\int T_{ij} dt}{10^2 \text{ Gyr}^{-1}} \right|^{1.16} \right] \left(\frac{\Delta t_{\text{sh}}}{10 \text{ Myr}}\right)^{-1}, \quad (7.1.59)$$

which they find to be relatively independent of the cluster profile considered. In this formalism, the ratio of the shock timescale to the shock duration can be calculated as

$$\left(\frac{t_{\text{sh}}}{\Delta t_{\text{sh}}}\right)_{\text{W19}} = 43.77 \left(\frac{m}{10^4 M_{\odot}}\right)^{0.59} \left(\frac{r_{\text{h}}}{4 \text{ pc}}\right)^{-1.77} \left(\sum_{ij} \left| \frac{\int T_{ij} dt}{10^2 \text{ Gyr}^{-1}} \right|^{1.16} \right)^{-1}, \quad (7.1.60)$$

in terms of the cluster mass and half-mass radius and the tidal field strength.

In order to evaluate which formalism is more disruptive on a given stellar cluster, we look at the ratio of the N-body fit timescale (Eq. 7.1.60) to the analytical timescale (Eq. 7.1.58),

$$\frac{t_{\text{sh,W19}}}{t_{\text{sh,K11}}} = 0.89 \left(\frac{m}{10^4 M_{\odot}}\right)^{-0.41} \left(\frac{r_{\text{h}}}{4 \text{ pc}}\right)^{1.23} \left(\frac{\sum_{ij} \left| \frac{\int T_{ij} dt}{10^2 \text{ Gyr}^{-1}} \right|^2 A_{\text{w},ij}}{\sum_{ij} \left| \frac{\int T_{ij} dt}{10^2 \text{ Gyr}^{-1}} \right|^{1.16}} \right). \quad (7.1.61)$$

For a given cluster half-mass density, the phenomenological fit predicts a stronger disruptive effect for tidal shocks, thus disrupting stellar clusters more quickly than in the analytical model. We also find that, for a given tidal shock, the N-body fit formalism favours the disruption of compact and low-mass clusters.

Our ‘on-the-fly’ description of the mass evolution of stellar clusters accounts for most of the physical processes that are suggested to dominate cluster disruption. The only missing relevant disruption mechanism is the effect of dynamical friction, i.e. the mass loss due to the in-spiral of the most massive stellar clusters towards the centre of galaxies. Applying this disruption mechanism during their cosmic evolution would result in stellar particles experiencing a diversity of forces due to their sub-grid cluster population. Hence, we can only account for this mechanism in post-processing with an approximate treatment. For that, we calculate the dynamical friction timescale for a cluster of mass m as (Lacey and Cole, 1993)

$$t_{\text{df}} = \frac{f(\epsilon)}{2B(v_c/\sqrt{2}\sigma)} \frac{\sqrt{2}\sigma r_c^2}{Gm \ln(\Lambda)}, \quad (7.1.62)$$

where $r_c(E)$ is the radius of a circular orbit with the same energy E , $\sigma(r_c)$ is the stellar velocity dispersion within r_c , and v_c is the circular velocity at that orbit. The Coloumb logarithm is calculated as $\ln(\Lambda) = \ln(1 + M(r_c)/m)$, with $M(r_c)$ being the total mass within the radius r_c , and the term $B(v_c/\sqrt{2}\sigma)$ is defined as $B(X) \equiv \text{erf}(X) - 2X \exp(-X^2)/\sqrt{\pi}$. Lastly, $\epsilon = J/J_c(E)$ corresponds to the circularity parameter, i.e. the angular momentum relative to that of a circular orbit of the same energy, and the term $f(\epsilon) = \epsilon^{0.78}$ (Lacey and Cole, 1993) accounts for the orbital eccentricity of the stellar cluster.

We calculate this timescale for all stellar clusters at each snapshot, and we identify their current host galaxy using the **SUBFIND** algorithm (Springel et al., 2001; Dolag et al., 2009). We consider that clusters are completely disrupted at the first snapshot in which the dynamical friction timescale is shorter than their age, $t_{\text{df}} < \tau_{\text{cl}}$, and we set the mass to zero. This is a simplified approach to account for the effects of dynamical friction, as more elaborate descriptions are available in the literature (e.g. Miller et al., 2020), but it suffices our purposes given the limitations of our sub-grid formalism.

Lastly, we also study the effect that the galactic environment has on the size of the sub-grid stellar clusters, and how this evolution in turn affects the survivability of stellar clusters. For that, we consider two scenarios. In the first one, we do not evolve the size of the clusters, which implies that their disruption solely depends on their mass. In the second scenario, we follow a strategy similar to the one applied to describe the total mass loss. We describe the time evolution of the half-mass radii of stellar clusters as a combination of the effects produced by stellar evolution, two-body interactions and tidal shocks,

$$\frac{dr_{\text{h}}}{dt} = \left(\frac{dr_{\text{h}}}{dt}\right)_{\text{ev}} + \left(\frac{dr_{\text{h}}}{dt}\right)_{\text{rlx}} + \left(\frac{dr_{\text{h}}}{dt}\right)_{\text{sh}}, \quad (7.1.63)$$

where the first and second terms correspond to the adiabatic expansion due to stellar evolution mass loss and two-body interactions, and the last term describes the shock-driven size evolution. As for the mass evolution, the stellar evolution term is only accounted for after applying the effects of the dynamical processes. We calculate the first term as a

fractional change to the size, which is given by the ratio of the stellar particle mass at the previous timestep relative to the current time.

The adiabatic expansion due to two-body interactions includes two regimes, depending on whether the cluster is in isolation or in a tidal environment (Gieles et al., 2011). We evaluate these regimes according to the ratio of the half-mass radius of the cluster relative to its tidal radius (Eq. 7.1.50), and we calculate the appropriate variation of the half-mass radius for a cluster of mass m as

$$\left(\frac{dr_h}{dt}\right)_{\text{rlx}} = \begin{cases} 0.0926 r_h t_{\text{rh}}^{-1} & \text{if } r_h/r_t < 0.05, \\ \left(\frac{0.0743}{t_{\text{rh}}} + \frac{2\Delta m_{\text{rlx}}}{m}\right) r_h & \text{if } r_h/r_t > 0.05, \end{cases} \quad (7.1.64)$$

where t_{rh} is the relaxation timescale at the half-mass radius (Eq. 7.1.55), and $\Delta m_{\text{rlx}} = (dm/dt)_{\text{rlx}} \Delta t$ corresponds to the mass lost due to two-body interactions over the timestep Δt .

Tidal interactions can either cause compression or elongations of stellar clusters, and their effect on the size evolution is more complex. Following Kruijssen et al., (2011) and Gieles and Renaud, (2016), we model the shock-driven evolution as

$$\left(\frac{dr_h}{dt}\right)_{\text{sh}} = (f - 1) \frac{\Delta E}{\Delta t} \frac{r_h}{E}, \quad (7.1.65)$$

where $E = 0.4Gm/(2r_h)$ is the total energy of a self-gravitating stellar system in virial equilibrium per unit cluster mass (e.g. Spitzer, 1987), and $\Delta E = (1/6)I_{\text{tid}}\bar{r}^2$ is the average energy change of the ensemble of stars in the cluster due to the tidal shock. The factor f is taken to be $\log_{10}(f) = -0.25[\log_{10}(I_{\text{tid}}r_h^2/(9|E|)) - 1]$ (Gieles and Renaud, 2016). We define the tidal heating parameter as $I_{\text{tid}} = \sum_{ij} (\int T_{ij} dt)^2 A_{w,ij}$ when using the analytical formalism for shock disruption (Prieto and Gnedin, 2008), and as $I_{\text{tid}} = \sum_{ij} |\int T_{ij} dt|^{1.16}$ when using the N -body based description (Webb et al., 2019a).

7.2 Initial conditions

We are interested in studying the formation and evolution of stellar clusters in a cold, clumpy ISM within L^* galaxies similar to our Milky Way. For that, we use two different setups of Milky Way-mass galaxies. We test our algorithms to calculate the gas surface density and the epicyclic frequency on the low resolution isolated disk initial conditions from the AGORA project (Kim et al., 2014, 2016) (see Section 7.4). Additionally, we aim at using the cosmological zoom-in initial conditions for MW09 from the E-MOSAICS project (Pfeffer et al., 2018; Kruijssen et al., 2019a) to study the evolution of stellar clusters over cosmic history. We provide further details on the initial conditions below, and summarize their main parameters in Table 7.1.

7.2.1 Isolated disk

The suite of isolated initial conditions offered by the AGORA project (Kim et al., 2014, 2016) were produced with the code `makenewdisk` (Springel et al., 2005), which is based on

Table 7.1: Main parameters used in our simulations. From left to right, they correspond to the baryonic target mass, the mass of high-resolution dark matter particles, the minimum comoving gravitational softening of the gas cells, the comoving and physical gravitational softenings of high-resolution dark matter and stellar particles, respectively, and the density and temperature thresholds used as star formation criteria.

Isolated galaxy simulation								
m_{target} [M_{\odot}]	m_{DM} [M_{\odot}]	$\epsilon_{\text{min, gas}}$ [pc]	$\epsilon_{\text{DM}}^{\text{com}}$ [h^{-1} cpc]	$\epsilon_{\text{stars}}^{\text{com}}$ [h^{-1} cpc]	$\epsilon_{\text{DM}}^{\text{ph}}$ [pc]	$\epsilon_{\text{stars}}^{\text{ph}}$ [pc]	n_{th} [H/cm^{-3}]	T_{th} [K]
8.59×10^4	1.074×10^6	80	–	–	300	80	1	5×10^3
Cosmological zoom-in simulation								
m_{target} [M_{\odot}]	m_{DM} [M_{\odot}]	$\epsilon_{\text{min, gas}}^{\text{com}}$ [h^{-1} cpc]	$\epsilon_{\text{DM}}^{\text{com}}$ [h^{-1} cpc]	$\epsilon_{\text{stars}}^{\text{com}}$ [h^{-1} cpc]	$\epsilon_{\text{DM}}^{\text{ph}}$ [pc]	$\epsilon_{\text{stars}}^{\text{ph}}$ [pc]	n_{th} [H/cm^{-3}]	T_{th} [K]
2.26×10^5	1.44×10^6	56.3	821.9	450.2	319.5	175	10	1.5×10^4

solving the Jeans equations for a quasi-equilibrium multi-component collisionless system, assuming a Maxwellian particle distribution function. These galaxies are described by four components: a DM halo, a stellar bulge and disk, and a gas disk. These components are generated by stochastically drawing positions and velocities from analytical distributions.

The mass of the DM halo is $M_{200} = 1.07 \times 10^{12} M_{\odot}$. This component follows a Navarro-Frenk-White density profile (Navarro et al., 1997) with a concentration parameter of $c = 10$ and spin parameter $\lambda = 0.04$. The stellar and gas disks are each described by exponential profiles as a function of the cylindrical radius R . The stellar disk has a mass of $M_{\text{d}} = 4.30 \times 10^{10} M_{\odot}$, a radial scale length, $h_{\text{R}} = 3.43$ kpc, and a vertical scale height, $h_{\text{z}} = 0.1h_{\text{R}}$. The gas disk follows a similar distribution with a gas fraction $f_{\text{gas}} = M_{\text{d, gas}}/M_{\text{d}} = 20$ per cent. The stellar bulge is described by a Hernquist, (1990) profile and has a mass of $M_{\text{b}} = 0.1M_{\text{d}}$.

The AGORA suite of initial conditions offers three different resolutions, only differing in the number of particles used to describe the multiple components. We use the initial conditions at the lowest resolution available. At this resolution, the DM halo, and the gas and stellar disks are described by 10^5 particles each, and the stellar bulge by 1.25×10^4 particles. Thus, the baryonic target mass is $m_{\text{gas}} \simeq 8.59 \times 10^4 M_{\odot}$, which is similar to the baryonic target mass in the cosmological zoom-in simulations, $m_{\text{gas}} \simeq 2.26 \times 10^5 M_{\odot}$.

In the isolated disk, the gas is initially at 10^4 K and at solar metallicity $Z_{\odot} = 0.0134$ (Asplund et al., 2009), and it quickly settles into equilibrium. We evolve this simulation over 1 Gyr until the SFR stabilizes. As described in Section 7.1.1, we use an adaptive scheme for the gravitational softening of the gas cells that is proportional to the cell radius. The minimum softening is set at $\epsilon_{\text{min, gas}} = 80$ pc, and the Plummer-equivalent gravitational softenings of the collisionless particles are $\epsilon_{\text{DM}} = 300$ pc for the DM, $\epsilon_{\text{stars}} = 80$ pc for the stars formed in the simulation and $\epsilon_{\text{bulge, disk}} = 100$ pc for the stellar particles present in the initial conditions.

7.2.2 Cosmological zoom-in galaxy

To study the cosmic formation and evolution of stellar cluster populations, we use ‘zoomed resimulations’ (Katz and White, 1993). These type of simulations resimulate a dark matter halo selected from a cosmological periodic volume simulation, which allows to follow the evolution of individual galaxies and their environment at higher resolution than the parent simulation. In particular, we use the initial conditions for the Milky Way-mass halo MW09 presented in Pfeffer et al., (2018).

The parent periodic volume of this halo is the Recal-L025N0752 simulation presented by Schaye et al., (2015). As described by Pfeffer et al., (2018), this galaxy belongs to the subset of ten galaxies already discussed by Mateu et al., (2017) that correspond to the most disc-dominated galaxies at $z = 0$ from the volume-limited sample of galaxies around $7 \times 10^{11} < M_{200}/M_{\odot} < 3 \times 10^{12}$ within that volume. After selecting the region of interest in the periodic volume, the zoomed initial conditions are created using the second-order Lagrangian perturbation theory method (Jenkins, 2010) and the public Gaussian code `Panphasia` (Jenkins, 2013). To do that, the same linear phases and cosmological parameters as for the parent volume were adopted (see table B1 in Schaye et al., 2015), which correspond to those provided by the *Planck* satellite: $\Omega_m = 0.307$, $\Omega_b = 0.048$, $\Omega_{\Lambda} = 0.693$, and $\sigma_8 = 0.829$. The *Hubble* constant is $H_0 = 100h$ km s⁻¹ Mpc⁻¹, with $h = 0.677$ (Planck Collaboration et al., 2014).

The initial conditions are generated with three resolutions for the DM particles, with decreasing mass resolution by a factor of $\sim 10^3$ between the highest and lowest. In each case, only the immediate environment of the galaxy is simulated at high resolution, and at $z = 0$, the Lagrangian region is roughly spherical with a radius of ~ 600 proper kpc centred on the target galaxy. Beyond this radius, the large-scale environment is described by DM particles, whose resolution decreases with distance from the fully-sampled region, and by large gas cells that are not allowed to refine and that are evolved adiabatically (Section 7.1.1).

In order to facilitate the comparison between our results and those from the E-MOSAICS project, we decide to match their mass and spatial resolution as closely as possible. For that, we keep the mass resolution of the cells that are allowed to refine to a target mass of roughly $m_{\text{target}} = 2.26 \times 10^5 M_{\odot}$. In order to resolve the substructure observed in the cold ISM of nearby galaxies (e.g. Colombo et al., 2019), which corresponds to the natal sites of massive cluster formation (e.g. Holtzman et al., 1992; Adamo et al., 2015) and that produce the tidal shocks that dominate stellar cluster disruption (e.g. Gieles et al., 2006; Elmegreen and Hunter, 2010), we need to reduce the gravitational softening relative to the values used in the E-MOSAICS project. Thus, we set the Plummer-equivalent, comoving gravitational softening of the collisionless particles to be $450.2 h^{-1}\text{cpc}$ for the stars and $821.9 h^{-1}\text{cpc}$ for the high-resolution DM particles until $z = 2.8$. Afterwards, their softenings are kept constant at 175 pc for the stars and 319.5 pc for the high-resolution DM particles. Following the strategy adopted by the IllustrisTNG simulations (Nelson et al., 2018; Pillepich et al., 2018), we set the minimum comoving gravitational softening of the gas cells to be an eighth of the comoving gravitational softening of the stellar particles, $\epsilon_{\text{min,gas}}^{\text{com}} = 56.3 h^{-1}\text{cpc}$.

Table 7.2: Summary of the four cluster formation scenarios considered in the isolated galaxy simulation. For each model, the bold font represents the ingredient that has been changed.

Name	Cluster formation	
	CFE	ICMF
Fiducial	$\Gamma(\Sigma_g, \kappa, Q)$ Kruijssen, (2012)	Double Schechter function $M_{\text{cl,min}}(\Sigma_g, \kappa, Q)$ & $M_{\text{cl,max}}(\Sigma_g, \kappa, Q)$ Trujillo-Gomez et al., (2019)
$\alpha = -2$	$\Gamma(\Sigma_g, \kappa, Q)$ Kruijssen, (2012)	Power law of slope $\alpha = -2$
$\Gamma = 10\%$	$\Gamma = 10\%$	Double Schechter function $M_{\text{cl,min}}(\Sigma_g, \kappa, Q)$ & $M_{\text{cl,max}}(\Sigma_g, \kappa, Q)$ Trujillo-Gomez et al., (2019)
No formation physics	$\Gamma = 10\%$	Power law of slope $\alpha = -2$

We identify galaxies in this resimulated zoom-in volume using the SUBFIND algorithm (Springel et al., 2001; Dolag et al., 2009). Firstly, the FoF algorithm (Friends-of-Friends Davis et al., 1985) is used to identify collapsed DM structures using a linking length of 0.2 times the mean interparticle distance. Then, gas and stars are associated to the nearest DM particle and its FoF group or halo. Within those halos, the SUBFIND algorithm identifies gravitationally bound substructures which are referred to as ‘subgroups’ or ‘galaxies’ interchangeably.

7.3 Preliminary results

In this section, we present some preliminary results on the formation of stellar clusters in the isolated galaxy initial conditions. In order to showcase the potential of this new approach, we have evolved these initial conditions with four different cluster formation models, which are described in Table 7.2. This allows us to model four parallel stellar cluster populations within the same galactic environment. To simplify their comparison, in these models we only switch on and off the environmental-dependence of two physical ingredients setting the formation of stellar cluster populations: the CFE and the shape of the ICMF. For that, we assume that all the stellar cluster populations have the same initial half-mass radius of $r_h = 4$ pc, which does not evolve over time, and that all the populations disrupt according to the shock formalism by Kruijssen et al., (2011). Additionally, as we are interested in the differences regarding cluster formation, we ignore the effects of dynamical friction on the evolved cluster populations.

We assume a constant star formation efficiency per free-fall time of $\epsilon_{\text{ff}} = 5$ per cent, and we evolve the isolated galaxy initial conditions with its four parallel stellar cluster populations over 1 Gyr. After this time, the initial starburst settles into a constant SFR of $\sim 3\text{--}4 M_{\odot}\text{yr}^{-1}$ (see Fig.7.1). These values are consistent with the current observed SFR in the Milky Way (e.g. Murray and Rahman, 2010; Robitaille and Whitney, 2010; Chomiuk

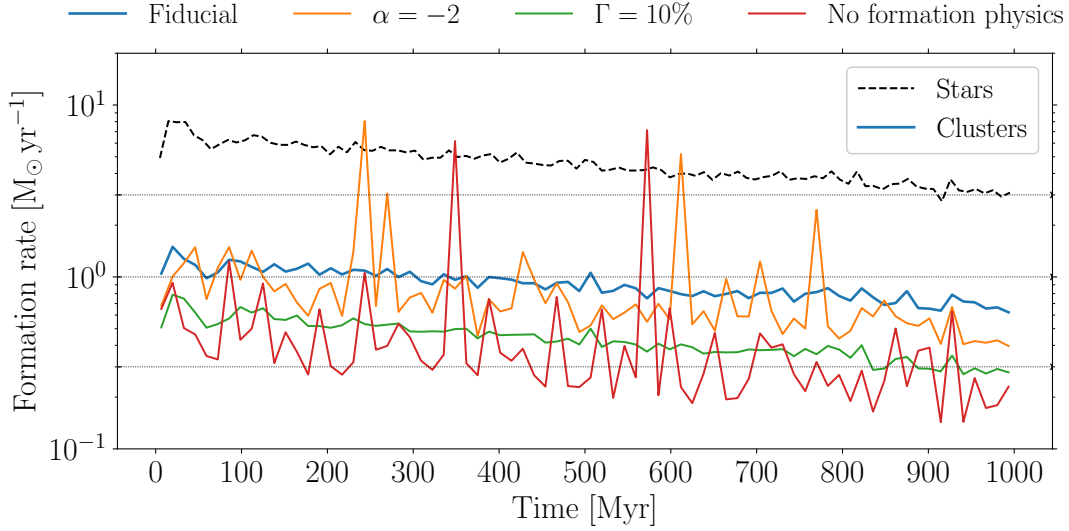


Figure 7.1: Star and cluster formation rates in the isolated galaxy simulation as a function of simulated time. The dashed line corresponds to the SFR, and the solid lines represent the cluster formation rates of the four cluster formation scenarios (Table 7.2).

and Povich, 2011; Licquia and Newman, 2015). We show in Fig. 7.2 the phase diagram of the gas cells, as well as the natal gas conditions of the stellar particles. This showcases that these simulations allow us to study the formation and evolution of stars and stellar clusters in a cold, clumpy ISM.

In Fig. 7.1, we also include the cluster formation rates of the four models considered. We find that the fiducial environmentally-dependent model forms clusters at a rate of $\sim 1 \text{ M}_{\odot} \text{ yr}^{-1}$, and the behaviour of the other three scenarios can be understood based on which formation ingredient is kept constant. When we fix the shape of the ICMF to be a power-law of slope $\alpha = -2$, there is a higher probability of sampling extremely massive clusters, and so, occasionally there is more mass forming in clusters than in their host stellar particles. On the other hand, fixing the CFE to a constant value of 10 per cent leads to lower formation rates than in those scenarios in which this value is environmentally-dependent. Combining both effects, the cluster model that does not include formation physics forms clusters at an overall lower and noisier rate than the fiducial model.

Similar results can be seen in the cluster mass distributions shown in Fig. 7.3. The relatively quiescent gas conditions in this isolated disk simulation result in predicted environmentally-dependent upper mass scales around $\sim 10^5 \text{ M}_{\odot}$. These values are about three orders of magnitude lower than the maximum cluster mass that can form from a power-law mass function, thus explaining the noisier cluster formation rates of the models with a fixed ICMF. In these models, stellar clusters as massive as $\sim 10^6\text{--}10^7 \text{ M}_{\odot}$ can form regardless of the gas conditions, which is in contradiction with the lack of such young massive clusters in the Milky Way or in M31 (Portegies Zwart et al., 2010; Adamo et al., 2020). This represents a strong drawback for those models that suggest that the natal gas

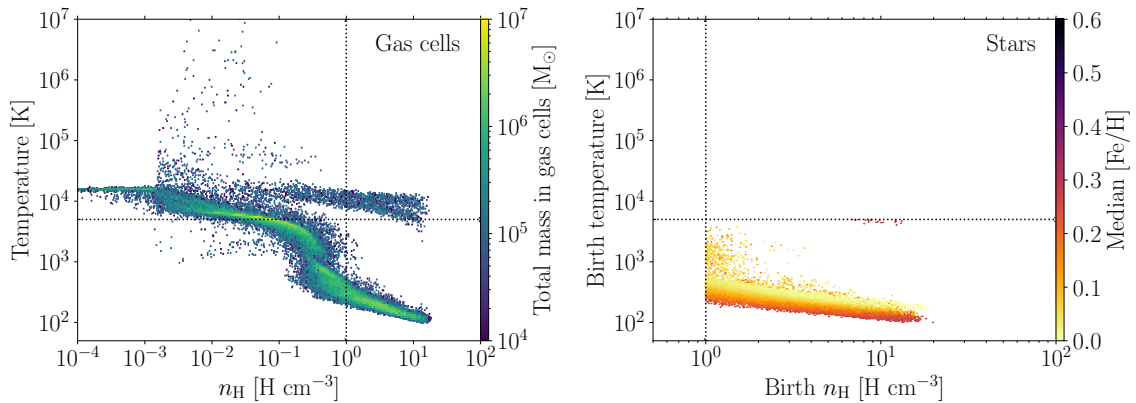


Figure 7.2: Phase diagram of the gas cells (*left panel*), and phase diagram of the natal conditions of stellar particles in the evolved isolated galaxy simulation. The hexagonal bins are colour-coded by the total mass in the gas cells per bin, and by the median stellar metallicity, respectively. The lower-right quadrant defined by the black dotted lines indicate the criteria considered for star formation: densities higher than $n_{\text{H}} \geq 1 \text{ H cm}^{-3}$ and temperatures lower than $T \leq 5 \times 10^3 \text{ K}$.

conditions do not influence the shape of the ICMF. Additionally, in Fig. 7.3 we see that fixing the CFE leads to a reduction of 50 per cent in the number of clusters (bottom row) relative to the corresponding environmentally-dependent formation scenario (upper row).

These preliminary results correspond to the evolution of an isolated Milky Way-mass galaxy with a multiphase ISM over 1 Gyr. In order to fully discriminate between cluster formation and evolution models, we need to simulate the formation and evolution of stellar clusters alongside their galaxies over cosmic history, and compare the resulting cluster demographics to those of the Milky Way and other extragalactic systems. We will address this issue in the paper currently in preparation.

7.4 Appendices

Here we present a description of the methods used to estimate the global gas properties, i.e. gas surface density and epicyclic frequency, at runtime.

7.4.1 Computing the gas surface density

A critical ingredient in our formalism of stellar cluster formation is the global gas surface density in the ISM. This is a challenging quantity to compute at runtime because the hydrodynamics is done at the local scale of each gas cell, which is below 100 pc in the star-forming regions. This section describes the method developed to calculate it. Using hydrodynamical simulations of isolated disks, we demonstrate that this method leads to good agreement with the azimuthally-averaged gas surface density radial profile.

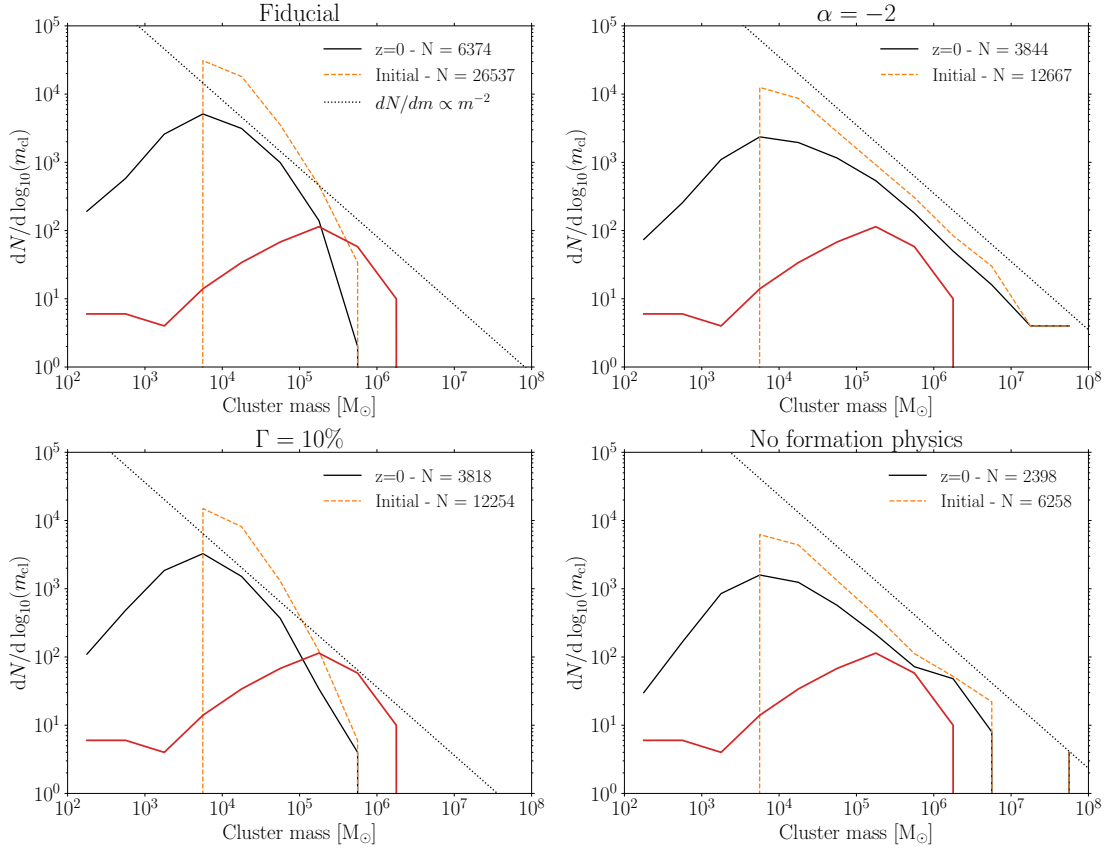


Figure 7.3: Initial and final cluster mass functions for the four cluster formation models in the isolated galaxy simulation. The orange dashed and the black solid lines represent the initial and final cluster masses in the stellar cluster populations, respectively. As a comparison, we also include a pure power-law distribution (black dotted line) and the mass function of stellar clusters in the Milky Way (red solid line; Harris, 2010). The total initial and final numbers of stellar clusters in each model are included in the legend.

In order to estimate the global gas surface density, we assume that the gas disk is in hydrostatic equilibrium (e.g. Elmegreen, 1989; Blitz and Rosolowsky, 2004; Krumholz and McKee, 2005) such that the mid-plane gas pressure can be written as

$$P_{\text{mp}} = \frac{\pi}{2} G \phi_{\text{P}} \Sigma_{\text{g}}. \quad (7.4.1)$$

This expression can be inverted to express the gas surface density Σ_{g} as

$$\Sigma_{\text{g}} = \sqrt{\frac{2P_{\text{mp}}}{\pi G \phi_{\text{P}}}}, \quad (7.4.2)$$

in terms of the mid-plane pressure P_{mp} and the factor ϕ_{P} describing the gravitational contribution of stars (Eq. 7.1.28). Due to the inclusion of the cold phase of the ISM in our description of the cosmic environment, the local total gas cell pressure of star-forming gas is dominated by the local turbulent pressure of the star-forming regions, $P \simeq P_{\text{turb}} = \rho \sigma_{\text{cl}}^2$, where σ_{cl} is the cloud velocity dispersion. Despite reproducing observations of GMCs in the local Universe (e.g. Colombo et al., 2019), this implies that the local total gas cell pressure in our simulations is not a good approximation of the mid-plane pressure of the disk. Additionally, stellar feedback can change the structure of the galaxy, which induces a time dependence of the galactic properties. Thus, standard methods that rely on local gas cell properties to calculate the gas surface density are no longer valid, and an alternative approach is needed to estimate it.

Our solution is to perform a neighbour search around each newborn star, and use the neighbour-weighted properties to calculate an approximation to the mid-plane pressure. Due to the global nature of the mid-plane pressure, we are required to survey a large volume to have an appropriate description of the large-scale gas distribution. We consider neighbours in a volume of radius $r = f \times h$, with the factor being $f = 5$ and $f = 10$ in the case of the isolated galaxy and the cosmological zoom-in initial conditions, respectively. The scale h is defined as

$$h = \max(h_{\text{cl}}, \epsilon_{\text{star}}), \quad (7.4.3)$$

and compares the size of the natal overdensity (Sect. 7.1.2.2) to the stellar gravitational softening. Given the strong dependence of the size of the natal overdensity on the gas density of the parent cell (Fig. 7.4), we impose a floor on the scale h to avoid high-density regions sampling volumes that are too small. In addition, in cases where the newborn star lies towards the inner part of the galactic potential well, we reduce this scale to be $h = h_{\text{cl}}$. This reduction is helpful to avoid using volumes that are too large and smooth over the large-scale features in the distribution of the ISM. To establish if a star particle is near the galactic center, we calculate the distance to the neighbour with the lowest gravitational potential energy. If this neighbour is within the edge of the region (i.e. $d < h/2$), we assume that the star particle is near the center of the galactic potential.

Within the chosen volume, we calculate a neighbour-weighted gas density and isotropic gas velocity dispersion. The neighbour contributions are weighted according to a Top-hat

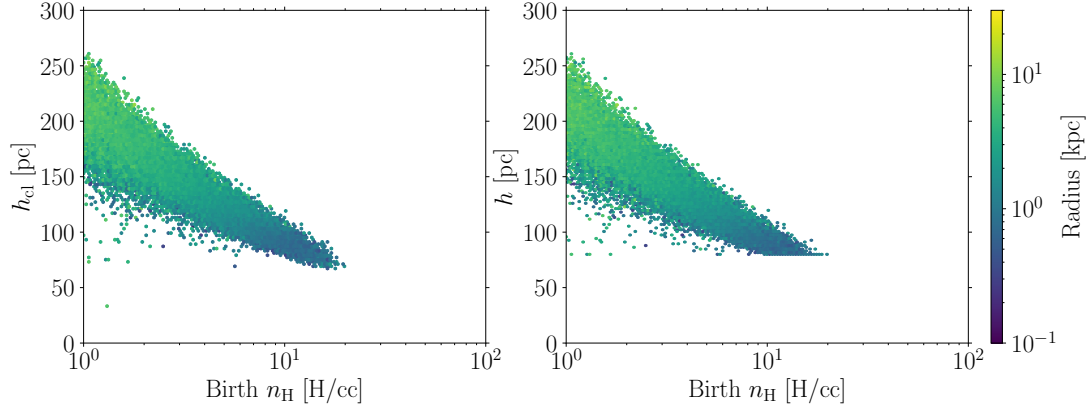


Figure 7.4: Size of the natal overdensity (*left*) and value of the scale h defining the volume explored (*right*) as a function of the birth gas density for all stellar particles that have formed in the isolated galaxy simulation, colour-coded by their galactocentric radius.

kernel, $w'_k = 1$, such that the density is computed as

$$\rho_{\text{ngbs}} = \frac{\sum_{k=0}^N m_k}{4\pi(fh)^3/3}, \quad (7.4.4)$$

and the isotropic velocity dispersion becomes,

$$\sigma_{\text{ngbs}}^2 = \frac{1}{3} \sum_i^3 \left[\frac{1}{N} \sum_{k=0}^N (v_i^k - v_i^{\text{star}})^2 - \left[\frac{1}{N} \sum_{k=0}^N (v_i^k - v_i^{\text{star}}) \right]^2 \right]. \quad (7.4.5)$$

Here N is the number of neighbouring gas cells within the volume considered. Using these quantities, the neighbour-weighted turbulent pressure is calculated as

$$P_{\text{mp}} \simeq P_{\text{ngbs}} = \rho_{\text{ngbs}} \sigma_{\text{ngbs}}^2. \quad (7.4.6)$$

Fig. 7.5 demonstrates the good agreement between this approximation of the global turbulent gas pressure and the mid-plane pressure.

Within the same volume, we also calculate the stellar velocity dispersion and the total mass in stars and in gas, from which the gas fraction can be computed. With these quantities, we can calculate the contribution of stars to the mid-plane pressure ϕ_P consistently. Finally, using the neighbour-weighted approximation to the mid-plane pressure and ϕ_P , we compute the global gas surface density using Eq. 7.4.2.

We evaluate the ability of this neighbour-weighted method to reproduce the global state of the gas by comparing the values calculated at runtime for the young stellar population with the azimuthally-averaged radial profile from the last snapshot in Fig. 7.5. The fact that both velocity dispersions are slightly too high relative to the corresponding vertical velocity dispersions profiles reflects that some radial motion is being captured by the assumption of isotropy. Overall, we find that the neighbour-based method provides a good description of the large-scale distribution of the gas.

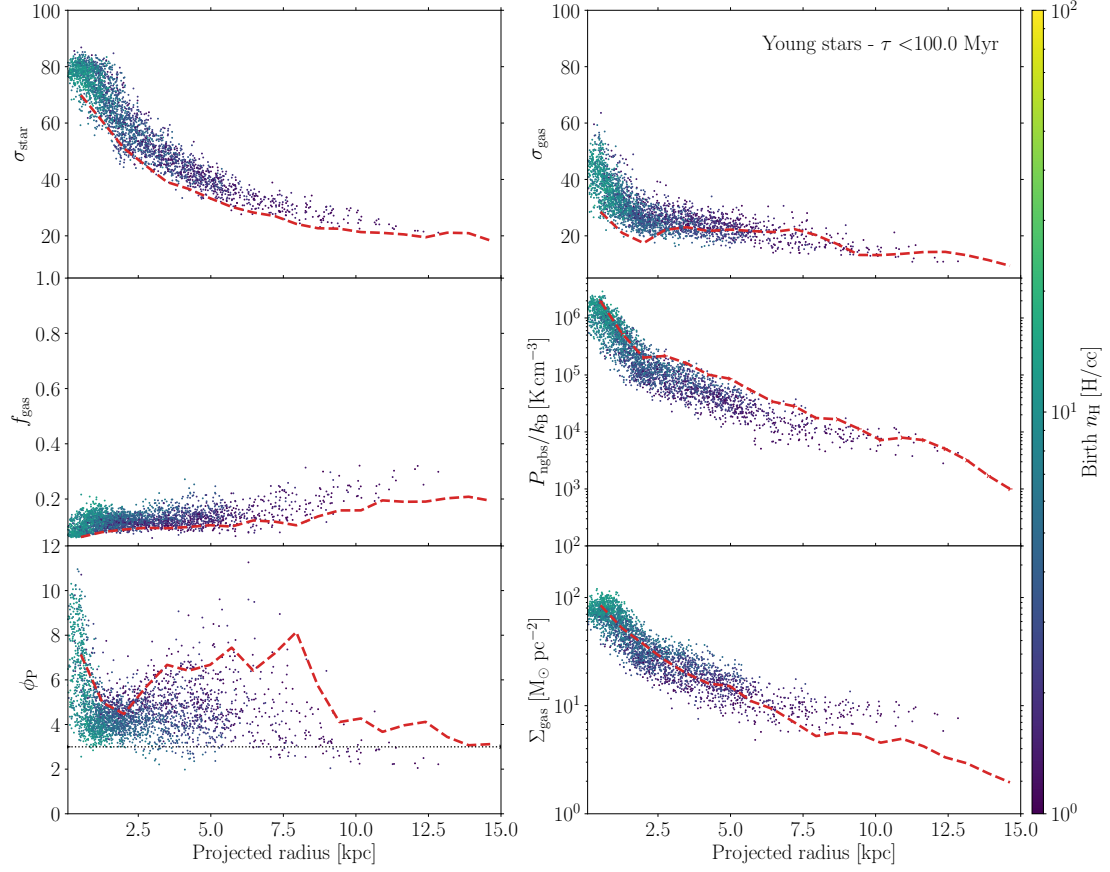


Figure 7.5: Stellar (*top left*) and gas (*top right*) velocity dispersions, gas fraction (*middle left*), neighbour-weighted gas pressure (*middle right*), contribution of stars to the mid-plane pressure (*bottom left*) and gas surface density (*bottom right*) as a function of the projected radius of the young stellar population (ages < 100 Myr) estimated using local quantities at runtime in the isolated galaxy simulation. The data points show the estimates for each young star and are colour-coded by their natal gas cell density, and the red dashed lines correspond to the azimuthally-averaged analytical profiles calculated in post-processing on linearly-spaced annuli. The black dotted line in the bottom left panel indicates the canonical value of $\phi_P = 3$.

7.4.2 Computing the epicyclic frequency

This section describes the method used to calculate the angular velocity and the epicyclic frequency at run time at any point in our simulations. Following appendix A in Pfeffer et al., (2018), we use the Poisson equation to relate the change in the potential with the mean enclosed density,

$$\nabla^2\Phi = 4\pi G\bar{\rho}. \quad (7.4.7)$$

Defining the angular velocity as $\Omega(r) = v_c(r)/r$, where $v_c(r)$ is the circular velocity at the galactocentric radius r (e.g. Binney and Tremaine, 2008), we can relate it to the change in the potential as

$$\Omega^2 = \frac{v_c^2(r)}{r^2} = \frac{GM(<r)}{r^3} = \frac{4\pi G}{3}\bar{\rho}(r) = \frac{1}{3}\nabla^2\Phi, \quad (7.4.8)$$

where $M(<r)$ is the mass enclosed within the galactocentric radius r . The potential term can be rewritten in terms of the tidal tensor $T_{ij} = -\partial^2\Phi/(\partial x_i\partial x_j)$ as

$$\Omega^2 = \frac{1}{3}\nabla^2\Phi = -\frac{1}{3}\sum_{i=1}^3\lambda_i, \quad (7.4.9)$$

where λ_i are the eigenvalues of the tidal tensor. Pfeffer et al., (2018) show that the epicyclic frequency can then be calculated from the eigenvalues of the tidal tensor as

$$\kappa^2 = -\sum_{i=1}^3\lambda_i + \lambda_1, \quad (7.4.10)$$

where λ_1 is the maximal eigenvalue of the tidal tensor.

Given the presence of the multiphase ISM in our simulations, the gas collapses into clumpy, high-density structures, which become the natal sites of stars and their sub-grid cluster populations. These natal structures are overdense relative to the mid-plane density of the ISM, and introduce graininess in the potential. This results in local estimations of the angular velocity and epicyclic frequency being tidally heated, i.e. resulting in large deviations relative to the value at the same galactocentric radius from the smooth potential. This effect can be seen in the top row of Fig. 7.6, where the magnitude of the eigenvalues increases strongly with the gas density at a fixed radius. It can also be seen in the epicyclic frequencies calculated from the local tidal tensors of the star-forming gas cells (left panel of Fig. 7.7), which deviate substantially from the radial profile towards the galactic outskirts.

In order to overcome the effect of tidal heating due to the natal environment, we calculate a neighbour-weighted tidal tensor using the neighbouring gas cells as tracers of the galactic potential. This approach mitigates the influence of the environment if a sufficiently large volume is sampled such that the surrounding gas is close to the average ISM density, as in this way the effect of the gas substructures becomes subdominant.

To do that, we calculate the tidal tensor at the location of each gas cell once stars are present in the simulation. We evaluate it over the gravitational softening of each cell at every timestep in which the cell is active. For each newborn star, we consider all gas

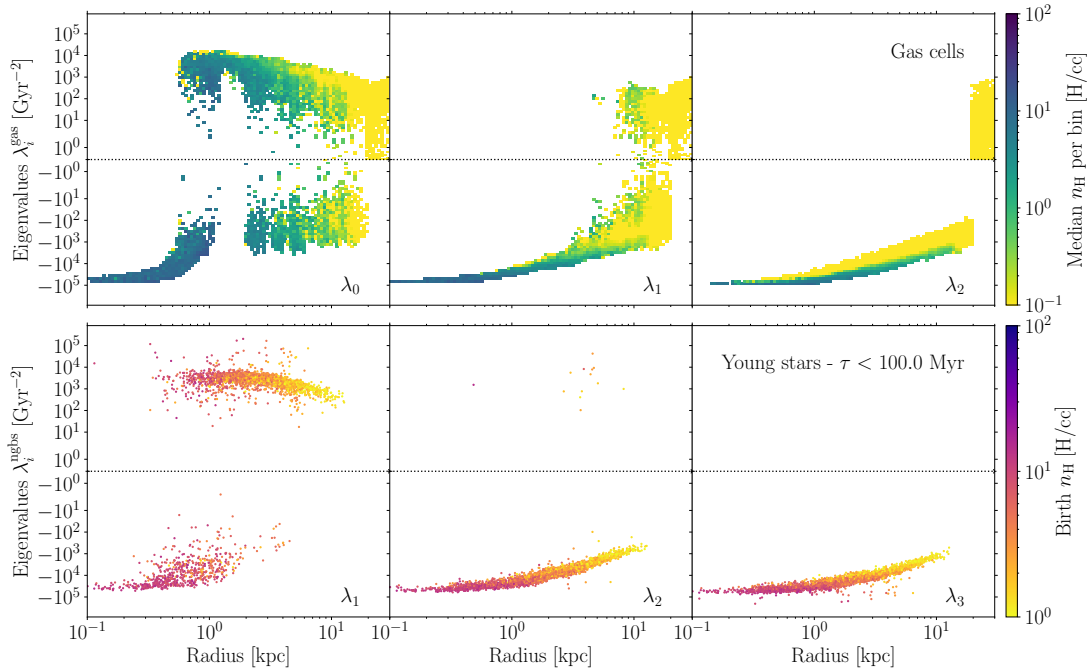


Figure 7.6: Eigenvalues of the tidal tensor calculated at the location of the gas cells (*top row*), and of the neighbour-weighted tidal tensor of young stars (ages < 100 Myr, *bottom row*) as a function of galactocentric radius for the isolated disk simulation. The eigenvalues are ordered by decreasing value from left to right. Bins and data points are colour-coded by the median gas density and the birth gas density in the top and bottom rows, respectively. The black dotted line corresponds to the limit between compressive ($\lambda < 0$) and extensive ($\lambda > 0$) tides.

neighbours within $2\text{--}10 \times h$ (see Sect. 7.4.1 for a discussion on the scale h), and we average over their tidal tensors,

$$T_{ij}^{\text{ngbs}} = \frac{\sum_k T_{ij}^k w'_k}{\sum_k w'_k}, \quad (7.4.11)$$

using the inverse of the gas cell density as a weight, $w'_k = 1/\rho_k$. Due to the lagrangian refinement used in AREPO, weighing the neighbours by the inverse of their density means that low density regions contribute more than overdense regions, thus reducing or smoothing the tidal heating caused by the cold, clumpy substructure of the ISM. The inner limit on the neighbour search is meant to prevent heating contamination from the natal overdensity. We show in Fig. 7.6 that the eigenvalues of the neighbour-weighted tidal tensors calculated at the location of the newborn stars (bottom row) are smoother than those calculated for the gas cells (top row). We have also considered other kernel weights (e.g. the cell volume, mass, its position relative to the newborn star) and distance limits, and we find that the combination of the inner limit and sampling up to at least $f \times h$ (see Section 7.4.1) is crucial to avoid the local tidal heating, and hence, to reproduce the angular velocity and epicyclic frequency radial profiles.

To demonstrate the ability of this method to retrieve the smooth description of the galactic potential, we calculate the epicyclic frequency (Eq. 7.4.10) from the local tidal tensors calculated at the location of the star-forming gas cells, and from the neighbour-weighted tidal tensors of newborn stars (Fig. 7.7). The natal cold gas substructures are expected to contaminate the determination of the epicyclic frequency due to the introduction of graininess in the galactic potential. This is clearly seen when comparing the epicyclic frequency measured at the location of star-forming gas cells (left column in Fig. 7.7) to the radial profile obtained from the enclosed mass (Eq. 7.4.8). Comparing these locally estimated epicyclic frequencies with the radial profile, we find that our approach recovers the behaviour of the smooth potential even at large radii where the heating is stronger. The slight deviation in the inner region ($r < 1$ kpc) is caused by the softening of the gravitational interactions.

7.4.3 The spatial scale of the tidal tensor

The tidal tensor describes the spatial variation of the gravitational potential,

$$T_{ij} = -\frac{\partial^2 \Phi}{\partial x_i \partial x_j}. \quad (7.4.12)$$

In order to calculate it numerically, it is necessary to define the scale over which the variation is being measured. In this appendix we study the effect of evaluating the tidal tensor over different spatial scales, and describe the values used in this work.

At runtime, the tidal tensor can be calculated from the numerical derivative of the gravitational acceleration field, $\mathbf{a} = -\nabla\Phi$. We consider the first order approximation of using the forward difference of the acceleration,

$$T_{ij} = \frac{\partial a_j}{\partial x_i} = \frac{a_j(\mathbf{x}') - a_j(\mathbf{x})}{|\mathbf{x}' - \mathbf{x}|}, \quad (7.4.13)$$

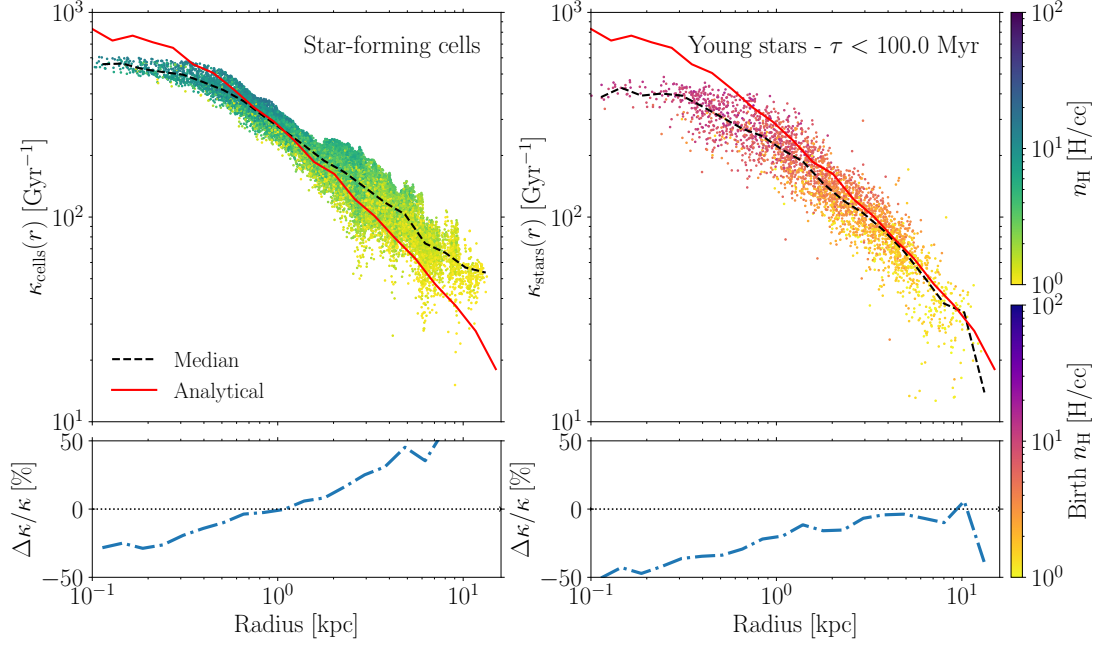


Figure 7.7: Radial profile of the epicyclic frequency calculated from the local tidal tensors of each star-forming gas cell (*left*), and from the neighbour-weighted tidal tensors of newborn stars ($\tau < 100$ Myr, *right*) for the isolated disk simulation. Gas cells are considered to be eligible for star formation if they are denser than $n_{\text{th}} = 1 \text{ H cm}^{-3}$ and colder than $T_{\text{th}} = 5 \times 10^3 \text{ K}$. Data points are colour-coded by the the gas density and the natal gas density, respectively, and the black line indicates the median at each bin. The red solid line represents to the analytical profile calculated from the enclosed mass in logarithmically-spaced radial bins. The bottom row corresponds to the relative error between the median and the analytical profiles.

where \mathbf{x} is the location of the particle and $\mathbf{x}' = \mathbf{x} + \Delta x \hat{\mathbf{x}}$ represents the displaced position along the axis $\hat{\mathbf{x}}$. To calculate this numerical derivative, we spawn three massless tracer particles displaced a distance Δx along the three main cartesian axes, and compute the gravitational accelerations at those positions as if the main particle had moved there. With this approach, there is no contamination from self-interactions within the gravitational softening in our simulated tidal tensors. The error of the numerical derivative is of order $O(\Delta x^2)$, so having a good estimation of what the spatial scale Δx should be to optimally recover the gravitational potential is crucial to avoid large numerical errors. We now explore a range of spatial scales in an idealized setup to identify the optimal scale for Δx .

To do this, we create an sphere of collisionless particles described by a Plummer potential (Plummer, 1911),

$$\Phi_{\text{Pl}}(r) = \frac{-GM}{\sqrt{r^2 + r_c^2}}, \quad (7.4.14)$$

of total mass $M = 10^{11} M_\odot$, characteristic radius of $r_c = 2$ kpc, and $N = 10^6$ particles. We evolve the ensemble of particles over 1 Gyr using a softening length of $\epsilon = 100$ pc, which lies between the softenings used in our cosmological simulations for gas cells and stars⁶. In these simulations, we keep track of the numerical tidal tensors calculated over different spatial scales $\Delta x = f \times \epsilon = 5, 10, 20, 50, 100$, and 200 pc.

We evaluate the gravitational acceleration using the TreePM method (Bagla, 2002) implemented in AREPO (Springel, 2005, 2010), which splits the gravitational interactions among short-range and long-range forces on a split scale r_s . The former are calculated using a Barnes-Hut oct-tree algorithm (Barnes and Hut, 1986) for nodes sitting at distances up to a cut-off radius r_{cut} . The long-range forces are then computed using a particle-mesh approach, which maps the mass distribution on a grid and solves for the gravitational potential using discrete Fourier transformations. For this test, we consider a grid dimension of 128, which leads to mesh cells of $l_{\text{cell}} \simeq 390$ pc, with a standard split scale of $r_s = 1.25 l_{\text{cell}}$ and a cut-off radius of $4.5 r_s$ (see Weinberger et al. 2019 for more details). Due to the mapping made to calculate the long range forces, the massless tracers can end up in a contiguous grid cell relative to their stellar particle, which leads to large deviations in the tidal tensor. To prevent this, we use reflective mesh cell borders, thus ensuring that tracers are in the same cell as their main particle.

The tidal tensor is generally described by its principal axes or eigenvectors, and the corresponding magnitude of the force along these axes or eigenvalues. The sign of these eigenvalues describes the direction of the tidal force; negative and positive eigenvalues correspond to compressive and extensive forces, respectively (e.g. Renaud et al., 2011). For an spherically symmetric potential, like a Plummer sphere, the eigenvalues correspond to the components of the tensor in spherically symmetric coordinates (e.g. Masi, 2007), with the radial component being

$$T_{\text{rr}} = -\frac{\partial^2 \Phi_{\text{Pl}}}{\partial r^2} = GM \frac{r_c^2 - 2r^2}{(r^2 + r_c^2)^{5/2}}, \quad (7.4.15)$$

⁶We have repeated this analysis with Plummer spheres evolved with gravitational softenings of 50 and 350 pc, and the results are not affected.

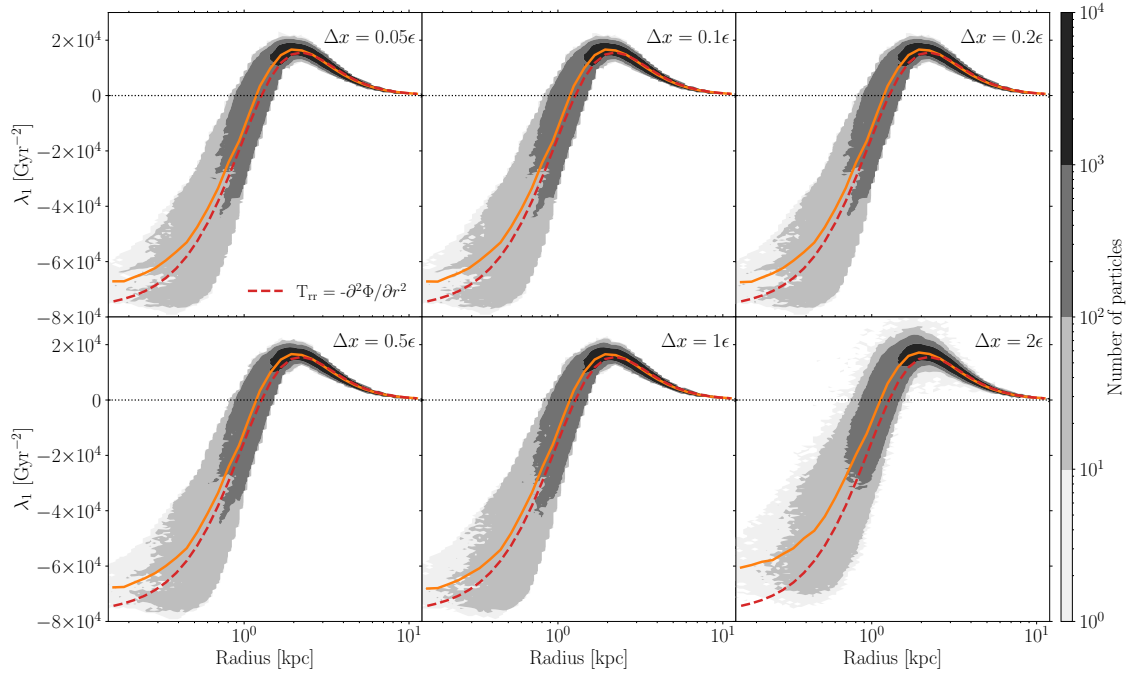


Figure 7.8: Distribution of the maximal eigenvalue of the numerical tidal tensors as a function of radius evaluated over different spatial scales in a Plummer sphere. The spatial scales considered range between $\Delta x = f \times \epsilon = 5\text{--}200$ pc. The red dashed line corresponds to the analytical tidal tensor component T_{rr} , and the orange solid line and shaded region indicate the median and 25–75th percentiles, respectively. The grayscale shading corresponds to the number of particles per bin.

and the azimuthal and polar components being

$$T_{\theta\theta} = T_{\phi\phi} = -\frac{1}{r} \frac{\partial\Phi_{\text{Pl}}}{\partial r} = \frac{GMr}{(r^2 + r_c^2)^{3/2}}. \quad (7.4.16)$$

We compute the eigenvalues λ_i of the simulated tidal tensors in the evolved Plummer spheres, for which we show the largest eigenvalues λ_1 in Fig. 7.8 as a function of radius for each spatial scale considered. We find good agreement with the analytical profile (Eq. 7.4.15) describing the tidal tensor component in the radial direction, with an increasing scatter in the inner 1–2 kpc as the spatial scale used to evaluate the tidal tensor increases. We also compare the radial profiles of the median eigenvalues to the analytical tidal tensor components in Fig. 7.9, and we find that there is good agreement for scales equal or smaller than the gravitational softening. These results rule out earlier suggestions that the tidal tensor should be evaluated on spatial scales larger than the softening length to avoid numerical noise (Renaud, 2010). Instead, evaluating the tensor on spatial scales larger than the softening length leads to systematic biases and an underestimation of the tidal shock strength. Thus, using a spatial scale equal to or smaller than the gravitational softening to evaluate the tidal tensor provides the best description of the potential.

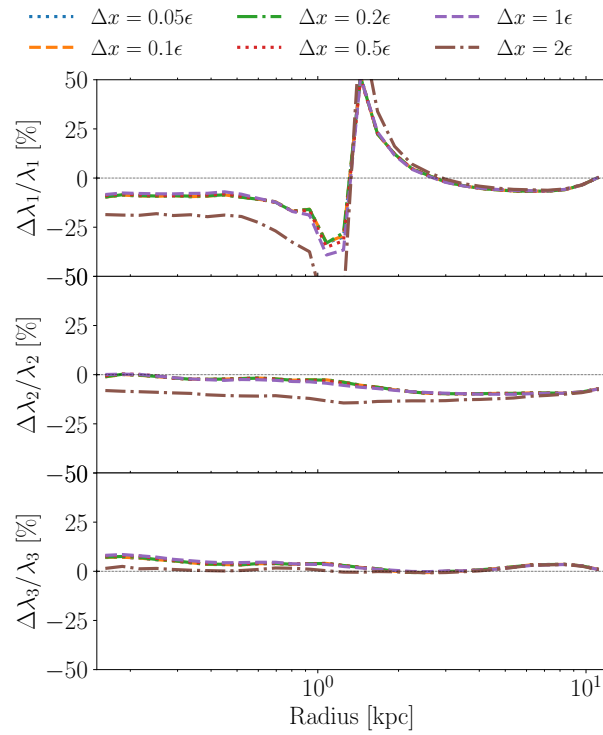


Figure 7.9: Median relative errors of the eigenvalues of simulated tidal tensors for particles within a Plummer sphere as a function of radius. From top to bottom, panels represent the eigenvalues in decreasing magnitude, $\lambda_1 > \lambda_2 > \lambda_3$.

Chapter 8

Conclusions

The aim of this PhD thesis is to foster our current understanding of the formation and evolution of stellar clusters in a cosmological context. This has been done under the hypothesis that the old and massive GCs are the relics of high-intensity star formation episodes at high redshift that have survived to the present day.

In the following pages, the contents and findings of the research presented in this thesis are summarized (Section 8.1). Then, the results obtained are discussed under four guiding ideas in Section 8.2, and we provide exciting future perspectives in Section 8.3.

8.1 Summary

This Section presents a brief summary of each of the chapters included in this thesis. For detailed descriptions of the methods used, the reader is directed to the corresponding chapters and to the original articles.

Part I - Formation and evolution of globular clusters

The first part of this thesis is devoted to exploring analytical descriptions of the influence of the cosmic environment on the demographics of stellar clusters. Firstly, we describe how the environment sets the upper mass scale of stellar clusters (Chapter 2), and then the evolution of stellar clusters due to tidal disruption is studied (Chapter 3).

Chapter 2 - A unified model for the maximum mass scales of molecular clouds, stellar clusters and high-redshift clumps Observations of young stellar cluster populations suggest that their masses can be well described by a Schechter function (e.g. Portegies Zwart et al., 2010; Adamo et al., 2020), with an upper mass scale that is found to be higher in starbursting environments (e.g. Larsen, 2009; Johnson et al., 2017). In addition, this upper mass scale is observed to be relatively constant as a function of radius within galaxies (Adamo et al., 2015; Messa et al., 2018; Adamo et al., 2020).

The upper mass scale of the mass distribution of young star clusters is expected to reflect the upper mass scale of their natal environments (e.g. Kruijssen, 2014), i.e. giant

molecular clouds (GMCs) and clumps. This upper cloud mass has been suggested to correspond to the maximum mass that is gravitationally unstable under centrifugal forces in a differentially-rotating disk in hydrostatic equilibrium (i.e. the Toomre mass; Toomre, 1964). The corresponding largest unstable wavelength is known as the Toomre lengthscale, and it can be described in terms of the gas surface density and the epicyclic frequency of the gas, $\lambda_T \propto \Sigma_{\text{gas}} \kappa^{-2}$. Typically, the faster decline of the epicyclic frequency as a function of galactocentric radius compared to the gas surface density implies that this unstable lengthscale increases towards the outskirts of galaxies, and it can even become larger than the galaxy itself. Hence, the predicted radial profile of the Toomre mass for a given galaxy rises towards larger radii, which is inconsistent with observations of GMCs and stellar clusters.

In order to overcome this inconsistency, we present in Chapter 2 an analytical model in which the collapse of the largest unstable region due to centrifugal forces can be halted by the stellar feedback of the newborn stars in that region (Reina-Campos and Kruijssen, 2017). This interplay of processes reduces the amount of mass that can collapse in a single GMC in environments with both low gas surface densities $\Sigma_{\text{gas}} \leq 100 \text{ M}_{\odot} \text{pc}^{-2}$ and low epicyclic frequencies $\kappa \leq 0.8 \text{ Myr}^{-1}$ for a Toomre stability parameter $Q = 1.5$ ¹, typical of galactic outskirts. In other galactic environments, stellar feedback from newborn stars is not sufficiently energetic to overcome the gravitational pull of the collapse, and so the entire centrifugally-unstable region collapses into a single cloud. Hence, the balance between the collapse and stellar feedback is critical for predicting a flat radial profile that reproduces observations of GMCs in the local Universe.

By assuming a direct relation between the upper cloud mass scale and the upper stellar cluster mass scale, we predict the maximum cloud and cluster mass scales for a variety of galaxies: from the Milky Way and nearby spirals such as M31 and M83, to a high-redshift galaxy at cosmic dawn ($z = 2.196$). For all of the galactic environments studied, we demonstrate that this analytical model provides a good description of the observed upper mass scales of clouds, clumps and clusters in the local Universe and beyond.

Chapter 3 - A systematic analysis of star cluster disruption by tidal shocks – I. Controlled N-body simulations and a new theoretical model

The lifetime of stellar clusters is typically defined as the timescale over which the cluster remains gravitationally bound. Several processes are known to have an influence in their survivability, but the dominant drivers of their evolution are tidal shocks with the dense structures of the ISM (Baumgardt and Makino, 2003; Lamers et al., 2005a; Gieles et al., 2006; Elmegreen, 2010; Elmegreen and Hunter, 2010; Kruijssen et al., 2012; Miholics et al., 2017). This mechanism dominates in the dense and gas-rich environments in which massive clusters form, and can quickly disrupt even relatively massive clusters (e.g. Miholics et al., 2017).

The prediction of the amount of mass lost during these tidal perturbations relies heavily on assumptions about the conversion between the energy injected and the mass lost, as well as on the shape of the distribution function of the stars in clusters. Analytical derivations

¹The limit for the gas surface density shifts towards higher (lower) values for lower (higher) values of the Toomre stability parameter Q , whereas the limit for the epicyclic frequency barely changes.

of the influence of tidal shocks on cluster disruption assume that tidal shocks are impulsive, i.e. that the shock proceeds much faster than the crossing timescale of the stellar system. Under these assumptions, the shock-driven disruption timescale is predicted to scale with the cluster density and the tidal heating parameter² as $t_{\text{sh}} \propto \rho^1 I_{\text{tid}}^{-2}$ (e.g. Prieto and Gnedin, 2008; Kruijssen et al., 2011). Hence, stronger shocks or lower density clusters result in a faster disruption for given equal-density clusters or tidal shocks, respectively.

Given this large number of assumptions, a simplified study of the effects of tidal shocks on individual stellar clusters is crucial to understand this process. With that aim, we present in Chapter 3 a suite of N -body simulations of individual clusters undergoing simplified tidal histories (Webb et al., 2019a). These tidal interactions are tailored to study the disruption caused by single or double-peaked shocks of defined intensity and duration, such that the integrated strength of each interaction is equal among the simulations. The description of the shocks is simplified by assuming that these only occur along the x -axis, so that their tidal strength is reduced to the first component of the tidal tensor. Additionally, we evaluate the influence of the cluster structure in setting their survivability to these controlled shocks by changing the size and mass of the cluster, as well as the radial profile considered.

By looking at the mass and size evolution of these simulated star clusters, we obtain an empirical description for the shock disruption timescale. This empirical fit has shallower scalings with the cluster density and with the tidal shock strength than the classical analytical description, $t_{\text{sh}} \propto \rho^{0.59} (\int T_{00} dt)^{-1.16}$. For a given cluster density, this new formalism predicts a stronger disruptive effect for tidal shocks, which implies that clusters will evolve faster in environments with more dense substructures that produce graininess in the potential.

In order to understand the discrepancy between the empirical and the classical analytical scalings, we derive an analytical model based on the idea that the kinetic energy injected by the shocks align the velocity vectors of the stars along their axis of action, thus increasing the probability for those stars to become unbound if the next shock comes from the same direction. This hypothesis leads to the finding that the shock-driven disruption timescale of stellar clusters presents extremely similar scalings as the ones found from the simulated clusters, $t_{\text{sh}} \propto \rho^{0.67} (\int T_{00} dt)^{-1.57}$. Hence, these simplified simulations allow to establish the critical role of tidal shocks in the disruption of stellar clusters during their evolution in gas-rich environments.

Part II - Globular clusters in a cosmological context

The results of the second part of this thesis use the suite of 25 self-consistent, hydrodynamical, cosmological simulations of present-day Milky Way-mass galaxies and their simulated stellar clusters of the E-MOSAICS project (for a detailed description, see Pfeffer et al., 2018; Kruijssen et al., 2019a) to study when clusters form (Chapter 4), and their disruption as a

²The tidal heating parameter describes the increase in heating due to a tidal shock (Gnedin, 2003) and is defined as $I_{\text{tid}} = \Sigma_{i,j} (\int T_{ij} dt)^2 A_{w,ij}$ in terms of the tidal tensor components $T_{ij} = -\partial^2 \Phi / \partial x_i \partial x_j$. The adiabatic correction terms $A_{w,ij}$ need to be considered to account for the energy loss due to the adiabatic expansion of the cluster (Weinberg, 1994a,b,c).

function of the galactic environment (Chapter 5). Lastly, these simulations are also used to trace the build-up of stellar haloes from their stellar cluster populations (Chapter 6).

Chapter 4 - Formation histories of stars, clusters, and globular clusters in the E-MOSAICS simulations Under the paradigm of GCs being the relics of high-intensity periods of star formation at high redshift that have survived to the present day, the process of massive cluster formation is expected to occur whenever there are conditions leading to bursts of star formation, i.e. high densities or gas pressures (Kruijssen, 2014; Krumholz et al., 2019). This expectation is explored by studying the formation histories of stars, clusters and GCs in the suite of Milky Way-mass galaxies of the E-MOSAICS project (Reina-Campos et al., 2019) in Chapter 4. In this work, we find that the peak of cosmic GC formation rate occurs at $z \sim 1-4$, close to the bulk of star formation ($z \sim 2$; Madau and Dickinson, 2014), thus following the expected behaviour with cosmic evolution.

With the aim of exploring the role of the cluster formation physics in setting their formation history, we consider three additional alternate suites of 10 Milky Way-mass simulations in which the two ingredients used to describe the formation, i.e. the CFE and the truncation mass of the initial cluster mass function, are deactivated one at a time. From this comparison, the main driver in setting the peak of cosmic GC formation rate is found to be the environmental description of the maximum cluster mass (Reina-Campos and Kruijssen, 2017). The analytical maximum cluster mass correlates with gas pressure because stellar feedback is less efficient in those environments (Chapter 2), which in turn implies a cosmic time dependence: as the Universe expands, haloes virialize at a lower density and gas inflow declines (e.g. Correa et al., 2015), thus reducing the gas pressure and the maximum mass that stellar clusters can have.

The GCs in the Milky Way have been observed to have different properties as a function of their metallicity (e.g. Kinman, 1959a,b; Zinn, 1985). This has led to the suggestion that there exists two subpopulations based on metallicity that might have formed under different formation channels (e.g. Zinn, 1985; Moore et al., 2006). However, star and cluster formation in the E-MOSAICS simulations are continuous processes, in which more metal-rich objects form in galaxies as they enrich over cosmic time. We therefore find that the observed differences between metallicity subpopulations are merely a reflection of their evolution in a cosmic environment. These simulated stellar cluster populations are shown to reproduce the observation that metal-poor GC subpopulation is older than the metal-rich one (e.g. Forbes and Bridges, 2010; Dotter et al., 2011; VandenBerg et al., 2013).

Lastly, the plausibility of a connection between reionization and the metal-poor subpopulation of GCs is also discussed. We conclude that neither is reionization needed to halt metal-poor cluster formation, nor are these objects likely to have been a dominant source of ionizing radiation.

Chapter 5 - Dynamical cluster disruption and its implications for multiple population models in the E-MOSAICS simulations GCs had long been considered to have formed as a single stellar population, but detailed photometrical and spectroscopical

observations of the chemical abundances of their stars have revealed the presence of multiple chemically-distinct stellar populations (e.g. Piotto et al., 2007; Carretta et al., 2010; Bastian and Lardo, 2018). The origin of this multiple population phenomenon is not yet fully understood, but plenty of effort has been placed at developing theoretical models that attempt to comply with all observational constraints (for a discussion, see Bastian and Lardo, 2018).

The majority of these models rely on the pollution of the gas by a subset of the original stellar population and subsequent star formation episodes to produce the different chemically-distinct subpopulations. However, the low pollution rates of the different polluters considered (de Mink et al., 2009) and the comparable (if not higher) fraction of polluted stars relative to the original subpopulation (e.g. Milone et al., 2017), imply that these models require stellar clusters to have been > 10 times more massive at birth, and to have lost most of that original mass over cosmic history. This is known as the mass-budget problem in the literature.

In Chapter 5, we use the simulated stellar clusters from the E-MOSAICS project to evaluate whether the dynamical disruption suffered is compatible with the theoretical descriptions of the multiple populations phenomenon (Reina-Campos et al., 2018). For that, the environmental dependence of cluster mass loss is explored by looking at the initial-to-present cluster mass ratio as a function of its present mass, its final galactocentric position, its metallicity and its natal gas pressure. Environments with higher gas pressures, such as those in the inner part of galaxies or those with higher metallicities, are expected to be more disruptive. Only intermediate mass clusters ($M \sim 10^3\text{--}10^5 M_\odot$) are found to show these expected dependences. However, higher and lower mass clusters are barely and strongly affected by disruption, respectively.

On top of that, massive stellar clusters ($M > 10^5 M_\odot$) are found to be only a factor 2–4 times more massive at birth, which is in conflict with the mass-budget problem required by current multiple population models. Using the simulated cluster disruption, we explore the fraction of enriched or polluted stars as a function of the present cluster mass. The simulated fraction exhibits an opposite trend relative to observational measurements, with more massive clusters having less polluted stars than observed due to their reduced disruption rates relative to low mass clusters.

In order to reconcile these results with the literature, two options are evaluated. Firstly, we explore the dependence on the size of the cluster, and we find that an unphysically-steep mass-radius relation is required to reproduce the observational trend. In this scenario, stellar clusters of $10^6 M_\odot$ would need to have half-mass radius of ~ 96 pc, which is an order of magnitude larger than observed (e.g. Krumholz et al., 2019). Alternatively, the results and observations can be reconciled if the initial amount of polluted stars in clusters increases with cluster mass, suggesting that either polluters that produce greater amounts of enriched material in higher mass clusters need to be considered (e.g. Gieles et al., 2018), or that some stellar evolutionary process is missing in our current understanding.

Chapter 6 - The mass fraction of halo stars contributed by the disruption of globular clusters in the E-MOSAICS simulations As a plethora of studies have

previously suggested (e.g. Shapley, 1918a; Trumpler, 1930b) and recently demonstrated (e.g. Myeong et al., 2018; Kruijssen et al., 2019b; Massari et al., 2019; Kruijssen et al., 2020), massive stellar clusters hold information about the structure, formation and assembly history of their host galaxies. Using a chemical-tagging technique, several authors aim to identify chemically-distinct stars among the field stars in the Galactic stellar halo. Assuming that these stars only form in GCs, as well as certain disruption ratios and fractions of enriched stars in clusters, they estimate that between 4–11 per cent of the Galactic halo has been contributed by the disruption of GCs (e.g. Martell and Grebel, 2010; Koch et al., 2019).

With a similar aim, we present in Chapter 6 an estimation of the amount of mass contributed by stellar clusters and GCs³ to the build-up of the galactic haloes in the suite of Milky Way-mass galaxies (Reina-Campos et al., 2020). Among this sample of galaxies, only a small percentage of the simulated stellar mass in halo field stars is found to correspond to the disrupted mass from stellar clusters and GCs, 2.3 and 0.3 per cent, respectively. Under the assumption that the entire initial stellar cluster population is disrupted and contributes to the halo, which allows us to place an upper constraint, this fraction increases only slightly to 5.9 and 1.9 per cent, respectively. This result places another strong constraint to mass budget-limited multiple population models, and implies that galactic stellar haloes are mostly contributed by the accretion of dwarf satellites (as suggested by e.g. Deason et al., 2015; Belokurov et al., 2018; Helmi et al., 2018; Conroy et al., 2019).

Part III - Stellar clusters in a cold and dense cosmic environment

The last part of this thesis introduces the next generation of cosmological simulations that include the description of the formation and evolution of stellar clusters in a cosmological context with a cold and clumpy ISM (Chapter 7).

Chapter 7 - Modelling the co-formation and evolution of stellar clusters and their host galaxies in EMP-*Pathfinder* Massive stellar clusters are observed to be forming in the densest gas structures, which predominantly contain cold molecular hydrogen (Kruijssen, 2014; Krumholz et al., 2019; Adamo et al., 2020, and see references therein). These giant and dense substructures are expected to dominate the graininess of the galactic potential, and to be the main source of cluster disruption via tidal interactions. Thus, an accurate description of the multiphase nature of the ISM is crucial to properly reproduce when stellar clusters form, and how they evolve over cosmic history.

The lack of a description of the cold gas phase of the ISM in the EAGLE galaxy formation model (Schaye et al. 2015, Crain et al. 2015) causes simulated stellar clusters from the E-MOSAICS project to disrupt too slowly, thus limiting the predictive power of these simulations (see discussion in appendix D, Kruijssen et al., 2019a). In order to overcome these problems, we present in Chapter 7 the methods used in the EMP-*Pathfinder*

³Defined as stellar clusters more massive than $5 \times 10^3 M_{\odot}$ and $10^5 M_{\odot}$, respectively.

suite of hydrodynamical, cosmological simulations (Reina-Campos et al. in prep.), as well as some preliminary results of the demographics of their stellar cluster populations.

These simulations describe the co-formation and evolution of stellar clusters and their host galaxies, with an improved MOSAICS sub-grid model for the formation and evolution of stellar clusters. The cold gas phase of the ISM is included in these simulations via a six-element non-equilibrium chemistry network from the GRACKLE cooling library (Smith et al., 2017), and the feedback ejecta in terms of mass, metals, yields, energy and momentum of AGB winds, SNII and SNIa is also considered. This self-consistent description of the cold and dense gas allows the modelling of the formation and evolution of stellar clusters in galaxies with a cold and clumpy medium, thus accurately describing where clusters form and how they evolve across cosmic history.

8.2 Discussion and reflection

During the development of this thesis, we have set ourselves to understand how stellar cluster formation and evolution proceeds in a cosmological context, with the emphasis placed on the most massive and oldest cluster population. This study is complex and multi-scale by nature, and it has to be undertaken at the intersection of different fields: from the large scales of cosmology and galaxy formation that describe the cosmic environment to the processes of star formation and feedback that heavily depend on the local ISM conditions.

Each of the chapters included in this thesis contains its own independent conclusions, which are summarized in the previous section, as well as in the corresponding chapters and publications. The findings that are common to some (or all) of the projects presented in this thesis are discussed here and constitute its concluding remarks. These can be summarized in four guiding ideas.

8.2.1 GC populations are shaped by cosmic evolution

As discussed in the introduction, there is a long-standing fascination in the literature about the origin of GC populations, and in particular, about whether nature or nurture are the main drivers of their demographics. In the former case, these cluster populations would have already formed with their observed properties, and in this scenario, authors advocate for unique and exotic channels for the formation of these massive objects (e.g. Zinn, 1985; Moore et al., 2006; Trenti et al., 2015; Boylan-Kolchin, 2017; Madau et al., 2020).

In this thesis we explore the latter case: that the demographics of stellar clusters are shaped by the galactic environment. In this scenario, a complete spectrum of stellar cluster properties is predicted to be observed, and their properties are expected to depend on the galactic conditions in which these objects formed and have evolved. This is not a novel idea as it has been explored before (e.g. Kruijssen, 2014; Krumholz et al., 2019; Adamo et al., 2020, and see references therein), but this thesis expands it to provide new theoretical interpretations.

A first example of how the galactic environment shapes the populations of stellar clusters is given in Chapter 2. This derived analytical description of the maximum mass for clouds

and stellar clusters is fundamented on an interplay between gravitational collapse and stellar feedback, and so it is strongly dependent on gas pressure. In high-pressure environments, stellar feedback is less efficient at halting the collapse of the centrifugally-unstable region, and so more massive clusters can form. This implies that high gas pressure environments are a necessary condition for the formation of massive stellar clusters, as it is observed in the natal sites of YMCs (Adamo et al., 2015).

Additionally, another example on the influence of the environment on the evolution of stellar clusters is presented in Chapter 3. Tidal interactions between stellar clusters and dense gas clouds are the main source of cluster disruption, dominating over other mechanisms even when integrating over the cluster lifetime (Lamers et al., 2005a; Gieles et al., 2006; Elmegreen, 2010; Elmegreen and Hunter, 2010; Kruijssen, 2012; Miholics et al., 2017). Despite representing a simplified setup, these simulations showcase that repeated strong tidal shocks can quickly disrupt even fairly massive clusters. These strong shocks are mostly due to the graininess in the potential produced by dense gas structures, which increase in number with the amount of gas and its pressure (Sun et al., 2018).

Interestingly, observations of high-redshift star-forming galaxies find that gas pressure is not constant over cosmic history (Tacconi et al., 2013); as the Universe expands, the cosmic gas inflow rate onto galaxies decreases, and so does their gas pressure (Correa et al., 2015). Conversely, at a given cosmic time, higher mass galaxies are expected to have higher gas pressure because of their deeper potential wells. Hence, the high gas pressure required for the formation of the most massive clusters (which are the ones that are more likely to survive to the present day) were more common at earlier cosmic times than in the local Universe. This result explains why observed GC populations are found to be massive and old: the conditions for massive cluster formation were more common at high redshift, and only massive clusters can survive over a Hubble time.

We look into the critical role played by the galactic environment in Chapter 4 by switching on and off the environmental dependence of the cluster formation physics in a suite of Milky Way-mass galaxies from the E-MOSAICS project. From this comparison, we conclude that the main driver of the peak of the cosmic GC formation history is the dependence of the maximum mass of stellar clusters on the gas pressure, as the decrease of the overall gas pressure shuts down massive cluster formation at later cosmic times. If cluster formation physics is assumed to be constant over cosmic history, the total mass in surviving GCs is overproduced by a factor of 5.5 relative to the Milky Way. Hence, accounting for the dependence on the cosmic environment when modelling stellar clusters is critical to reproduce the observed cluster populations.

8.2.2 Evolution of stellar clusters in a cosmological context cannot explain multiple stellar populations

A critical problem for the majority of models describing the origin of multiple stellar populations is the so-called mass-budget problem: stellar clusters are required to have been several times ($\gtrsim 10$) more massive at birth, and there must have been a preferential mass-loss of chemically-unenriched stars such that at present day both populations have similar ratios. This problem has been explored in the literature in a number of occasions

(e.g. see Cabrera-Ziri et al., 2014, for an observational discussion), but in this thesis we take a general approach to place constraints on models addressing this problem.

The requirement for stellar clusters to have been at least ten times more massive at birth ($M_{\text{init}} \gtrsim 10^6 M_{\odot}$ for a typical GC of $10^5 M_{\odot}$) implies that, under the environmental description of the maximum cluster mass (Chapter 2), their birth conditions must have been even more extreme than currently estimated. As shown in Section 2.3, there are few galactic environments in the local Universe in which the maximum cloud mass from which stellar clusters form is not limited by the effect of stellar feedback. Only circumnuclear starbursts and high-redshift galaxies reach the high pressures needed to have the extremely massive clouds that would lead to the formation of these massive clusters, but these events are observed to be extremely rare (e.g. Adamo et al., 2017; Messa et al., 2018; Adamo et al., 2020). Thus, the formation of the vast majority of the GC population as extremely massive clusters is disfavoured by both this environmental interpretation and observations of YMC populations.

Another approach to this problem is done by using the suite of Milky Way-mass galaxies from the E-MOSAICS project and their simulated stellar cluster populations. These simulations have been found to reproduce many of the observed properties of the old and young massive cluster populations (e.g. Pfeffer et al., 2018; Kruijssen et al., 2019a; Pfeffer et al., 2019b), so they provide an excellent framework within which to examine if the mass-budget problem required by multiple population models can be accommodated.

By looking at the initial-to-present mass ratio of all surviving stellar clusters in Chapter 5, we find that the most massive stellar clusters ($M \geq 10^5 M_{\odot}$) are only a factor 2–4 times more massive at birth. This implies that these clusters are not sufficiently massive at birth and they do not lose enough mass to be compatible with mass budget-limited models of multiple populations. We find this ratio to increase towards lower cluster masses, thus making them compatible with the models. Despite that, chemical inhomogeneities have only been observed in fairly massive clusters ($M \gtrsim 10^4 M_{\odot}$; Bastian and Lardo, 2018). In order to reconcile these results with observational data, we find that stellar polluters that produce increasingly larger amounts of polluted material with cluster mass are favoured over currently considered stellar polluters.

Additionally, in Chapter 6, the simulated stellar cluster populations in the E-MOSAICS simulations are estimated to only contribute a small percentage to the build-up of the galactic stellar haloes, even under the consideration that the entire initial population gets disrupted. These estimated fractions are in agreement with the upper limits placed by observational studies using chemical-tagging techniques to find chemically-distinct stars in the Galactic halo (e.g. Martell and Grebel, 2010; Koch et al., 2019). This implies that the large amounts of cluster disruption advocated for current models of multiple stellar populations cannot be accommodated within this self-consistent framework of the co-formation and evolution of stellar clusters and their host galaxies.

Moreover, it has recently been observed that the age of the stellar cluster can be a major factor for the onset of the multiple population phenomenon (Martocchia et al., 2018), with the amount of N-enrichment increasing with age in GCs older than 2 Gyr. This either suggests that the cosmic environment in which these clusters form has changed

over the past 2 Gyr, or that the detectability of the chemical inhomogeneities increases with age, linking them to yet-to-be understood stellar evolutionary processes. Looking at the formation histories of stellar clusters presented in Chapter 4, we find that there is no significant change in the formation rates over the past few Gyrs. Hence, this favours the latter suggestion that the origin of the multiple population phenomenon is likely linked to stellar evolutionary processes in crowded environments, or to the hierarchically-build-up of the most massive clusters (Howard et al., 2018, 2019).

8.2.3 Stellar clusters are tracers of galaxy formation and assembly

An interesting feature of GC populations is their use as beacons in the darkness to infer the structure of galaxies (e.g. Shapley, 1918a; Kinman, 1959a; Harris and Petrie, 1978; Frenk and White, 1980; van Dokkum et al., 2018). The avalanche of data from the *Gaia* mission (Gaia Collaboration et al., 2018; Baumgardt et al., 2019; Vasiliev, 2019), combined with recent developments in the modelling of stellar clusters, has enabled to link GC populations to the formation and assembly history of their host galaxies in a quantitative manner (Myeong et al., 2018; Kruijssen et al., 2019a,b; Massari et al., 2019; Forbes, 2020; Horta et al., 2020b; Kruijssen et al., 2020). Using its own GC population, the Milky Way has been found to have assembled from five main satellites, each of which brought its own cluster population (for a recent review, see Helmi, 2020). This is an exciting new avenue, and in this thesis we touch upon this topic.

The first point that we explore is the relation between metal-poor GCs and reionization. In order to explain the old ages of Galactic metal-poor GCs, some authors invoke cosmic reionization; either reionization is considered to stop the formation of metal-poor objects, and thus explain its old ages, or these objects are suggested to have been a dominant source of ionizing radiation. The formation histories of surviving GCs (Chapter 4)⁴ show that only 10 per cent of the mass in metal-poor GCs had formed by the end of cosmic reionization ($6 \lesssim z \lesssim 10$; Robertson et al., 2015), so in this framework, metal-poor GCs are not a dominant source of ionizing radiation (see also Pfeffer et al., 2019a). Moreover, despite lacking a mechanism to halt metal-poor GC formation, we reproduce the trend of GCs ages with metallicity, i.e. the fact that metal-poor objects are the oldest subpopulation (e.g. Forbes and Bridges, 2010; Dotter et al., 2011; VandenBerg et al., 2013). Thus, we conclude that in this framework there is no dominant relation between metal-poor GCs and reionization.

Based on the mass-budget problem, it has been argued that a large fraction of the Galactic stellar halo corresponds to unenriched stars that have been disrupted from massive stellar clusters (e.g. Martell and Grebel, 2010). The estimated fraction depends on the assumptions taken, so we explore the build-up of stellar haloes from simulated stellar cluster populations in Chapter 6. We find that only a small percentage of the simulated stellar haloes has been contributed from the disruption of stellar clusters, even if the entire initial populations are assumed to disrupt. This favours the idea that the dominant contribution

⁴The most massive end of the cluster population loses only about half of its initial mass due to evolution (Chapter 5), so it is a representative subpopulation to estimate the massive cluster formation history.

to the build-up of stellar haloes is given by the accretion of dwarf satellites (e.g. Deason et al., 2015; Belokurov et al., 2018; Helmi et al., 2018; Conroy et al., 2019).

8.2.4 Accounting for the cold ISM is critical for the formation and evolution of stellar cluster populations

One of the main characteristics that comes to mind when thinking about the origin of GC populations is the fact that they seem to mostly reside in the outskirts and haloes of galaxies (e.g. Harris and Racine, 1979; Harris, 1988), where there is almost no gas. This observation has fostered a long-time puzzle, as peculiar formation channels are needed to explain the formation of those massive and old clusters in such gas-poor environments (e.g. Peebles and Dicke, 1968; Fall and Rees, 1985). However, observations of current massive cluster formation in high-density regions within starbursting galaxies in the local Universe (e.g. Holtzman et al., 1992; Adamo et al., 2017) have promoted the interpretation that massive clusters formation is a high-pressure extension of normal star formation, and their migration to a gas-poor environment is crucial for avoiding their complete disruption (e.g. Elmegreen and Hunter, 2010; Kruijssen, 2015; Pfeffer et al., 2018; Keller et al., 2020).

In this scenario, the cold gas phase of the ISM is a critical piece for describing the origin and evolution of stellar cluster populations: clusters form in the high-density peaks of its substructure, and the cold, dense and massive molecular clouds that are expected to dominate the graininess of the galactic potential drive most of the dynamical disruption via tidal shocks (e.g. Kruijssen, 2014; Krumholz et al., 2019). This has become apparent in this thesis, as we have found that the dense natal sites of clusters determine their maximum mass (Chapter 2), and their lifetime in gas-rich environments is shortened due to tidal interactions (Chapter 3).

Moreover, the crucial role of the cold gas has also been highlighted when analysing the simulated stellar cluster populations of the E-MOSAICS project. Despite the significant progress achieved at linking GC populations with their birth environments, the lack of a description for the cold ISM in the EAGLE galaxy formation model implies that the simulated stellar clusters disrupt too slowly. This underdisruption affects specially the subpopulation of clusters that spend most of their lifetimes in a disruptive environment, i.e. the young, metal-rich and low-mass clusters, producing stellar cluster populations that are not representative towards that end of the distribution (for a detailed discussion, see Kruijssen et al., 2019a). For that reason, the simulated stellar cluster populations in Chapters 4 to 6 are restricted to the mass, metallicity or birth gas pressure range that is less affected by this underdisruption ($M \geq 10^5 M_\odot$, $[\text{Fe}/\text{H}] \in [-2.5, -0.5]$ or $P/k_B \geq 10^6 \text{ K cm}^{-3}$, see fig. 17 by Pfeffer et al. 2018).

In order to overcome this problem, during this thesis we have developed the next generation of cosmological simulations that describe the co-formation and evolution of stellar clusters in a cold, clumpy cosmic environment (Chapter 7). These simulations are based on the moving-mesh hydrodynamical code AREPO (Springel, 2010; Weinberger et al., 2019), and this improved modelling allows us to accurately describe where entire cluster populations form and how they dissolve across cosmic history.

8.3 Future directions

The research presented in this thesis can be expanded in a number of different directions. Before concluding, we would like to discuss some of these future perspectives, and briefly suggest exciting avenues that are yet to be explored.

8.3.1 Closing the circle: predictions for JWST and future observatories

With the deployment of the JWST scheduled in 2022, and the construction of thirty-meter class telescopes like the ELT, the GMT, and the TMT⁵, we will soon be able to directly observe the birth sites of nascent massive stellar clusters that might survive to become the GCs observed in the local Universe (e.g. Bouwens et al., 2017; Johnson et al., 2017; Vanzella et al., 2017, 2019, 2020). Interpreting this future wealth of observational data to understand how gas environments shape the properties of the nascent cluster population requires a general framework describing cluster formation in a cosmological context.

In this thesis, we set ourselves to foster our understanding of the entire lifetime of stellar clusters in a cosmic environment, from their birth as massive bound systems in dense molecular clouds to their disruption over cosmic history. Using the research presented, we have developed a framework (Chapter 7) that includes a model for stellar cluster formation and evolution in a cold and dense cosmological context, and that provides an end-to-end description of stellar cluster populations over cosmic history.

Using these simulations, one could explore the natal properties of stellar clusters, and so predict the demographics of the nascent cluster population at high redshift. These include their stellar cluster masses, sizes, metallicities and UV luminosities, as well as their numbers and expectancy of survival after a Hubble time of evolution in a hierarchical galaxy assembly context. Together, these quantities would allow us to provide an interpretative framework for the observational data collected by these future facilities, and additional predictions can be made when their huge discovery potential leads to unexpected revelations.

8.3.2 New perspectives on galactic archaeology

The unprecedented volume of astrometric information for $\sim 10^9$ stars in the Milky Way from the *Gaia* mission (Gaia Collaboration et al., 2018) has revolutionised the fields of near-field cosmology and galactic archaeology, demonstrating that GCs are outstanding probes for tracing the assembly history of the Milky Way (e.g. Ibata et al., 2019; Massari et al., 2019). Additionally, recent work using the E-MOSAICS simulations has been able to link properties of the GC populations to the formation and assembly history of their host galaxies (e.g. Kruijssen et al., 2019a; Trujillo-Gomez et al., 2020). These studies have provided quantitative predictions on the assembly history of the Milky Way (Kruijssen et al., 2019b, 2020), that have since been confirmed using *Gaia* DR2 and SDSS/APOGEE chemical information (e.g. Massari et al., 2019; Horta et al., 2020a,b). However, further predictions are obstructed by the underdisruption of stellar clusters due to the omission of

⁵These correspond to the *Extremely Large Telescope*, the *Giant Magellan Telescope* and the *Thirty Meter Telescope*, respectively.

a cold ISM. Thus, a framework that includes the cold, clumpy medium, such as the *EMP-Pathfinder* simulations presented in Chapter 7, is necessary to fully realise the potential of GC populations as tracers of galaxy assembly.

These simulations allow us to investigate how the properties of the GC populations (e.g. ages, metallicities, orbits) correlate with the properties of the assembly histories of their host galaxies. With the description of the cold, clumpy gas, for the first time we can accurately describe how clusters dissolve over cosmic history due to tidal shocks. Using these simulated cluster populations, one could predict the number of tidal structures, their mass content, and their spatial distribution. In addition, these simulations track the detailed gas phase and stellar abundances for more than 30 elements. Together, these chemo-dynamical quantities represent critical tests of cluster disruption, dwarf galaxy accretion, and near-field cosmology, and are ideally suited for comparison with the currently available *Gaia* data (e.g. Ibata et al., 2019), as well as upcoming observations with the LSST⁶.

8.3.3 It’s not just about GCs: further implications

Since the first observations of GCs, these have been considered to be peculiar objects in terms of their properties. Their use as beacons that has allowed the exploration of the structure of extragalactic systems would have not been possible without their high luminosities. In this last section we would like to briefly highlight how their properties can be related to other open questions in the literature, and we discuss them going from larger to smaller scales.

A first example is given by the observational evidence that a Hubble time of cosmic evolution is not sufficient to fully disrupt the most massive end of the stellar cluster population, which can be related to models regarding the nature of dark matter. Some of these models predict that dark matter would coalesce in low-mass substructures that could potentially lead to an increase of the mass lost due to tidal interactions (see recent review by Buckley and Peter, 2018). This idea is already being examined by several authors using N -body simulations of stellar clusters orbiting in galaxies with these small structures (Webb et al., 2019b; Webb and Bovy, 2020), as well as by trying to reproduce observed gaps in the structure of stellar streams from disrupted clusters (Bonaca and Hogg, 2018; Bonaca et al., 2019; Webb and Bovy, 2019). As more stellar streams are discovered in *Gaia* and LSST data, further and better constraints can be placed on the nature of this elusive component of the Universe.

Secondly, the role played by the environment in shaping stellar cluster populations implies that the natal conditions of stellar clusters are encoded in their demographics. This is particularly true in the most massive end ($M \gtrsim 10^5 M_{\odot}$), as it is less affected by dynamical disruption. Thus, an exciting step forward would be to use massive stellar cluster populations and this environmental description of their formation to reverse-engineer the galactic environment from which these clusters form. A first attempt is presented by Trujillo-Gomez et al., (2019) to the Fornax dwarf spheroidal galaxy, in which an extended environmental description of the initial cluster distribution is used to find that ~ 10 – 12 Gyr

⁶The Large Scale Synoptic Survey (LSST) or Vera C. Rubin Observatory.

ago the progenitor of the galaxy was forming stars in a high gas surface density and strong shearing environment ($\Sigma_{\text{gas}} \simeq 700\text{--}110 \text{ M}_{\odot}\text{pc}^{-2}$ and $\kappa \simeq 0.6\text{--}1.6 \text{ Myr}^{-1}$). Applying this methodology to other galactic systems with peculiar cluster populations is likely going to lead to an exciting new way of exploring galaxy evolution.

Moreover, the crucial role played by the cold ISM in shaping the stellar cluster populations as presented in Chapter 7 showcases the importance of accurately describing the baryonic physics involved in the processes of star formation and evolution, as these will in turn modify the structure of the ISM. This implies that a better description of these processes is needed in current cosmological simulations as higher mass and spatial resolutions are achieved. Following this philosophy, the EMP simulations (Kruijssen et al. in prep., Keller et al. in prep.) are adding a suite of empirically-motivated sub-grid descriptions for star formation and stellar feedback to the moving-mesh code **AREPO** (Gensior et al. 2020, Keller et al. in prep.). The empirical description of these processes is expected to reproduce the structure of the ISM within galaxies in cosmological, hydrodynamical simulations.

Going towards smaller scales, the constraints for models describing the origin of the multiple population phenomenon that are obtained and discussed in this thesis (Section 8.2.2) imply that the mass loss required by these models cannot be accommodated in this framework of stellar clusters in a cosmological context. The implications from this are two-fold. On one hand, it validates the use of a self-consistent model of stellar cluster formation and evolution in a cosmic environment to test these theoretical models despite lacking a description for this phenomenon. On the other hand, non-standard polluters or star formation and evolutionary processes in crowded environments seem to be required to produce the chemical inhomogeneities observed in massive clusters.

At even smaller scales, observations of gravitational waves produced by mergers of exotic products of stellar evolution by LIGO (Abbott et al., 2016) suggest that the populous and crowded stellar clusters are natural cradles for these events. The detectability of cluster-located events by current and future detectors such as LIGO and LISA is already being explored (Arca-Sedda and Gualandris, 2018; Arca Sedda et al., 2019). An exciting step forward would be to combine prescriptions regarding the frequency of these type of events with our framework for stellar cluster formation and evolution in a cold, clumpy cosmic environment. This would lead to predictions regarding the number of expected events as a function of cosmic time and galactic environment, which could in turn be used to interpret the wealth of observational data that is starting to come from these observatories.

In this thesis, we have emphasized the exciting role that stellar clusters have in unveiling the conditions of the cosmic environment, from large to small scales, as well as the need of accurately modelling all the physical processes involved in their formation and evolution. Our current knowledge of stellar clusters in a cosmic context is yet far from being complete, but we believe that this work goes a step forward in this direction and that it will lead to new avenues of exploration.

With these final remarks, this thesis is concluded.

Acknowledgements

Developing this thesis has been a personal challenge over the past four years, and without the support of great people around me, it would not have been as fun.

First and foremost, I would like to thank my advisor, Diederik Kruijssen, for all our discussions on how to do science, and for trusting me since the beginning. It has been with your guidance that I have grown into the scientist that I am today. Besides him, I have been extremely lucky in having Eva Grebel and Friedrich Röpke as my thesis committee members, as well as Hans-Walter Rix and James Hinton in my examination committee.

I gratefully acknowledge the fellowship from the International Max Planck Research School (IMPRS-HD) that has supported me during these years.

The work presented in this thesis would have not been possible without my collaborators: Nate Bastian, Rob Crain, Meghan Hughes, Joel Pfeffer, and Jeremy Webb. Thanks to all of you for always welcoming my ideas, and for supporting my development as an early scientist. I would also like to thank Andreas Koch and Chris Usher for sharing their knowledge with me.

I owe my gratitude to Alis Deason for being such a welcoming host during my visit to Durham, and for supporting me, both personally and professionally, during this career stage. Thanks to her support, I have been able to develop the *EMP-Pathfinder* simulations in the COSMA facilities at Durham University.

It is my pleasure to thank the MUSTANG group for the lively and supportive working environment that we have: Alex Hygate, Daniel Haydon, Sarah Jeffreson, Mélanie Chevance, Jake Ward, Ben Keller, Jindra Gensior, Sebastian Trujillo-Gomez, Maya Petkova, Jaeyeon Kim, Andrew Winter and Verena Fürnkranz. Some of you already set sails for new shores, and some of us are still roaming in the old library building, but to all of you, thanks for having been there. Special thanks to Sarah, for all the shared adventures.

This journey would have been much lonelier without the people from the IMPRS, and specially for the ARI (and adopted) crowd: Michael Hanke, Jonas Klüter, Zdeněk Prudil, Manuel Riener, Paula Sarkis, and Faezeh Shabani. It might have been the blue stuff, but I really enjoyed those music nights.

And last, I would not be here if it were not for my family: papá, mamá, Miguel, Lara, María, and Gonzalo. Thanks for all your love and support before, during and hopefully after. Ahora toca celebrar con una tapita de croquetas!

Bibliography

- Abbott, B. P. et al. (2016). “Observation of Gravitational Waves from a Binary Black Hole Merger”. *Phys. Rev. Lett.* 116.6, 061102, 061102. arXiv: 1602.03837 [gr-qc] (cit. on p. 144).
- Abel, Tom et al. (1997). “Modeling primordial gas in numerical cosmology”. *New Ast.* 2.3, 181–207. arXiv: astro-ph/9608040 [astro-ph] (cit. on p. 93).
- Adamo, A. et al. (2015). “Probing the role of the galactic environment in the formation of stellar clusters, using M83 as a test bench”. *MNRAS* 452, 246–260. arXiv: 1505.07475 (cit. on pp. 7, 102, 104, 114, 131, 138).
- Adamo, A. et al. (2017). “Legacy ExtraGalactic UV Survey with The Hubble Space Telescope: Stellar Cluster Catalogs and First Insights Into Cluster Formation and Evolution in NGC 628”. *ApJ* 841.2, 131, 131. arXiv: 1705.01588 [astro-ph.GA] (cit. on pp. 9, 139, 141).
- Adamo, A. et al. (2020). “Star Clusters Near and Far; Tracing Star Formation Across Cosmic Time”. *Space Sci. Rev.* 216.4, 69, 69. arXiv: 2005.06188 [astro-ph.GA] (cit. on pp. 2, 6, 7, 13, 102, 104, 116, 131, 136, 137, 139).
- Agertz, Oscar et al. (2013). “Toward a Complete Accounting of Energy and Momentum from Stellar Feedback in Galaxy Formation Simulations”. *ApJ* 770.1, 25, 25. arXiv: 1210.4957 [astro-ph.CO] (cit. on p. 98).
- Aguilar, L., P. Hut, and J. P. Ostriker (1988). “On the evolution of globular cluster systems. I - Present characteristics and rate of destruction in our Galaxy”. *ApJ* 335, 720–747 (cit. on p. 109).
- Airy, G. B. (1836). “History of nebulae and clusters of stars”. *MNRAS* 3, 167 (cit. on p. 2).
- Alexander, Poul E. R. et al. (2014). “A prescription and fast code for the long-term evolution of star clusters - III. Unequal masses and stellar evolution”. *MNRAS* 442.2, 1265–1285. arXiv: 1405.1086 [astro-ph.GA] (cit. on p. 107).
- Ambartsumian, V. A. (1938). *TsAGI Uchenye Zapiski* 22, 19–22 (cit. on p. 109).
- Anninos, Peter et al. (1997). “Cosmological hydrodynamics with multi-species chemistry and nonequilibrium ionization and cooling”. *New Ast.* 2.3, 209–224. arXiv: astro-ph/9608041 [astro-ph] (cit. on p. 93).
- Arca Sedda, Manuel et al. (2019). “The Missing Link in Gravitational-Wave Astronomy: Discoveries waiting in the decihertz range”. *arXiv e-prints*, arXiv:1908.11375, arXiv:1908.11375. arXiv: 1908.11375 [gr-qc] (cit. on p. 144).

- Arca-Sedda, Manuel and Alessia Gualandris (2018). “Gravitational wave sources from inspiralling globular clusters in the Galactic Centre and similar environments”. *MNRAS* 477.4, 4423–4442. arXiv: 1804.06116 [astro-ph.GA] (cit. on p. 144).
- Arp, H. C. (1965). “Globular Clusters in the Galaxy”. *Galactic structure. Edited by Adriaan Blaauw and Maarten Schmidt. Published by the University of Chicago Press*, 401 (cit. on p. 4).
- Arp, H. C. and A. Sandage (1985). “Spectra of the two brightest objects in the amorphous galaxy NGC 1569 : superluminous young star clusters - or stars in a nearby peculiar galaxy ?” *AJ* 90, 1163–1171 (cit. on p. 5).
- Ashman, Keith M. and Stephen E. Zepf (1992). “The Formation of Globular Clusters in Merging and Interacting Galaxies”. *ApJ* 384, 50 (cit. on pp. 5, 6, 101).
- Asplund, M. et al. (2009). “The Chemical Composition of the Sun”. *ARA&A* 47, 481–522. arXiv: 0909.0948 [astro-ph.SR] (cit. on p. 113).
- El-Badry, K. et al. (2019). “The formation and hierarchical assembly of globular cluster populations”. *MNRAS* 482, 4528–4552. arXiv: 1805.03652 (cit. on p. 12).
- Bagla, J. S. (2002). “TreePM: A Code for Cosmological N-Body Simulations”. *Journal of Astrophysics and Astronomy* 23, 185–196. arXiv: astro-ph/9911025 [astro-ph] (cit. on p. 126).
- Bailey, Solon I. (1908). “A catalogue of bright clusters and nebulae”. *Annals of Harvard College Observatory* 60, 199–230.10 (cit. on p. 2).
- Baldry, Ivan K. et al. (2004). “Quantifying the Bimodal Color-Magnitude Distribution of Galaxies”. *ApJ* 600.2, 681–694. arXiv: astro-ph/0309710 [astro-ph] (cit. on p. 8).
- Barnard, E. E. (1920). “On the comparative distances of certain globular clusters and the star clouds of the Milky Way”. *AJ* 33, 86–86 (cit. on p. 4).
- Barnes, J. and P. Hut (1986). “A hierarchical $O(N \log N)$ force-calculation algorithm”. *Nature* 324, 446–449 (cit. on pp. 92, 93, 126).
- Bastian, Nate (2008). “On the star formation rate - brightest cluster relation: estimating the peak star formation rate in post-merger galaxies”. *MNRAS* 390.2, 759–768. arXiv: 0807.4687 [astro-ph] (cit. on pp. 6, 102).
- Bastian, Nate and Carmela Lardo (2018). “Multiple Stellar Populations in Globular Clusters”. *ARA&A* 56.1. eprint: <https://doi.org/10.1146/annurev-astro-081817-051839>. URL: <https://doi.org/10.1146/annurev-astro-081817-051839> (cit. on pp. 11, 135, 139).
- Bastian, Nate et al. (2009). “The spatial evolution of stellar structures in the Large Magellanic Cloud”. *MNRAS* 392, 868–878. arXiv: 0809.1943 (cit. on p. 6).
- Bastian, Nate et al. (2020). “The globular cluster system mass-halo mass relation in the E-MOSAICS simulations”. *arXiv e-prints*, arXiv:2005.05991, arXiv:2005.05991. arXiv: 2005.05991 [astro-ph.GA] (cit. on pp. iv, 13).
- Baumgardt, H. (1998). “The initial distribution and evolution of globular cluster systems”. *A&A* 330, 480–491 (cit. on p. 8).
- Baumgardt, H. and P. Kroupa (2007). “A comprehensive set of simulations studying the influence of gas expulsion on star cluster evolution”. *MNRAS* 380, 1589–1598. arXiv: 0707.1944 (cit. on p. 106).

- Baumgardt, H. and J. Makino (2003). “Dynamical evolution of star clusters in tidal fields”. *MNRAS* 340, 227–246 (cit. on pp. 9, 132).
- Baumgardt, H. et al. (2013). “The star cluster formation history of the LMC”. *MNRAS* 430, 676–685. arXiv: 1207.5576 (cit. on p. 8).
- Baumgardt, H. et al. (2019). “Mean proper motions, space orbits, and velocity dispersion profiles of Galactic globular clusters derived from Gaia DR2 data”. *MNRAS* 482.4, 5138–5155. arXiv: 1811.01507 [astro-ph.GA] (cit. on p. 140).
- Beasley, M. A. et al. (2002). “On the formation of globular cluster systems in a hierarchical Universe”. *MNRAS* 333.2, 383–399. arXiv: astro-ph/0202191 [astro-ph] (cit. on pp. 11, 12).
- Belokurov, V. et al. (2018). “Co-formation of the disc and the stellar halo”. *MNRAS* 478.1, 611–619. arXiv: 1802.03414 [astro-ph.GA] (cit. on pp. 13, 14, 136, 141).
- Bigiel, F. et al. (2008). “The Star Formation Law in Nearby Galaxies on Sub-Kpc Scales”. *AJ* 136, 2846–2871. arXiv: 0810.2541 (cit. on pp. 94, 95).
- Binney, James and Scott Tremaine (2008). *Galactic Dynamics: Second Edition* (cit. on pp. 9, 122).
- Blitz, L. and E. Rosolowsky (2004). “The Role of Pressure in Giant Molecular Cloud Formation”. *ApJ* 612, L29–L32. eprint: arXiv:astro-ph/0407492 (cit. on p. 119).
- Blondin, John M. et al. (1998). “Transition to the Radiative Phase in Supernova Remnants”. *ApJ* 500.1, 342–354 (cit. on p. 99).
- Boley, Aaron C. et al. (2009). “Globular Cluster Formation Within a Cosmological Context”. *ApJ* 706.1, L192–L196. arXiv: 0908.1254 [astro-ph.CO] (cit. on p. 5).
- Bonaca, Ana and David W. Hogg (2018). “The Information Content in Cold Stellar Streams”. *ApJ* 867.2, 101, 101. arXiv: 1804.06854 [astro-ph.GA] (cit. on p. 143).
- Bonaca, Ana et al. (2019). “The Spur and the Gap in GD-1: Dynamical Evidence for a Dark Substructure in the Milky Way Halo”. *ApJ* 880.1, 38, 38. arXiv: 1811.03631 [astro-ph.GA] (cit. on p. 143).
- Bouvier, P. and G. Janin (1970). “Disruption of Star Clusters Through Passing Interstellar Clouds Investigated by Numerical Experiments”. *A&A* 9, 461 (cit. on p. 9).
- Bouwens, R. J. et al. (2017). “Very low-luminosity galaxies in the early universe have observed sizes similar to single star cluster complexes”. *arXiv e-prints*, arXiv:1711.02090, arXiv:1711.02090. arXiv: 1711.02090 [astro-ph.GA] (cit. on pp. 8, 142).
- Boylan-Kolchin, Michael (2017). “The globular cluster-dark matter halo connection”. *MNRAS* 472.3, 3120–3130. arXiv: 1705.01548 [astro-ph.GA] (cit. on pp. 5, 137).
- Brodie, J. P. and J. Strader (2006). “Extragalactic Globular Clusters and Galaxy Formation”. *ARA&A* 44, 193–267. eprint: arXiv:astro-ph/0602601 (cit. on p. 7).
- Buckley, Matthew R. and Annika H. G. Peter (2018). “Gravitational probes of dark matter physics”. *Phys. Rep.* 761, 1–60. arXiv: 1712.06615 [astro-ph.CO] (cit. on p. 143).
- Cabrera-Ziri, I. et al. (2014). “Constraining globular cluster formation through studies of young massive clusters - II. A single stellar population young massive cluster in NGC 34”. *MNRAS* 441.3, 2754–2759. arXiv: 1404.4056 [astro-ph.GA] (cit. on p. 139).
- Carretta, E. et al. (2010). “M54 + Sagittarius = ω Centauri”. *ApJ* 714, L7–L11. arXiv: 1002.1963 [astro-ph.GA] (cit. on pp. 10, 135).

- Cen, Renyue (2001). “Synchronized Formation of Subgalactic Systems at Cosmological Reionization: Origin of Halo Globular Clusters”. *ApJ* 560.2, 592–598. arXiv: [astro-ph/0101197](#) [[astro-ph](#)] (cit. on p. 5).
- Cen, Renyue and Jeremiah P. Ostriker (1992). “Galaxy Formation and Physical Bias”. *ApJ* 399, L113 (cit. on p. 95).
- Chabrier, Gilles (2003). “Galactic Stellar and Substellar Initial Mass Function”. *PASP* 115, 763–795. eprint: [astro-ph/0304382](#) (cit. on p. 106).
- (2005). “The Initial Mass Function: From Salpeter 1955 to 2005”. *The Initial Mass Function 50 Years Later*. Ed. by E. Corbelli, F. Palla, and H. Zinnecker. Vol. 327. Astrophysics and Space Science Library, 41 (cit. on pp. 96, 109).
- Chandar, Rupali, S. Michael Fall, and Bradley C. Whitmore (2015). “The Link Between the Formation Rates of Clusters and Stars in Galaxies”. *ApJ in press*, [arXiv:1506.08846](#). arXiv: [1506.08846](#) (cit. on p. 104).
- Chandar, Rupali et al. (2017). “The Fraction of Stars That Form in Clusters in Different Galaxies”. *ApJ* 849.2, 128, 128. arXiv: [1806.11537](#) [[astro-ph.GA](#)] (cit. on p. 104).
- Chevance, Mélanie et al. (2020). “The lifecycle of molecular clouds in nearby star-forming disc galaxies”. *MNRAS* 493.2, 2872–2909. arXiv: [1911.03479](#) [[astro-ph.GA](#)] (cit. on p. 104).
- Choksi, Nick and Oleg Y. Gnedin (2019). “Formation of globular cluster systems - II. Impact of the cut-off of the cluster initial mass function”. *MNRAS* 486.1, 331–343. arXiv: [1810.01888](#) [[astro-ph.GA](#)] (cit. on p. 12).
- Choksi, Nick, Oleg Y. Gnedin, and Hui Li (2018). “Formation of globular cluster systems: from dwarf galaxies to giants”. *MNRAS* 480.2, 2343–2356. arXiv: [1801.03515](#) [[astro-ph.GA](#)] (cit. on pp. 11, 12).
- Choksi, Nick and J. M. Diederik Kruijssen (2019). “On the initial mass-radius relation of stellar clusters”. *arXiv e-prints*, arXiv:[1912.05560](#), arXiv:[1912.05560](#). arXiv: [1912.05560](#) [[astro-ph.GA](#)] (cit. on pp. 101, 107).
- Chomiuk, Laura and Matthew S. Povich (2011). “Toward a Unification of Star Formation Rate Determinations in the Milky Way and Other Galaxies”. *AJ* 142.6, 197, 197. arXiv: [1110.4105](#) [[astro-ph.GA](#)] (cit. on p. 115).
- Colombo, D. et al. (2019). “The integrated properties of the molecular clouds from the JCMT CO(3-2) High-Resolution Survey”. *MNRAS* 483.4, 4291–4340. arXiv: [1812.04688](#) [[astro-ph.GA](#)] (cit. on pp. 114, 119).
- Conroy, Charlie et al. (2019). “Resolving the Metallicity Distribution of the Stellar Halo with the H3 Survey”. *arXiv e-prints*, arXiv:[1909.02007](#), arXiv:[1909.02007](#). arXiv: [1909.02007](#) [[astro-ph.GA](#)] (cit. on pp. 14, 136, 141).
- Correa, C. A. et al. (2015). “The accretion history of dark matter haloes - III. A physical model for the concentration-mass relation”. *MNRAS* 452, 1217–1232. arXiv: [1502.00391](#) (cit. on pp. 134, 138).
- Crain, R. A. et al. (2015). “The EAGLE simulations of galaxy formation: calibration of subgrid physics and model variations”. *MNRAS* 450, 1937–1961. arXiv: [1501.01311](#) (cit. on pp. 12, 136).

- Crampin, J. and F. Hoyle (1961). “On the change with time of the integrated colour and luminosity of an M67-type star group”. *MNRAS* 122, 27 (cit. on p. 10).
- Curtis, Heber D. (1917). “Novae in the Spiral Nebulae and the Island Universe Theory”. *PASP* 29.171, 206–207 (cit. on p. 3).
- (1920). “Modern Theories of the Spiral Nebulae”. *JRASC* 14, 317 (cit. on p. 3).
- da Silva, Robert L., Michele Fumagalli, and Mark R. Krumholz (2012). “SLUG - Stochastically Lighting Up Galaxies. I. Methods and Validating Tests”. *ApJ* 745, 145, 145. arXiv: 1106.3072 [astro-ph.IM] (cit. on p. 96).
- (2014). “SLUG - Stochastically Lighting Up Galaxies - II. Quantifying the effects of stochasticity on star formation rate indicators”. *MNRAS* 444.4, 3275–3287. arXiv: 1403.4605 [astro-ph.GA] (cit. on p. 96).
- Davis, M. et al. (1985). “The evolution of large-scale structure in a universe dominated by cold dark matter”. *ApJ* 292, 371–394 (cit. on p. 115).
- Davis, T. A. et al. (2014). “The ATLAS^{3D} Project - XXVIII. Dynamically driven star formation suppression in early-type galaxies”. *MNRAS* 444, 3427–3445. arXiv: 1403.4850 [astro-ph.GA] (cit. on p. 96).
- de Mink, S. E. et al. (2009). “Massive binaries as the source of abundance anomalies in globular clusters”. *A&A* 507, L1–L4. arXiv: 0910.1086 [astro-ph.SR] (cit. on pp. 10, 135).
- Deason, A. J., V. Belokurov, and D. R. Weisz (2015). “The progenitors of the Milky Way stellar halo: big bricks favoured over little bricks.” *MNRAS* 448, L77–L81. arXiv: 1501.02806 [astro-ph.GA] (cit. on pp. 14, 136, 141).
- Diemand, Jürg, Piero Madau, and Ben Moore (2005). “The distribution and kinematics of early high- σ peaks in present-day haloes: implications for rare objects and old stellar populations”. *MNRAS* 364.2, 367–383. arXiv: astro-ph/0506615 [astro-ph] (cit. on p. 5).
- Doherty, C. L. et al. (2014). “Super and massive AGB stars - II. Nucleosynthesis and yields - $Z = 0.02, 0.008$ and 0.004 ”. *MNRAS* 437, 195–214. arXiv: 1310.2614 [astro-ph.SR] (cit. on p. 97).
- Dolag, K. et al. (2009). “Substructures in hydrodynamical cluster simulations”. *MNRAS* 399, 497–514. arXiv: 0808.3401 (cit. on pp. 111, 115).
- Dotter, A., A. Sarajedini, and J. Anderson (2011). “Globular Clusters in the Outer Galactic Halo: New Hubble Space Telescope/Advanced Camera for Surveys Imaging of Six Globular Clusters and the Galactic Globular Cluster Age-metallicity Relation”. *ApJ* 738, 74, 74. arXiv: 1106.4307 (cit. on pp. 8, 13, 134, 140).
- Dreyer, J. L. E. (1888). “A New General Catalogue of Nebulae and Clusters of Stars, being the Catalogue of the late Sir John F. W. Herschel, Bart, revised, corrected, and enlarged”. *MmRAS* 49, 1 (cit. on p. 2).
- Dunlop, James (1828). “A Catalogue of Nebulae and Clusters of Stars in the Southern Hemisphere, Observed at Paramatta in New South Wales”. *Philosophical Transactions of the Royal Society of London Series I* 118, 113–151 (cit. on p. 2).

- Ekström, S. et al. (2012). “Grids of stellar models with rotation. I. Models from 0.8 to 120 M_{sun} at solar metallicity ($Z = 0.014$)”. *A&A* 537, A146, A146. arXiv: 1110.5049 [astro-ph.SR] (cit. on p. 105).
- Elmegreen, B. G. (1989). “A Pressure and Metallicity Dependence for Molecular Cloud Correlations and the Calibration of Mass”. *ApJ* 338, 178 (cit. on pp. 103, 119).
- (2002). “Star Formation from Galaxies to Globules”. *ApJ* 577, 206–220 (cit. on p. 105).
- (2010). “The Globular Cluster Mass Function as a Remnant of Violent Birth”. *ApJ* 712.2, L184–L188. arXiv: 1003.0798 [astro-ph.CO] (cit. on pp. 5, 9, 132, 138).
- (2011). “Star Formation Patterns and Hierarchies”. *EAS Publications Series*. Ed. by Corinne Charbonnel and Thierry Montmerle. Vol. 51. EAS Publications Series, 31–44. arXiv: 1101.3111 [astro-ph.GA] (cit. on pp. 6, 7, 104).
- Elmegreen, B. G. and Y. N. Efremov (1997). “A Universal Formation Mechanism for Open and Globular Clusters in Turbulent Gas”. *ApJ* 480, 235–+ (cit. on pp. 5, 8, 10, 101).
- Elmegreen, B. G. and D. A. Hunter (2010). “On the Disruption of Star Clusters in a Hierarchical Interstellar Medium”. *ApJ* 712, 604–623. arXiv: 1002.2823 (cit. on pp. 6, 9, 109, 114, 132, 138, 141).
- Enoch, Melissa L. et al. (2008). “The Mass Distribution and Lifetime of Prestellar Cores in Perseus, Serpens, and Ophiuchus”. *ApJ* 684.2, 1240–1259. arXiv: 0805.1075 [astro-ph] (cit. on p. 106).
- Fall, S. M. and M. J. Rees (1985). “A theory for the origin of globular clusters.” *ApJ* 298, 18–26 (cit. on pp. 5, 8, 141).
- Fall, S. M. and Q. Zhang (2001). “Dynamical Evolution of the Mass Function of Globular Star Clusters”. *ApJ* 561, 751–765 (cit. on p. 8).
- Forbes, D. A. (2020). “Reverse engineering the Milky Way”. *MNRAS* 493.1, 847–854. arXiv: 2002.01512 [astro-ph.GA] (cit. on pp. 4, 140).
- Forbes, D. A. and T. Bridges (2010). “Accreted versus in situ Milky Way globular clusters”. *MNRAS* 404, 1203–1214. arXiv: 1001.4289 [astro-ph.GA] (cit. on pp. 4, 8, 13, 134, 140).
- Forbes, D. A. et al. (2018). “Globular cluster formation and evolution in the context of cosmological galaxy assembly: open questions”. *Proceedings of the Royal Society of London Series A* 474, 20170616, 20170616. arXiv: 1801.05818 (cit. on p. 11).
- Frenk, C. S. and S. D. M. White (1980). “The kinematics and dynamics of the galactic globular cluster system”. *MNRAS* 193, 295–311 (cit. on pp. 4, 140).
- (1982). “The form of the galactic globular cluster system and the distance to the galactic centre.” *MNRAS* 198, 173–192 (cit. on p. 4).
- Gaia Collaboration et al. (2018). “Gaia Data Release 2. Kinematics of globular clusters and dwarf galaxies around the Milky Way”. *A&A* 616, A12, A12. arXiv: 1804.09381 [astro-ph.GA] (cit. on pp. 140, 142).
- Gensior, Jindra, J. M. Diederik Kruijssen, and Benjamin W. Keller (2020). “Heart of darkness: the influence of galactic dynamics on quenching star formation in galaxy spheroids”. *MNRAS* 495.1, 199–223. arXiv: 2002.01484 [astro-ph.GA] (cit. on pp. 95, 96, 144).

- Gieles, M., E. Athanassoula, and S. F. Portegies Zwart (2007). “The effect of spiral arm passages on the evolution of stellar clusters”. *MNRAS* 376, 809–819. eprint: [arXiv: astro-ph/0701136](#) (cit. on p. 9).
- Gieles, M. and H. Baumgardt (2008). “Lifetimes of tidally limited star clusters with different radii”. *MNRAS* 389.1, L28–L32. [arXiv: 0806.2327 \[astro-ph\]](#) (cit. on pp. 6, 9, 109).
- Gieles, M., D. C. Heggie, and H. Zhao (2011). “The life cycle of star clusters in a tidal field”. *MNRAS* 413, 2509–2524. [arXiv: 1101.1821 \[astro-ph.GA\]](#) (cit. on p. 112).
- Gieles, M. and F. Renaud (2016). “If it does not kill them, it makes them stronger: collisional evolution of star clusters with tidal shocks”. *MNRAS* 463, L103–L107. [arXiv: 1605.05940](#) (cit. on p. 112).
- Gieles, M. et al. (2006). “Star cluster disruption by giant molecular clouds”. *MNRAS* 371, 793–804. eprint: [astro-ph/0606451](#) (cit. on pp. 9, 109, 114, 132, 138).
- Gieles, M. et al. (2018). “Concurrent formation of supermassive stars and globular clusters: implications for early self-enrichment”. *ArXiv e-prints*. [arXiv: 1804.04682](#) (cit. on p. 135).
- Giersz, M. and D. C. Heggie (1994). “Statistics of N-Body Simulations - Part One - Equal Masses Before Core Collapse”. *MNRAS* 268, 257. [arXiv: astro-ph/9305008 \[astro-ph\]](#) (cit. on pp. 9, 109).
- Girardi, L. et al. (2000). “Evolutionary tracks and isochrones for low- and intermediate-mass stars: From 0.15 to 7 M_{sun} , and from $Z=0.0004$ to 0.03”. *A&AS* 141, 371–383. [arXiv: astro-ph/9910164 \[astro-ph\]](#) (cit. on pp. 97, 108).
- Glatt, K., E. K. Grebel, and A. Koch (2010). “Ages and luminosities of young SMC/LMC star clusters and the recent star formation history of the Clouds”. *A&A* 517, A50, A50. [arXiv: 1004.1247 \[astro-ph.GA\]](#) (cit. on p. 8).
- Glatt, K. et al. (2009). “Structural Parameters of Seven Small Magellanic Cloud Intermediate-Age and Old Star Clusters”. *AJ* 138.5, 1403–1416. [arXiv: 0909.1329 \[astro-ph.CO\]](#) (cit. on p. 8).
- Glatt, K. et al. (2011). “Present-day Mass Function of Six Small Magellanic Cloud Intermediate-age and Old Star Clusters”. *AJ* 142.2, 36, 36 (cit. on p. 8).
- Gnedin, Oleg Y. (2003). “Tidal Effects in Clusters of Galaxies”. *ApJ* 582.1, 141–161. [arXiv: astro-ph/0302497 \[astro-ph\]](#) (cit. on pp. 9, 110, 133).
- Gnedin, Oleg Y. and Jeremiah P. Ostriker (1999). “On the Self-consistent Response of Stellar Systems to Gravitational Shocks”. *ApJ* 513, 626–637. eprint: [arXiv: astro-ph/9902326](#) (cit. on p. 9).
- Goddard, Q. E., N. Bastian, and R. C. Kennicutt (2010). “On the fraction of star clusters surviving the embedded phase”. *MNRAS* 405.2, 857–869. [arXiv: 1002.2894 \[astro-ph.CO\]](#) (cit. on p. 7).
- Gouliermis, Dimitrios A. et al. (2015). “Hierarchical star formation across the ring galaxy NGC 6503”. *MNRAS* 452.4, 3508–3528. [arXiv: 1506.03928 \[astro-ph.GA\]](#) (cit. on p. 6).
- Grasha, K. et al. (2015). “The Spatial Distribution of the Young Stellar Clusters in the Star-forming Galaxy NGC 628”. *ApJ* 815.2, 93, 93. [arXiv: 1511.02233 \[astro-ph.GA\]](#) (cit. on p. 6).

- Grasha, K. et al. (2017a). “Hierarchical Star Formation in Turbulent Media: Evidence from Young Star Clusters”. *ApJ* 842.1, 25, 25. arXiv: 1705.06281 [astro-ph.GA] (cit. on p. 6).
- Grasha, K. et al. (2017b). “The Hierarchical Distribution of the Young Stellar Clusters in Six Local Star-forming Galaxies”. *ApJ* 840.2, 113, 113. arXiv: 1704.06321 [astro-ph.GA] (cit. on p. 6).
- Griffen, B. F. et al. (2010). “Globular cluster formation within the Aquarius simulation”. *MNRAS* 405, 375–386. arXiv: 0910.0310 (cit. on p. 5).
- Griffen, B. F. et al. (2013). “The inhomogeneous reionization of the local intergalactic medium by metal-poor globular clusters”. *MNRAS* 431, 3087–3102. arXiv: 1209.6069 (cit. on p. 11).
- Gunn, J. E. (1980). “Some thoughts concerning the origin of globular clusters”. *Globular Clusters*. Ed. by D. Hanes and B. Madore, 301 (cit. on p. 5).
- Haardt, Francesco and Piero Madau (2012). “Radiative Transfer in a Clumpy Universe. IV. New Synthesis Models of the Cosmic UV/X-Ray Background”. *ApJ* 746.2, 125, 125. arXiv: 1105.2039 [astro-ph.CO] (cit. on p. 94).
- Halbesma, Timo L. R. et al. (2020). “The globular cluster system of the Auriga simulations”. *MNRAS* 496.1, 638–648. arXiv: 1909.02630 [astro-ph.GA] (cit. on p. 12).
- Harris, H. C. and R. Canterna (1979). “The Washington system: photometric properties and standard stars.” *AJ* 84, 1750–1755 (cit. on p. 3).
- Harris, W. E. (1976). “Spatial structure of the globular cluster system and the distance to the galactic center.” *AJ* 81, 1095–1116 (cit. on p. 4).
- (1988). “An overview of globular cluster systems in distant galaxies.” *The Harlow-Shapley Symposium on Globular Cluster Systems in Galaxies*. Ed. by Jonathan E. Grindlay and A. G. Davis Philip. Vol. 126. IAU Symposium, 237–250 (cit. on p. 141).
- (2010). “A New Catalog of Globular Clusters in the Milky Way”. *arXiv e-prints*, arXiv:1012.3224, arXiv:1012.3224. arXiv: 1012.3224 [astro-ph.GA] (cit. on p. 118).
- Harris, W. E. and P. L. Petrie (1978). “The space distribution of globular clusters in M49.” *ApJ* 223, 88–93 (cit. on p. 140).
- Harris, W. E. and Ralph E. Pudritz (1994). “Supergiant Molecular Clouds and the Formation of Globular Cluster Systems”. *ApJ* 429, 177 (cit. on p. 5).
- Harris, W. E. and R. Racine (1979). “Globular clusters in galaxies.” *ARA&A* 17, 241–274 (cit. on p. 141).
- Hayford, Phyllis (1932). “A study of galactic rotation with special reference to the radial velocities of the galactic star clusters”. *Lick Observatory Bulletin* 448, 53–75 (cit. on p. 4).
- Helmi, Amina (2008). “The stellar halo of the Galaxy”. *A&A Rev.* 15.3, 145–188. arXiv: 0804.0019 [astro-ph] (cit. on p. 4).
- (2020). “Streams, substructures and the early history of the Milky Way”. *arXiv e-prints*, arXiv:2002.04340, arXiv:2002.04340. arXiv: 2002.04340 [astro-ph.GA] (cit. on pp. 4, 140).

- Helmi, Amina et al. (1999). “Debris streams in the solar neighbourhood as relicts from the formation of the Milky Way”. *Nature* 402.6757, 53–55. arXiv: astro-ph/9911041 [astro-ph] (cit. on p. 13).
- Helmi, Amina et al. (2018). “The merger that led to the formation of the Milky Way’s inner stellar halo and thick disk”. *Nature* 563.7729, 85–88. arXiv: 1806.06038 [astro-ph.GA] (cit. on pp. 13, 14, 136, 141).
- Hénon, M. (1961). “Sur l’évolution dynamique des amas globulaires”. *Annales d’Astrophysique* 24, 369 (cit. on pp. 9, 109).
- Hernquist, L. (1990). “An analytical model for spherical galaxies and bulges”. *ApJ* 356, 359–364 (cit. on p. 113).
- Herschel, John Frederick William (1864). “A General Catalogue of Nebulae and Clusters of Stars”. *Philosophical Transactions of the Royal Society of London Series I* 154, 1–137 (cit. on p. 2).
- Herschel, William (1786). “Catalogue of One Thousand New Nebulae and Clusters of Stars. By William Herschel, LL.D. F. R. S.” *Philosophical Transactions of the Royal Society of London Series I* 76, 457–499 (cit. on p. 2).
- (1789). “Catalogue of a Second Thousand of New Nebulae and Clusters of Stars; With a Few Introductory Remarks on the Construction of the Heavens. By William Herschel, L L. D. F. R. S.” *Philosophical Transactions of the Royal Society of London Series I* 79, 212–255 (cit. on pp. 2, 4).
- (1800). “Catalogue of 500 New Nebulae, Nebulous Stars, Planetary Nebulae, and Clusters of Stars; with Remarks on the Construction of the Heavens. [Abstract]”. *Proceedings of the Royal Society of London Series I* 1, 98–100 (cit. on p. 2).
- Holtzman, J. A. et al. (1992). “Planetary Camera Observations of NGC 1275: Discovery of a Central Population of Compact Massive Blue Star Clusters”. *AJ* 103, 691 (cit. on pp. 5, 14, 101, 114, 141).
- Holtzman, J. A. et al. (1996). “Star Clusters in Interacting and Cooling Flow Galaxies”. *AJ* 112, 416 (cit. on pp. 6, 101).
- Hopkins, Philip F. et al. (2018). “FIRE-2 simulations: physics versus numerics in galaxy formation”. *MNRAS* 480.1, 800–863. arXiv: 1702.06148 [astro-ph.GA] (cit. on p. 99).
- Horta, Danny et al. (2020a). “Evidence from APOGEE for the presence of a major building block of the halo buried in the inner Galaxy”. *arXiv e-prints*, arXiv:2007.10374, arXiv:2007.10374. arXiv: 2007.10374 [astro-ph.GA] (cit. on pp. 13, 142).
- Horta, Danny et al. (2020b). “The chemical compositions of accreted and in situ galactic globular clusters according to SDSS/APOGEE”. *MNRAS* 493.3, 3363–3378. arXiv: 2001.03177 [astro-ph.GA] (cit. on pp. 13, 140, 142).
- Howard, Corey S., Ralph E. Pudritz, and William E. Harris (2018). “A universal route for the formation of massive star clusters in giant molecular clouds”. *Nature Astronomy* 2, 725–730. arXiv: 1808.07080 [astro-ph.GA] (cit. on p. 140).
- Howard, Corey S. et al. (2019). “On the origin of multiple populations during massive star cluster formation”. *MNRAS* 486.1, 1146–1155. arXiv: 1808.07081 [astro-ph.GA] (cit. on p. 140).

- Hubble, E. P. (1929). “A spiral nebula as a stellar system, Messier 31.” *ApJ* 69, 103–158 (cit. on p. 3).
- Hughes, Meghan E. et al. (2019). “Fossil stellar streams and their globular cluster populations in the E-MOSAICS simulations”. *MNRAS* 482.2, 2795–2806. arXiv: 1810.09889 [astro-ph.GA] (cit. on p. v).
- Hughes, Meghan E. et al. (2020). “The $[\alpha/\text{Fe}]$ - $[\text{Fe}/\text{H}]$ relation in the E-MOSAICS simulations: its connection to the birth place of globular clusters and the fraction of globular cluster field stars in the bulge”. *MNRAS* 491.3, 4012–4022. arXiv: 1912.01660 [astro-ph.GA] (cit. on p. iv).
- Ibata, R. A., G. Gilmore, and M. J. Irwin (1994). “A dwarf satellite galaxy in Sagittarius”. *Nature* 370.6486, 194–196 (cit. on pp. 4, 13).
- Ibata, Rodrigo A., Khyati Malhan, and Nicolas F. Martin (2019). “The Streams of the Gaping Abyss: A Population of Entangled Stellar Streams Surrounding the Inner Galaxy”. *ApJ* 872.2, 152, 152. arXiv: 1901.07566 [astro-ph.GA] (cit. on pp. 142, 143).
- Jeans, J. H. (1916). “On the law of distribution in star-clusters”. *MNRAS* 76, 567 (cit. on p. 2).
- Jenkins, Adrian (2010). “Second-order Lagrangian perturbation theory initial conditions for resimulations”. *MNRAS* 403.4, 1859–1872. arXiv: 0910.0258 [astro-ph.CO] (cit. on p. 114).
- (2013). “A new way of setting the phases for cosmological multiscale Gaussian initial conditions”. *MNRAS* 434.3, 2094–2120. arXiv: 1306.5968 [astro-ph.CO] (cit. on p. 114).
- Johnson, H. L. (1954). “Galactic Clusters and Stellar Evolution.” *ApJ* 120, 325 (cit. on pp. 3, 10).
- Johnson, H. L. et al. (1961). “Galactic clusters as indicators of stellar evolution and galactic structure”. *Lowell Observatory Bulletin* 5.113, 133–147 (cit. on p. 4).
- Johnson, L. C. et al. (2016). “Panchromatic Hubble Andromeda Treasury. XVI. Star Cluster Formation Efficiency and the Clustered Fraction of Young Stars”. *ApJ* 827, 33, 33. arXiv: 1606.05349 (cit. on p. 102).
- Johnson, L. C. et al. (2017). “Panchromatic Hubble Andromeda Treasury. XVIII. The High-mass Truncation of the Star Cluster Mass Function”. *ApJ* 839, 78, 78. arXiv: 1703.10312 (cit. on pp. 7, 8, 104, 131, 142).
- Jordán, Andrés et al. (2007). “The ACS Virgo Cluster Survey. XII. The Luminosity Function of Globular Clusters in Early-Type Galaxies”. *ApJS* 171.1, 101–145. arXiv: astro-ph/0702496 [astro-ph] (cit. on p. 7).
- Karakas, A. I. and M. Lugaro (2016). “Stellar Yields from Metal-rich Asymptotic Giant Branch Models”. *ApJ* 825, 26, 26. arXiv: 1604.02178 [astro-ph.SR] (cit. on p. 97).
- Katz, Neal (1992). “Dissipational Galaxy Formation. II. Effects of Star Formation”. *ApJ* 391, 502 (cit. on p. 95).
- Katz, Neal and Simon D. M. White (1993). “Hierarchical Galaxy Formation: Overmerging and the Formation of an X-Ray Cluster”. *ApJ* 412, 455 (cit. on p. 114).

- Keller, Benjamin W. et al. (2020). “Where did the globular clusters of the Milky Way form? Insights from the E-MOSAICS simulations”. MNRAS 495.4, 4248–4267. arXiv: 2005.05342 [astro-ph.GA] (cit. on pp. iv, 6, 141).
- Kennicutt Jr., R. C. (1989). “The star formation law in galactic disks”. ApJ 344, 685–703 (cit. on p. 96).
- (1998). “The Global Schmidt Law in Star-forming Galaxies”. ApJ 498, 541–+. eprint: arXiv:astro-ph/9712213 (cit. on p. 94).
- Kim, Ji-hoon et al. (2014). “The AGORA High-resolution Galaxy Simulations Comparison Project”. ApJS 210.1, 14, 14. arXiv: 1308.2669 [astro-ph.GA] (cit. on pp. 92, 112).
- Kim, Ji-hoon et al. (2016). “The AGORA High-resolution Galaxy Simulations Comparison Project. II. Isolated Disk Test”. ApJ 833.2, 202, 202. arXiv: 1610.03066 [astro-ph.GA] (cit. on pp. 92, 112).
- Kim, Ji-hoon et al. (2018). “Formation of globular cluster candidates in merging proto-galaxies at high redshift: a view from the FIRE cosmological simulations”. MNRAS 474, 4232–4244. arXiv: 1704.02988 (cit. on pp. 11, 101).
- King, Ivan (1957). “The dynamical lifetime of a star cluster.” AJ 62, 144 (cit. on p. 9).
- (1962). “Density Law in Spherical Stellar Systems.” AJ 67, 274–275 (cit. on p. 108).
- Kinman, T. D. (1959a). “Globular clusters, II. The spectral types of individual stars and of the integrated light”. MNRAS 119, 538 (cit. on pp. 3, 134, 140).
- (1959b). “Globular clusters, III. An analysis of the cluster radial velocities”. MNRAS 119, 559 (cit. on pp. 3, 134).
- Koch, Andreas, Eva K. Grebel, and Sarah L. Martell (2019). “Purveyors of fine halos: Re-assessing globular cluster contributions to the Milky Way halo buildup with SDSS-IV”. A&A 625, A75, A75. arXiv: 1904.02146 [astro-ph.GA] (cit. on pp. 136, 139).
- Kravtsov, A. V. and O. Y. Gnedin (2005). “Formation of Globular Clusters in Hierarchical Cosmology”. ApJ 623, 650–665. eprint: astro-ph/0305199 (cit. on p. 5).
- Kruijssen, J. M. Diederik (2012). “On the fraction of star formation occurring in bound stellar clusters”. MNRAS 426, 3008–3040. arXiv: 1208.2963 [astro-ph.CO] (cit. on pp. 6, 7, 102, 105, 115, 138).
- (2014). “Globular cluster formation in the context of galaxy formation and evolution”. *Classical and Quantum Gravity* 31.24, 244006, 244006. arXiv: 1407.2953 [astro-ph.GA] (cit. on pp. 5–7, 104, 131, 134, 136, 137, 141).
- (2015). “Globular clusters as the relics of regular star formation in ‘normal’ high-redshift galaxies”. MNRAS 454, 1658–1686. arXiv: 1509.02163 (cit. on pp. 5, 6, 8, 9, 101, 141).
- Kruijssen, J. M. Diederik et al. (2011). “Modelling the formation and evolution of star cluster populations in galaxy simulations”. MNRAS 414, 1339–1364. arXiv: 1102.1013 [astro-ph.CO] (cit. on pp. 6, 8, 9, 12, 101, 108–110, 112, 115, 133).
- Kruijssen, J. M. Diederik et al. (2012). “Formation versus destruction: the evolution of the star cluster population in galaxy mergers”. MNRAS 421, 1927–1941. arXiv: 1112.1065 [astro-ph.CO] (cit. on pp. 9, 102, 132).
- Kruijssen, J. M. Diederik et al. (2019a). “The E-MOSAICS project: tracing galaxy formation and assembly with the age-metallicity distribution of globular clusters”. MNRAS 486.3,

- 3134–3179. arXiv: 1904.04261 [astro-ph.GA] (cit. on pp. 4, 12–14, 91, 92, 101, 102, 112, 133, 136, 139–142).
- Kruijssen, J. M. Diederik et al. (2019b). “The formation and assembly history of the Milky Way revealed by its globular cluster population”. MNRAS 486.3, 3180–3202. arXiv: 1806.05680 [astro-ph.GA] (cit. on pp. v, 4, 8, 13, 136, 140, 142).
- Kruijssen, J. M. Diederik et al. (2020). “Kraken reveals itself – the merger history of the Milky Way reconstructed with the E-MOSAICS simulations”. *arXiv e-prints*, arXiv:2003.01119, arXiv:2003.01119. arXiv: 2003.01119 [astro-ph.GA] (cit. on pp. iv, 13, 136, 140, 142).
- Krumholz, Mark R. and Christopher F. McKee (2005). “A General Theory of Turbulence-regulated Star Formation, from Spirals to Ultraluminous Infrared Galaxies”. ApJ 630, 250–268 (cit. on pp. 103, 105, 107, 119).
- Krumholz, Mark R., Christopher F. McKee, and Joss Bland-Hawthorn (2019). “Star Clusters Across Cosmic Time”. ARA&A 57, 227–303. arXiv: 1812.01615 [astro-ph.GA] (cit. on pp. 2, 6, 7, 10, 13, 101, 107, 134–137, 141).
- Krumholz, Mark R. et al. (2015). “SLUG - stochastically lighting up galaxies - III. A suite of tools for simulated photometry, spectroscopy, and Bayesian inference with stochastic stellar populations”. MNRAS 452.2, 1447–1467. arXiv: 1502.05408 [astro-ph.GA] (cit. on p. 96).
- Lacey, Cedric and Shaun Cole (1993). “Merger rates in hierarchical models of galaxy formation”. MNRAS 262.3, 627–649 (cit. on p. 111).
- Lada, Charles J. and Elizabeth A. Lada (2003). “Embedded Clusters in Molecular Clouds”. ARA&A 41, 57–115. arXiv: astro-ph/0301540 [astro-ph] (cit. on pp. 6, 104).
- Lahén, Natalia et al. (2019). “The Formation of Low-metallicity Globular Clusters in Dwarf Galaxy Mergers”. ApJ 879.2, L18, L18. arXiv: 1905.09840 [astro-ph.GA] (cit. on pp. 11, 101).
- Lamers, H. J. G. L. M., M. Gieles, and S. F. Portegies Zwart (2005a). “Disruption time scales of star clusters in different galaxies”. A&A 429, 173–179. eprint: astro-ph/0408235 (cit. on pp. 9, 132, 138).
- Lamers, H. J. G. L. M. et al. (2005b). “An analytical description of the disruption of star clusters in tidal fields with an application to Galactic open clusters”. A&A 441, 117–129 (cit. on pp. 9, 109).
- Larsen, S. S. (2009). “The mass function of young star clusters in spiral galaxies”. A&A 503.2, 467–468 (cit. on pp. 7, 104, 131).
- Larsen, S. S. and T. Richtler (2000). “Young massive star clusters in nearby spiral galaxies. III. Correlations between cluster populations and host galaxy properties”. A&A 354, 836–846. arXiv: astro-ph/0001198 [astro-ph] (cit. on p. 6).
- Larson, Richard B. (1996). “Globular Clusters as Fossils of Galaxy Formation”. *Formation of the Galactic Halo...Inside and Out*. Ed. by Heather L. Morrison and Ata Sarajedini. Vol. 92. Astronomical Society of the Pacific Conference Series, 241 (cit. on p. 5).
- Li, Hui, Oleg Y. Gnedin, and Nickolay Y. Gnedin (2018). “Star Cluster Formation in Cosmological Simulations. II. Effects of Star Formation Efficiency and Stellar Feedback”. ApJ 861.2, 107, 107. arXiv: 1712.01219 [astro-ph.GA] (cit. on pp. 11, 101).

- Li, Hui et al. (2017). “Star Cluster Formation in Cosmological Simulations. I. Properties of Young Clusters”. *ApJ* 834.1, 69, 69. arXiv: 1608.03244 [astro-ph.GA] (cit. on pp. 11, 101).
- Licquia, Timothy C. and Jeffrey A. Newman (2015). “Improved Estimates of the Milky Way’s Stellar Mass and Star Formation Rate from Hierarchical Bayesian Meta-Analysis”. *ApJ* 806.1, 96, 96. arXiv: 1407.1078 [astro-ph.GA] (cit. on p. 116).
- Lutz, D. (1991). “NGC 3597 : formation of an elliptical via merging ?” *A&A* 245, 31 (cit. on p. 5).
- Ma, Xiangcheng et al. (2020a). “Self-consistent proto-globular cluster formation in cosmological simulations of high-redshift galaxies”. *MNRAS* 493.3, 4315–4332. arXiv: 1906.11261 [astro-ph.GA] (cit. on pp. 11, 101).
- Ma, Xiangcheng et al. (2020b). “The contribution of globular clusters to cosmic reionization”. *arXiv e-prints*, arXiv:2006.10065, arXiv:2006.10065. arXiv: 2006.10065 [astro-ph.GA] (cit. on p. 11).
- Madau, Piero and Mark Dickinson (2014). “Cosmic Star-Formation History”. *ARA&A* 52, 415–486. arXiv: 1403.0007 [astro-ph.CO] (cit. on pp. 5, 134).
- Madau, Piero et al. (2020). “Globular Cluster Formation from Colliding Substructure”. *ApJ* 890.1, 18, 18. arXiv: 1905.08951 [astro-ph.GA] (cit. on pp. 5, 137).
- Martell, S. L. and E. K. Grebel (2010). “Light-element abundance variations in the Milky Way halo”. *A&A* 519, A14, A14. arXiv: 1005.4070 [astro-ph.GA] (cit. on pp. 136, 139, 140).
- Martocchia, S. et al. (2018). “Age as a major factor in the onset of multiple populations in stellar clusters”. *MNRAS* 473.2, 2688–2700. arXiv: 1710.00831 [astro-ph.GA] (cit. on pp. 8, 10, 139).
- Masi, Marco (2007). “On compressive radial tidal forces”. *American Journal of Physics* 75.2, 116–124. arXiv: 0705.3747 [astro-ph] (cit. on p. 126).
- Massari, D., H. H. Koppelman, and A. Helmi (2019). “Origin of the system of globular clusters in the Milky Way”. *A&A* 630, L4, L4. arXiv: 1906.08271 [astro-ph.GA] (cit. on pp. 4, 13, 136, 140, 142).
- Mateu, Cecilia et al. (2017). “Predictions for the detection of tidal streams with Gaia using great-circle methods”. *MNRAS* 469.1, 721–743. arXiv: 1609.08653 [astro-ph.GA] (cit. on p. 114).
- McCrea, W. H. (1961). “Star Formation with Special Reference to Stellar Cluster”. *Proceedings of the Royal Society of London Series A* 260.1301, 152–159 (cit. on p. 5).
- (1982). “Origin of stars and galaxies”. *Progress in Cosmology*. Ed. by A. W. Wolfendale. Vol. 99. Astrophysics and Space Science Library, 239–257 (cit. on p. 5).
- McLaughlin, D. E. and S. M. Fall (2008). “Shaping the Globular Cluster Mass Function by Stellar-Dynamical Evaporation”. *ApJ* 679, 1272–1287. arXiv: 0704.0080 (cit. on p. 8).
- Melotte, P. J. (1915). “A Catalogue of Star Clusters shown on Franklin-Adams Chart Plates”. *MmRAS* 60, 175 (cit. on p. 2).
- Messa, M. et al. (2018). “The young star cluster population of M51 with LEGUS - II. Testing environmental dependences”. *MNRAS* 477, 1683–1707. arXiv: 1803.08527 (cit. on pp. v, 7, 9, 104, 105, 131, 139).

- Messier, Charles (1781). *Catalogue des Nébuleuses et des Amas d'Étoiles (Catalog of Nebulae and Star Clusters)*. Connaissance des Temps ou des Mouvements Célestes (cit. on p. 2).
- Miholics, M., J. M. D. Kruijssen, and A. Sills (2017). “A tight relation between the age distributions of stellar clusters and the properties of the interstellar medium in the host galaxy”. MNRAS 470, 1421–1435. arXiv: 1705.10803 (cit. on pp. 9, 132, 138).
- Miller, Tim B. et al. (2020). “Dynamical self-friction: how mass loss slows you down”. MNRAS 495.4, 4496–4507. arXiv: 2001.06489 [astro-ph.GA] (cit. on p. 111).
- Milone, A. P. et al. (2017). “The Hubble Space Telescope UV Legacy Survey of Galactic globular clusters - IX. The Atlas of multiple stellar populations”. MNRAS 464, 3636–3656. arXiv: 1610.00451 [astro-ph.SR] (cit. on pp. 10, 135).
- Moore, B. et al. (2006). “Globular clusters, satellite galaxies and stellar haloes from early dark matter peaks”. MNRAS 368, 563–570. eprint: astro-ph/0510370 (cit. on pp. 4, 134, 137).
- Muratov, A. L. and O. Y. Gnedin (2010). “Modeling the Metallicity Distribution of Globular Clusters”. ApJ 718, 1266–1288. arXiv: 1002.1325 [astro-ph.GA] (cit. on p. 11).
- Murray, Norman and Mubdi Rahman (2010). “Star Formation in Massive Clusters Via the Wilkinson Microwave Anisotropy Probe and the Spitzer Glimpse Survey”. ApJ 709.1, 424–435. arXiv: 0906.1026 [astro-ph.GA] (cit. on p. 115).
- Murray, Stephen D. and Douglas N. C. Lin (1992). “Globular Cluster Formation: The Fossil Record”. ApJ 400, 265 (cit. on p. 5).
- Myeong, G. C. et al. (2018). “The Sausage Globular Clusters”. ApJ 863.2, L28, L28. arXiv: 1805.00453 [astro-ph.GA] (cit. on pp. 13, 136, 140).
- Myeong, G. C. et al. (2019). “Evidence for two early accretion events that built the Milky Way stellar halo”. MNRAS 488.1, 1235–1247. arXiv: 1904.03185 [astro-ph.GA] (cit. on p. 13).
- Navarro, J. F., C. S. Frenk, and S. D. M. White (1997). “A Universal Density Profile from Hierarchical Clustering”. ApJ 490, 493–+. eprint: arXiv:astro-ph/9611107 (cit. on p. 113).
- Nelson, Dylan et al. (2018). “First results from the IllustrisTNG simulations: the galaxy colour bimodality”. MNRAS 475.1, 624–647. arXiv: 1707.03395 [astro-ph.GA] (cit. on p. 114).
- Niederhofer, F. et al. (2017). “The search for multiple populations in Magellanic Cloud clusters - I. Two stellar populations in the Small Magellanic Cloud globular cluster NGC 121”. MNRAS 464.1, 94–103. arXiv: 1609.01595 [astro-ph.SR] (cit. on p. 8).
- Noeske, K. G. et al. (2007). “Star Formation in AEGIS Field Galaxies since $z=1.1$: The Dominance of Gradually Declining Star Formation, and the Main Sequence of Star-forming Galaxies”. ApJ 660.1, L43–L46. arXiv: astro-ph/0701924 [astro-ph] (cit. on p. 8).
- North, Eve V. et al. (2019). “WISDOM project - V. Resolving molecular gas in Keplerian rotation around the supermassive black hole in NGC 0383”. MNRAS 490.1, 319–330. arXiv: 1909.05884 [astro-ph.GA] (cit. on p. 96).
- Oklopčić, A. et al. (2017). “Giant clumps in the FIRE simulations: a case study of a massive high-redshift galaxy”. MNRAS 465, 952–969. arXiv: 1603.03778 (cit. on p. 104).

- Padoan, Padoan et al. (2017). “Supernova Driving. IV. The Star-formation Rate of Molecular Clouds”. *ApJ* 840, 48, 48. arXiv: 1702.07270 (cit. on p. 95).
- Padoan, Paolo, Troels Haugbølle, and Åke Nordlund (2012). “A Simple Law of Star Formation”. *ApJ* 759.2, L27, L27. arXiv: 1208.3758 [astro-ph.GA] (cit. on p. 95).
- Parmentier, G. and G. Gilmore (2007). “The origin of the Gaussian initial mass function of old globular cluster systems”. *MNRAS* 377, 352–372. eprint: arXiv:astro-ph/0702258 (cit. on p. 8).
- Peebles, P. J. E. (1984). “Dark matter and the origin of galaxies and globular star clusters”. *ApJ* 277, 470–477 (cit. on p. 5).
- Peebles, P. J. E. and R. H. Dicke (1968). “Origin of the Globular Star Clusters”. *ApJ* 154, 891 (cit. on pp. 5, 141).
- Pfeffer, Joel L. et al. (2018). “The E-MOSAICS project: simulating the formation and co-evolution of galaxies and their star cluster populations”. *MNRAS* 475, 4309–4346. arXiv: 1712.00019 (cit. on pp. 9, 12, 13, 91, 92, 101, 102, 108, 109, 112, 114, 122, 133, 139, 141).
- Pfeffer, Joel L. et al. (2019a). “The evolution of the UV luminosity function of globular clusters in the E-MOSAICS simulations”. *MNRAS* 487.4, 4550–4564. arXiv: 1906.01755 [astro-ph.GA] (cit. on pp. v, 140).
- Pfeffer, Joel L. et al. (2019b). “Young star cluster populations in the E-MOSAICS simulations”. *MNRAS*, arXiv:1907.10118, arXiv:1907.10118. arXiv: 1907.10118 [astro-ph.GA] (cit. on pp. iv, 13, 102, 139).
- Pfeffer, Joel L. et al. (2020). “Predicting accreted satellite galaxy masses and accretion redshifts based on globular cluster orbits in the E-MOSAICS simulations”. *arXiv e-prints*, arXiv:2003.00076, arXiv:2003.00076. arXiv: 2003.00076 [astro-ph.GA] (cit. on p. iv).
- Pickering, Edward C. (1889). “Variable Star in Cluster G.C. 3636”. *Astronomische Nachrichten* 123, 207 (cit. on p. 2).
- Pillepich, Annalisa et al. (2018). “First results from the IllustrisTNG simulations: the stellar mass content of groups and clusters of galaxies”. *MNRAS* 475.1, 648–675. arXiv: 1707.03406 [astro-ph.GA] (cit. on p. 114).
- Piotto, G. et al. (2007). “A Triple Main Sequence in the Globular Cluster NGC 2808”. *ApJ* 661, L53–L56. eprint: arXiv:astro-ph/0703767 (cit. on pp. 10, 135).
- Planck Collaboration et al. (2014). “Planck 2013 results. XVI. Cosmological parameters”. *A&A* 571, A16, A16. arXiv: 1303.5076 [astro-ph.CO] (cit. on p. 114).
- Plummer, H. C. (1911). “On the problem of distribution in globular star clusters”. *MNRAS* 71, 460–470 (cit. on pp. 2, 126).
- Portegies Zwart, S. F., S. L. W. McMillan, and M. Gieles (2010). “Young Massive Star Clusters”. *ARA&A* 48, 431–493. arXiv: 1002.1961 [astro-ph.GA] (cit. on pp. 6, 104, 116, 131).
- Power, C. et al. (2003). “The inner structure of Λ CDM haloes - I. A numerical convergence study”. *MNRAS* 338.1, 14–34. arXiv: astro-ph/0201544 [astro-ph] (cit. on p. 93).

- Price, D. J. and J. J. Monaghan (2007). “An energy-conserving formalism for adaptive gravitational force softening in smoothed particle hydrodynamics and N-body codes”. MNRAS 374.4, 1347–1358. arXiv: astro-ph/0610872 [astro-ph] (cit. on p. 93).
- Prieto, J. L. and O. Y. Gnedin (2008). “Dynamical Evolution of Globular Clusters in Hierarchical Cosmology”. ApJ 689, 919–935 (cit. on pp. 8, 9, 101, 109, 112, 133).
- Recchi, S. et al. (2017). “Globular Cluster formation in a collapsing supershell”. Ap&SS 362.10, 183, 183. arXiv: 1708.05053 [astro-ph.GA] (cit. on p. 5).
- Reina-Campos, Marta and J. M. Diederik Kruijssen (2017). “A unified model for the maximum mass scales of molecular clouds, stellar clusters and high-redshift clumps”. MNRAS 469.2, 1282–1298. arXiv: 1704.00732 [astro-ph.GA] (cit. on pp. iii, 7, 104–106, 132, 134).
- Reina-Campos, Marta et al. (2018). “Dynamical cluster disruption and its implications for multiple population models in the E-MOSAICS simulations”. MNRAS 481.3, 2851–2857. arXiv: 1809.03499 [astro-ph.GA] (cit. on pp. iii, iv, 135).
- (2019). “Formation histories of stars, clusters, and globular clusters in the E-MOSAICS simulations”. MNRAS 486.4, 5838–5852. arXiv: 1905.02217 [astro-ph.GA] (cit. on pp. iii, 13, 134).
- Reina-Campos, Marta et al. (2020). “The mass fraction of halo stars contributed by the disruption of globular clusters in the E-MOSAICS simulations”. MNRAS 493.3, 3422–3428. arXiv: 1910.06973 [astro-ph.GA] (cit. on pp. iii, iv, 13, 136).
- Renaud, Florent (2010). “Dynamics of the Tidal Fields and Formation of Star Clusters in Galaxy Mergers”. PhD thesis. - (cit. on p. 128).
- Renaud, Florent, Oscar Agertz, and Mark Gieles (2017). “The origin of the Milky Way globular clusters”. MNRAS 465, 3622–3636. arXiv: 1610.03101 (cit. on p. 12).
- Renaud, Florent, Mark Gieles, and Christian M. Boily (2011). “Evolution of star clusters in arbitrary tidal fields”. MNRAS 418.2, 759–769. arXiv: 1107.5820 [astro-ph.CO] (cit. on pp. 108, 109, 126).
- Robertson, B. E. et al. (2015). “Cosmic Reionization and Early Star-forming Galaxies: A Joint Analysis of New Constraints from Planck and the Hubble Space Telescope”. ApJ 802, L19, L19. arXiv: 1502.02024 (cit. on p. 140).
- Robitaille, Thomas P. and Barbara A. Whitney (2010). “The Present-Day Star Formation Rate of the Milky Way Determined from Spitzer-Detected Young Stellar Objects”. ApJ 710.1, L11–L15. arXiv: 1001.3672 [astro-ph.GA] (cit. on p. 115).
- Schaye, J. et al. (2015). “The EAGLE project: simulating the evolution and assembly of galaxies and their environments”. MNRAS 446, 521–554. arXiv: 1407.7040 (cit. on pp. 12, 114, 136).
- Schechter, P. (1976). “An analytic expression for the luminosity function for galaxies.” ApJ 203, 297–306 (cit. on pp. 7, 104).
- Schweizer, Francois (1982). “Colliding and merging galaxies. I. Evidence for the recent merging of two disk galaxies in NGC 7252.” ApJ 252, 455–460 (cit. on p. 5).
- (1987). “Star Formation in Colliding and Merging Galaxies”. *Nearly Normal Galaxies. From the Planck Time to the Present*. Ed. by Sandra M. Faber, 18 (cit. on pp. 5, 6).

- Searle, L. and R. Zinn (1978). “Composition of halo clusters and the formation of the galactic halo.” *ApJ* 225, 357–379 (cit. on p. 4).
- Seitz, Ivo R. et al. (2013). “Three-dimensional delayed-detonation models with nucleosynthesis for Type Ia supernovae”. *MNRAS* 429.2, 1156–1172. arXiv: 1211.3015 [astro-ph.SR] (cit. on p. 98).
- Shapiro, Kristen L., Reinhard Genzel, and Natascha M. Förster Schreiber (2010). “Star-forming galaxies at $z \sim 2$ and the formation of the metal-rich globular cluster population”. *MNRAS* 403.1, L36–L40. arXiv: 1001.1740 [astro-ph.CO] (cit. on pp. 5, 101).
- Shapley, Harlow (1917). “Studies of Magnitude in Star Clusters. VII. A Method for the Determination of the Relative Distances of Globular Clusters”. *Proceedings of the National Academy of Science* 3.7, 479–484 (cit. on p. 2).
- (1918a). “No. 152. Studies based on the colors and magnitudes in stellar clusters. Seventh paper: The distances, distribution in space, and dimensions of 69 globular clusters.” *Contributions from the Mount Wilson Observatory / Carnegie Institution of Washington* 152, 1–28 (cit. on pp. 2–4, 9, 10, 136, 140).
- (1918b). “No. 155. Studies based on the colors and magnitudes in stellar clusters. Tenth paper: A critical magnitude in the sequence of stellar luminosities.” *Contributions from the Mount Wilson Observatory / Carnegie Institution of Washington* 155, 1–12 (cit. on pp. 3, 13).
- (1918c). “Studies based on the colors and magnitudes in stellar clusters. VI. On the determination of the distances of globular clusters.” *ApJ* 48, 89–124 (cit. on p. 2).
- (1918d). “Studies based on the colors and magnitudes in stellar clusters. VII. The distances, distribution in space, and dimensions of 69 globular clusters.” *ApJ* 48, 154–181 (cit. on p. 2).
- (1919). “Studies based on the colors and magnitudes in stellar clusters. XII. Remarks on the arrangement of the sidereal universe.” *ApJ* 49, 311–336 (cit. on p. 3).
- (1930). *Star Clusters*. Vol. 2 (cit. on p. 3).
- Shapley, Harlow and Martha B. Shapley (1919). “No. 161. Studies based on the colors and magnitudes in stellar clusters. Fourteenth paper: Further remarks on the structure of the galactic system.” *Contributions from the Mount Wilson Observatory / Carnegie Institution of Washington* 161, 1–34 (cit. on p. 3).
- Silva-Villa, E. et al. (2014). “The age distribution of stellar clusters in M83.” *MNRAS* 440, L116–L120. arXiv: 1402.3595 [astro-ph.GA] (cit. on p. 9).
- Smith, B. D. et al. (2017). “GRACKLE: a chemistry and cooling library for astrophysics”. *MNRAS* 466, 2217–2234. arXiv: 1610.09591 (cit. on pp. 14, 93, 137).
- Spitzer Lyman, Jr. (1940). “The stability of isolated clusters”. *MNRAS* 100, 396 (cit. on pp. 9, 109).
- (1958). “Disruption of Galactic Clusters.” *ApJ* 127, 17 (cit. on pp. 8, 9).
- (1987). *Dynamical evolution of globular clusters*. Princeton, NJ, Princeton University Press, 1987, 191 p. (cit. on pp. 9, 109, 112).
- Spitzer Lyman, Jr. and Richard Harm (1958). “Evaporation of Stars from Isolated Clusters.” *ApJ* 127, 544 (cit. on p. 9).

- Spitzer Lyman, Jr. and Michael H. Hart (1971). “Random Gravitational Encounters and the Evolution of Spherical Systems. I. Method”. *ApJ* 164, 399 (cit. on pp. 9, 109).
- Springel, V. (2005). “The cosmological simulation code GADGET-2”. *MNRAS* 364, 1105–1134. eprint: [arXiv:astro-ph/0505010](#) (cit. on pp. 93, 126).
- (2010). “E pur si muove: Galilean-invariant cosmological hydrodynamical simulations on a moving mesh”. *MNRAS* 401, 791–851. [arXiv: 0901.4107 \[astro-ph.CO\]](#) (cit. on pp. 92, 126, 141).
- Springel, V., T. Di Matteo, and L. Hernquist (2005). “Modelling feedback from stars and black holes in galaxy mergers”. *MNRAS* 361, 776–794. eprint: [arXiv:astro-ph/0411108](#) (cit. on p. 112).
- Springel, V. et al. (2001). “Populating a cluster of galaxies - I. Results at $z=0$ ”. *MNRAS* 328, 726–750. eprint: [astro-ph/0012055](#) (cit. on pp. 111, 115).
- Sukhbold, T. et al. (2016). “Core-collapse Supernovae from 9 to 120 Solar Masses Based on Neutrino-powered Explosions”. *ApJ* 821, 38, 38. [arXiv: 1510.04643 \[astro-ph.HE\]](#) (cit. on p. 97).
- Sun, Jiayi et al. (2018). “Cloud-scale Molecular Gas Properties in 15 Nearby Galaxies”. *ApJ* 860.2, 172, 172. [arXiv: 1805.00937 \[astro-ph.GA\]](#) (cit. on p. 138).
- Tacconi, L. J. et al. (2013). “Phibss: Molecular Gas Content and Scaling Relations in $z \sim 1$ -3 Massive, Main-sequence Star-forming Galaxies”. *ApJ* 768, 74, 74. [arXiv: 1211.5743 \[astro-ph.CO\]](#) (cit. on pp. 6, 102, 138).
- Toomre, A. (1964). “On the gravitational stability of a disk of stars”. *ApJ* 139, 1217–1238 (cit. on pp. 7, 132).
- Trenti, M., P. Padoan, and R. Jimenez (2015). “The Relative and Absolute Ages of Old Globular Clusters in the Λ CDM Framework”. *ApJ* 808, L35, L35. [arXiv: 1502.02670](#) (cit. on pp. 5, 137).
- Truelove, J. Kelly et al. (1997). “The Jeans Condition: A New Constraint on Spatial Resolution in Simulations of Isothermal Self-gravitational Hydrodynamics”. *ApJ* 489.2, L179–L183 (cit. on p. 94).
- Trujillo-Gomez, Sebastian, Marta Reina-Campos, and J. M. Diederik Kruijssen (2019). “A model for the minimum mass of bound stellar clusters and its dependence on the galactic environment”. *MNRAS* 488.3, 3972–3994. [arXiv: 1907.04861 \[astro-ph.GA\]](#) (cit. on pp. iv, 7, 101, 105, 106, 115, 143).
- Trujillo-Gomez, Sebastian et al. (2020). “The kinematics of globular cluster populations in the E-MOSAICS simulations and their implications for the assembly history of the Milky Way”. *arXiv e-prints*, [arXiv:2005.02401](#), [arXiv:2005.02401](#). [arXiv: 2005.02401 \[astro-ph.GA\]](#) (cit. on pp. iv, 13, 142).
- Trumpler, Robert Julius (1929). “Comparison and classification of star-clusters”. *Publications of the Allegheny Observatory of the University of Pittsburgh* 6.4, 45–74 (cit. on p. 3).
- (1930a). “Globular Star Clusters”. *Leaflet of the Astronomical Society of the Pacific* 1.29, 117 (cit. on p. 3).
- (1930b). “Preliminary results on the distances, dimensions and space distribution of open star clusters”. *Lick Observatory Bulletin* 420, 154–188 (cit. on pp. 4, 136).

- (1931). “Star Clusters: A Review”. *PASP* 43.252, 145 (cit. on p. 3).
- Usher, Christopher et al. (2018). “The origin of the ‘blue tilt’ of globular cluster populations in the E-MOSAICS simulations”. *MNRAS* 480.3, 3279–3301. arXiv: 1807.03084 [astro-ph.GA] (cit. on pp. v, 13).
- Utomo, Dyas et al. (2018). “Star Formation Efficiency per Free-fall Time in nearby Galaxies”. *ApJ* 861.2, L18, L18. arXiv: 1806.11121 [astro-ph.GA] (cit. on p. 105).
- van den Bergh, Sidney (1962). “The Old Galactic Cluster NGC 7142 and Stellar Evolution”. *JRASC* 56, 41 (cit. on p. 9).
- (1971). “The Post-Eruptive Galaxy M 82”. *A&A* 12, 474 (cit. on p. 5).
- van Dokkum, Pieter et al. (2018). “A galaxy lacking dark matter”. *Nature* 555.7698, 629–632. arXiv: 1803.10237 [astro-ph.GA] (cit. on p. 140).
- VandenBerg, D. A. et al. (2013). “The Ages of 55 Globular Clusters as Determined Using an Improved $\Delta V^{\text{HB}}_{\text{TO}}$ Method along with Color-Magnitude Diagram Constraints, and Their Implications for Broader Issues”. *ApJ* 775, 134, 134. arXiv: 1308.2257 [astro-ph.GA] (cit. on pp. 8, 13, 134, 140).
- Vanzella, E. et al. (2017). “Paving the way for the JWST: witnessing globular cluster formation at $z > 3$ ”. *MNRAS* 467.4, 4304–4321. arXiv: 1612.01526 [astro-ph.GA] (cit. on pp. 8, 142).
- Vanzella, E. et al. (2019). “Massive star cluster formation under the microscope at $z = 6$ ”. *MNRAS* 483.3, 3618–3635. arXiv: 1809.02617 [astro-ph.GA] (cit. on pp. 8, 142).
- Vanzella, E. et al. (2020). “Ionizing the intergalactic medium by star clusters: the first empirical evidence”. *MNRAS* 491.1, 1093–1103. arXiv: 1904.07941 [astro-ph.GA] (cit. on pp. 8, 142).
- Vasiliev, Eugene (2019). “Proper motions and dynamics of the Milky Way globular cluster system from Gaia DR2”. *MNRAS* 484.2, 2832–2850. arXiv: 1807.09775 [astro-ph.GA] (cit. on p. 140).
- Vassiliadis, E. and P. R. Wood (1993). “Evolution of Low- and Intermediate-Mass Stars to the End of the Asymptotic Giant Branch with Mass Loss”. *ApJ* 413, 641 (cit. on pp. 97, 108).
- Vietri, Mario and Enrico Pesce (1995). “Yet Another Theory for the Origin of Halo Globular Clusters and Spheroid Stars”. *ApJ* 442, 618 (cit. on p. 5).
- Villanova, S. et al. (2013). “Ruprecht 106: The First Single Population Globular Cluster?” *ApJ* 778.2, 186, 186. arXiv: 1310.5900 [astro-ph.GA] (cit. on p. 10).
- Webb, Jeremy J. and Jo Bovy (2019). “Searching for the GD-1 stream progenitor in Gaia DR2 with direct N-body simulations”. *MNRAS* 485.4, 5929–5938. arXiv: 1811.07022 [astro-ph.GA] (cit. on p. 143).
- (2020). “And In The Darkness Unbind Them: High-Resolution Simulations of Dark Matter Subhalo Disruption in a Milky Way-like Tidal Field”. *arXiv e-prints*, arXiv:2006.06695, arXiv:2006.06695. arXiv: 2006.06695 [astro-ph.GA] (cit. on p. 143).
- Webb, Jeremy J., Marta Reina-Campos, and J. M. Diederik Kruijssen (2019a). “A systematic analysis of star cluster disruption by tidal shocks - I. Controlled N-body simulations and a new theoretical model”. *MNRAS* 486.4, 5879–5894. arXiv: 1812.00014 [astro-ph.GA] (cit. on pp. iii, 9, 101, 110, 112, 133).

- Webb, Jeremy J. et al. (2019b). “Modelling the effects of dark matter substructure on globular cluster evolution with the tidal approximation”. *MNRAS* 488.4, 5748–5762. arXiv: 1907.13132 [astro-ph.GA] (cit. on p. 143).
- Weinberg, M. D. (1994a). “Adiabatic invariants in stellar dynamics. 1: Basic concepts”. *AJ* 108, 1398–1402. eprint: arXiv:astro-ph/9404015 (cit. on pp. 9, 110, 133).
- (1994b). “Adiabatic invariants in stellar dynamics. 2: Gravitational shocking”. *AJ* 108, 1403–1413. eprint: arXiv:astro-ph/9404016 (cit. on pp. 9, 110, 133).
- (1994c). “Adiabatic invariants in stellar dynamics, 3: Application to globular cluster evolution”. *AJ* 108, 1414–1420. eprint: arXiv:astro-ph/9404017 (cit. on pp. 9, 110, 133).
- Weinberger, Rainer, Volker Springel, and Rüdiger Pakmor (2019). “The Arepo public code release”. *arXiv e-prints*, arXiv:1909.04667, arXiv:1909.04667. arXiv: 1909.04667 [astro-ph.IM] (cit. on pp. 92, 126, 141).
- Whitaker, Katherine E. et al. (2012). “The Star Formation Mass Sequence Out to $z = 2.5$ ”. *ApJ* 754.2, L29, L29. arXiv: 1205.0547 [astro-ph.CO] (cit. on p. 8).
- Whitmore, Bradley C. and Francois Schweizer (1995). “Hubble Space Telescope Observations of Young Star Clusters in NGC 4038/4039, “The Antennae” Galaxies”. *AJ* 109, 960 (cit. on pp. 6, 101).
- Whitmore, Bradley C. et al. (1999). “The Luminosity Function of Young Star Clusters in “the Antennae” Galaxies (NGC 4038-4039)”. *AJ* 118.4, 1551–1576. arXiv: astro-ph/9907430 [astro-ph] (cit. on pp. 6, 101).
- Woltjer, L. (1975). “The galactic halo: globular clusters.” *A&A* 42, 109–118 (cit. on p. 4).
- Wong, Tony and Leo Blitz (2002). “The Relationship between Gas Content and Star Formation in Molecule-rich Spiral Galaxies”. *ApJ* 569.1, 157–183. arXiv: astro-ph/0112204 [astro-ph] (cit. on p. 95).
- Zepf, Stephen E. et al. (1999). “The Formation and Evolution of Candidate Young Globular Clusters in NGC 3256”. *AJ* 118.2, 752–764. arXiv: astro-ph/9904247 [astro-ph] (cit. on pp. 6, 101).
- Zhang, Q. and S. M. Fall (1999). “The Mass Function of Young Star Clusters in the “Antennae” Galaxies”. *ApJ* 527, L81–L84 (cit. on p. 104).
- Zinn, R. (1985). “The Globular Cluster System of the Galaxy. IV. The Halo and Disk Subsystems”. *ApJ* 293, 424 (cit. on pp. 3, 4, 134, 137).